

Design of 2D Sparse Array Transducers for Anomaly Detection associated with a Transcranial Ultrasound System

Xiaotong Li

Department of Electronic and Electrical Engineering

University of Strathclyde

A thesis submitted for the degree of

Doctor of Philosophy

July 2020

Copyright

This thesis is the result of the author's original research. It has been composed by the author and has not been previously submitted for examination which has led to the award of a degree.

The copyright of this thesis belongs to the author under the terms of the United Kingdom Copyright Acts as qualified by University of Strathclyde Regulation 3.50. Due acknowledgement must always be made of the use of any material contained in, or derived from, this thesis.

Signed:

Date:

Acknowledgements

It has been almost five years since I started my PhD with the Centre for Ultrasonic Engineering (CUE). This experience has become one of the most valued experiences in my life. I would like to take this opportunity to express my thanks to all the people who have helped me during the past few years.

Firstly, I would like to thank my supervisors, Prof. Anthony Gachagan and Dr Paul Murray, for their supervision and guidance through my PhD. It has been a great honour and valuable experience to work with them. They have always been supportive and patient, even when the project didn't go well. The knowledge they taught me would be a great help to my future work.

Secondly, I would like to say thanks to Thomas McCunnie, Grant Smillie, John Mackersie, and Alexander Ward, who have offered great help in designing and manufacturing the transducers and other experimental equipment relative to my project.

Thirdly, I want to thank all the members in CUE. They are always enthusiastic and willing to help. Special thanks to Dr Richard O'Leary, Dr Jerzy Dziwierz, Dr Zhen Qiu, and Dr David Line, who have helped me a lot in both academic knowledge and experiment process.

I would also like to thank my friends for being there with me in the past few years. It was their help that supported me through the difficult times.

Finally, I would like to thank my family for their support, both mentally and financially. I am grateful that they always respect and support my decisions. I might not be able to get so far without their support.

Abstract

Ultrasound imaging is a low cost and non-invasive technique, with many biomedical and industrial applications. In many applications, operator dependency can significantly influence the quality of the acquired information. Transcranial ultrasound is one such application, and this Thesis will investigate both transducer design and image processing techniques inspired by the desire to improve the ability of an ultrasonic system to detect and size anomalies in the blood flow.

Aperiodic sparse 2D ultrasonic array configurations, including random array, log spiral array, and sunflower spiral array, have been considered for their potential as a conformable transducer able to image within a focal range of 30-80 mm, at an operating frequency of 2 MHz. Optimisation of the imaging performance of potential array patterns has been undertaken based on their simulated far field directivity functions. Subsequently, two log spiral array patterns have been selected: one is the overall optimal design; the other is a compromise design to accommodate in-house manufacturing limitations. Both conventional 1-3 (C13) piezocomposite and piezoceramic fibre Composite Element Composite Array Transducer (CECAT) structures have been fabricated and characterised. The CECAT device provides a conformable piezocomposite material and demonstrated reduced mechanical cross-talk between neighbouring array elements and improved the operational bandwidth, while the

mechanically stiff C13 devices perform better in terms of sensitivity. Moreover, the C13 device incorporating the overall optimal array pattern performs best in terms of the image background noise level, while for transducers based on the compromise design, the CECAT device offers better axial resolution when imaging multiple reflectors.

Image processing algorithms, such as Hough transform and Morphological Opening, have been implemented to automatically detect and dimension particles located within a fluid-filled tube structure, in a variety of experimental scenarios. This includes bespoke phantoms using tissue mimicking material to simulate a basic transcranial ultrasound arrangement. The image processing algorithms were initially developed using data collected from a commercial 1D linear array transducer. Subsequent experiments using the fabricated CECAT log spiral 2D array transducer demonstrated that this algorithmic approach was able to detect the walls of the tube structure and stationary anomalies within the tube with a precision of ~ 0.1 mm.

Contents

Contents	vi
List of Figures	xi
List of Tables	xxxi
Abbreviations	xxxiii
Symbols	xxxv
1. Introduction.....	1
1.1. Motivation.....	1
1.1.1. Background.....	1
1.1.2. Objectives.....	...4
1.2. Contribution to Knowledge.....	5
1.3. Thesis Structure.....	7
1.4. Publications.....	9
2. Background Review.....	10
2.1. Introduction.....	10
2.2. Piezoelectric Effect.....	10
2.3. Piezoelectric Composite Material.....	14
2.3.1. Conventional 1-3 Piezocomposite.....	16
2.3.2. Composite Element Composite Array Configuration.....	23

2.3.3. Alternative 1-3 Composite Configurations and Manufacturing Techniques	25
2.4. Ultrasonic Transducers	28
2.4.1. Structure of Ultrasonic Transducers	29
2.4.2. Single-element Ultrasonic Transducers	32
2.4.3. Ultrasonic Arrays	33
2.5. Field Modelling Algorithm	41
2.5.1. Rayleigh Integral Method	42
2.5.2. Spatial Impulse Response Method	44
2.5.3. Angular Spectrum Method	44
2.5.4. Fourier Transform Method	45
2.5.5. Finite Element Analysis	47
2.6. Ultrasonic Imaging Algorithms	48
2.6.1. Plane B-scan	51
2.6.2. Focused B-scan	52
2.6.3. Sector B-scan	53
2.6.4. Total Focusing Method	55
2.6.5. Doppler Imaging	56
2.7. Standard Image Processing Algorithms	57
2.7.1. Difference Imaging	57
2.7.2. Morphological Image Processing	58
2.7.3. Hough Transform	62
2.8. Review of Transcranial Ultrasound Applications	64

2.8.1.	Conventional Transcranial Doppler Ultrasound	65
2.8.2.	Transcranial Colour-Coded Duplex Ultrasonography.....	65
2.8.3.	3D Transcranial Ultrasound Imaging	66
3.	Design of 2D Sparse Array Pattern	68
3.1.	Introduction.....	68
3.2.	Peak Side Lobe Level (<i>PSL</i>) and Integrated Side Lobe Ratio (<i>ISLR</i>)	70
3.3.	Sparse Array Configurations.....	73
3.3.1.	Random Array Element Approach.....	73
3.3.2.	Logarithmic Spiral Array	78
3.3.3.	Special Fermat Spiral Array – Sunflower Spiral Array	83
3.4.	Optimisation Process	90
3.5.	Optimisation Process – Phase I	99
3.5.1.	Step 1 – Simulate All Three Configurations.....	99
3.5.2.	Step 2 – Analysis of Random Array Configuration	102
3.5.3.	Step 2 – Analysis of Log Spiral Array	104
3.5.4.	Step 2 – Analysis of Sunflower Spiral Array.....	107
3.5.5.	Summary of Optimisation Process – Phase I	109
3.6.	Optimisation Process – Phase II.....	112
3.7.	Summary.....	116
4.	Transducer Manufacturing and Characterisation	119
4.1.	Introduction.....	119
4.2.	Manufacturing Prototype Transducers.....	120

4.2.1.	Piezoelectric Active Layer.....	120
4.2.2.	Electrical Connection	137
4.2.3.	Housing	141
4.2.4.	Matching Layer	142
4.2.5.	Final Device Packaging	146
4.3.	Prototype Transducers Characterisation.....	147
4.3.1.	Electrical Impedance Response	147
4.3.2.	Mechanical Cross-Talk Between Neighbouring Array Elements	155
4.3.3.	Pulse-Echo Test	163
4.4.	Summary.....	170
5.	Development of Image Processing Algorithms	172
5.1.	Introduction.....	172
5.2.	Data Acquisition	173
5.3.	Development Process of the Tube Size Estimation Algorithm	174
5.4.	Development Process of the Particle Detection Algorithm	183
5.5.	Summary.....	197
6.	System Integration and Evaluation	198
6.1.	Introduction.....	198
6.2.	Imaging Small Diameter Reflectors	200
6.2.1.	Imaging Small Diameter Reflectors with Different Size	200
6.2.2.	Imaging Single Small Diameter Reflector at Different Distances	209
6.3.	Imaging Multiple Reflectors	213

6.4. Imaging Tube-Tank Phantom.....	217
6.5. Imaging Medical Phantom	223
6.6. Imaging Lab Phantoms	231
6.6.1. Imaging Lab Phantoms with Tube Placed Along the <i>y-axis</i>	234
6.6.2. Imaging the Angle H Phantom	242
6.7. Summary.....	244
7. Conclusion and Future Work	248
7.1. Conclusion.....	248
7.2. Future Work	253
7.2.1. Modification of the Manufacturing Process	253
7.2.2. Modification of the Phantoms.....	254
7.2.3. Modification of the Ultrasonic Imaging Methods	255
References	256
Appendices	270
Appendix A: Properties for Materials Selected from CUE Database	270
Appendix B: TFM Images of Single Small Diameter Reflectors with Different Size from the Three Prototype Transducers.....	271
Appendix C: TFM Images of 0.8 mm Small Diameter Reflector within Different Depth Range from CECAT_79.....	275
Appendix D: TFM Images of the Wire Phantom from the Three Prototype Transducers.....	277

List of Figures

Figure 2.1 Illustration of (a) the direct piezoelectric effect and (b) the converse piezoelectric effect. The grey blocks represent the piezoelectric materials before (the solid line) and after (the dashed line) applying excitation source. The blue indicators represent the external source (arrows stand for the pressure and + - represent the electrical energy) applied on the piezoelectric materials. 11

Figure 2.2 The coordinate system defined in the IEEE standard on piezoelectricity [17].
..... 13

Figure 2.3 Illustration of the (a) 1-3, (b) 2-2, and (c) 0-3 composite connectivity patterns. The dark grey represents the piezoelectric material, and the light grey represents the polymer. 15

Figure 2.4 Illustration of the unit cell of the C13 composite. The dark grey represents the piezoelectric material, while the light grey represents the polymer. 16

Figure 2.5 Example of the impedance response for the thickness-mode..... 20

Figure 2.6 Illustration of the ‘dice and fill’ method. The dark grey represents the piezoelectric material, while the light grey represents the polymer. The silver structure shown in the second step is the dicing saw. 22

Figure 2.7 Illustration of top view for (a) the regular CECAT and (b) the fibre CECAT. The dark grey represents the piezoelectric material while the light grey represents the polymer. 24

Figure 2.8 Illustration of typical ultrasonic transducer structure..... 29

Figure 2.9 Illustration of the transmission and reflection for an ultrasound wave (*UTinput*) when arriving at an interface between two materials which have different acoustic impedances ($Z1$ and $Z2$)..... 32

Figure 2.10 Illustration of achieving (a) the unfocused beam, (b) the focused beam, (c) the steering beam, and (d) the focused and steering beam by applying corresponding focal law. The blue bars represent the array elements. 34

Figure 2.11 Examples of typical array configurations including (a) the 1D linear array, (b) the 2D matrix array, and (c) the 2D annular array, where blue indicates an array element. 35

Figure 2.12 Normalised simulated directivity functions for an 81x81 element dense array (the red line) and a 5x5 element sparse array (the black line). The aperture size is set to be the same for both arrays..... 37

Figure 2.13 Examples of the sparse array. From (a) to (f) are the grid array, the segmented annular array, the Vernier array, the random array, the Fermat spiral array, and the log spiral array. The blue circles represent the elements which work as a transmitter and receiver. The yellow circles represent the elements which work as a receiver only. 39

Figure 2.14 Illustration of inter-element cross-talk in an ultrasonic array. (a) represents the ideal vibration, and (b) represents the real situation with cross-talk..... 41

Figure 2.15 Illustration of the Rayleigh Integral Method. The vibration surface (the unfilled large rectangle) is in the XY plane. dA (the filled small rectangle) represents the sub-area which is extracted from the vibration surface.	43
Figure 2.16 Illustration of the parameters needed in conversing the 3D coordinate into the u-v space.	46
Figure 2.17 Example results for analysing a 3x3 element array using the 2D FFT method. (a) The blue points represent the centres for the elements. (b) The binary image of the array pattern. (c) The estimated far-field directivity function generated by applying 2D FFT to (b).	47
Figure 2.18 Illustration of the basic ultrasonic imaging principle.	49
Figure 2.19 Illustration of the Full Matrix Capture (FMC) process.	50
Figure 2.20 Schematic diagram of plane B-scan, where shaded array elements constitute the active sub-aperture.	52
Figure 2.21 Schematic diagram of focused B-scan, where shaded array elements constitute the active sub-aperture.	53
Figure 2.22 Schematic diagram of sector B-scan, where shaded array elements constitute the active sub-aperture.	54
Figure 2.23 Schematic diagram of total focusing method (TFM), where shaded array element is the transmitter and all array elements are receivers.	55
Figure 2.24 Illustration of the Doppler Effect.	56
Figure 2.25 Illustration of the difference imaging algorithm.	58

Figure 2.26 A simple example of applying erosion and dilation on (a) a 9x9 pixel image using (b) a 3x3 pixel SE. (c) The resultant image for erosion. (d) The resultant image for dilation..... 59

Figure 2.27 Illustration of applying (a) erosion, (b) dilation, (c) opening, and (d) closing to (e) the original image. 61

Figure 2.28 Illustration of the basic idea for Hough Transform. The blue line in the x - y coordinate system (a) is transferred into the blue point in the γ - r coordinate system (b). The red points at the blue line are transferred into the red curves in the γ - r coordinate system (b). 63

Figure 2.29 Illustration of detecting lines in an image using the Hough Transform. (a) The original image. (b) The Hough space generated from (a). The red spots represent the peaks in the Hough transform, which are formed by the lines in the original image. (c) The original image with detected lines, which are marked using green lines..... 63

Figure 2.30 The three acoustic windows used in the TCD test [104]. 64

Figure 3.1 2D dense matrix array with 4669 elements. The ratio of element diameter to element gap is 4:1. 69

Figure 3.2 Three sparse array configurations which have been simulated in this work: (a) random array; (b) log spiral array; and (c) Fermat spiral array..... 70

Figure 3.3 Illustration of main lobe and side lobes. 71

Figure 3.4 Illustration of the method used to determine the upper limit of elements within a random array. The red markers (+) represent the centre of each circle. The black circle represents the aperture with a radius of R . The black square is the maximum

internal square of the black circle (aperture). The red square represents the sub-square with ele_pitch side length. The red circle is the element with the radius ele_r . The distance between the centre of the red circles equals to ele_pitch . Assuming the available aperture area is within the black rectangle, and the area of each element is the area of the red rectangle. 74

Figure 3.5 The process to generate a random array configuration. In (a), the black dots represent the remaining points at the end of each step. The red markers represent the removed or alternative points. The large red circle and the black circle represent the 3 cm aperture and the reduced aperture, respectively. Step 1-4 are repeated until all the remaining points in step 4 are inside the black circle. This final stage is represented in (b) and illustrates the random array configuration. The blue circles are the array elements. 77

Figure 3.6 An illustration of the minimum distance between the first elements of adjacent spirals. a is a constant parameter representing the minimum distance from the origin to an arm and θ is the rotational angle between adjacent spiral arms. 79

Figure 3.7 Influence of parameter a on PSL and $ISLR$. The blue line represents the change of PSL , while the red line represents the change of $ISLR$ 80

Figure 3.8 The maximum radial distance and maximum polar angle of a log spiral arm configuration within a fixed aperture size. 82

Figure 3.9 Fermat spiral with symmetric branches. The blue line is the positive branch, while the red line is the negative branch. 84

Figure 3.10 The process to generate a sunflower spiral array using (a). Method A and (b). Method B. The black dots represent the initial points. The red dots represent the new

points after expanding the array which is formed by the initial points. The small red circles represent the pair of elements which gives min_dis . The small blue circles are the array elements. The dashed circle and the red circle are the reduced aperture size and the original aperture size separately..... 88

Figure 3.11 Change of d over n and m . The value of dis is represented by colour. The right figure is the zoomed in result of the area within the black rectangle in the left figure. Under condition $n < m$, dis reaches its minimum when $m = 4$ and $n = 1$. The minimum point is marked by the red point. 89

Figure 3.12 Change of performance for 20 random array configurations which are generated using the same parameters..... 93

Figure 3.13 Performance of a random array configuration with respect to the number of elements within the array. 94

Figure 3.14 PSL and $ISLR$ performance of sunflower array configuration with respect to number of elements within the array. The sunflower array is formed by setting ‘ a_fmrt ’ first (Method A)..... 95

Figure 3.15 PSL and $ISLR$ performance of sunflower array configuration with respect to number of elements within the array. The sunflower array is formed by setting ‘ $nlast$ ’ first (Method B). 96

Figure 3.16 PSL and $ISLR$ with change of the number of arms within a log spiral array. The blue dots stand for the PSL values, while the red dots stand for the $ISLR$ values. .. 98

Figure 3.17 Optimisation results of the random array. The red dot represents the configuration that has the lowest *PSL* (-17.85 dB) with a corresponding *ISLR* of 2.92 dB. The configuration is formed using 0.9 mm *ele_r*, 0.25 mm *ele_gr*, and 94 *ele_num*... 100

Figure 3.18 Optimisation results of the log spiral array. The red dot represents the configuration that has the lowest *PSL* (-21.33 dB) with a corresponding *ISLR* of 3.07 dB. The configuration is formed using 0.7 mm *ele_r*, 0.45 mm *ele_gr*, 8 *ele_per_arm*, 17 arms, and 1.3 b..... 100

Figure 3.19 . Optimisation results of the sunflower array. The red dot represents the configuration that has the lowest *PSL* (-17.43 dB) with a corresponding *ISLR* of 1.8 dB. The configuration is formed using 0.7 mm *ele_r*, 0.3 mm *ele_gr*, and 181 *ele_num*... 101

Figure 3.20 Comparison of *ISLR* for log spiral array configurations with *PSL* lower than -19.5 dB..... 102

Figure 3.21 Random array configurations with *PSL* lower than -17 dB (blue line), or *ISLR* lower than 3 dB (yellow line) are shown in the plot. The black dots represent the configurations that meet both conditions. The red dots indicate the results of the minimum point as illustrated in Figure 3.16. 103

Figure 3.22 Log spiral array configurations with *PSL* lower than -20 dB (blue line), or *ISLR* lower than 4 dB (yellow line) are shown in the plot. The black dots represent the configurations that meet both conditions. The red dots indicate the results of the minimum point as illustrated in Figure 3.17. 105

Figure 3.23 Sunflower spiral array configurations with *PSL* lower than -17 dB (blue line), or *ISLR* lower than 2 dB (yellow line) are shown in the plot. The black dots

represent the configurations that meet both conditions. The red dots indicate the results of the minimum point as illustrated in Figure 3.18. 108

Figure 3.24 (a) The log spiral array, (c) the sunflower spiral array, and (e) the random array configurations designed from optimisation process (a) Phase I and (b, d, f) the corresponding directivity functions. The blue circles represent the array elements. The red circle represents the array aperture. The black dots are the centres of the array elements..... 111

Figure 3.25 Optimisation results for log spiral array with increased parameter, a . The red dot represents the configuration that has the lowest PSL (-20.29 dB) with a corresponding $ISLR$ of 3.32 dB. The configuration is formed using 0.7 mm ele_r , 0.4 mm ele_gr , 8 ele_per_arm , 15 arms, and 1.2 b. 113

Figure 3.26 Log spiral array configurations with PSL lower than -19 dB (blue line), or $ISLR$ lower than 3 dB (yellow line) are shown in the plot. The black dots represent the configurations that meet both conditions. The red dots indicate the results of the minimum point as illustrated in Figure 3.22. 114

Figure 3.27 (a) The log spiral array configuration designed from optimisation process Phase II and (b) the corresponding directivity function. The blue circles represent the array elements. The red circle represents the array aperture. The black dots are the centres of the array elements. 116

Figure 4.1 Illustration of the prototype transducers' structure. 120

Figure 4.2 The jig which was used in manufacturing the CECAT active layer. 122

Figure 4.3 (a) Top view and (b) side view of the fibre CECAT assembly after inserting PZT fibres.....	122
Figure 4.4 (a) The fibre CECAT assembly inside the rectangular mould. (b) The fully cured fibre CECAT piezocomposite block after removal from the mould.	124
Figure 4.5 (a) A test sample of a fibre CECAT piezocomposite block which was improperly cured. (b) A piece of fibre CECAT piezocomposite sliced from the block shown in (a).	124
Figure 4.6 The PZFlex model used to simulate the electrical impedance response for the centre element in the CECAT_79 active layer. Blue represents the PZT fibre, while cyan represents the medium set epoxy.	126
Figure 4.7 The simulated impedance response for the centre element in the CECAT_79 active layer. f_e is 1948 kHz, while f_m is 2491 kHz.....	126
Figure 4.8 The fibre CECAT active layer with the 79-element log spiral array pattern (a) before and (b) after applying electrodes.....	128
Figure 4.9 Poling process setup for the fibre CECAT active layer. The active layer is fixed under the circular plate of a jig. The poling voltage is 1.5kV.	128
Figure 4.10 The electrical impedance response for the centre element in the CECAT_79 active layer. The solid lines represent the experimental results (blue for impedance and orange for phase), while the dashed line represents the simulated results. The measured f_e is 2035 kHz and the measured f_m is 2538 kHz.....	129

Figure 4.11 The PZFlex model used to simulate the impedance response for the C13 piezocomposite active layer. Blue represents the PZT5A pillar, while cyan represents the medium set epoxy..... 130

Figure 4.12 The simulated impedance response for the C13 composite active layer. f_e is 1928 kHz, while f_m is 2438 kHz..... 131

Figure 4.13 Diced ceramic inside the mould and filled with medium set epoxy. 132

Figure 4.14 The C13_79 active layer (a) before applying electrodes and (b) after applying electrodes. 134

Figure 4.15 The impedance response of the C13_79 active layer. The solid lines represent the experimental results (blue for impedance and orange for phase), while the dashed line represents the re-simulated results at thickness of 0.78 mm. The measured f_e is 1877 kHz and the measured f_m is 2308 kHz. The simulated f_e is 1854 kHz and the simulated f_m is 2344 kHz..... 134

Figure 4.16 The C13_106 active layer (a) before applying electrodes and (b) after applying electrodes. 136

Figure 4.17 The impedance response of the C13_106 active layer. The solid lines represent the experimental results (blue for impedance and orange for phase), while the dashed line represents the re-simulated results at the increased thickness of 0.78 mm. The measured f_e is 1841 kHz and the measured f_m is 2280 kHz. The simulated f_e is 1854 kHz and the simulated f_m is 2344 kHz. 136

Figure 4.18 (a) The flexible PCB used to achieve electrical connection for CECAT_79 device. (b) Comparison of the circle pads pattern in flexible PCB and the array elements

in the CECAT_79 active layer. (c) Illustration of how the ground side of the CECAT_79 active layer is connected to the PCB.....	138
Figure 4.19 Illustration of the setup used to bond the active layer to the flexible PCB.	139
Figure 4.20 (a) Illustration of how the twisted-pair wires are connected to the PCB. (b) Illustration of the adaptor and the phased array controller. (c) Illustration of how the twisted-pair wires are connected to the adaptor through external connector housings.	140
Figure 4.21 (a) The housing which is used to package the active layer and the flexible PCB. (b) The lid of the housing. (c) The body of the housing.....	141
Figure 4.22 Simulated TVR results for an element of the CECAT active layer with (the solid line) and without (the dashed line) matching layer.	144
Figure 4.23 Simulated impedance response results for an element of the CECAT active layer with (the solid line) and without (the dashed line) matching layer.....	145
Figure 4.24 Illustration of the setup used to apply the matching layer.....	145
Figure 4.25 Front surface of (a) the C13_79, (b) the CECAT_79 and (c) the C13_106 after applying the matching layer.	146
Figure 4.26 Appearance of the fibre CECAT prototype transducer from different angles.	147
Figure 4.27 Impedance response of all array elements for (a) the C13_79 active layer, (b) the CECAT_79 active layer and (c) the C13_106 active layer.	148
Figure 4.28 Illustration of the element numbering scheme for (a) the 79-element array configuration and (b) the 106-element array configuration.	151

Figure 4.29 (a) *fe*, (b) *fm* and (c) *kt* of all 79 array elements for the CECAT_79 active layer. The black solid lines represent the mean values, while the red dash lines represent the $\pm 5\%$ bars..... 152

Figure 4.30 (a) *fe*, (b) *fm* and (c) *kt* of all 79 array elements for the C13_79 active layer. The black solid lines represent the mean values, while the red dash lines represent the $\pm 5\%$ bars..... 153

Figure 4.31 (a) *fe*, (b) *fm* and (c) *kt* of all 106 array elements for the C13_106 active layer. The black solid lines represent the mean values, while the red dash lines represent the $\pm 5\%$ bars..... 154

Figure 4.32 Illustration of the experimental set up for cross-talk measurement. 156

Figure 4.33 Illustration of how the LDV scanning has been processed for (a) the 79-element array pattern and (b) the 106-element array pattern. The black circle represents the fired array element, and the blue block represents the area that has been scanned. The grey circles represent the array elements which will be fired individually later. 157

Figure 4.34 Mechanical cross-talk contours for the CECAT_79 when firing the central element and the elements in the 3rd arm individually. (a) is the first element in the arm through to (f) being the outer most element in the arm, with (g) presenting the centre element result. The red circles represent the theoretical position of the neighbouring elements..... 160

Figure 4.35 Mechanical cross-talk contours for the C13_79 when firing the central element and the elements in the 3rd arm individually. (a) is the first element in the arm through to (f) being the outer most element in the arm, with (g) presenting the centre

element result. The red circles represent the theoretical position of the neighbouring elements.....	161
Figure 4.36 Mechanical cross-talk contours for the C13_106 when firing the central element and the elements in the 1st arm individually. (a) is the first element in the arm through to (g) being the outer most element in the arm, with (h) presenting the centre element result. The red circles represent the theoretical position of the neighbouring elements.....	162
Figure 4.37 Pulse echo test setup.....	164
Figure 4.38 Pulse echo response of the centre element for the CECAT_79.....	165
Figure 4.39 Pulse echo response of the centre element for the C13_79.....	166
Figure 4.40 Pulse echo response of the centre element for the C13_106.....	166
Figure 4.41 Pulse-echo response spectrum for all elements in (a) the CECAT_79, (b) the C13_79, and (c) the C13_106.....	169
Figure 5.1 Illustration of the experimental setup for imaging the tank-tube phantom using the 2.25 MHz 1D linear Array transducer.	174
Figure 5.2 TFM image of the tube with no particles from the 1D linear array transducer.	175
Figure 5.3 (a) The Original Frame (<i>OrgF</i>). (b) A zoomed-in area extracted from (a). (c) The Thresholded Frame (<i>TF</i>). (d) A zoomed-in area extracted from (c).	179
Figure 5.4 (a) Illustration of how the <i>TF</i> has been divided into blocks. The yellow dashed lines represent the block edges. (b) A block picked from the <i>TF</i> . (c) The intensity	

for the pixels marked using the yellow line, as shown in (b). The red dots are the pixels that have been selected to represent the tube wall.	180
Figure 5.5 The block from Figure 5.4(a) with only the four peak pixels of each column (the white pixels) remaining. The solid green lines represent the tube walls. The solid red line illustrates the distance from the middle point of the detected top inner wall (the red dot) to the bottom inner wall. The estimated inner diameter for the piece of the tube within this block is 3.45 mm.	182
Figure 5.6 The results after applying the tube size estimation algorithm across the entire Original Frame. The yellow dashed lines illustrate the edges of the blocks. The solid green lines are the detected inner walls. The red dots represent the middle point of the corresponding top inner wall, while the solid red lines illustrate the inner diameter estimated for each block.....	182
Figure 5.7 The blue line represents the estimated inner diameter for each block. The dashed red line represents the averaged inner diameter of the results, which is 3.47 mm.	183
Figure 5.8 Block diagram to illustrate the particle detecting algorithm.	184
Figure 5.9 (a) TFM image of the tube-tank phantom with three ball bearings (the bright spots between the tube walls) inside the tube from the 1D linear array transducer. (b) Greyscale image (Current Frame), which has been converted from (a).	185
Figure 5.10 (a), (b), and (c) are the first three frames from the image series, which have been used to created (d) the Background Frame.	187
Figure 5.11 The Difference Frame (<i>DF</i>) generated using the example Current Frame (<i>CF</i>) and the Background Frame (<i>BF</i>).	188

Figure 5.12 The Thresholded Difference Frame (*TDF*). 188

Figure 5.13 The 5x5 disk mask that has been used in the Morphological Opening step of the particle detection algorithm. 191

Figure 5.14 The Opened Frame (*OpnF*). The blue lines represent the RG, within which a particle has been detected. The dashed yellow lines indicate regions in which a particle has been detected. 191

Figure 5.15 The *RG* in (a) the Current Frame and (b) the Opened Frame where contains the 2 mm particle. (c) The result after multiplying (a) and (b). The red dot represents the estimated position of the 2 mm particle. 192

Figure 5.16 The *BLK(3)* which has been extracted from the Background Frame. The green lines indicate the detected inner walls of the tube. The red lines represent the distance from the detected position of the 2 mm particle (red dot) to the inner walls of the tube. 193

Figure 5.17 The Current Frame with the particles detected. The dashed yellow lines indicate the regions in which a particle has been detected. The solid red lines represent the distance from the particles (red dots) to the top and bottom inner walls of the tube (solid green lines). 194

Figure 5.18 Results for (a) the 2 mm particle, (b) the 1.5 mm particle, and (c) the 1 mm particle. The yellow lines represent the real size of the particles. The averaged estimated particle size is 2.02 mm for the 2 mm particle, 1.53 mm for the 1.5 mm particle, and 0.99 mm for the 1 mm particle., while the averaged tube inner diameter is 3.46 mm, 3.47 mm, and 3.45 mm, separately. 196

Figure 6.1 Illustration of the experimental setup for imaging a single small diameter reflector (brass rod).....	201
Figure 6.2 TFM images for imaging the 2 mm small diameter reflector using (a) the CECAT_79, (b) the C13_79, and (c) the C13_106. Colour scale is in dB.	203
Figure 6.3 TFM images for imaging the 0.4 mm small diameter reflector using (a) the CECAT_79 (b) the C13_79, and (c) the C13_106. Colour scale is in dB.	204
Figure 6.4 Rod size measurement errors with different thresholds for (a) the CECAT_79, (b) the C13_79, and (c) the C13_106.....	206
Figure 6.5 Simulated beam profile in Y-Z plane for (a) the CECAT_79 and (b) the C13_79. (c) and (d) are zoomed in images which have been extracted from (a) and (b), respectively.....	208
Figure 6.6 Axial resolution for all three transducers with -5 dB threshold.....	209
Figure 6.7 The TFM image of the 0.8 mm rod within the depth range of (a) 30 mm to 35 mm and (b) 75 mm to 80 mm.....	211
Figure 6.8 Measurement errors of the 0.8 mm rod imaged at a depth between 30 mm to 80 mm using the CECAT_79. The dots represent the values of the errors, while the bars represent the depth ranges.	212
Figure 6.9 Illustration of the experimental setup for imaging the wire phantom (Brass rods and the plastic box).	215
Figure 6.10 The TFM images of the wire phantom from (a) the CECAT_79, (b) the C13_79, and (c) the C13_106.....	215
Figure 6.11 The <i>sizem</i> results of (a) the 0.5 mm rod, (b) the 0.8 mm rod, (c) the 1.5 mm rod, and (d) the 2 mm rod. The black dashed lines represent the real size of the rods..	216

Figure 6.12 (a) An example TFM image of the tube with no particles inside from the CECAT and (b) the corresponding frame converted from (a). The yellow dashed lines illustrate the edges of the blocks that have been extracted from the frame. The solid green lines are the detected inner walls. Within each block, the red dot represents the middle point of the top inner wall, while the solid red lines illustrate the estimated inner diameter. The averaged estimated inner diameter of the tube computed from this frame is 3.4 mm. 219

Figure 6.13 TFM images of the tube with the 2 mm particle at different positions from the CECAT_79. 220

Figure 6.14 Results of (a) the 1 mm particle, (b) 1.5 mm particle, and (c) the 2 mm particle. The averaged estimated particle size is 1 mm for the 1 mm particle, 1.44 mm for the 1.5 mm particle, and 2.06 mm for the 2 mm particle. The estimated inner tube diameters are 3.4 mm for all three situations. 221

Figure 6.15 An example Current Frame from the CECAT_79 with the particles detected. The dashed yellow lines indicate the regions in which a particle has been detected. The solid red lines represent the distance from the particles (red dots) to the top and bottom inner walls of the tube (solid green lines). The estimated size is 1.1 mm for the 1 mm particle, 1.6 mm for the 1.5 mm particle, and 2.15 mm for the 2 mm particle. The averaged estimated inner diameter calculated from results of all three pieces of the tube within each *BLK* (the rectangle with dashed yellow edges) is 3.4 mm. 223

Figure 6.16 2D illustration of the experimental setup for imaging the MDU phantom using the CECAT_79. 224

Figure 6.17 TFM image of the MDU phantom from the CECAT_79. 225

Figure 6.18 TFM image of the tube-tank phantom from the CECAT_79. 226

Figure 6.19 Illustration of how the reflected signals are affected by the angle between the tube and the transducer. The angle between the tube and the transducer is (a) 0° (in parallel) and (b) α . TX represents the transmitted sound waves, and RX represents the reflected sound waves. 227

Figure 6.20 Illustration of creating different angles between the tube and the CECAT_79. 228

Figure 6.21 TFM images of the tank tube phantom with the tube placed at different angles. From (a) to (f), the angle between the tube and the transducer are 5° , 8° , 10° , 13° , 15° , and 20° , respectively. 229

Figure 6.22 TFM images of the MDU phantom from the 1D Linear Array Transducer with (a) the full 128 array elements and (b) the first 40 array elements. 230

Figure 6.23 Example lab phantom. 231

Figure 6.24 Illustrations of the basic structures of the lab phantoms. Name of the phantoms from (a) to (e) is the 55 mm phantom, the 65 mm phantom, the 75 mm phantom, the Angle V phantom, and the Angle H phantom, respectively. 233

Figure 6.25 Illustration of the experimental setup for imaging the lab phantom using the CECAT_79. 234

Figure 6.26 Example TFM images of (a) the 55 mm phantom, (b) the 65 mm phantom, (c) the 75 mm phantom, and (d) the Angle V phantom, with no particles from the CECAT_79. 236

Figure 6.27 The results after applying the tube size estimation algorithm to the frames which have been converted from the example TFM images of (a) the 55 mm phantom, (b) the 65 mm phantom, (c) the 75 mm phantom, and (d) the Angle V phantom, with no particles from the CECAT_79. The yellow dashed lines illustrate the edges of the blocks. The solid green lines are the detected inner walls. The red dots represent the middle point of the corresponding top inner wall, while the solid red lines illustrate the inner diameter estimated for each block. 237

Figure 6.28 Illustration of the size and shape of the TMM particle. The 2 mm ball bearing is used as a reference. 239

Figure 6.29 TFM image of (a) the 55 mm phantom, (b) the 65 mm phantom, (c) the 75 mm phantom, and (d) the Angle V phantom with the TMM particle placed inside the tube from the CECAT_79. 240

Figure 6.30 The results after applying the particle detection algorithm to the frames which have been converted from the example TFM images of (a) the 55 mm phantom, (b) the 65 mm phantom, (c) the 75 mm phantom, and (d) the Angle V phantom, with the TMM particle placed inside the tube from the CECAT_79. The dashed yellow lines indicate the regions in which a particle has been detected. The solid red lines represent the distance from the particles (red dots) to the top and bottom inner walls of the tube (solid green lines)..... 241

Figure 6.31 (a) An example TFM image of the Angle H phantom with no particles from the CECAT_79. (b) The frame converted from (a) which has been analysed using the tube size estimation algorithm. The yellow dashed lines illustrate the edges of the block that have been extracted from the frame. The solid green lines are the detected inner

walls, while the red dot represents the middle point of the top inner wall. The solid red line illustrates the estimated inner diameter, which is 3.2 mm. 243

Figure 6.32 (a) An example TFM image of the Angle H phantom with the TMM particle from the CECAT_79. (b) The frame converted from (a) which has been analysed using the particle size estimation algorithm. The dashed yellow lines indicate the region in which the TMM particle has been detected. The solid red line represents the distance from the particle (red dot) to the top and bottom inner walls of the tube (solid green lines). The estimated size of the TMM particle is 1.65 mm, while the estimated tube inner diameter is 3.2 mm..... 243

List of Tables

Table 2.1 Variables and coefficients in the piezoelectric equations..... 12

Table 3.1 Parameters and candidate values for each array configuration..... 92

Table 3.2 Parameters and candidate values used to determine interval of *num_of_arm*
..... 98

Table 3.3 Candidates for Random Array 104

Table 3.4 Alternative Designs for Log Spiral Array 106

Table 3.5 Alternative Designs for Sunflower Spiral Array..... 109

Table 3.6 Key parameters for selected configurations..... 110

Table 3.7 Alternative Designs for Log Spiral Array - Second Analysis 113

Table 3.8 Alternative Designs for Log Spiral Array - Second Analysis with Reduced
PSL interval..... 115

Table 3.9 Array Configuration Details for Devices to be Manufactured..... 118

Table 4.1 Analysed parameters for all three active layers 150

Table 4.2 Number of array elements outside of the tolerance intervals for all three active
layers 150

Table 4.3 Maximum cross-talk level (dB) for all three prototype transducers 159

Table 4.4 Pulse-echo response for all three prototype transducers 170

Table 5.1 The estimated results for the example Current Frame..... 194

Table 6.1 Rod size measurement results for all three prototype transducers using -5 dB threshold.....	207
Table 6.2 Size measurement results for the 0.8 mm rod imaging at different distances using the CECAT_79 transducer.....	212
Table 6.3 Size measurement results of the wire phantom.....	217
Table 6.4 Tube size estimation settings and results for the lab phantoms with the tube placed along the y-axis.....	238
Table 6.5 Results for applying the particle size estimation algorithm on TFM images shown in Figure 6.30.....	242

Abbreviations

ASM	Angular Spectrum method
BF	Background Frame
BMM	Blood Mimicking Material
CECAT	Composite Element Composite Array Transducer
CF	Current Frame
CT	Computed Tomography
CUE	Centre for Ultrasonic Engineering
CW	Continuous Wave
DDF	Dynamic Depth Focusing
DF	Directivity Function
DF	Difference Frame
DRI	Discrete Rayleigh Integral
ER	Emergency Room
FEA	Finite Element Analysis
FFT	Fast Fourier Transform
FMC	Full Matrix Capture
GA	Genetic Algorithm
GPU	Graphics Processing Unit
ISLR	Integrated Side Lobe Ratio
LDV	Laser Doppler Vibrometer
MDU	Medical Devices Unit
MPAR	Maximum Pillar Aspect Ratio
MRI	Magnetic Resonance Imaging
NDE	Non-Destructive Evaluation
<i>OpnF</i>	Opened Frame
<i>OrgF</i>	Original Frame

PCB	Printed Circuit Board
PSL	Peak Side Lobe Ratio
PSF	Point Spread Function
RIM	Rayleigh Integral Method
SA	Simulated Annealing
SE	Structuring Element
SIR	Spatial Impulse Response method
SNR	Signal to Noise Ratio
TCCS	Transcranial Colour-Coded Duplex Ultrasonography
TCD	Transcranial Doppler Ultrasound
TDF	Thresholded Difference Frame
TF	Thresholded Frame
TFM	Total Focusing Method
TMM	Tissue Mimicking Material
tPA	Tissue Plasminogen Activator
TVR	Transmitting Voltage Response

Symbols

k	Electromechanical Coupling Factor	-
W_t	Energy input into the piezoelectric material	W
W_s	Energy stored in the piezoelectric material	W
T_c	Curie Temperature	$^{\circ}C$
Q_m	Mechanical Quality Factor	-
v	Speed of Sound	m/s
ρ	Density	kg/m^3
Z	Acoustic Impedance	$MRayl$
w_{pillar}	Ceramic Pillar Width	m
w_{pitch}	Unit Cell Width (or Pitch)	m
tk	Ceramic Pillar Height (Thickness)	m
VF	Volume Fraction	-
AR	Aspect Ratio	-
w_k	Kerf Width	m
f	Frequency	Hz
RF	Reflection Coefficient	-
TR	Transmission Coefficient	-
P	Pressure	Pa
A	Area	m^2
ω	Angular Velocity	rad/s
λ	Wavelength	m
$\delta()$	Dirac's Delta Function	-
Amp	Amplitude	-

Elb	Energy in the Lobe	W
ele_r	Element Radius	m
ele_g	Element Gap	m
ele_num	Element Number	-
ele_pitch	Pitch between Elements	m
ele_num_max	Upper Limit of Element Number	-
R	Aperture Radius	m
$R_{reduced}$	Reduced Aperture Radius	m
r	Radial Distance	m
γ	Polar Angle	rad or $^\circ$
a	Constant parameter of Log Spiral Array	-
b	Constant parameter of Log Spiral Array	-
θ	Rotational Angle of Log Spiral Array	rad or $^\circ$
l_{arc}	Arc Length	m
a_{frmt}	Constant parameter of Fermat Spiral Array	-
β	Golden Angle	rad or $^\circ$
d	Distance between Two Points	m
sf	Scaling Factor	-
V	Voltage	V
I	Pixel Intensity	-

Chapter 1

Introduction

1.1. Motivation

This project was initially motivated to reduce the operator dependency of transcranial ultrasound, which is used for stroke diagnosis, through discussion with the Medical Devices Unit, within the Greater Glasgow & Clyde National Health Centre. This Thesis will focus primarily on the system engineering aspects, with the biomedical application not core, but still aligned to the research. This section will introduce the background and objectives of this project.

1.1.1. Background

Stroke is a sign of vascular originated brain dysfunction [1]. Generally, there are two types of stroke, one is the ischemic stroke, and the other is the haemorrhagic stroke [2]. The former is caused by blockage of the blood supply to the brain, while the latter is due to bleeding in/around the brain [2]. When a stroke happens, the blood supply to the brain will be affected, leading to reduced oxygen levels and abnormal brain function. A long period of abnormal oxygen level could cause damage to the brain or even death. Thus, to

enhance the survival rate and the rehabilitation rate, researchers have been working on developing fast and accurate diagnostic and therapeutic methods for stroke.

Brain and vessel imaging techniques, such as computed tomography (CT), magnetic resonance imaging (MRI), and ultrasound imaging, are commonly used for stroke diagnosis. Depending on the actual situation, one or more diagnostic techniques might be used to improve the diagnosis efficiency.

CT uses X-ray beams to create high-quality images of the brain. It is a rapid imaging technique and is widely available in hospitals. CT is very sensitive to haemorrhagic stroke and can also be used to make a diagnosis in most of the major ischemic stroke cases [3]. But CT is not suitable to be used in detecting minor ischemic stroke due to low sensitivity [3]. Contrast material could be used to enhance the CT image [4], but some patients may have an allergic reaction to the contrast material. Moreover, radiation exposure makes CT not suitable for certain patients and may affect the working status of life-supporting equipment in certain conditions [5].

MRI detects tissue based on their magnetic properties. MRI has better spatial resolution than CT and performs better in detecting ischemic strokes [4]. It also benefits from no radiation exposure. However, it requires longer execution time and is not widely available in clinical environments [4]. It is also reported that the loud noise emitted during the MRI can make patients feel uncomfortable. Moreover, MRI has a strict ban over metals and therefore, it cannot be used to patients who have metallic implants [4].

Ultrasound was first used for transcranial imaging by Aaslid in 1982 [6]. Since then, transcranial ultrasonography has become an important method for vessel imaging. It is a non-invasive, low-cost, and safe test. No noise or radiation will be generated during the test, making ultrasonography a more comfortable and suitable test for most patients. Moreover, with the increasing number of portable ultrasonic imaging equipment, transcranial ultrasonography has the potential to be widely used in the emergency rooms (ERs) and ambulances. This will help reduce the diagnosis time for acute stroke patients and increase patients' survival and functional recovery rates. Also, transcranial ultrasonography is an important diagnostic technique for patients who are unstable or patients who are allergic to the dyes used in CT and MRI.

In addition to diagnostic value, transcranial ultrasonography can also be used as a therapeutic method for ischemic stroke. Tissue plasminogen activator (tPA) is an approved treatment used for ischemic stroke [7]. It works by dissolving the clots in blood vessels, thus restoring the blood supply to the brain. Researchers have been working on enhancing tPA's thrombolysis effect. It has been reported that the thrombolysis can be enhanced when synchronously applying tPA and transcranial ultrasonography [8].

The main disadvantage of transcranial ultrasound is its operator dependency [9]. Unlike CT and MRI, transcranial ultrasound cannot provide an image of the brain but only information associated with blood flow situation. To identify the blood vessels, the operator must manipulate the probe to get signals from different directions throughout the test. Thus, the experience of the operator could highly affect the diagnostic

efficiency. This drawback has limited the application of transcranial ultrasound in situations when experienced ultrasound operators are not available.

1.1.2. Objectives

The main objective of this project is to design a 2D sparse array ultrasonic transducer, which could help reduce the operator dependency of current transcranial ultrasound. A 2D ultrasonic array can provide multiple images of the object under detection at a fixed position. The sparse array pattern is used to reduce the number of elements contained in the transducer, so that high manufacturing and instrumentation cost could be avoided. A flexible piezoelectric ceramic structure [10], called the composite element composite array transducer (CECAT), is used as the basis for a novel 2D array configuration. Furthermore, to reduce operator dependency, an image processing algorithm that can help detect the anomalies in the blood flow is of interest. In this Thesis, these two areas of research will be explored within an engineering laboratory environment.

To achieve these two research objectives, a series of strategic tasks need to be addressed.

1. Design a sparse array pattern that has the potential to be used in the specified application, i.e., the transcranial ultrasound. The array pattern should be able to cover the whole imaging window and to achieve appropriate imaging capability. Moreover, the array pattern should be able to be fabricated into a fully functioning transducer in Centre for Ultrasonic Engineering's (CUE's) fabrication facilities.

2. Develop an appropriate fabrication process to assemble the transducers, including electrical interconnection when the array dimensions and the element size is taken into consideration.
3. Fabricate additional transducers using conventional techniques and incorporating the same array pattern, for comparison purposes.
4. Characterise properties of the prototype transducers to ensure the transducers are working properly and to compare the performance between transducers with different structures.
5. Develop image processing algorithms using standard laboratory instrumentation to automatically detect features within a mock set-up to represent a simple vascular scenario.
6. Evaluate the imaging performance of the prototype transducers. Imaging performance, such as the resolution, the sizing accuracy, and the ability to image multi-reflectors, should be compared between the fabricated transducers. This will include testing using bespoke phantoms which are made from a tissue mimicking material (TMM) to evaluate the potential for the developed 2D CECAT array to be used as a transcranial diagnostic tool.

1.2. Contribution to Knowledge

The main outcome of this project is a 2D sparse array transducer with a novel structure, which has been shown to achieve lower cross-talk and wider bandwidth, when compared to 2D arrays fabricated using conventional 1-3 piezocomposite technology. This prototype transducer demonstrated good imaging performance in the TMM phantom

experiments, which indicates that it has the potential to be applied in the biomedical imaging field. The key contributions to knowledge that have been made through the project progress are:

1. Developed a 2D model in Matlab, which can simulate the far-field directivity function by applying the 2D Fast Fourier Transform (FFT) on an aperiodic sparse array's aperture function.
2. Explored the side lobe level of three aperiodic sparse array patterns, including the random array, the log spiral array, and the sunflower spiral array, within a fixed aperture. Two criteria, the Peak Side Lobe Level (*PSL*) and the Integrated Side Lobe Ratio (*ISLR*), were used to evaluate their performance. The results show that the sunflower spiral array tends to have lower *ISLR*, while the log spiral array performs better in terms of *PSL*.
3. Selected two log spiral array patterns based on the simulations results. One is the optimal design, as it has the best combination of *PSL* and *ISLR*. However, due to the manufacturing limitations within the CUE fabrication laboratory, the optimal design cannot be made as a CECAT transducer. Thus, a second log spiral array pattern generated using modified parameters and contained an appropriate combination of *PSL* and *ISLR* has been chosen to be fabricated as the CECAT transducer used in the remainder of this study.
4. Fabricated three prototype transducers: one using the optimal array pattern and conventional 1-3 piezocomposite technology; and the other two with the modified array pattern, using both the CECAT and 1-3 piezocomposite structures.

The characterisation results show that the transducer with the optimal design performs the best in terms of sizing capability and has the lowest imaging background noise. For those two with the modified array pattern, the one using the CECAT structure has lower cross-talk, wider bandwidth, better axial resolution and higher coupling factor.

5. Implemented Full Matrix Capture (FMC) for data capture and Total Focussing Method (TFM) for image generation with the 2D aperiodic array transducers.
6. Developed two imaging algorithms by combining standard image processing techniques, such as the Morphological Opening and the Hough transform, that can be used to automatically detect the tube and particles inside the tube from the ultrasonic image. Initially, the algorithms were developed using data collected from a commercial ultrasonic array. The algorithms were then used to analyse the image generated from the CECAT prototype transducer and demonstrated the system capability to detect and size anomalies in the experimental tests carried out in the laboratory.

1.3. Thesis Structure

This Thesis consists of seven chapters in total. Chapter 1 is an introduction to the project and the Thesis. Chapter 2 to Chapter 6 explains the project process in detail, while Chapter 7 makes a summarization of this project. Details of each chapter are introduced below.

Chapter 2 reviews the background knowledge and literature related to this project. Basic working principles, key parameters, and basic design rules of the piezoelectric ultrasonic transducer are introduced. This Chapter also provides an overview of the ultrasonic transducer and the ultrasonic imaging algorithms. The image processing algorithms, which are used in this project, are also introduced. Finally, a review of the application of ultrasound in the transcranial imaging field is included at the end of this Chapter.

Chapter 3 explains the array pattern design process. It introduces the two parameters, Peak Side Lobe Level (*PSL*) and Integral Side Lobe Ratio (*ISLR*), which are used to evaluate the performance of the candidate array patterns. The mathematical expression and design rules for each array pattern are then discussed. The optimisation process, the simulation results, and the analysing process are also included in this Chapter.

Chapter 4 describes the manufacturing process and the characterisation results for the prototype transducers. Key parameters of each transducer, such as the materials used in making the active layer, the active layer thickness, and the matching layer recipe, are presented. Three characterisation tests are produced for each transducer, including the electrical impedance response, the cross-talk level, and the pulse-echo test.

Chapter 5 introduces the development of the tube size estimation algorithm and the particle detection algorithm. A commercial 1D linear array transducer is used to image a tank-tube phantom to acquire data for algorithm development. Details about the experimental setup are described. The basic concept and detailed process of each imaging algorithm are explained using images generated from the linear array transducer.

Chapter 6 explains the evaluation process for the prototype transducers. The prototype transducers are initially used to image small diameter reflectors to evaluate and compare their imaging and sizing capability. The CECAT transducer was then tested to ensure it can cover the desired imaging depth range. Results of using the CECAT transducer to image in both a standard laboratory and TMM phantoms are finally presented in this Chapter.

Chapter 7 provides an overall conclusion of this research work and proposes a number of possible improvements which can be achieved in the future.

1.4. Publications

X. Li, A. Gachagan and P. Murray, "Design of a 2D sparse array transducer for integration into an ergonomic transcranial ultrasound system," *2017 IEEE International Ultrasonics Symposium (IUS)*, Washington, DC, 2017, pp. 1-1.

X. Li, A. Gachagan and P. Murray, "Characterisation and Evaluation of Sparse Array Transducers for Small Particle Detection," *2019 IEEE International Ultrasonics Symposium (IUS)*, Glasgow, United Kingdom, 2019, pp. 1742-1745.

X. Li, A. Gachagan and P. Murray, "Design of 2D Sparse Array Transducers for Anomaly Detection in Medical Phantoms," *Sensors*, 20, 5370, 2020.

Chapter 2

Background Review

2.1. Introduction

This Chapter aims to review the background knowledge and the literature work that is related to the research fields associated with this Thesis. The review starts with introducing the concept of the piezoelectric effect and piezoelectric materials, along with ultrasonic transducers and field modelling algorithms. Next, ultrasound imaging and image processing algorithms are discussed. The last Section reviews the literary works associated with transcranial ultrasound field.

2.2. Piezoelectric Effect

The piezoelectric effect describes the conversion between mechanical energy and electrical energy within appropriate materials. It consists of two concepts, one is the direct piezoelectric effect (Figure 2.1(a)), and the other is the converse piezoelectric effect (Figure 2.1(b)). The direct piezoelectric effect was first discovered in crystals by Pierre Curie and Jacques Curie in 1880 [11], where they found that certain crystals could generate electrical charge under pressure. Then, in 1881, Gabriel Lippmann predicted the converse piezoelectric effect, which relates to the conversion from electrical energy

to mechanical energy [12] and was then experimentally proven by the Curie brothers [12]. Ever since then, the piezoelectric effect has been of significant interest to researchers and been used in a wide range of applications [14] - [16].

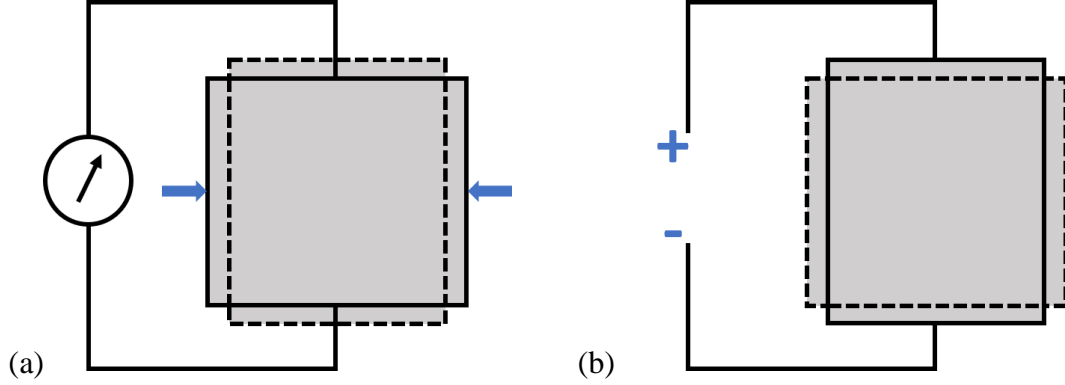


Figure 2.1 Illustration of (a) the direct piezoelectric effect and (b) the converse piezoelectric effect. The grey blocks represent the piezoelectric materials before (the solid line) and after (the dashed line) applying excitation source. The blue indicators represent the external source (arrows stand for the pressure and + - represent the electrical energy) applied on the piezoelectric materials.

There are four pairs of equations that can be used to express the piezoelectric effect [17]:

$$D_m = e_{mj}S_j + \varepsilon_{mn}^S E_n \quad T_i = c_{ij}^E S_j - e_{ni} E_n \quad (2.1)$$

$$D_m = d_{mj}T_j + \varepsilon_{mn}^T E_n \quad S_i = s_{ij}^E T_j + d_{ni} E_n \quad (2.2)$$

$$E_m = -g_{mj}T_j + \beta_{mn}^T D_n \quad S_i = s_{ij}^D T_j + g_{ni} D_n \quad (2.3)$$

$$E_m = -q_{mj}S_j + \beta_{mn}^S D_n \quad T_i = c_{ij}^D S_j - q_{ni} D_n \quad (2.4)$$

where the variables and the coefficients contained in these equations are summarised in Table 2.1. The superscripts represent the conditions of corresponding constant variables. For example, ε^T is the permittivity at constant stress. The subscript notations, $i, j =$

1,2, ...,6 and $m, n = 1,2,3$, refer to the coordinate system, as shown in Figure 2.2. I have reproduced the terminology from the IEEE standard and that the symbols used here are only relevant to this Section. Therefore, as these symbols are not utilised in the remainder of the Thesis, they are not listed in the Symbol Table to ensure no confusion with other terminology used in the Thesis.

Table 2.1 Variables and coefficients in the piezoelectric equations

	Symbol	Name
Variables	T	Stress
	S	Strain
	E	Electric field strength
	D	Electric displacement
Coefficients	s	Elastic compliance
	c	Elastic stiffness
	ϵ	Permittivity
	β	Impermittivity
	d	Piezoelectric strain constant
	e	Piezoelectric stress constant
	g	Piezoelectric voltage constant
	q	Piezoelectric stiffness constant

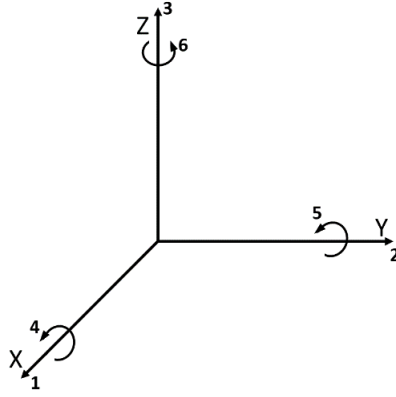


Figure 2.2 The coordinate system defined in the IEEE standard on piezoelectricity [17].

In addition to the coefficients listed in Table 2.1, there are some other coefficients which can be used to evaluate the performance of a piezoelectric material. One of the most important coefficients of piezoelectric material is the electromechanical coupling factor, k [18]. It can be expressed as:

$$k = \sqrt{\frac{W_s}{W_t}} \quad (2.5)$$

where W_t represents the total electrical (or mechanical) energy input into the piezoelectric material and W_s represents the mechanical (or electrical) energy stored in the piezoelectric material. As indicated in the expression, k represents the efficiency of the piezoelectric material in the conversion between electrical energy and mechanical energy. As with the other piezoelectric coefficients, k can be expressed with different electromechanical boundary conditions, as k_{mn} , where m refers to the axis of the electrical load and n refers to the axis of the stress. Within the k matrix, there are two factors which have been used more often than the others; one is the k_{33} , and the other is

the k_t [19]. k_{33} is the coupling factor when a 1D stress is applied on a tall narrow bar along the z -axis. k_t is the thickness mode coupling factor when the strain in the XY -plane is zero.

There are some other piezoelectric parameters which are important to ultrasound transducer design, including the Curie temperature T_c , the mechanical quality factor Q_m , the speed of sound v (v_l for longitudinal wave and v_s for shear wave), the material density ρ , and the characteristic acoustic impedance Z . The Curie temperature determines the usable temperature range of the piezoelectric material, above which the piezoelectric material will lose its piezoelectricity [20]. Q_m reflects the sharpness of the resonance spectrum for the piezoelectric material [11] and equals the inverse of mechanical loss [21]. This parameter provides information on the operational bandwidth associated with a piezoelectric material. In a solid material, the characteristic acoustic impedance can be calculated using:

$$Z = \rho * v = \sqrt{\rho c} \quad (2.6)$$

Differences in Z between two adjacent materials will affect the acoustic energy transfer and is a critical factor in understanding wave propagation across boundaries [11].

2.3. Piezoelectric Composite Material

When designing an ultrasound transducer for medical diagnostic applications, two piezoelectric properties, k and Z , are two of the most important parameters that need to be considered [14]. To ensure the acoustic energy conversion efficiency between the ultrasound transducer and biological tissue, the piezoelectric material should have

relatively high k and low Z . Depending on the shape of the piezoelectric material, a specific form of k will be of interest. For example, k_{33} is of interest for a bar shaped piezoelectric material, while k_t should be used for a plate. However, a conventional piezoelectric material cannot meet both requirements. One way to solve this problem is to combine a piezoelectric material (high k , also called the active material) with a polymer (low Z , also called the passive material) to form a piezoelectric ceramic composite material (piezocomposite), which can be designed to achieve a compromise between k and Z .

Piezocomposites can be classified by their dimensional connectivity patterns [22]. A m - n connectivity piezocomposite consists of piezoelectric material, which is connected in m dimensions, and polymer, which is connected in n dimensions. Figure 2.3 shows some examples of the most common piezocomposite connectivity patterns. Among all the patterns, the 1-3 connectivity pattern, as shown in Figure 2.3(a), which consists of piezoceramic pillars (such as Lead Zirconate Titanate (PZT)) and polymer matrix (such as epoxy resin), has been most widely used in ultrasonic transducers [14]. This kind of piezocomposite will be referred to as the conventional 1-3 (C13) piezocomposite in the remainder of this Thesis.

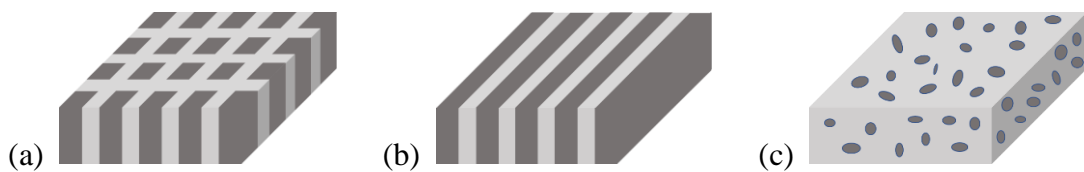


Figure 2.3 Illustration of the (a) 1-3, (b) 2-2, and (c) 0-3 composite connectivity patterns. The dark grey represents the piezoelectric material, and the light grey represents the polymer.

2.3.1. Conventional 1-3 Piezocomposite

a. Key Parameters

Figure 2.4 illustrates the unit cell of the C13 material. It consists of a rectangular piezoceramic pillar, which has a square surface in the XY -plane, and the surrounding polymer. For a standard C13 design, the spacing between two adjacent pillars is the same in both x -axis and y -axis. The structure of the unit cell can be defined using three geometric parameters: the ceramic pillar width w_{pillar} , the unit cell width (or pitch) w_{pitch} , and the ceramic pillar height (or thickness) tk .

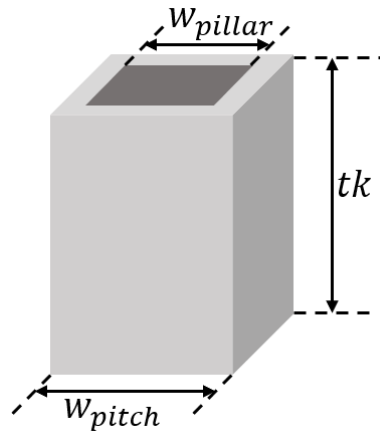


Figure 2.4 Illustration of the unit cell of the C13 composite. The dark grey represents the piezoelectric material, while the light grey represents the polymer.

Based on these three basic geometric parameters, the following parameters which have influence on the performance of the C13 composite can be calculated:

$$\text{Volume Fraction (VF):} \quad VF = (w_{pillar}/w_{pitch})^2 \times 100\% \quad (2.7)$$

$$\text{Aspect Ratio (AR):} \quad AR = w_{pillar}/tk \quad (2.8)$$

$$\text{Kerf Width (}w_k\text{):} \quad w_{kerf} = w_{pitch} - w_{pillar} \quad (2.9)$$

VF can be used to predict the equivalent thickness mode piezoelectric parameters for the C13 composite through expressions derived in [23]. Researchers have also used the finite element analysis (FEA) method to explore the relationships between VF and piezoelectric parameters of the 1-3 composite microstructure, such as k_t , Z , and v_l [24] - [26]. The key results show that there is a positive correlation between Z and VF [25]. When VF is in range 0.2 to 0.8, it has relatively little effect on k_t and v_l [25]. For a piece of 1-3 composite designed to operate as both a transmitter and a receiver, it should have a VF between 30% and 70% [26].

Published work in [24] and [27] proved that the effect from AR on v_l and k_t is associated with the value of VF . When VF is lower than 20%, both v_l and k_t are going to decrease with a corresponding increase in AR . In general, 1-3 composites with small AR and high VF tend to have the best performance in terms of k_t . For a given VF , there is an upper limit to the value of AR , called the Maximum Pillar Aspect Ratio (MPAR) [26]. AR with value lower than the MPAR ensures that the 1-3 composite has a pseudo uniform thickness mode vibration. which is not influenced by the other resonance modes. The spacing between the ceramic pillars is defined as w_{kerf} . In practice, the possible values for w_{kerf} is dependent on manufacturing capability. The interactional relations

among VF , AR , and w_{kerf} means that when designing a C13 composite, trade-offs must be made to achieve both appropriate performance and machinability.

b. Resonance Modes in a 1-3 Piezocomposite

There are four major resonance modes for the C13 connectivity composite, including the thickness mode, the width-dilational mode, the inter-pillar mode, and the intra-pillar mode. The first two modes are related to the macrostructure of the composite (e.g. the shape of the composite), while the last two modes are related to the microstructure of the composite (e.g. the relationship between the ceramic pillar and the passive polymer phase) [26]. The thickness mode is also called the longitudinal mode and travels in the 3 direction (i.e. the z -axis) of the composite. The width-dilational mode, the inter-pillar mode, and the intra-pillar mode can also be collectively described as the lateral modes. These modes travel in the 1 and 2 directions (i.e. the x -axis and the y -axis) of the composite. The influence from the lateral modes on the performance of the 1-3 composite is associated with the composite's AR .

- *Thickness Mode*

The thickness mode is directly related to the finite thickness of a piezoelectric material and its longitudinal velocity. The relationship between the thickness mode resonance frequency and the thickness of the composite can be expressed as [28]:

$$f_t = \frac{n * v_l}{2 * tk} \quad (2.10)$$

where f_t is the thickness mode resonance frequency, n is the wavenumber for the odd harmonics (i.e. $n = 1, 3, 5 \dots$), v_l is the estimated equivalent longitudinal sound velocity in the composite using the VF and individual velocities of each constituent material, and tk is the thickness of the composite. The fundamental thickness frequency, which is typically used in ultrasonic imaging transducers [29], is the one when n equals to 1. The other thickness mode frequencies with n larger than 1 are caused due to multiple reverberations within the composite [28]. However, those thickness modes are highly damped because of their increased frequency.

The thickness mode coupling factor, k_t , can be experimentally determined from the impedance response test using:

$$k_t = \sqrt{\frac{\pi f_e}{2 f_m} \cot\left(\frac{\pi f_e}{2 f_m}\right)} \quad (2.11)$$

where f_e and f_m are the electrical and mechanical resonance frequencies respectively, as highlighted in Figure 2.5. f_e is the frequency of the minimum impedance and is the resonance frequency when the composite is short circuit [24]. f_m is the frequency of the maximum impedance and is the resonance frequency when the composite is open circuit [24]. From the transducer design perspective, f_e is the optimal operational frequency for transmission, while f_m is the optimal operational frequency for reception.

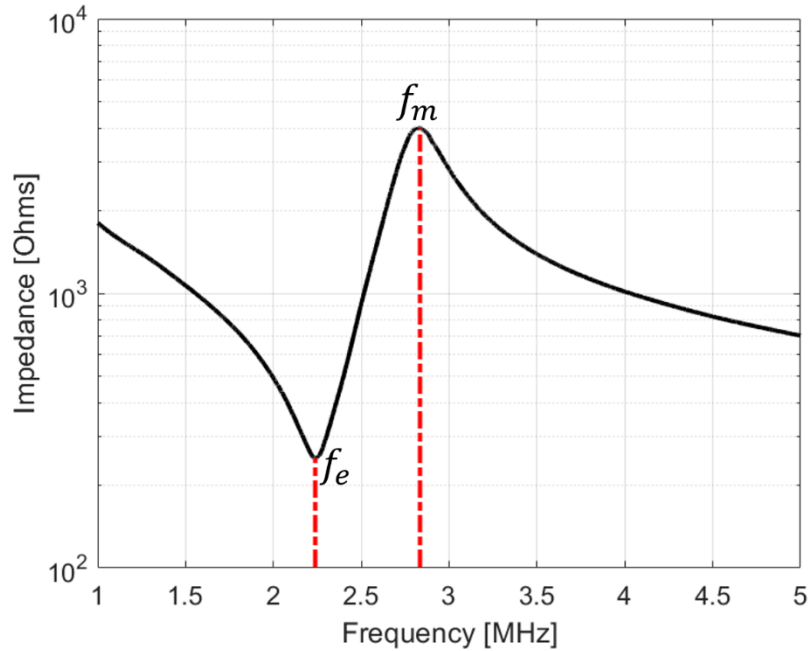


Figure 2.5 Example of the impedance response for the thickness-mode.

- *Width-dilational Mode*

The width-dilational mode arises due to the finite lateral dimensions of the piezocomposite, such as the width for a rectangular-shaped composite or the diameter for a circular shaped composite. It is also termed as the plate mode for the rectangular plate or the radial mode for the disk plate. This mode involves mechanical motion in the lateral directions (1 and 2) when an electric field is applied to the 3 direction [29]. A diagnostic transducer would typically have the lateral dimension significantly greater (at least a factor of 10) than the material thickness and hence, the width-dilational mode resonance is normally much lower than that of the fundamental thickness mode. Thus, the influence from the width-dilational mode on the thickness mode can usually be ignored [26]. For the 1-3 piezocomposite structure, since only the polymer is connected

in the 1 and 2 directions, the width-dilational mode is highly damped compared to a pure piezoceramic material with the same lateral dimension [26].

- *Inter-pillar Mode*

The inter-pillar mode is related to the periodic microstructure within the piezocomposite itself. This mode must be understood when designing a C13 piezocomposite because it can be coupled with the fundamental thickness mode frequency and influence the performance of the piezocomposite. To avoid the problems caused by this mode, the VF should be at least larger than 30% [28].

To ensure a pseudo uniform thickness motion, the inter-pillar mode should be pushed to a frequency range which is at least twice of the thickness mode frequency [30]. According to [31], the kerf width (w_{kerf}) should be less than one quarter of the shear wavelength. Moreover, the spacing between the centre points of two adjacent pillars, which is equal to the pitch width (w_{pitch}), should be no larger than the thickness of the piezocomposite (tk) [32].

- *Intra-pillar Mode*

The intra-pillar mode is associated with the finite lateral dimensions of an individual ceramic pillar. For AR in the range of 0.5 to 2, the intra-pillar mode frequency will occur in the same frequency range as the thickness mode. However, it does not have a significant effect on the thickness mode when the AR is smaller than 0.5 and for such cases is usually ignored in the transducer design process [28].

c. Piezocomposite Dice and Fill Manufacturing Technique

The most commonly used manufacturing process for the C13 piezocomposite is the ‘dice and fill’ method [33], as illustrated in Figure 2.6. A bulk ceramic is firstly diced into a pillar matrix with a specified pitch, w_{pitch} . This takes into account the minimum machinable values of w_{kerf} and w_{pillar} which are limited by the precision of the dicing machine and the available saw blade dimensions. The vibration of the blade during the dicing process can increase w_{kerf} to a value larger than the thickness of the blade and can cause pillar fracture for devices with small w_{pillar} . Once the matrix of piezoceramic pillars has been produced, the grooves are filled with the selected polymer and degassed under vacuum to remove any trapped air bubbles. After the curing process, during which the polymer will solidify, the raw composite will be machined into the desired shape, typically thickness for desired operational frequency. In some cases, the resultant composite material might need to be poled before being assembled into the final transducer to maximise the piezoelectric effect of the device.

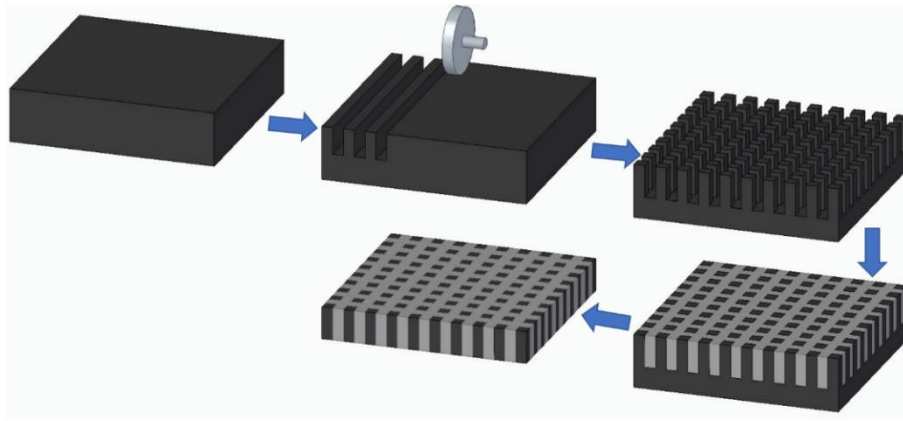


Figure 2.6 Illustration of the ‘dice and fill’ method. The dark grey represents the piezoelectric material, while the light grey represents the polymer. The silver structure shown in the second step is the dicing saw.

2.3.2. Composite Element Composite Array Configuration

The composite element composite array configuration was proposed in [10] to increase the flexibility of a piezoceramic based ultrasonic transducer. This transducer configuration has been named as Composite Element Composite Array Transducer (CECAT). Figure 2.7 illustrates the two primary examples of CECAT configurations studied in [10]. As shown in the Figure, the piezoelectric pillars are divided into groups which are connected through the epoxy resin. This arrangement makes it possible for the composite to be conformed in two dimensions, which means it can fit the surface of the curved structure better. Two arrangements of the piezoelectric pillars have been studied, one using the regular matrix configuration as shown in Figure 2.7(a) and the other using the random configuration, as shown in Figure 2.7(b). The former configuration is similar to a standard C13 device in which two different w_{kerf} values have been used to define a larger regular array pattern, with each array element is effectively a fine scale C13 structure. Whereas, the latter configuration consists of piezoelectric fibres which are randomly placed within designated areas (array elements) and surrounded by epoxy resin. The former configuration will be referred to as the regular CECAT, and the latter configuration will be referred to as the fibre CECAT since piezoelectric fibres are used as the active material. Both simulation and experimental results proved that piezocomposite with the random configuration has similar performance in terms of sensitivity and bandwidth compared with the matrix configuration [34]. Moreover, the random configuration can suppress the inter-pillar mode since it breaks the periodic pillar arrangement in the matrix configuration.

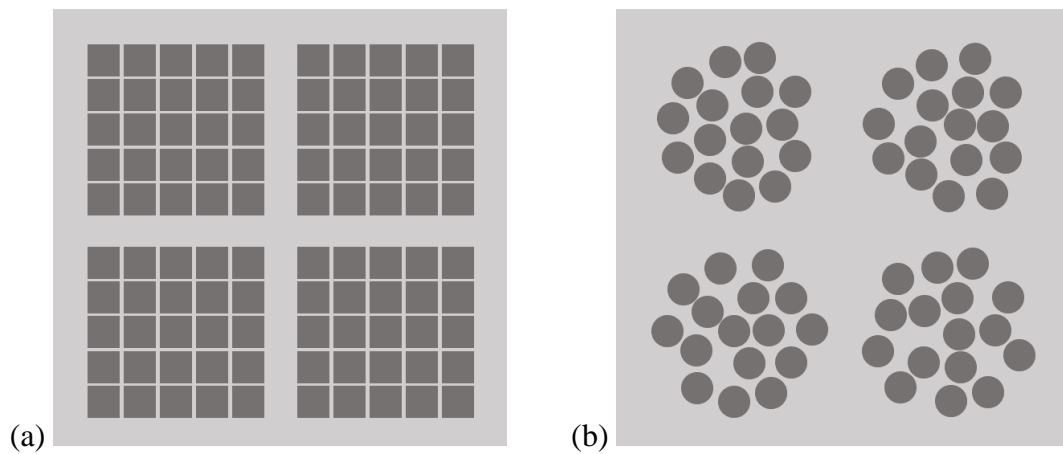


Figure 2.7 Illustration of top view for (a) the regular CECAT and (b) the fibre CECAT. The dark grey represents the piezoelectric material while the light grey represents the polymer.

A manufacturing process called ‘place and fill’ has been used for the fibre CECAT devices. Firstly, the piezoelectric fibres are placed into a mould which is designed to hold the fibres at desired positions. Then, the fibres and the mould are filled with the epoxy resin and left to cure. A section of the composite with the desired thickness will then be sliced from the cured composite block. Finally, the removed slice of fibre CECAT will be poled following the manufacturer’s (Smart Material Corp., Sarasota, FL) description [35]. Compared to the conventional ‘dice and fill’ method, the ‘place and fill’ is less time consuming when manufacturing small scaled devices as multiple pieces of composites can be fabricated in one manufacturing process. Specific details about the ‘place and fill’ method used in this Thesis will be introduced in Chapter 4.

2.3.3. Alternative 1-3 Composite Configurations and Manufacturing Techniques

Researchers have been working on improving the properties of the 1-3 composite by modifying its constituent materials or configuration. The modifications of the 1-3 composite configuration mainly focus on three aspects, 1) the pillar shape, 2) the pillar arrangement, and 3) the epoxy resin configuration. The changes in the 1-3 composite configuration have also led to the development of new manufacturing techniques.

a. Alternative 1-3 Composite Configurations

A number of papers have explored the influence of pillar shape, triangular and cylindrical, on the composite's properties compared to the conventional square pillar configuration [24], [27], [36]. In their studies, the pillars were placed in a matrix, which was the same as the periodic arrangement of the C13 composite. Their research indicated that the rectangular pillar and the cylindrical pillar had similar performance, while the triangle pillar could achieve improved thickness mode performance and increase the M_{PAR}. Moreover, they proved that the triangle pillar could reduce the lateral resonance interference within the composite, when the pillars were arranged to have no parallel facing surfaces. However, these papers were mainly focused on relatively low frequencies (under 1 MHz), with the design guidelines proposed making it difficult to fabricate high-frequency 1-3 composite. Brown et al. designed a 1-3 composite with 45° isosceles triangular pillars which had a *AR* larger than the *M_{PAR}* [37]. This configuration achieved a high fundamental resonance frequency (in the range

30 MHz – 40 MHz) and broad bandwidth, with an acceptable sensitivity performance. Yin et al. further investigated the effect from the isosceles angle on the performance of the 1-3 composite with the isosceles triangular pillar [38]. They found that the composite with 45° triangular pillars was least affected by the lateral modes.

In [39], Hossack et al. proposed a method to reduce the inter pillar resonant modes by introducing multiple ceramic pillar dimensions into the 1-3 composite with rectangle pillars. Similarly, Yuan et al. discovered that composites with rectangular pillars and random pitches (w_{pitch}) could achieve significant suppression of the lateral resonant modes [40]. Rouffaud et al. designed and fabricated a novel 1-3 composite with the square pillars arranged in a super-cell configuration in order to reduce the effect from the lateral modes [41]. Experimental results showed that the super-cell composite performed better in terms of bandwidth when compared to the C13 composites, which had the same pitch and thickness.

Researchers have also explored the potential to improve the performance of the 1-3 composite by modifying the shape and arrangement of the pillars at the same time. Yang et al. developed a novel 1-3 composite configuration with the bulk ceramic crossly cut in two different angles relative to the horizontal [42], [43]. This operation caused the ceramic pillars to have different shapes, which had been termed as the pseudo-random configuration. Experimental results showed that the pseudo-random configuration could suppress the lateral modes and improve the sensitivity and bandwidth of the composite. Fang et al. designed a 1-3 composite which used triangular pillars of different sizes to form a fractal pattern, called the Sierpinski gasket (SG) [44]. The SG composite was

shown to be able to achieve broader bandwidth when compared to a conventional C13 composite design.

Modifying the configuration of the epoxy resin is another method that researchers have studied to improve composite performance. It had been proposed in [39] that the lateral modes could be reduced by filling the ceramic grooves with multiple polymers. Huang et al. designed a 1-3 composite with the pillars divided into groups which are insulated by two kinds of epoxy resins [45]. He et al. developed an air-based 1-3 composite which contained air gaps between the pillar-epoxy unit cells [46]. Qin et al. proposed a modified 1-3 connectivity configuration which had the ceramic pillars firstly surrounded by a soft polymer and then embedded into a hard polymer [47]. Mi et al. extended the work in [47] and fabricated a composite with the square pillar firstly surrounded by cylindrical silicon rubber and then embedded into an epoxy resin [48]. Zhong et al. and Zhang et al. investigated the performance of the 1-3 composites which had more than one layer of epoxy resin [49], [50]. Results from all the research mentioned here have demonstrated that by modifying the polymer configuration, the 1-3 composite can achieve improvements in both the electromechanical coupling factor and acoustic impedance, resulting in an improved energy conversion efficiency between the transducer and the object under test.

b. Alternative Manufacturing Techniques

Although the conventional ‘dice and fill’ method has been widely used in fabricating the 1-3 composite, it is not suitable to fabricate some of the 1-3 composites with novel configurations and finer scales. Thus, researchers have been trying to develop new

manufacturing techniques that could be used to fabricate 1-3 composites with diversified configurations. A manufacturing technique, called the viscous polymer processing, had been used in [51] and [52] to make composites with pillars which had different shapes and sizes smaller than $100\mu m$. Gebhardt et al. fabricated composites with different configurations using a method called the soft mold process [53]. Based on those samples, they found that effects from the lateral modes on the fundamental resonance mode could be reduced by arranging the pillars in a hexagonal pattern. Gunther et al. extended the work done in [53] and developed a fully functioning 40 MHz transducer [54]. Researchers have also investigated using 3D printing technology to efficiently fabricate piezocomposites with relatively complex configurations [55] [56].

2.4. Ultrasonic Transducers

An ultrasonic transducer is a device that can generate and receive mechanical waves with a frequency higher than the upper limit of human hearing, i.e. 20 kHz. There are several ways to generate ultrasound, such as electromagnetic, optical and capacitive techniques [19]. However, the most common method used in designing ultrasonic transducers is using piezoelectric materials [19]. Ultrasonic transducers have been widely used in many fields, such as the non-destructive evaluation (NDE), underwater sonar and biomedicine [14] - [15]. According to the number of elements contained in the transducer, ultrasonic transducers can be divided into two groups: single-element ultrasonic device; and array ultrasonic transducer.

2.4.1. Structure of Ultrasonic Transducers

Figure 2.8 illustrates the typical structure of a single-element ultrasonic transducer. Three functional layers, including the backing material, active layer, and matching layer, are enclosed inside the housing material, which is used to protect these intra-housing components. The active layer is the most fundamental component of the ultrasonic transducer. It contains the active piezoelectric layer, such as a piezocomposite material, which is used to generate and receive the ultrasonic energy. Electrical connection to the active layer is achieved through individual wiring to the electrodes of the active material. This wiring is then either extended through a water-proof tubing/encapsulation or connected to an electrical connector fixed into the transducer housing, for example BNC connector, to provide electrical connection to external instrumentation.

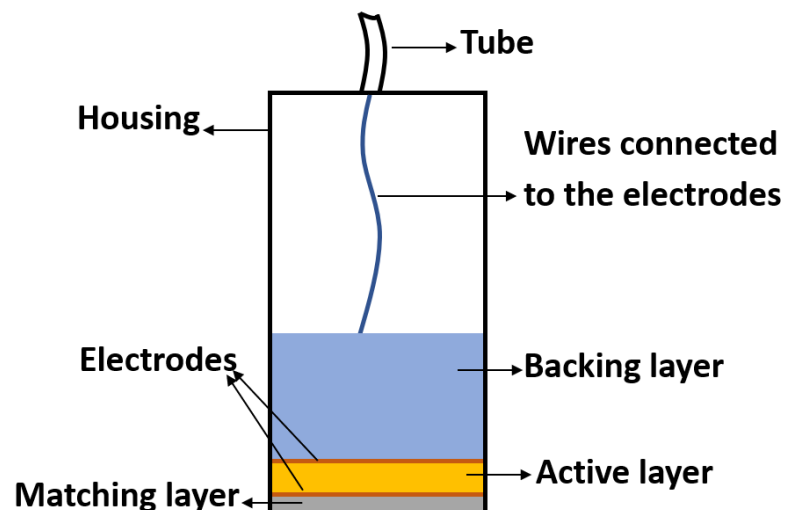


Figure 2.8 Illustration of typical ultrasonic transducer structure.

The backing layer and the matching layer are used to modify the performance of the ultrasonic device. As illustrated in Figure 2.9, when an ultrasonic wave arrives at the interface of two materials which have different acoustic impedances (Z_1 and Z_2), a proportion of the wave will be reflected, while the remainder of the wave will be transmitted into the second material (Z_2). The reflection coefficient (RF) and the transmission coefficient (TR) can be expressed as [57]:

$$RF = \frac{Z_2 - Z_1}{Z_2 + Z_1} \quad (2.12)$$

$$TR = \frac{2Z_2}{Z_2 + Z_1} \quad (2.13)$$

As indicated in Equations 2.12 and 2.13, a large acoustic impedance mismatch will lead to a large RF . In terms of the response from an ultrasonic transducer, if there is nothing attached to the rear surface of the active layer, i.e. the rear surface of the active layer is exposed to air, then the large acoustic impedance mismatch between the piezoelectric material and air will result in reverberation within the active layer. This could lead to an increase in the ring-down time for a generated ultrasound signal, which will lead to a decrease in the transducer bandwidth [58]. To solve this problem, the backing layer is introduced to reduce reflection of the ultrasound waves at the rear surface of the active layer. Ideally, the acoustic impedance of the backing layer should be close to that of the active layer to maximise transmission into the backing material [14]. However, the sensitivity of the transducer will be reduced due to the application of a backing layer. Moreover, the attenuation coefficient and thickness of the backing layer should also be carefully designed to ensure appropriate absorption of the ultrasound energy [14].

At the transducer front face, if the RF is large between the active layer and the load material, the transmission efficiency of the ultrasonic transducer will be affected and lead to a decrease in the transducer sensitivity. Thus, a matching layer can be introduced to reduce this acoustic impedance mismatch. Theoretically, to achieve optimal transmission, the acoustic impedance of the matching layer (Z_m) should be:

$$Z_m = \sqrt{Z_a Z_l} \quad (2.14)$$

where Z_a and Z_l are the acoustic impedance of the active layer and the load material, respectively [59]. For the transducer applications which require broad bandwidth operation, Z_m could be calculated using a modified equation [60]:

$$Z_m = \sqrt[3]{Z_a Z_l^2} \quad (2.15)$$

Typically, to optimise the transmission efficiency of the transducer, the thickness of the designed matching layer should be a quarter of the ultrasound wavelength at the resonance frequency of the transducer. Multiple matching layers could also be used to further improve the acoustic match between the active layer and the load material [60].

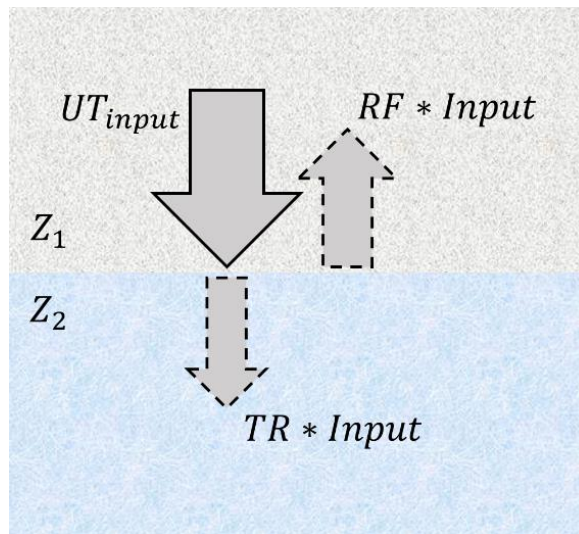


Figure 2.9 Illustration of the transmission and reflection for an ultrasound wave (UT_{input}) when arriving at an interface between two materials which have different acoustic impedances (Z_1 and Z_2).

2.4.2. Single-element Ultrasonic Transducers

The structure of a typical single-element transducer is shown in Figure 2.8. Electrodes are fully applied on both the top and the bottom sides of the active piezoelectric. Two wires, each attached to one side of the active layer, are used to connect the active layer to external equipment. The single-element ultrasound transducer does not have an inherent focusing ability, however by adding an extra lens to the front face of the transducer, the sound beam can be focused on the desired region in the load medium [14]. The beam shape of a single-element ultrasonic transducer is related to the element dimension. The perpendicular distance from the transducer to where the beam reaches its narrowest width is called the Fresnel-zone (near-zone) length [61]. As the distance becomes longer than the near-zone length, the beam becomes diverged. For circular transducers working under the same frequency, a transducer with a larger diameter tends to have a longer

Fresnel-zone length and narrower divergence, i.e. better lateral resolution. Since the single-element transducer can only transmit/receive one beam, it cannot directly provide images of the region/medium of interest and will require to be mechanically scanned to achieve imaging performance.

2.4.3. Ultrasonic Arrays

An ultrasonic array consists of more than one active element within a single transducer housing. Each element is individually electroded and connected through an individual wire to a phased array controller. Through the sophisticated phased array controller instrumentation, each active element can be controlled individually, which can be used to generate and control different ultrasound beam shapes. Figure 2.10 shows examples of making the ultrasound beam focus on a specific position or steer at an angle, by applying appropriate electronic time delays to specific elements. These time delays are termed as the focal law. Compared to the unfocused ultrasound beam, the focused beam profile can improve the transducer's lateral resolution in the focused area [62].

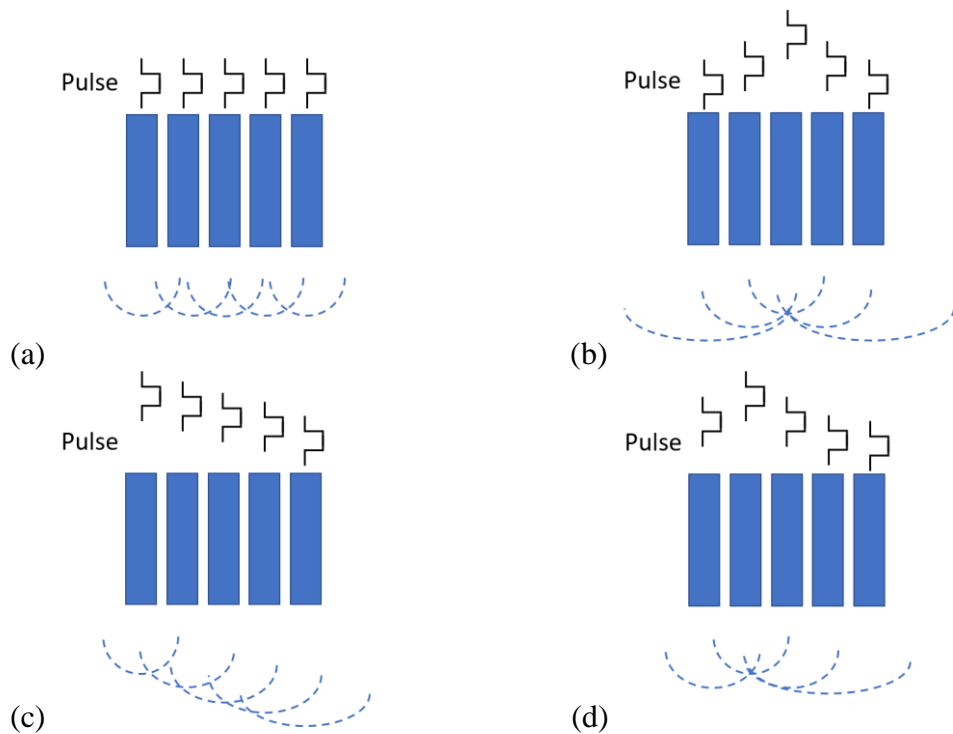


Figure 2.10 Illustration of achieving (a) the unfocused beam, (b) the focused beam, (c) the steering beam, and (d) the focused and steering beam by applying corresponding focal law. The blue bars represent the array elements.

Depending on the array configuration, the ultrasonic array can be loosely classified into three main groups: the 1D array, the 2D array, and the annular array [63]. Figure 2.11 shows an example of each configuration. For the 2D array, except for example shown in Figure 2.11(b), which contains same number of elements in both row and column directions, there also exist arrays which have less elements in the row directions. This type of array is defined as the 1.5D array. They are designed to achieve limited focusing capability, while trying to avoid significantly increase the number of array elements [64]. One thing to note is that beam steering is not applicable for the annular array as it is primarily designed to achieve multi-focal depth scanning [63].

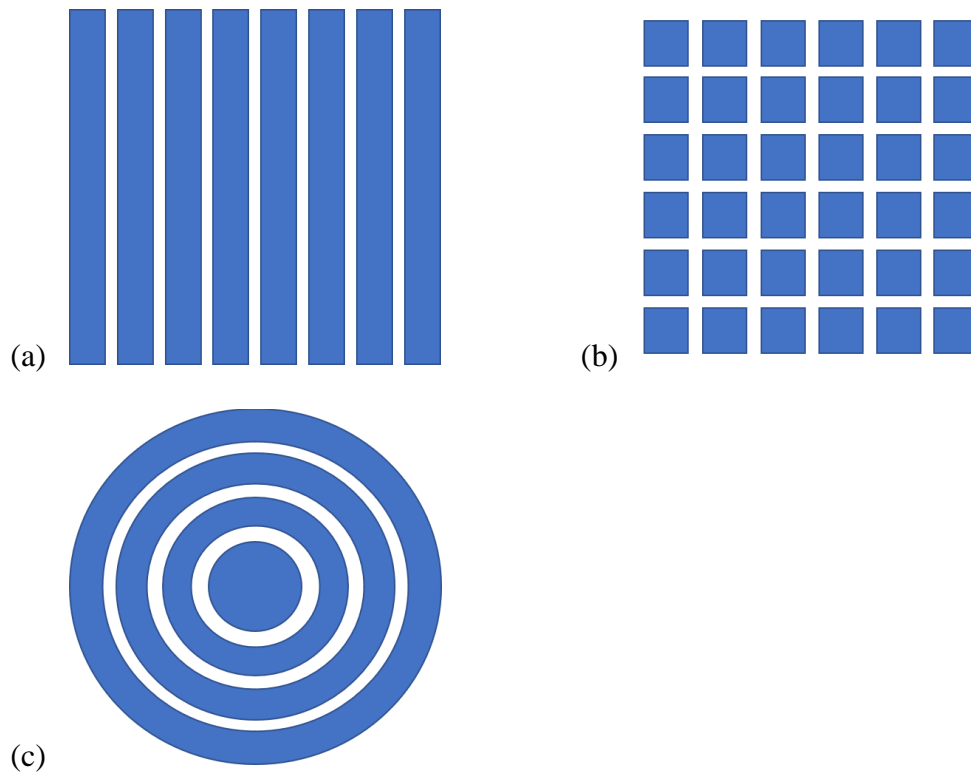


Figure 2.11 Examples of typical array configurations including (a) the 1D linear array, (b) the 2D matrix array, and (c) the 2D annular array, where blue indicates an array element.

There is a half-wavelength design rule for ultrasonic array transducers, which is related to the Nyquist sampling theory [65]. According to this rule, the centre-to-centre spacing between two adjacent elements, i.e. the element pitch, should be no larger than half of the ultrasound wavelength in the load material. The ultrasonic array which follows this design rule is termed as the dense, or the fully sampled, array. The dense array benefits from no imaging artefacts as it avoids the generation of grating lobes, an artefact of spatial undersampling with respect to element pitch, in addition to the main ultrasonic beam [66].

However, the dense array may not be practical when designing a 2D array transducer. To achieve high resolution, the aperture of a dense 2D array needs to be large enough, while satisfying the half-wavelength design rule at the same time [67]. For a 1D linear dense array with 32 elements, to expand it into a 2D dense array with the same aperture size, the required number of elements is 32×32 (1024). Such a large increase in array elements may cause manufacturing difficulties and an increase in the manufacturing and instrumentation cost [68]. Moreover, the corresponding reduction in array element size may lead to a weak signal to noise ratio (SNR) in terms of transducer performance [68].

To avoid these problems, another kind of ultrasonic array, which is called the sparse array, is introduced. The main idea of the sparse array is to reduce the number of elements within the fixed aperture of the device. The reduction in the number of elements reduces the manufacturing and instrumentation costs. It also means the element size could be increased to improve the system SNR performance, however, this will be at the expense of an increase in the sidelobe levels, degrading the imaging contrast [69]. Figure 2.12 shows the simulated directivity functions of an 81×81 element dense array and a 5×5 element sparse array using 2D Fast Fourier Transform method, which will be explained later in Section 2.5.4. For comparison purpose, the size of the aperture and the element are set to be the same for both arrays. In other words, the 5×5 sparse array is achieved by simply increasing the element pitch. As shown in the figure, the sidelobe levels for the sparse array become much higher than that of the dense array and become close to the main lobe level. Thus, when designing a sparse array, a compromise is

usually made to ensure both reduction in number of array elements and acceptable image contrast.

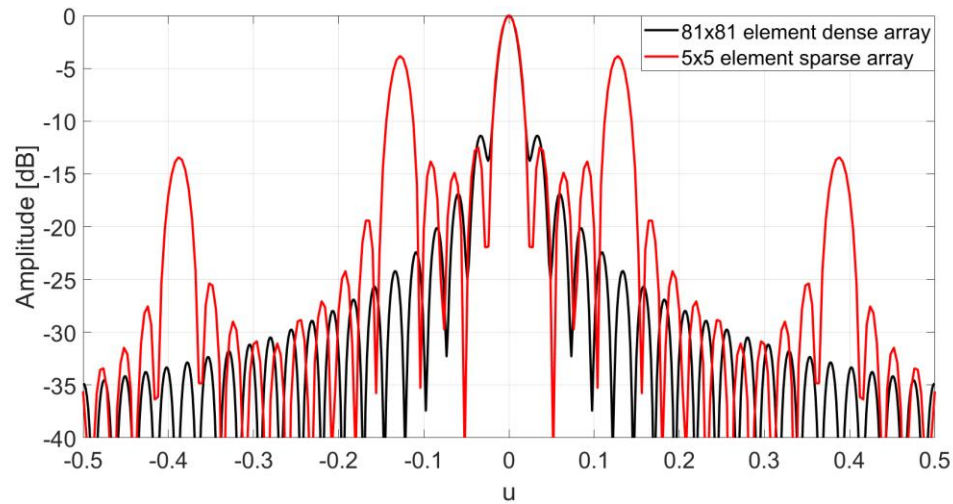


Figure 2.12 Normalised simulated directivity functions for an 81x81 element dense array (the red line) and a 5x5 element sparse array (the black line). The aperture size is set to be the same for both arrays.

According to the element distribution, the sparse array can be further divided into two groups, one is the periodic sparse array and the other is the aperiodic sparse array. Figure 2.13 shows some typical sparse array patterns. The design process of the periodic sparse array is relatively straight forward. It is mainly about increasing the element pitch of the conventional dense array. However, the sidelobe and grating lobe level of the periodic sparse array can be relatively high [70]. Compared to the periodic sparse array; the aperiodic sparse array can avoid the formation of grating lobes since the aperiodic configuration reduces the interaction between elements [70].

Lots of methods have been proposed to design the sparse array transducer. Some are based on optimisation algorithms, such as the simulated annealing (SA) [71], genetic

algorithm (GA) [72], and minimum redundancy linear-array [73]. Generally, these methods are used to find the set of elements that can achieve a desired beam pattern, by analysing a large amount of periodically arranged grids [74]. An approach using SA and non-gridded elements has also been proposed [75], where the non-gridded layout shows improved results but requires more complex algorithms and is time-consuming to design.

Another element pattern that has been studied for sparse array designing is the spiral pattern. The spiral pattern avoids the periodic structure that forms the grating lobes. At the same time, it allows for more control over the position of each element [70]. Two types of spirals have been well studied for sparse array design, one is the Fermat spiral, and the other is the logarithmic spiral. The Fermat spiral has been used in designing antennas [76] and ultrasound sparse array transducers [67] [74]. Combined with the density tapering, these designs can achieve low sidelobe levels while keeping acceptable sensitivity. The Fermat spiral, which is shown in Figure 2.13(e) is a special case when the step angle is set to be 137.51° [67] and because of its shape, this spiral is also called the sunflower spiral [74]. The logarithmic spiral was used in [70] to design a 2D sparse array used in NDE. As a fractal structure, the logarithmic spiral benefits from its self-similarity property. The logarithmic spiral performs better in spreading the sidelobe energy [70]. The sunflower spiral and logarithmic spiral array patterns will be discussed further in Chapter 3.

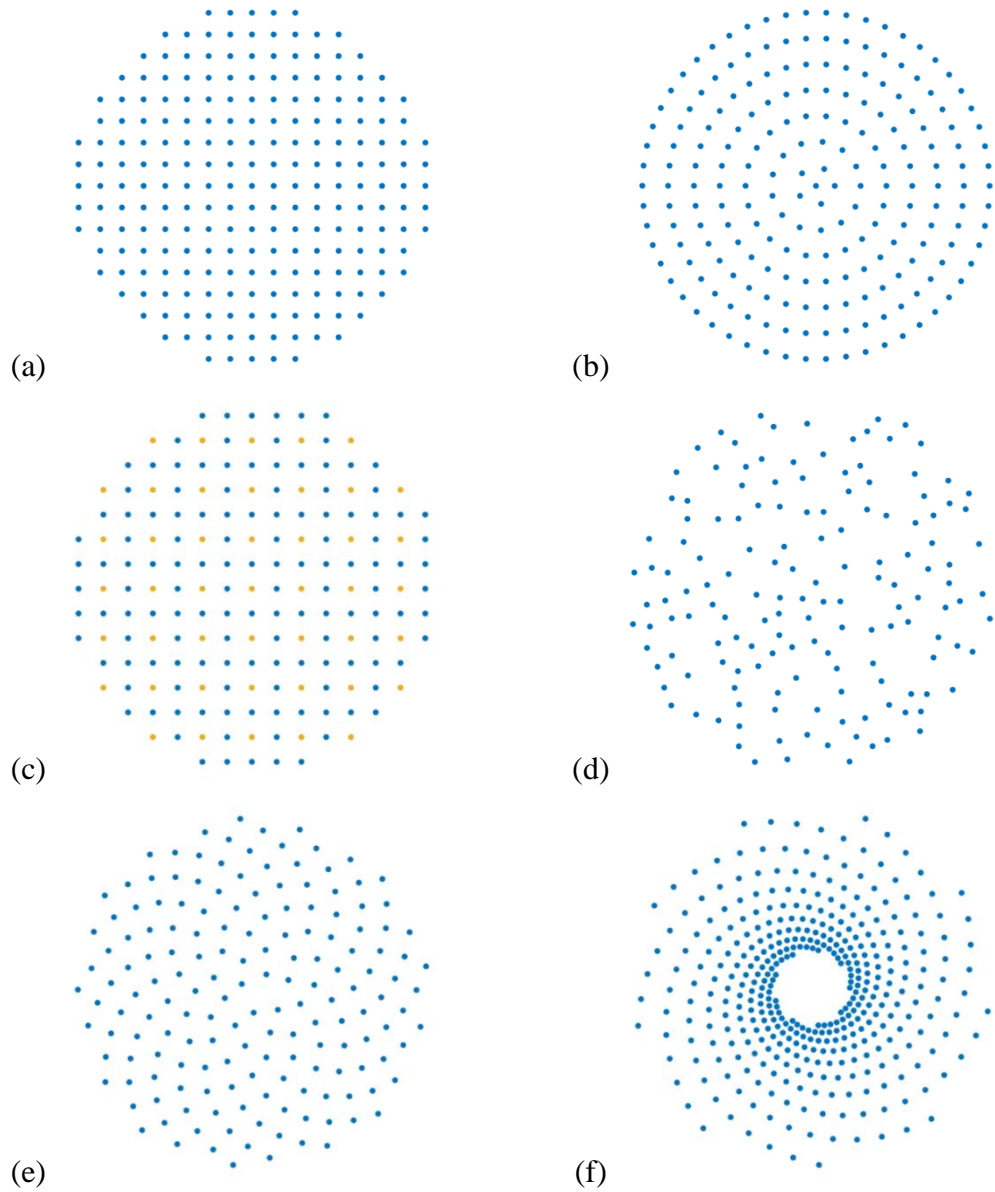


Figure 2.13 Examples of the sparse array. From (a) to (f) are the grid array, the segmented annular array, the Vernier array, the random array, the Fermat spiral array, and the log spiral array. The blue circles represent the elements which work as a transmitter and receiver. The yellow circles represent the elements which work as a receiver only.

When designing ultrasonic arrays, another aspect that needs to be noticed is the cross-talk between adjacent array elements. Cross-talk can be classified into two aspects, one

is the electrical cross-talk, and the other is the mechanical cross-talk [77]. The former can be avoided by introducing electrical shielding into individual channels. The latter is associated with the acoustic wave propagation within the array. As shown in Figure 2.14(a), ideally, when exciting a single element in the array, only that element should vibrate and generate an output acoustic signal, while the rest of the elements in the array should remain inactive. However, in practice, cross talk can occur between the excited and adjacent elements. This can be as a result of electrical cross-talk in the cabling or as a result of mechanical cross-talk within the array aperture. Mechanical cross-talk arises due to Lamb modes propagating laterally [78] [79], these mechanical waves undergo positive reinforcement due to secondary piezoelectric action as the Lamb modes propagate under adjacent elements – a schematic of this is shown in Figure 2.14(b). This will cause an increase of the active aperture, which results in a narrower and non-omni-directional beam from the element. Eventually, these undesired acoustic signals will cause distortion of array directivity patterns and affect the performance of the transducer in terms of the pulse response [80]. Further information on this in the context of the experimental performance of the arrays implemented in the course of this work will be discussed in Section 4.3.2.

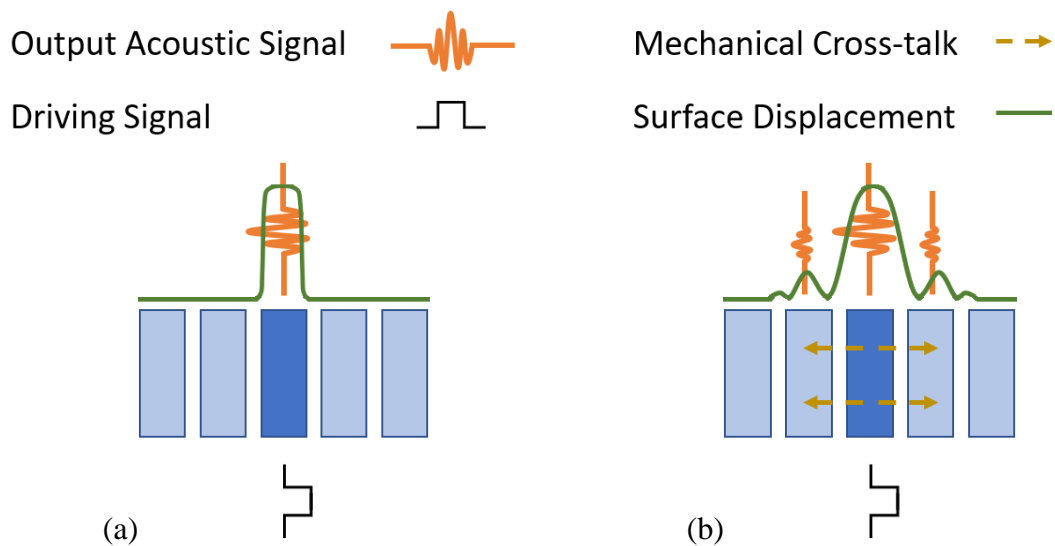


Figure 2.14 Illustration of inter-element cross-talk in an ultrasonic array. (a) represents the ideal vibration, and (b) represents the real situation with cross-talk.

2.5. Field Modelling Algorithm

Acoustic field modelling is a significant part of the ultrasonic transducer design process. It provides a method to find the appropriate design by comparing the acoustic field generated by candidate array patterns. Different field modelling methods might be used depending on the design requirements, such as the execution speed and accuracy. Five acoustic field modelling methods will be reviewed in this Section, including the Rayleigh Integral Method, the spatial impulse response method, the angular spectrum method, the Fourier transform method and finite element analysis (FEA). The Fourier Transform method has been used in the array design process, with details presented in Chapter 3. The FEA has been utilised to simulate the performance of the devices, including the impedance response and the transmitting voltage response (TVR), in Chapter 4.

2.5.1. Rayleigh Integral Method

The Rayleigh Integral Method (RIM) is derived from the Rayleigh integral, which states that the velocity potential at a point in the acoustic field can be predicted by the surface integral of the radiating surface [81]. When using the RIM, the vibrating surface (the transducer) is assumed to be surrounded by an infinite rigid baffle, where Figure 2.15 illustrates the geometry of RIM. The velocity potential can be further used to calculate the acoustic pressure in the field. The continuous integral expression can be written as [82]:

$$P(\vec{y}) = 2i\omega\rho_0 \int_A \frac{e^{-i2\pi|\vec{y}-\vec{x}|/\lambda}}{4\pi|\vec{y}-\vec{x}|} v_n(\vec{x}) dA \quad (2.16)$$

where P is the field pressure, v_n is the normal vibration speed of the source, \vec{y} is a point in the acoustic field and \vec{x} is a point on the vibrating surface, which has an area of A . ω and λ are the angular velocity and the wavelength of the wave, respectively. ρ_0 is the density of the load medium.

This continuous integral expression can be transferred into a numerical model by replacing the surface integral with the summation of a series of sub-areas [83]. The position of each sub-area, d_A , is represented by its central point. This is also termed as the ‘simple source method’ or the Discrete Rayleigh Integral (DRI) method. The DRI is relatively simple to be built into a model that can be processed by software (e.g. Matlab). It can be used to simulate acoustic fields for transducers with different shapes.

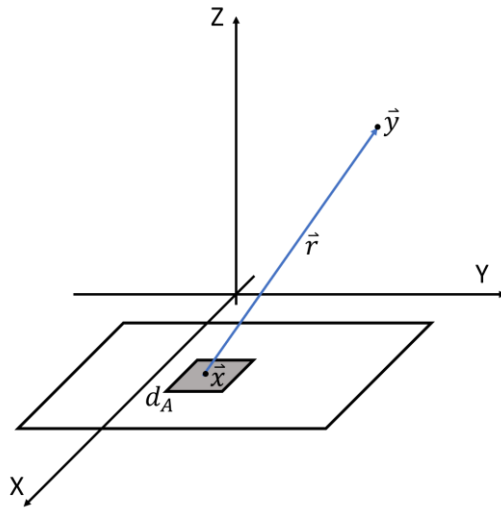


Figure 2.15 Illustration of the Rayleigh Integral Method. The vibration surface (the unfilled large rectangle) is in the XY plane. d_A (the filled small rectangle) represents the sub-area which is extracted from the vibration surface.

The main disadvantage of the basic RIM approach is that it is mainly designed for transducers which are excited by a continuous wave (CW). For typical NDE and biomedical applications, the transducer is usually under pulsed mode excitation. Thus, results from the basic RIM could be inaccurate for those two applications. It is possible to extend the use of RIM to the pulsed situation by introducing inverse Fourier techniques into the RIM algorithm [84]. However, for the pulsed transducer, the sidelobe level is worse when the transducer is driven using CW at the working frequency [70]. Thus, it worth using the RIM as a quick method to compare the performance of different array patterns.

2.5.2. Spatial Impulse Response Method

The Spatial Impulse Response method (SIR) is also developed from the Rayleigh integral [81]. It reduces the Rayleigh integral by expressing the velocity potential as a convolution of spatial impulse response and a time-dependent excitation. The spatial response is calculated using [85]:

$$h(\vec{y}, t) = \int_A \frac{\delta(t - \frac{|\vec{y} - \vec{x}|}{v})}{2\pi|\vec{y} - \vec{x}|} dA \quad (2.17)$$

where $\delta()$ is the Dirac's delta function, and v is the propagation speed of the wave. The definitions for the rest variables are the same as mentioned in Section 2.5.1.

This method is usually used for transducers which are operating under pulsed mode. It can be used to either simulate the acoustic field generated by a proposed array pattern or to simulate the imaging of a material consisting of lots of point scatters, which is often the case for biomedical applications [85]. However, compared to DRI, the SIR method more complex as the spatial impulse response has to be calculated [70].

2.5.3. Angular Spectrum Method

The Angular Spectrum method (ASM) can be used to analyse the propagation of a plane wave. It was originally developed for optical waves [86] but has been extensively applied in the analysis of acoustic fields. The processing steps of the ASM are:

1. Sample the plane wave at the surface of the source plane and record it as the input plane wave.
2. Apply 2D Fourier transform on the input plane wave to get the angular spectrum.

3. Propagate the transform to the desired plane by multiplying the transform with a complex phasing matrix.
4. Apply inverse Fourier transform on the angular spectrum from Step 3 to get the pressure at the desired plane.

The basic ASM is suitable for transducers with a planar surface and working under CW mode. However, with some modification, the ASM can also be applied on transducers under pulsed mode [87] or on transducers with a curved surface [88].

2.5.4. Fourier Transform Method

The Fourier transform method is similar to the ASM method. It was developed from the equivalencies between expressions for the far-field directivity of a 1D linear array and the Fourier transform [89], and can be extended to a 2D array by applying the 2D Fourier transform. A numerical model can be built based on this method by using the Fast Fourier Transform (FFT) algorithm. The resultant directivity function is in dB and presented in the u-v space [90], which is converted from the 3D coordinates using:

$$u = r * \sin (\vartheta) \cos (\varphi) \quad (2.18)$$

$$v = r * \sin (\vartheta) \sin (\varphi) \quad (2.19)$$

r is the distance from the original point in the 3D coordinate to a point in the same coordinate space. ϑ and φ are as shown in Figure 2.16.

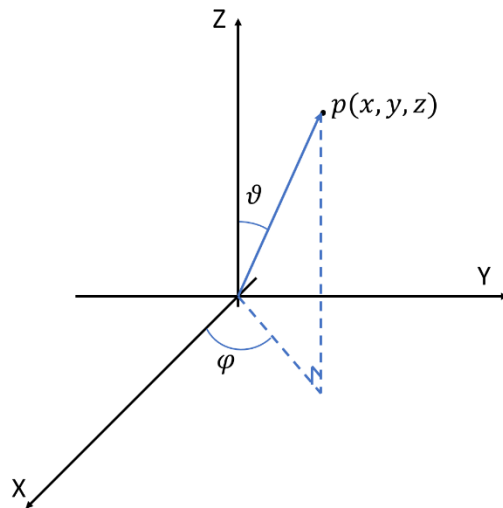


Figure 2.16 Illustration of the parameters needed in converting the 3D coordinate into the u - v space.

The FFT method can be divided into four steps:

1. Define the position of each element by its central point.
2. Divide the element position (unit of meter) by the propagation wavelength to get the aperture function of the array.
3. Create a binary image of the aperture function with the pixels within each element set to 1 (white) and the others set to 0 (black).
4. Apply 2D Fast Fourier transform to the binary image and reshape the results to ensure the main lobe is in the centre. Moreover, according to the possible values of u and v , only pixels which have both values within -1 to 1 are kept.

Figure 2.17 shows an example of using the Fourier transform method to analyse the far-field directivity function of a 2D array with nine elements (3x3). The element is designed to be square with 5 mm width. The gap between neighbouring elements is set

to 0.5 mm. 2D Fast Fourier Transform with 20 samples per wavelength has been applied to the binary image of the array pattern. The simulation results indicate that the transducer has a peak sidelobe level of -12.69 dB.

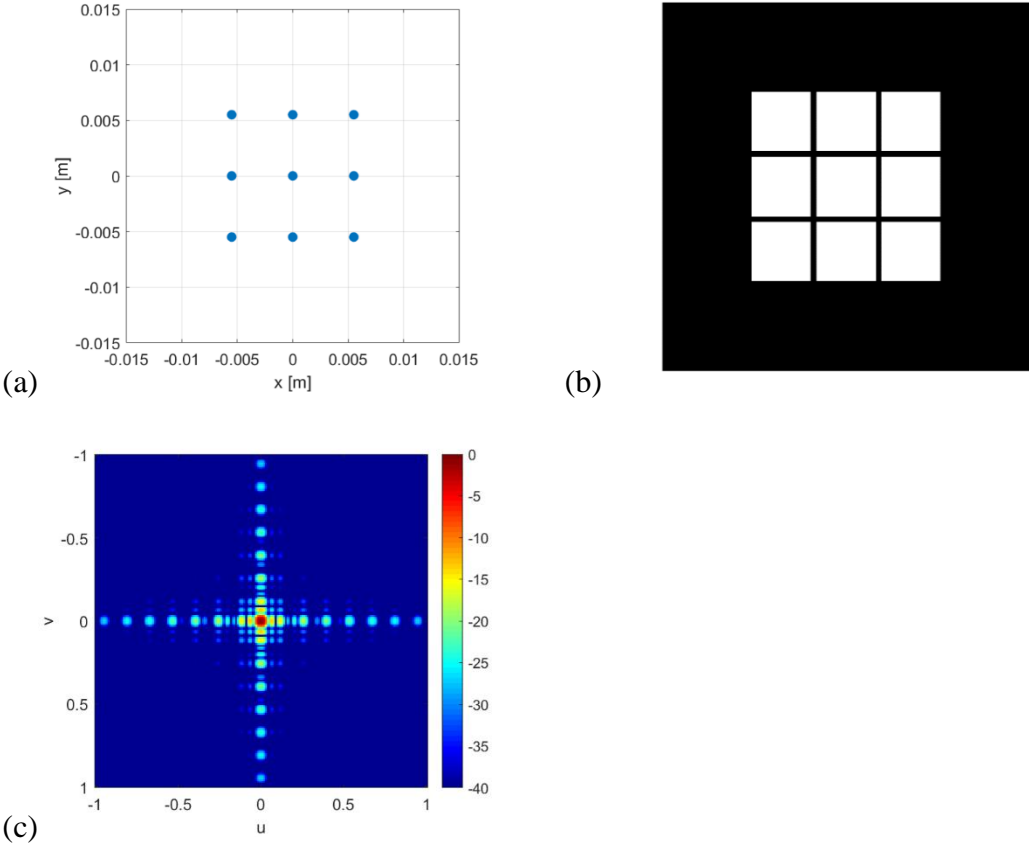


Figure 2.17 Example results for analysing a 3x3 element array using the 2D FFT method. (a) The blue points represent the centres for the elements. (b) The binary image of the array pattern. (c) The estimated far-field directivity function generated by applying 2D FFT to (b).

2.5.5. Finite Element Analysis

Finite element analysis (FEA) can be used to simulate the behaviour of a structure by breaking it into a series of small units, which are defined as elements, and assigning corresponding physical properties. Each element contains only a single kind of material.

The connecting points of the elements are called nodes. The FEA can adapt well to different transducer operational situations and has advantages in analysing complex structures. However, the execution time can be problematic, especially when the 3D model of the transducer is required. Researchers have been working on accelerating the execution speed by using the Graphics Processing Unit (GPU)-based parallel computing algorithms [69] and cloud based simulation approaches [91].

2.6. Ultrasonic Imaging Algorithms

Ultrasound tests can detect the internal structure of an object based on the reflected ultrasonic signals. Scatters inside the object under inspection with different acoustic impedances will reflect the ultrasound waves back to the transducer. As shown in Figure 2.18, by combining the time of arrival of a reflection and the velocity of sound in the load material, the reflected signals can be used to locate the position of the scatter. A single trace of the reflected ultrasonic signal is termed as the A-scan, which is mostly used by the single-element transducer since there is only one receiver.

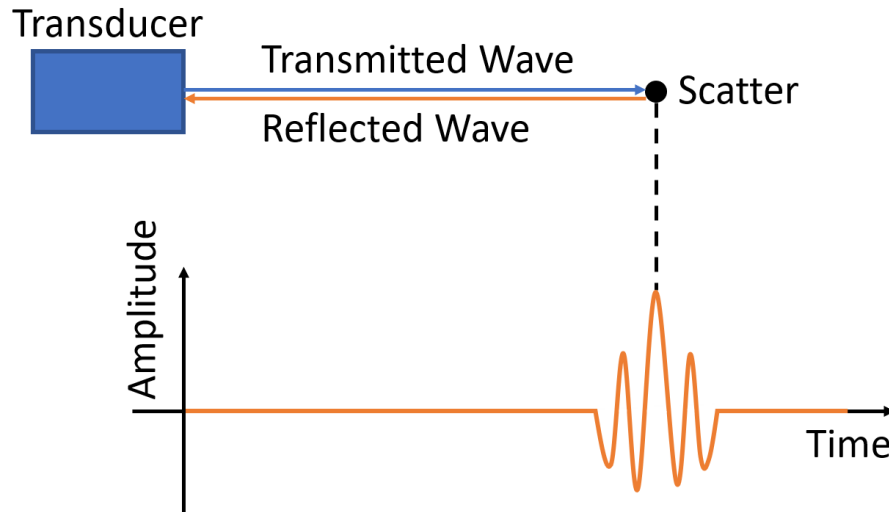


Figure 2.18 Illustration of the basic ultrasonic imaging principle.

More flexible imaging techniques can be achieved by using an ultrasonic array. Conventionally, the ultrasonic array is controlled to produce multiple beams, with each generated from a group of elements and can be treated as a series of A-scan traces. Pre-defined focal laws can be loaded to the array to achieve beam focusing and/or steering. These A-scan traces can be stitched together to form an image, which is termed as the B-scan image. Compared to the A-scan, the B-scan image is a more intuitive way to analyse the object under detection.

Another data acquisition method, called the Full Matrix Capture (FMC), as shown in Figure 2.19, was proposed in [92]. FMC consists of the A-scan traces for all the transmit-receive element combinations of the entire array. To get the FMC data for an array with N elements, N transmissions are required. For each transmission, only one element of the array is fired, while all the elements including the fired one are used to capture the reflected signals. Thus, the FMC dataset will comprise $N \times N$ A-scan traces

and can then be used to generate a variety of image representations through post-processing.

Three conventional ultrasonic imaging algorithms, plane B-scan, focused B-scan and sector B-scan, plus the total focusing method (TFM) can be processed using the FMC captured data. Another imaging algorithm, Doppler imaging, is often used to detect a moving object. The basic principles of these algorithms will be introduced in this Section.

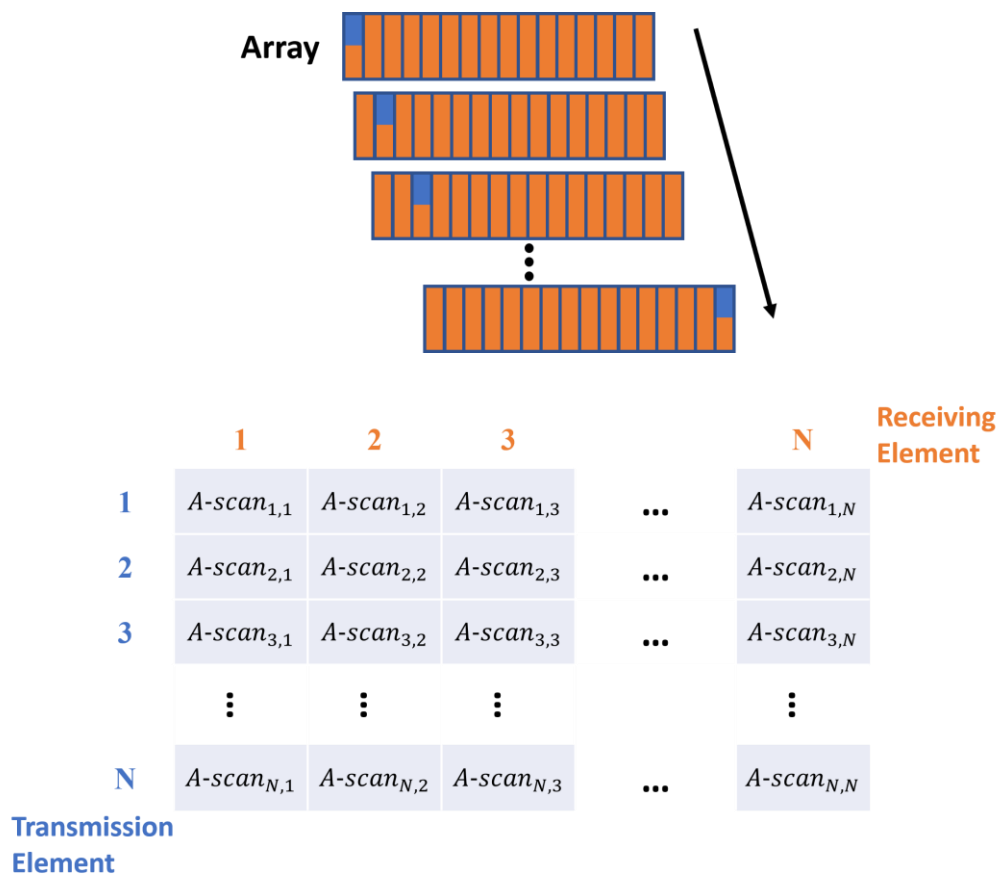


Figure 2.19 Illustration of the Full Matrix Capture (FMC) process.

2.6.1. Plane B-scan

Figure 2.20 illustrates the basic principle to process a plane B-scan. The whole ultrasonic array aperture is divided into several groups, with each containing the same number of array elements. Each group of elements is termed as a sub-aperture. Generally, there exists an element overlap between neighbouring groups. The sub-apertures are successively activated from one end of the array to the other end. Each activation will create one line of the image. During each activation, all the elements within the sub-aperture are simultaneously fired to form a plane wave front. Each element works as a transmitter and receiver. The receiving signals for all elements within the sub-aperture are averaged to form one line of the image. The intensity of a point $p(x_0, z_0)$ on the axial line associated within a sub-aperture can be calculated using:

$$I(x_0, z_0) = \left| \sum_{tx=N_1}^{N_2} \sum_{rx=N_1}^{N_2} h_{tx,rx}\left(\frac{2z_0}{v}\right) \right| \quad (2.20)$$

where N_1 and N_2 are the indices of the first and the last element of a sub-aperture, $h_{tx,rx}()$ is the A-scan trace from the FMC data, tx and rx are the number of the transmitter and the receiver, respectively, and v is the ultrasound propagation speed in the load material.

The plane B-scan algorithm is relatively easy to achieve as it does not require the calculation of a specific focal law. However, its non-focusing characteristic also limits the achievable imaging resolution.

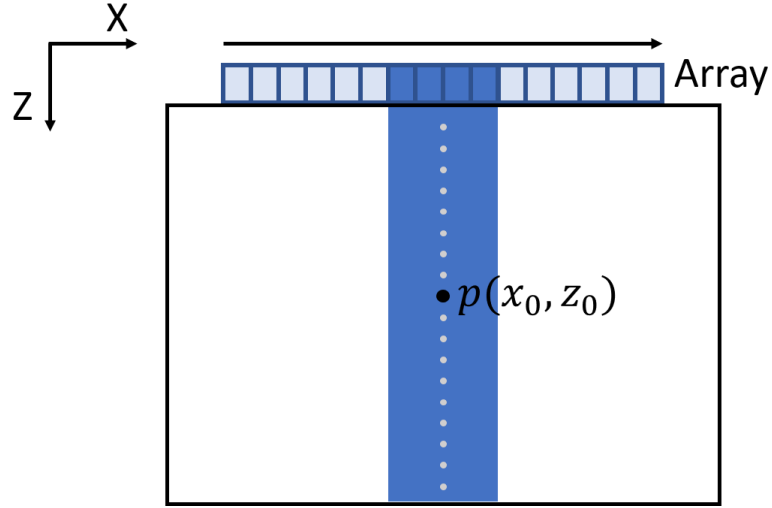


Figure 2.20 Schematic diagram of plane B-scan, where shaded array elements constitute the active sub-aperture.

2.6.2. Focused B-scan

The processing of the focused B-scan, as shown in Figure 2.20, is similar to that of the plane B-scan. It also requires a sub-aperture shift along the full array aperture. The main difference is that the focused B-scan employs a focal law to each sub-aperture so that the lateral resolution at the specific area can be improved. As shown in Figure 2.21, the beam for the aperture, which consists of the central four elements, is focused at a point $p(x_0, z_0)$. Then, the image intensity for any other point $p(x_0, z_n)$, which locates along the beam, can be expressed as:

$$I(x_0, z_n) = \sum_{tx=N_1}^{N_2} \sum_{rx=N_1}^{N_2} h_{tx,rx} \left(\frac{\sqrt{(x_{tx} - x_0)^2 + z_0^2} + \sqrt{(x_{rx} - x_0)^2 + z_0^2} + 2(z_n - z_0)}{v} \right) \quad (2.21)$$

where x_{tx} and x_{rx} are the x -axis coordinates for the transmitter and the receiver, respectively. The definitions for other variables are the same as defined before.

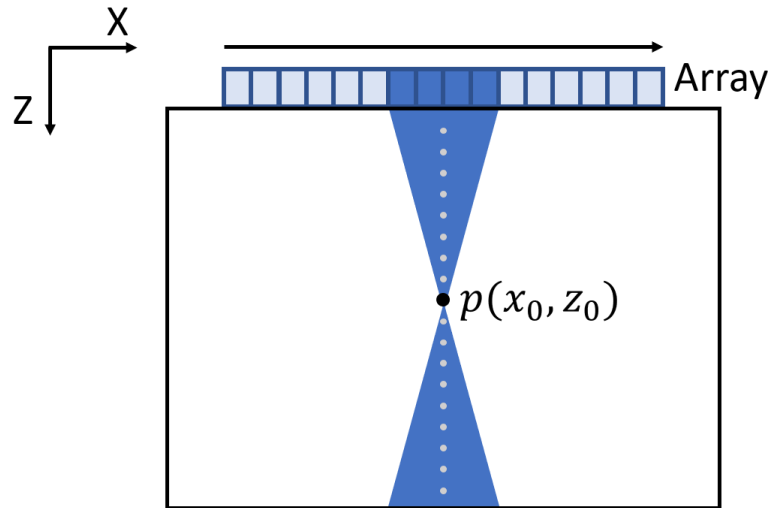


Figure 2.21 Schematic diagram of focused B-scan, where shaded array elements constitute the active sub-aperture.

One disadvantage of the focused B-scan is that, since the ultrasound beam is forced to focus at a specific depth, the lateral resolution at other depths along the beam will be affected. This issue can be improved by applying multiple focal laws, which are focused at different depths. This is termed as the Dynamic Depth Focusing (DDF) method [93]. However, increasing the number of focusing depths will lead to a decrease in the imaging frame rate. Thus, depending on the requirement of the applications, a compromise might need to be made to achieve appropriate resolution and imaging frame rate.

2.6.3. Sector B-scan

Sector B-scan can achieve a wider view in the lateral direction of the image by steering the beam to a desired angle. It is also referred to as the S-scan. As shown in Figure 2.22, the beam from each sub-aperture is controlled to steer to a specific angle and contribute

one line of the final sectorial B-scan image. Different from the plane and focused B-scans, the sector B-scan uses the polar coordinate to create the image. The intensity of a point within a sub-aperture of the sector B-scan can be calculated using:

$$I(r_0, \gamma_0) = \sum_{tx=N_1}^{N_2} \sum_{rx=N_1}^{N_2} h_{tx,rx} \left(\frac{2r_0 + x_{tx} \sin(\gamma_0) + x_{rx} \sin(\gamma_0)}{v} \right) \quad (2.22)$$

where r is the distance from the point to the centre of the sub-aperture and γ is the steering angle of the beam.

Sector B-scan can also achieve focusing by applying appropriate focal law to the sub-aperture. By combining the sector B-scan with DDF, an image with both high resolution and a wider view can be achieved.

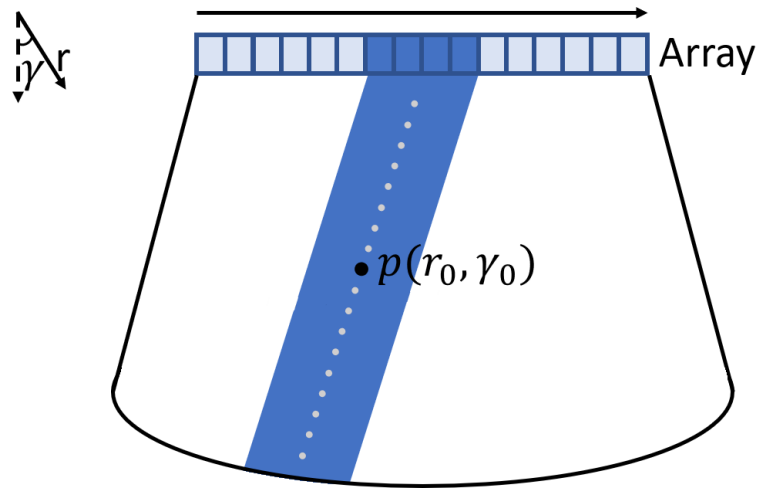


Figure 2.22 Schematic diagram of sector B-scan, where shaded array elements constitute the active sub-aperture.

2.6.4. Total Focusing Method

Total focusing method (TFM) is an advanced imaging algorithm which has been developed based on the FMC technique [92]. It can achieve focusing at all target points in the image by applying appropriate time delays to the full FMC data as shown in Figure 2.23. The intensity of a point in the TFM image can be calculated as:

$$I(x_0, z_0) = \sum_{tx=1}^N \sum_{rx=1}^N h_{tx,rx} \left(\frac{\sqrt{(x_{tx} - x_0)^2 + z_0^2} + \sqrt{(x_{rx} - x_0)^2 + z_0^2}}{v} \right) \quad (2.23)$$

where N is the total number of elements in the array. Definitions for other symbols are the same as mentioned previously.

TFM algorithm can provide an image with high resolution and contrast. However, the large amount of calculations limits its application, especially in the situation when a real-time imaging is required.

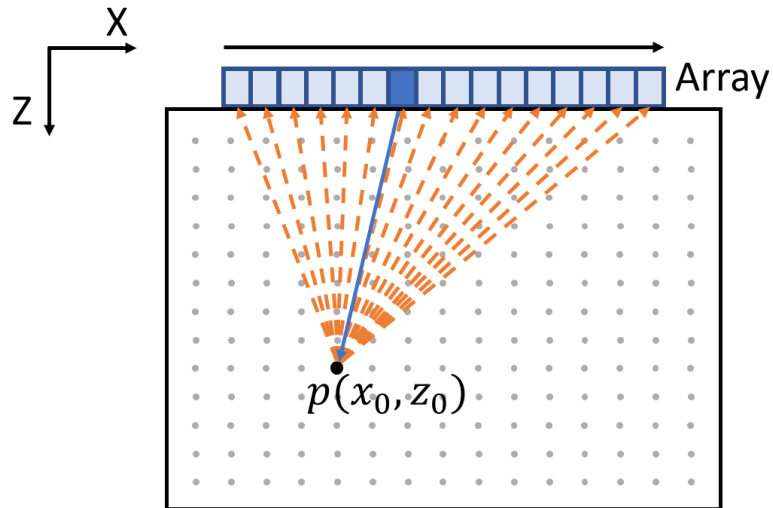


Figure 2.23 Schematic diagram of total focusing method (TFM), where shaded array element is the transmitter and all array elements are receivers.

2.6.5. Doppler Imaging

In the medical ultrasound imaging field, the Doppler Effect is used to detect the motion of tissue and blood. As illustrated in Figure 2.24, the Doppler Effect associates the frequency shifts to the velocity of the detected object. The relationship can be expressed as [94]:

$$f_S = f_T - f_R = \frac{2f_T v_{ob} \cos(\sigma)}{v} \quad (2.24)$$

Where f_S is the frequency shift, f_T and f_R are the transmitted frequency and the reflected frequencies respectively, v_{ob} is the velocity of the moving object relative to the transmitted signal, σ is the angle between the beam direction and the motion direction of the moving object, and v is the propagation speed of ultrasound in the load material.

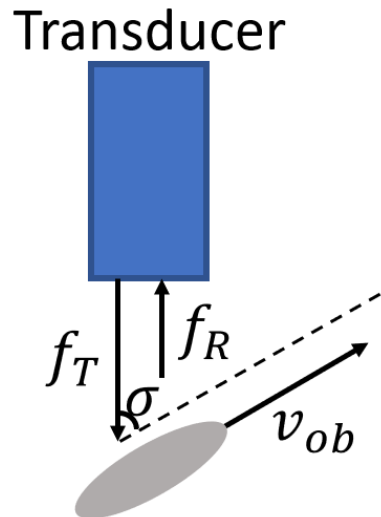


Figure 2.24 Illustration of the Doppler Effect.

According to the differences in resulting images, the Doppler imaging can be further divided into two categories: Colour Doppler Velocity imaging and Power Doppler imaging [95]. The Colour Doppler Velocity imaging represents the motion direction using different colours. Normally, red represents motion towards the surface of the transducer, while blue represents the opposite situation. The Power Doppler imaging does not measure the velocity and instead shows only the occurrence of the movement [95]. However, the Power Doppler imaging is more sensitive than Colour Doppler Velocity imaging, which makes it more suitable for imaging small vessels.

2.7. Standard Image Processing Algorithms

This Section reviews the three algorithms that have been used in developing the detection algorithms described in Chapter 5.

2.7.1. Difference Imaging

Difference imaging is an image subtraction technique, which aims to detect the intensity changes between images associated with the same image space. As shown in Figure 2.25, it works by subtracting a reference image from the target image. The reference image can be a single image picked from the dataset or be generated by averaging several images in the dataset [96]. For some applications, the reference image is convolved by a kernel to increase accuracy [97].

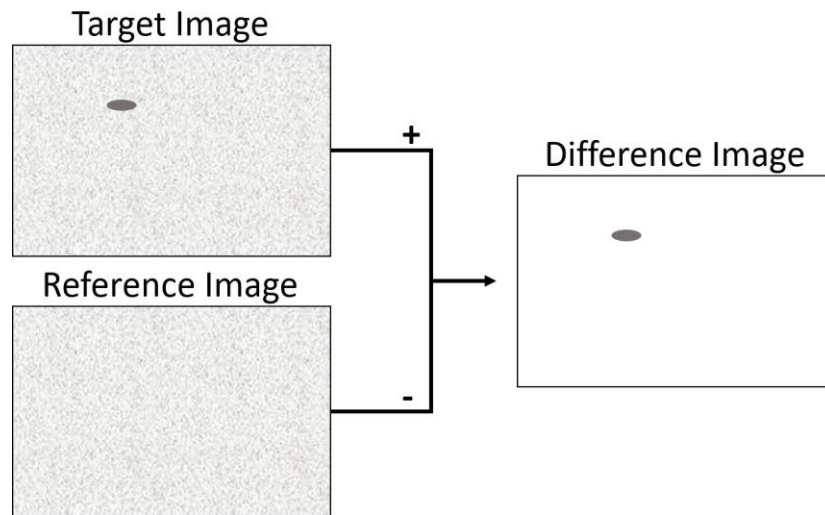


Figure 2.25 Illustration of the difference imaging algorithm.

2.7.2. Morphological Image Processing

Morphological image processing is based on set theory and aims to extract information related to the shape and structure of the object in an image. Morphological operations are mainly applied to binary images but can be extended to greyscale images as well [98]. A structuring element (SE) which consists of a set of binary pixels, is used to interact with the targeted image. For each pixel in the targeted image, a section, which is central to that pixel and has the same dimension as the SE , is selected. This section will be compared to SE following pre-defined rules to determine the intensity of that pixel in the resultant image. The two fundamental morphological operations are erosion and dilation. They are basically logical operations. For erosion, the logical AND operation is used to compare the section and the SE , while, for dilation, the logical OR operation is used [99].

Figure 2.26 shows an example of applying erosion and dilation on a 9x9 binary image with a 3x3 SE. As shown in the figure, erosion shrinks the object contained in the original image, and dilation expands it. Based on their properties, erosion can be used to remove unwanted components in an image, while the dilation can be used to bridge gaps.

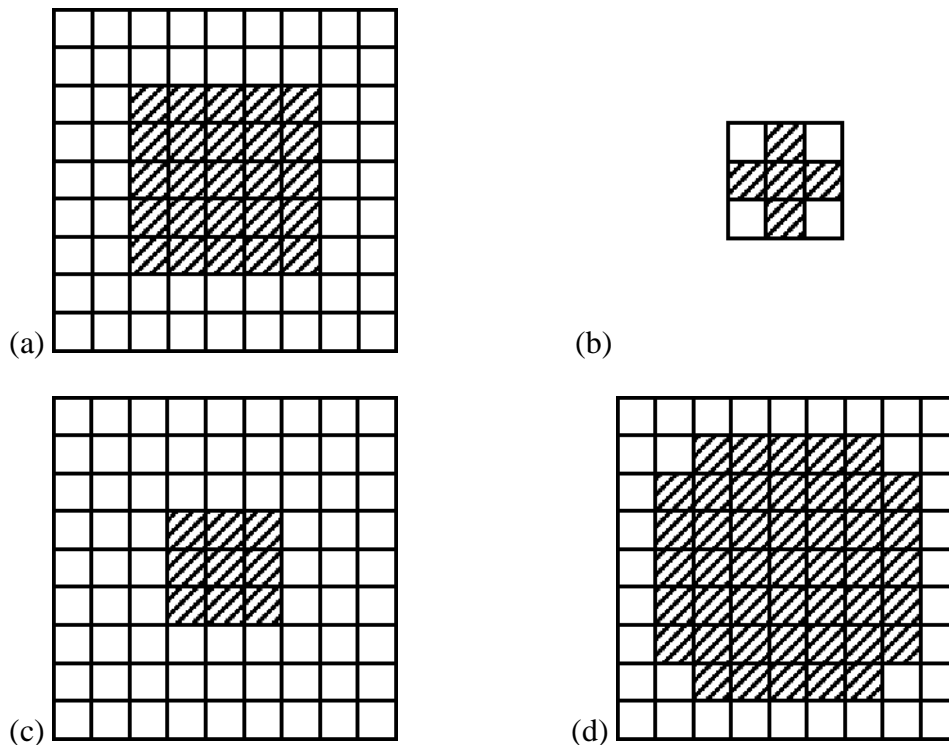


Figure 2.26 A simple example of applying erosion and dilation on (a) a 9x9 pixel image using (b) a 3x3 pixel SE. (c) The resultant image for erosion. (d) The resultant image for dilation.

Another two important morphological operations are the opening and the closing. In simple terms, they are a combination of the erosion and the dilation, but in different orders. For the opening, the targeted image is eroded first and then dilated, while the closing is the opposite. Although both opening and closing can smooth the object in an

image, opening tends to remove narrow bridges and minor extensions in the object, while closing tends to fill gaps [100]. Figure 2.27 shows an example of applying erosion, dilation, opening, and closing separately to the same targeted image, aiming to provide a more intuitive explanation of those four morphological operations.

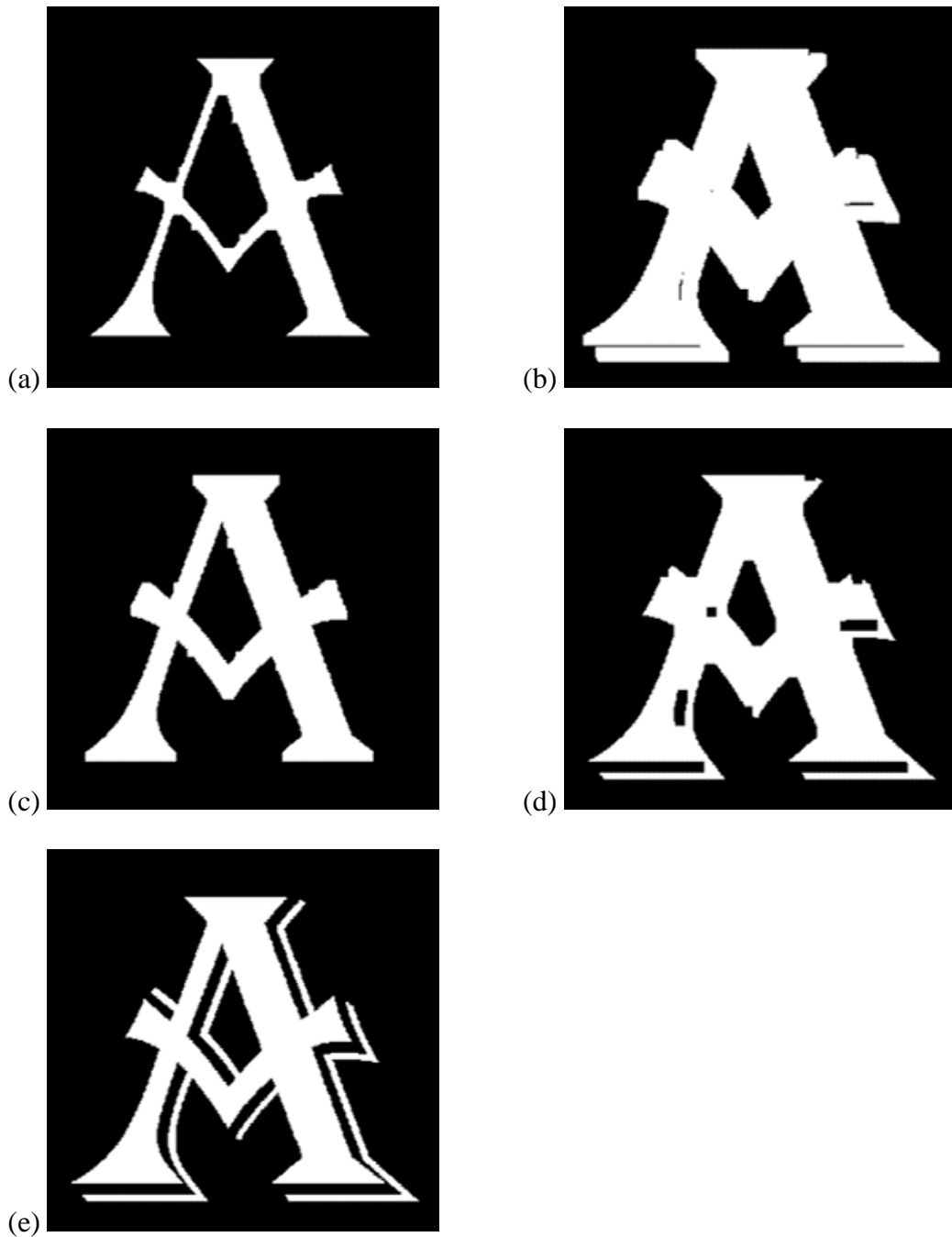


Figure 2.27 Illustration of applying (a) erosion, (b) dilation, (c) opening, and (d) closing to (e) the original image.

2.7.3. Hough Transform

In 1972, Paul Hough invented a transform aiming to extract lines in an image [101]. The basic idea is to present straight lines using a new coordinate system, where the x -axis is replaced by the slope and y -axis is replaced by the y -intercept. A straight line in the x - y coordinate system will be represented by a single point in the slope-intercept coordinate system. Conversely, a point in the x - y coordinate will form a straight line in the slope-intercept coordinate system. This means lines in the slope-intercept coordinate system, which represents the points contributed to a straight line in an image, will pass through the same point. Thus, it is possible to detect straight lines in an image by finding the intersection points in the corresponding slope-intercept coordinate system.

However, the slope-intercept method does not suit vertical lines which will cause unbounded slope values. To solve this problem, Duda and Hart proposed an improved model, where the x -axis was replaced by the polar angle (γ) and the y -axis was replaced by the polar radius (r) [102]. As shown in Figure 2.28, points form the same line in the x - y coordinate system are represented by crossed curved lines in the γ - r coordinate system. Again, by searching the intersection points, it is possible to detect the straight lines in the original image. When analysing an image, the matrix which contains the γ - r parameters is termed as the Hough space. Except for detecting straight lines, the Hough transform can also be modified to detect circles and other irregular shaped objects in an image [103].

Figure 2.29 shows an example of detecting the straight lines in an image using the in-built Hough transform algorithm in Matlab. As shown in the Figure, the three straight

lines in the original image cause the three peak intersection points in the Hough space. These peaks are in turn used to detect the straight lines in the original image.

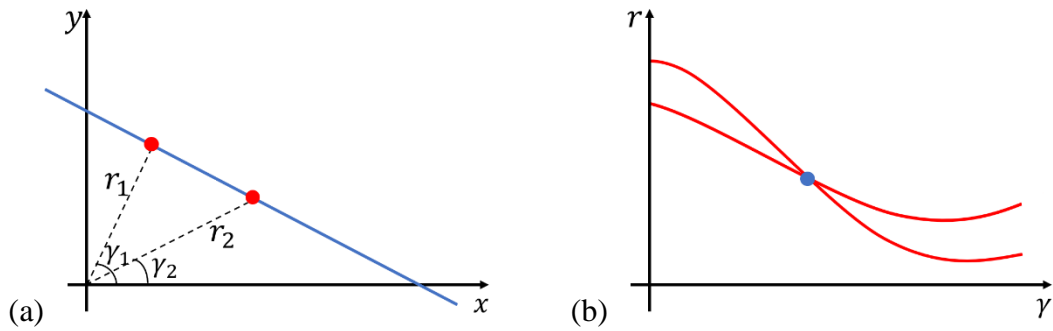


Figure 2.28 Illustration of the basic idea for Hough Transform. The blue line in the x - y coordinate system (a) is transferred into the blue point in the γ - r coordinate system (b). The red points at the blue line are transferred into the red curves in the γ - r coordinate system (b).

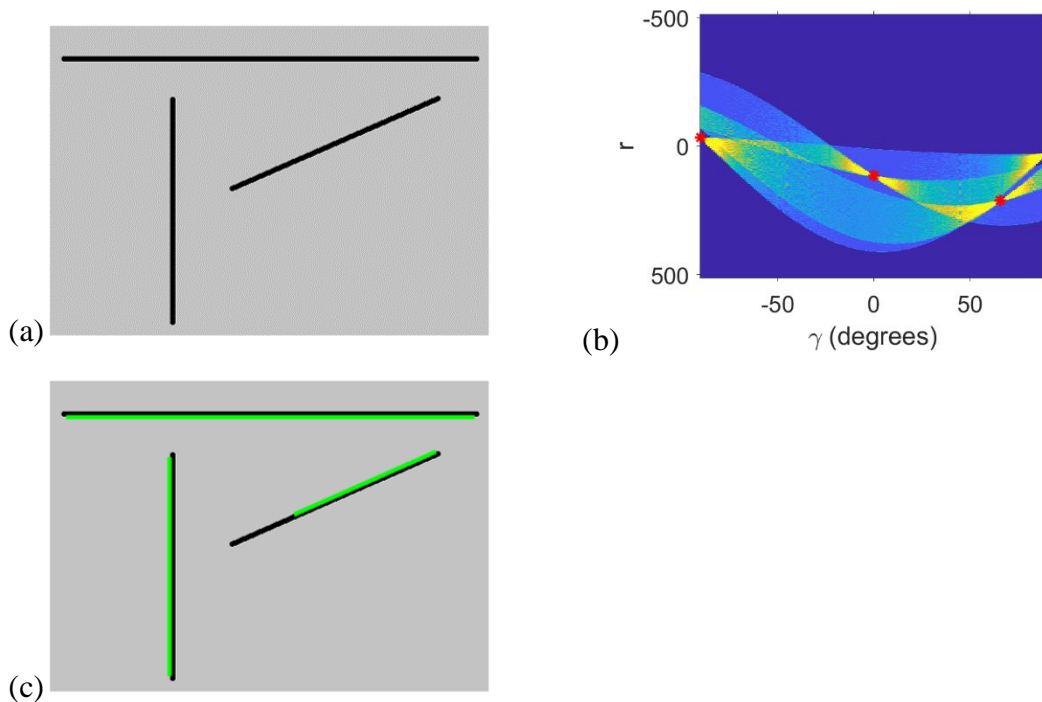


Figure 2.29 Illustration of detecting lines in an image using the Hough Transform. (a) The original image. (b) The Hough space generated from (a). The red spots represent the peaks in the Hough transform, which are formed by the lines in the original image. (c) The original image with detected lines, which are marked using green lines.

2.8. Review of Transcranial Ultrasound Applications

Transcranial testing is a medical technique which aims to test the health condition in human brains. One of the most commonly used transcranial testing techniques is the Transcranial Doppler Ultrasound (TCD), which can be used to detect blood flow parameters by using the Doppler Effect.

The key point to process a successful TCD test is finding the appropriate acoustic windows [104]. These windows are where the ultrasound can travel through the skull and reach the targeted blood vessels. Moreover, operators need these windows to locate the blood vessels under detection. There are three acoustic windows, including the transtemporal window, the transorbital window, and the transforaminal window [104]. The positions of these windows are shown in Figure 2.30.

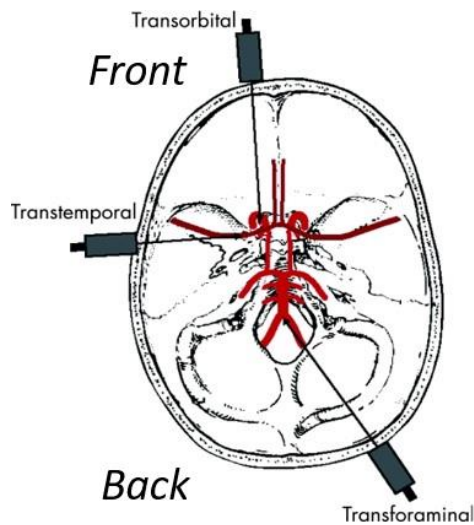


Figure 2.30 The three acoustic windows used in the TCD test [104].

According to the transducer used in the test and the imaging algorithms used in post-processing, TCD can be divided into three groups, including the conventional TCD, the transcranial colour-coded duplex ultrasonography (TCCS), and the 3D transcranial ultrasound imaging.

2.8.1. Conventional Transcranial Doppler Ultrasound

Conventional TCD uses a single-element transducer to detect the blood flow. The results are shown as non-image time-domain spectral waveforms. When using TCD to locate the blood vessels, several factors, including the position of the probe, the depth of the echoes, the measured direction of the blood flow, and the properties of the received signal, must be considered [104]. As a non-imaging technique, the conventional TCD is highly operator dependent. However, experienced sonographers are not widely available. Thus, immediate diagnosis using the conventional TCD in an ambulance or emergency room is not realistic [8].

2.8.2. Transcranial Colour-Coded Duplex Ultrasonography

Transcranial colour-coded duplex ultrasonography (TCCS) is able to generate 2D images for intracranial vessels. The direction of blood flow with respect to the probe is coded the same way as discussed in Section 2.6.5 on Doppler imaging. Usually, the colour-coded Doppler images are combined with a B-scan image for better information presentation [105].

Same as for conventional TCD, TCCS is also an operator-dependent test. Since typical TCCS can only provide a single 2D image, the probe must be moved around the acoustic

window to locate the blood vessels. At present, no reliable head frames have been produced for typical TCCS transducer fixation [8]. Thus, the operators need to hold the probe during the whole test. According to some clinical guidelines, a transcranial ultrasonography test can take from 20min up to 60min [106] [107]. Even for experienced operators, fatigue is a factor that will influence their diagnosis. Moreover, although TCCS has also been tested for ischemic stroke therapy, research to address safety concerns is not sufficient when compared to TCD [8].

2.8.3. 3D Transcranial Ultrasound Imaging

3-D transcranial ultrasonography can be considered as an expanded technique of typical TCCS. The purpose of 3D TCD is to show 3D images for intracranial vessels, providing more easy-to-understand diagnostic information for operators. However, the 3D images might not be displayed in real-time because of the long data acquisition and processing times. The research that has been reported in this technique all need to construct the 3D models based on the received TCD waveforms offline.

Real-time 3D transcranial ultrasonography has been successful in in-vivo experiments. A helmet, which is built up based on multi-layer circuits, is produced to hold two 2D sparse phased array transducers [108]. Those two transducers are put at opposite sides of the transtemporal windows to synchronously image both sides of the brain. Contrast agents and aberration corrections have been studied to improve the quality of 3D images [109] [110]. However, the images that can be displayed in real-time are the same 2D colour-coded Doppler images as mentioned in typical TCCS. The 3D images for the

vessels are only constructed offline after all data has been acquired. Another drawback is that the transducers used in this study are not attached to matching layers. Thus, mismatches in acoustic impedance between the active layer and skull could be one of the factors that cause degradation in image quality. Also, since this device is tested on healthy volunteers, images for abnormal vessels are not available.

Chapter 3

Design of 2D Sparse Array Pattern

3.1. Introduction

Considering the medical application motivation for the transducers developed in this work, the array transducer aperture size should be set to match the size of the temporal window, which is 2 to 3 cm in diameter [110]. Although it is based on the largest dimension, the transducer aperture will be designed within a circular aperture of 3 cm diameter. This is to simplify the fabrication of the prototype array and it is anticipated that a practical array device should be limited to 2 cm diameter to ensure compatibility across all patients. The speed of sound in human tissue is assumed to be 1540 m/s [111]. Hence, for an operating frequency of 2 MHz, which is the working frequency for most TCD transducers [8], the wavelength is 0.77 mm. Due to the associated half-wavelength limit of element pitch in dense array designs [65], a full matrix 2D array transducer which has comparable resolution to a 1D linear array transducer would require an extremely large number of elements. Figure 3.1 shows an example of a dense array with half-wavelength pitch (0.385 mm). There are 4669 elements in total within the array aperture. This presents a huge challenge for both manufacturing and controlling the array. One way to reduce the number of elements is by using a 2D sparse array

transducer which, if designed correctly, can achieve acceptable imaging capability while using fewer elements.

Four parameters are used to describe an array layout: the aperture size and shape; the element position; and the element size. Circular elements will be utilized to achieve rotational symmetry. Three aperiodic array configurations have been simulated to find the optimised design: a random array element approach; the logarithmic spiral array; and the Fermat spiral array. Figure 3.2 illustrates examples of these array configurations. In this work, the position of an element is determined by the coordinate of its centre point. The 2D FFT method, as described in Section 2.5.4, is used to estimate the far field directivity function (DF) of an array configuration. Two parameters, Peak Side Lobe (*PSL*) and Integrated Side Lobe Ratio (*ISLR*), which are calculated based on the DF, are used to estimate the performance of these configurations.

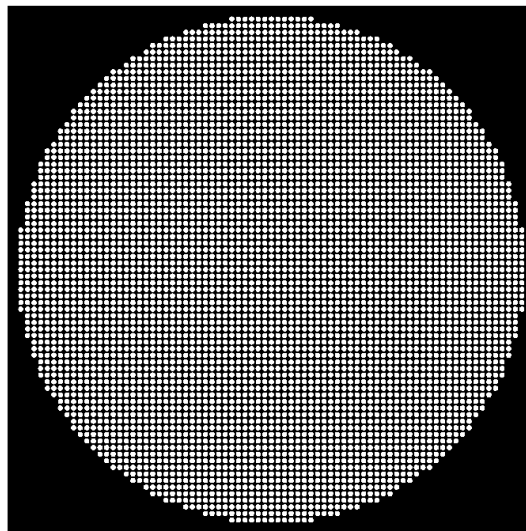


Figure 3.1 2D dense matrix array with 4669 elements. The ratio of element diameter to element gap is 4:1.

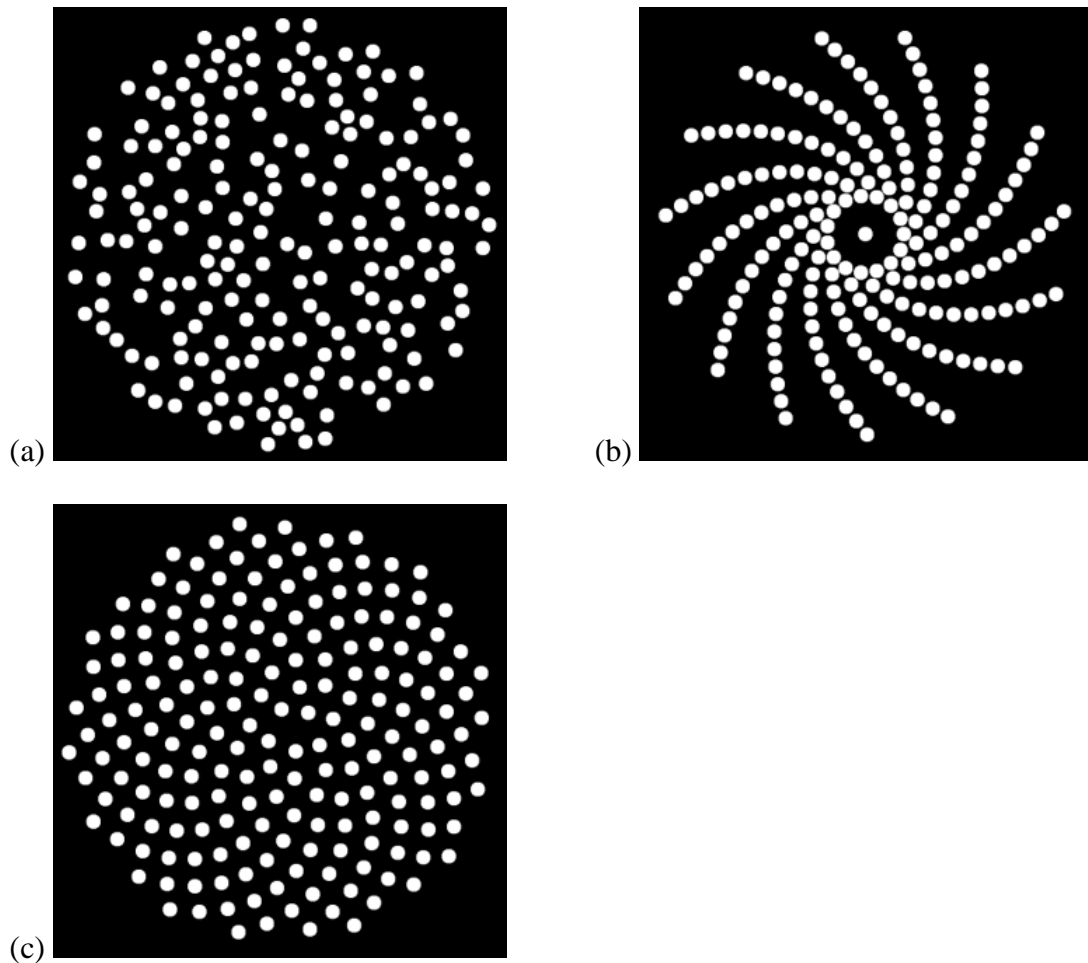


Figure 3.2 Three sparse array configurations which have been simulated in this work: (a) random array; (b) log spiral array; and (c) Fermat spiral array.

3.2. Peak Side Lobe Level (*PSL*) and Integrated Side Lobe Ratio (*ISLR*)

Two metrics known as, Peak Side Lobe Level (*PSL*) and Integrated Side Lobe Ratio (*ISLR*) are used to estimate the performance of the array configurations in terms of their imaging capability [112] [70]. These two parameters reflect the relative relationship between the main-lobe and the associated side-lobes, which are illustrated in Figure 3.3.

PSL is defined as the ratio of the maximum side-lobe value to the maximum main-lobe value. *ISLR* is defined as the ratio of the total energy contained outside the main-lobe (side-lobes area) to the energy contained inside the main-lobe. These two parameters can be expressed using:

$$PSL = 20 \log_{10}(Amp_s/Amp_m) \quad (3.1)$$

$$ISLR = 10 \log_{10}(Elb_s/Elb_m) \quad (3.2)$$

where *Amp* and *Elb* represent for the amplitude and the energy in the lobe(s) respectively. The side-lobe is represented by subscript *s*, while the main-lobe is represented by subscript *m*.

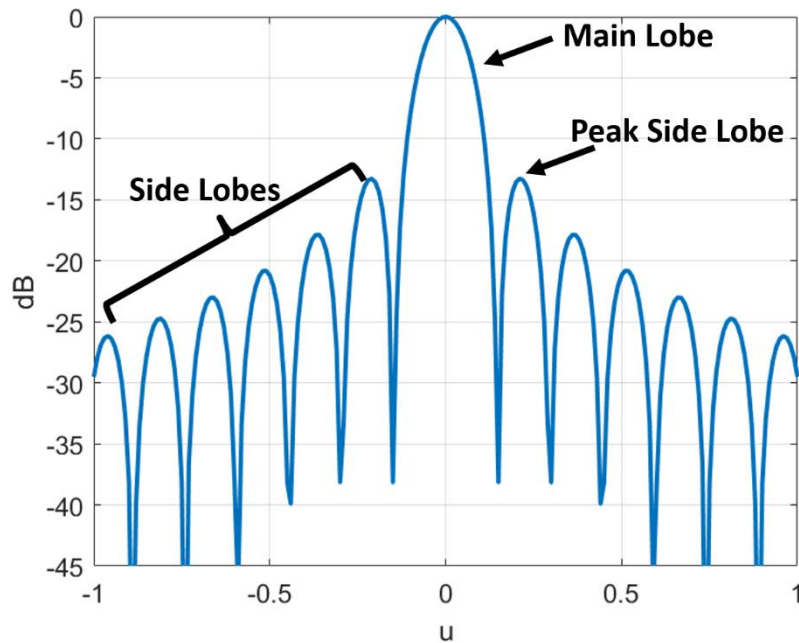


Figure 3.3 Illustration of main lobe and side lobes.

Both *PSL* and *ISLR* are related to the quality of image which could be achieved by an ultrasonic transducer. They reflect the ability of the imaging system to identify the target in the main-lobe path in the presence of targets or scatters in the side-lobes regions. High *PSL* or *ISLR* values could indicate a problem when the target in the main-lobe path is weak [112], or when imaging low contrast materials [70]. Thus, an appropriate transducer should have a low *PSL* value, as well as low *ISLR*. For the purpose of the work described in this thesis, *PSL* has been given higher priority to ensure the weak reflector along the main-lobe can be detected. Meanwhile, as the tissue mimicking material (TMM), which will be used to test the imaging performance of the prototype transducers, is a low contrast material, *ISLR* should be maintained at a low level as well. Thus, compromise must be made to ensure the selected array pattern has relatively low *PSL* as well as *ISLR*. Details of this process will be discussed later in Section 3.5 and Section 3.6.

To calculate *PSL* and *ISLR*, it is necessary to predict the propagation of ultrasound waves in the imaging material. Method such as the Huygens' theory [113] and the Rayleigh's integral [81] could be used. These methods either assume the piezoelectric element as a point source or an integral of differential planes. Both of them require a large number of operations which could be time consuming. To reduce the computational time, in this work, a 2D Fast Fourier Transform is (FFT) used to predict the propagation of ultrasound waves in the far-field area [89]. For an array transducer with 30 mm aperture, working at 2 MHz, the far-field is approximately 292 mm away

from the transducer's front surface. The directivity function is achieved by applying the 2D FFT on the aperture function of the array [89].

3.3. Sparse Array Configurations

3.3.1. Random Array Element Approach

The positions of the elements in the random array are randomly picked within the aperture. Three parameters are used to define a random array layout: the radius of each element (ele_r); the minimum gap between two elements (ele_g); and the number of elements in the array (ele_num). To avoid overlapping between array elements, a minimum distance between two elements is set which equals to the pitch as expressed in Equation 3.3.

$$ele_pitch = 2 * ele_r + ele_g \quad (3.3)$$

Figure 3.4 illustrates the relations of key parameters in a simple graphical form. Since the aperture size is fixed in this work, there is an upper limit to ele_num . In the design process, the upper limit to the number of elements within a random array with fixed aperture size is defined as the maximum number of sub-squares that can be placed inside the maximum internal square of the aperture. The side length of the sub-squares equals to the pitch. This definition can be expressed as:

$$ele_num_max = \left\lfloor \frac{(2R)^2}{ele_pitch^2} \right\rfloor \quad (3.4)$$

where ele_num_max is the upper limit and R is the radius of the aperture within which the centres of the elements are placed. Since the points represent the centre of the circle elements, the accessible aperture radius (R) for the points could be expressed as:

$$R = R_{org} - ele_r, \text{ where } R_{org} = 15mm \quad (3.5)$$

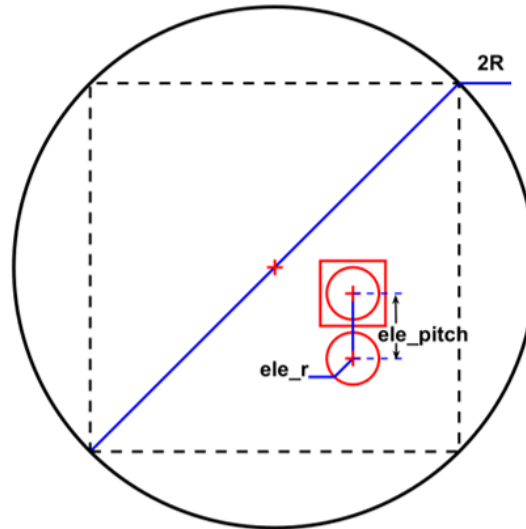


Figure 3.4 Illustration of the method used to determine the upper limit of elements within a random array. The red markers (+) represent the centre of each circle. The black circle represents the aperture with a radius of R . The black square is the maximum internal square of the black circle (aperture). The red square represents the sub-square with ele_pitch side length. The red circle is the element with the radius ele_r . The distance between the centre of the red circles equals to ele_pitch . Assuming the available aperture area is within the black rectangle, and the area of each element is the area of the red rectangle.

A random array can be simulated in the following 5 basic steps:

1. Set the minimum distance (***ele_pitch***) between array elements to avoid overlapping.

2. Randomly place the desired number of points (*ele_num*) on a rectangular aperture of $2R$ dimension.
3. Remove the points which are outside of the $2R$ diameter circular aperture.
4. Calculate the distance between each pair of points. If the distance is smaller than *ele_pitch*, remove the point which is generated later.
5. If the number of points remaining in the circular aperture (*ele_num_real*) is fewer than *ele_num*, place another $ele_r - ele_num_real$ points and repeat step 2 to step 4 until *ele_num_real* equals to *ele_num*.

Figure 3.5 uses an example random array generator to illustrate the process. The example random array shown in Figure 3.5(a) aims to place 100 circular elements with 0.8 mm radius and 0.5 mm minimum gap inside the 3 cm aperture. These are arbitrarily chosen parameters except for the aperture size. The generation process starts from randomly placing a specific number of points ($ele_num = 100$) within a rectangle whose edge length equals to $2R$. Then, any points outside a circular area which is defined by R radius, will be eliminated first. Next, for the points remaining inside the reduced aperture, calculate the distance from the target point to all the other points. After that, check if there are any distances which are smaller than the minimum pitch. If so, those points which are too close to the target point will be eliminated. As can be imagined, there could be pairs of points which are ‘too close’ to each other. In such situation, the point which is generated later will be eliminated. It is possible, albeit unlikely, that all the points generated in step 1 are within the desired area and no points are too close to each other. In most cases, after processing the first three steps, the

number of elements left inside the desired area will be smaller than the desired value. In the example shown in Figure 3.5(a), only 42 points are accepted by the end of step 3. Thus, the following step is to introduce another 58 points into this process. The new 58 points along with the previous 42 points will be repeat the process from step 1 again. All these 4 steps will be repeated until the number of points accepted by the end of step 3 is the same as the number of points specified at the beginning of the whole process. At this point, the fully populated (*ele_num*) array can be illustrated as shown in Figure 3.5(b).

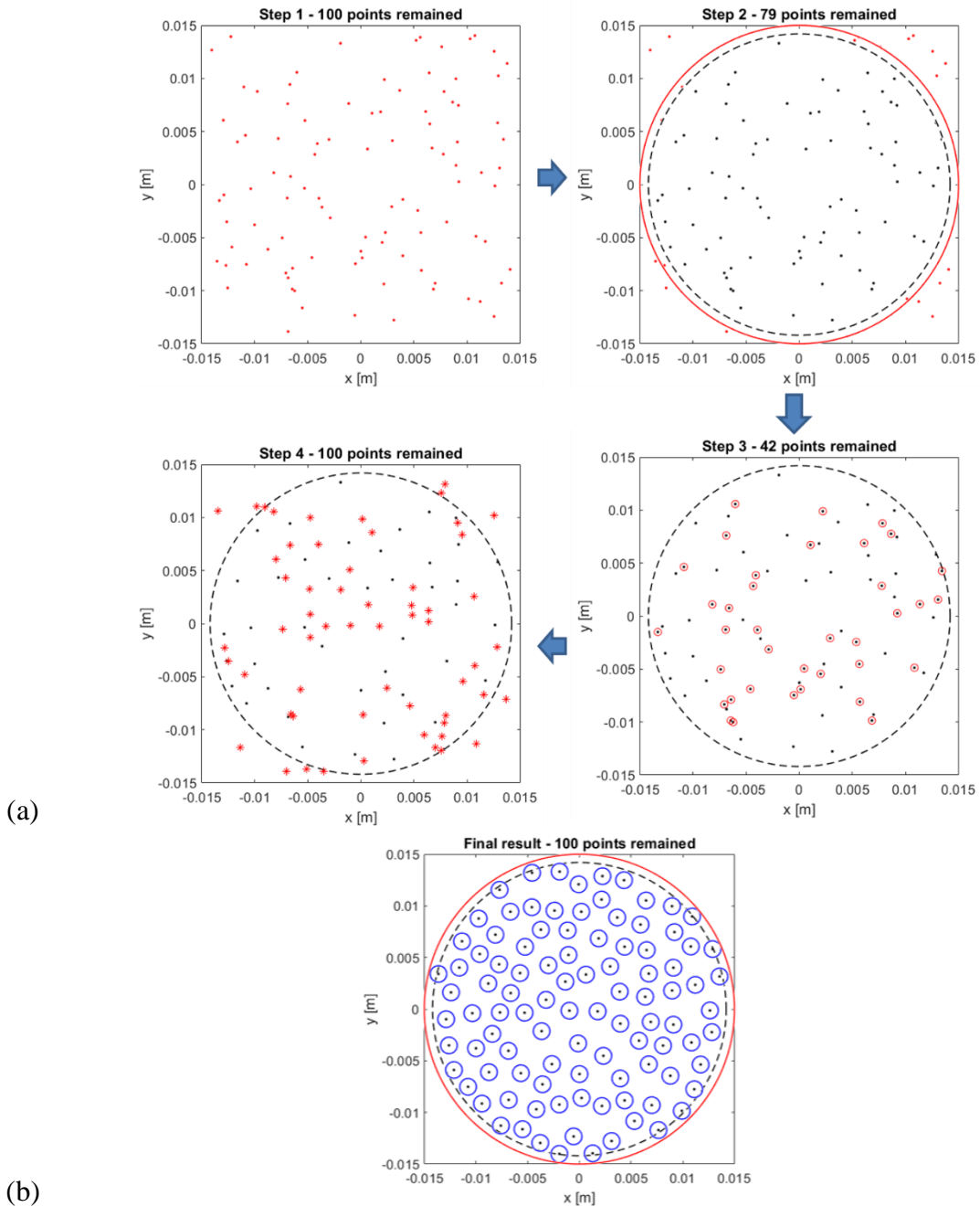


Figure 3.5 The process to generate a random array configuration. In (a), the black dots represent the remaining points at the end of each step. The red markers represent the removed or alternative points. The large red circle and the black circle represent the 3 cm aperture and the reduced aperture, respectively. Step 1-4 are repeated until all the remaining points in step 4 are inside the black circle. This final stage is represented in (b) and illustrates the random array configuration. The blue circles are the array elements.

3.3.2. Logarithmic Spiral Array

A logarithmic spiral array consists of one or several log spiral lines (arms), as illustrated in Figure 3.2(b), and can be expressed with the following polar equation:

$$r = a * e^{b(\gamma+\theta)} \quad (3.6)$$

where r is the radial distance, γ is the polar angle, a and b are constant parameters that effect the shape of the spiral. a determines the minimum distance from the origin to an arm, while b controls the curvature of each spiral arm. θ is the rotational angle between two adjacent spirals, which is determined by the number of arms num_of_arm as:

$$\theta = 2\pi/num_of_arm \quad (3.7)$$

To make sure no arms overlap with each other, the parameters a and b need to be adjusted. The first thing is to make the minimum distance between the first elements of two adjacent arms larger than the diameter of the element, as shown in Figure 3.6. This condition can be expressed as:

$$2a * \sin\left(\frac{\theta}{2}\right) > 2ele_r \quad (3.8)$$

where θ is the rotational angle between two adjacent arms and ele_r is the radius of the element. This can also be written as:

$$a = ele_r / \sin\left(\frac{\theta}{2}\right) + K \quad (3.9)$$

where K is a constant.

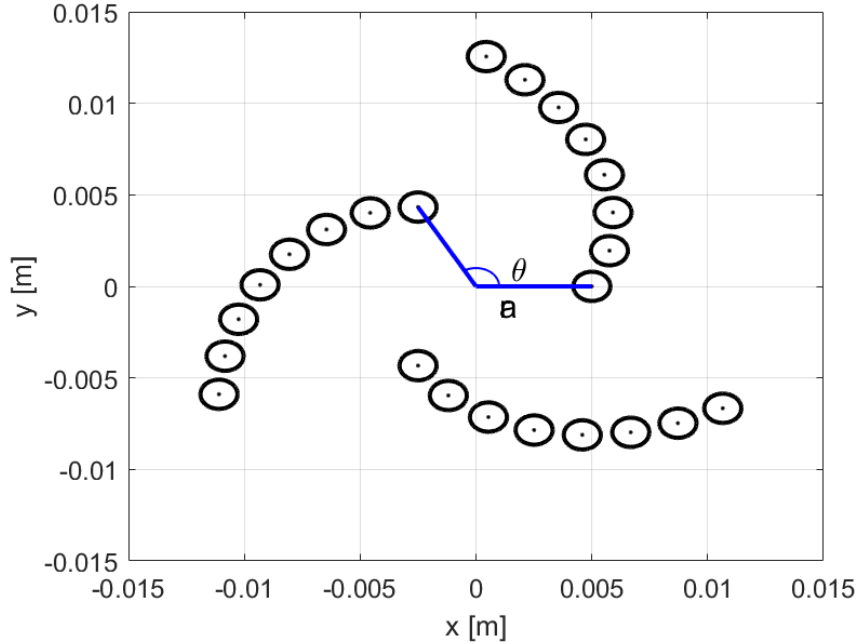


Figure 3.6 An illustration of the minimum distance between the first elements of adjacent spirals. a is a constant parameter representing the minimum distance from the origin to an arm and θ is the rotational angle between adjacent spiral arms.

Figure 3.7 presents an example of the change of PSL and $ISLR$ due to the variation in a . This Figure has been generated to illustrate the key relationship between PSL , $ISLR$ and a . As shown in the Figure, an increase in a will lead to increases in both PSL and $ISLR$. For an appropriate design, both PSL and $ISLR$ should be low, which means that correspondingly a should be as small as possible, which indicates that K should also be as small as possible. During the optimisation process the parameter a was initially set as:

$$a = \frac{ele_r}{\sin(\theta/2)} + ele_g/2 \quad (3.10)$$

where ele_g is the gap between adjacent elements along the same arm. Based on Equation 3.9, the real gap between first elements of adjacent arms is $ele_g * \sin(\theta/2)$.

The parameter b will be adjusted manually to an appropriate value after all the other parameters are decided.

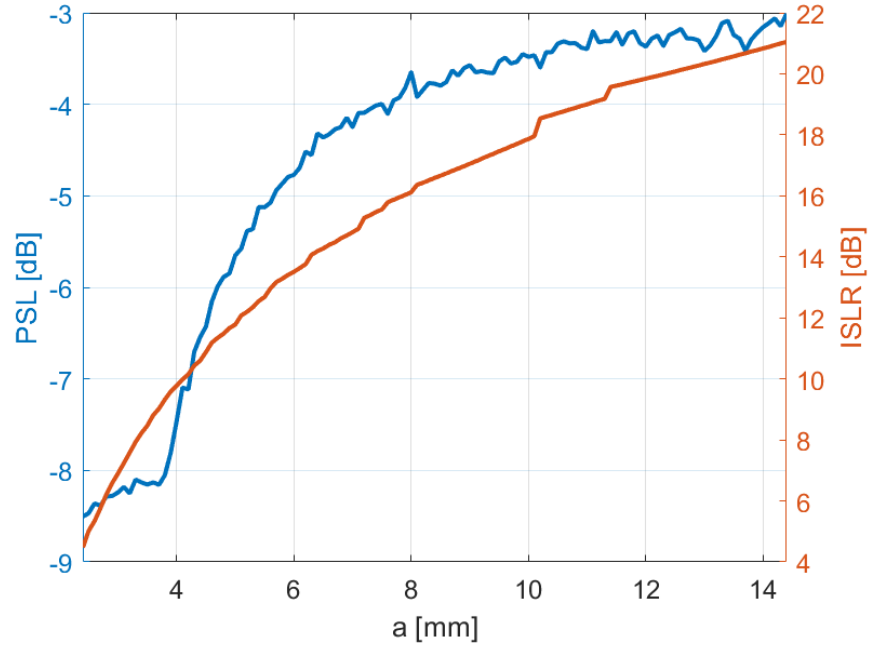


Figure 3.7 Influence of parameter a on PSL and ISLR. The blue line represents the change of PSL, while the red line represents the change of ISLR.

In a logarithmic spiral configuration, all the arms have the same shape and the same number of elements. Within each arm, the elements are placed along the arm with equal space. The length of the space is set as the ele_pitch of the log spiral array. The length of an arc can be expressed with the polar equation:

$$l_{arc} = \int_{\gamma_1}^{\gamma_2} \sqrt{r^2 + \left(\frac{dr}{d\gamma}\right)^2} d\gamma \quad (3.11)$$

where l_{arc} is the length of the arc and r is the polar expression of the arc. γ_1 and γ_2 are polar angles for the beginning point and the ending point separately. Thus, the length for a log spiral can be expressed as:

$$l_{arc} = \int_{\gamma_1}^{\gamma_2} a e^{b\gamma} \sqrt{1 + b^2} d\gamma \quad (3.12)$$

where all the symbols are the same as defined previously. During the design process, the polar angle γ is set to start from 0. Thus, Equation 3.12 can be further simplified to:

$$l_{arc} = \frac{a}{b} \sqrt{1 + b^2} (e^{b\gamma} - 1) \quad (3.13)$$

Since the elements are equally spaced, the length of an arm with n elements can also be expressed as:

$$l_{arc} = (n - 1) * ele_pitch \quad (3.14)$$

where ele_pitch is the same as defined in Equation 3.3. Combining Equation 3.13 and Equation 3.14 gives the polar angle, γ_n , of the n th element in an arm as:

$$\gamma_n = \frac{1}{b} \ln\left(\frac{(n - 1)pb}{a\sqrt{1 + b^2}} + 1\right) \quad (3.15)$$

To make sure the entire spiral lines are within the aperture area, the maximum radial distance r_{max} should be smaller than the aperture radius. In this project, as the spiral arms are discretely sampled to form the elements in the array, so that r_{max} is defined as the distance from the origin of coordinates to the last element in each arm as shown in Figure 3.8. As the same reason described in Section 3.3.1, the upper limit of r_{max} is set

to equal the reduced aperture size R . Since r_{max} can also be expressed by Equation 3.6, the maximum polar angle, γ_{max} , will be:

$$\gamma_{max} = \frac{1}{b} \ln \frac{R}{a} \quad (3.16)$$

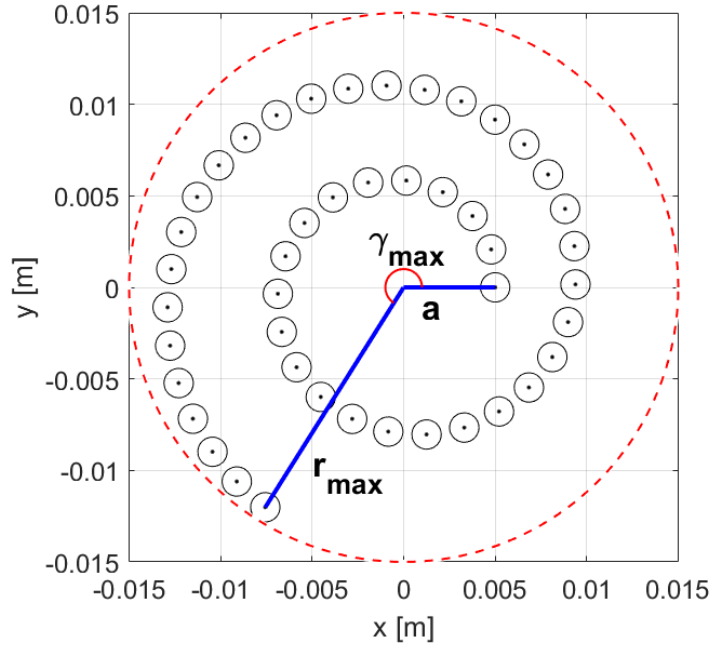


Figure 3.8 The maximum radial distance and maximum polar angle of a log spiral arm configuration within a fixed aperture size.

Once the parameters are fixed, the layout of log spiral array is set. The design process can be express as:

1. Set the minimum pitch between array elements along the same spiral arm.
2. Set parameters including: the number of spiral arms within the array

num_of_arm; the number of elements within each arm ***ele_per_arm***; and the constant parameter ***b***.

3. Generate the log spiral array based on the parameters selected in step 2.
4. Remove the points which fall outside of the 30 mm circular aperture. Modify ***b*** if the elements in the inner circle are overlapped.
5. Place an additional element in the centre of the log spiral array to help the orientation of the ultrasound beam while having minimal influence on the *PSL* and *ISLR* [70].

3.3.3. Special Fermat Spiral Array – Sunflower Spiral Array

The Fermat spiral is an example of an Archimedean spiral which can be expressed as:

$$r^2 = a_{frmt}^2 \gamma \quad (3.17)$$

where r is the radial distance, γ is the polar angle, and a_{frmt} is a constant parameter.

Equation 3.17 can also be written as:

$$r = \pm a_{frmt} \sqrt{\gamma} \quad (3.18)$$

In other words, for a Fermat spiral with fixed a_{frmt} , there are two symmetric spirals, one positive branch and one negative branch, as shown in Figure 3.9.

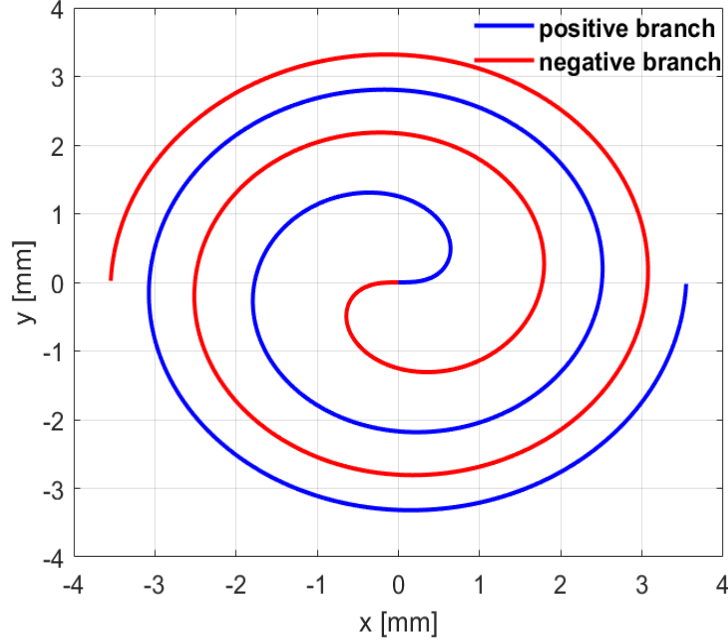


Figure 3.9 Fermat spiral with symmetric branches. The blue line is the positive branch, while the red line is the negative branch.

To form a Fermat spiral array, the spiral line(s) needs to be translated into discrete points which represent the centre points of the elements in the array. There is a special case when the points are placed along one Fermat spiral line with a fixed and specific differential polar angle, the golden angle [67]. The polar angle of the n^{th} point in the spiral, γ_n , is:

$$\gamma_n = n\beta, \quad \beta = 137.508^\circ \quad (2.4 \text{ rad}) \quad (3.19)$$

where β is the golden angle. Taking Equation 3.19 into the positive branch of Equation 3.18 gives:

$$r_n = a_{frmt} \sqrt{\gamma_n} = a_{frmt} \sqrt{n\beta} \quad (3.20)$$

where r_n is the distance from the original point to the n^{th} point and can also be written as:

$$x_n = r_n * \cos(n\beta), y_n = r_n * \sin(n\beta) \quad (3.21)$$

where x_n and y_n are the rectangular coordinates of point n . This kind of Fermat spiral is called the ‘sunflower spiral’ because of its special shape and is illustrated in Figure 3.2(c).

The process to generate the sunflower spiral array can be divided into following steps:

1. Set the minimum distance (***ele_pitch***) between array elements to avoid overlapping.
2. Generate a sunflower array with desired number of elements (***ele_num***).
3. Find the minimum distance between these elements (***ele_pitch_{real}***).
4. If ***ele_pitch_{real}*** is not smaller than ***ele_pitch***, the generation process could be stopped. Otherwise, expand the whole array to make them equal.
5. After expansion, remove any points that falls outside of the 30 mm diameter circular aperture.

The process to generate a sunflower spiral array starts from generating a set of points which distribute along the sunflower spiral. These points are called initial points. All the initial points should be placed within the area bounded by the reduced fixed aperture R (Equation 3.5) as these points represent the position of elements in the array. This limitation can be expressed as:

$$r_{last} = a_{fmrt} \sqrt{\gamma_{last}} = a_{fmrt} \sqrt{n_{last} * \beta} \leq R \quad (3.22)$$

where r_{last} and γ_{last} are the radial distance and the polar angle of the last initial point, n_{last} , separately. According to Equation 3.22, a_{fmrt} and n_{last} are dependent on each other. Thus, there are two methods to generate the initial points. One sets a_{fmrt} first, the other sets n_{last} first. In this Chapter, the former method is defined as ‘Method A’, while the later method is defined as ‘Method B’. Figure 3.10 show examples to generate a sunflower spiral array using Method A and Method B. The radius of array element is 0.8 mm and the minimum gap between two elements is 0.5 mm. Thus, ele_pitch is 2.1 mm. For Method A, a_{fmrt} is set to 0.5, while for Method B, n_{last} is set to 300. These parameters are randomly selected. According to Equation 3.22, Method A generated 336 initial points at step 1, while Method B generated 300 initial points.

The next step is calculating and recording the distance between each pair of the initial points. The distance between the closest pair of the initial points is recorded as the overall minimum distance (min_dis). As shown in Figure 3.10, the pair of the initial points which gives the min_dis are highlighted using red circles. Differing from the random array design, for the sunflower spiral array min_dis can be predicted using parameter a_{frmt} . Arbitrarily picking two points, m and n , from the initial points, the distance between these two points, d , can be calculated by:

$$d^2 = (x_n - x_m)^2 + (y_n - y_m)^2, \quad \text{where } n < m \quad (3.23)$$

Combining with Equation 3.20 and Equation 3.21, Equation 3.23 can be rewritten as:

$$d^2 = a_{fmrt}^2 \beta \{n + m - 2\sqrt{mn} \cos[(n - m)\beta]\} \quad (3.24)$$

As a_{fmrt} and β are constants, d can be treated as a variable with respect to n and m . Figure 3.11 shows changing of d with different combinations of n and m . As shown in the Figure, this function reaches its minimum when $n = 1$ and $m = 4$. Thus, the overall minimum distance, min_dis , can be expressed by Equation 24 as:

$$min_dis^2 = a_{fmrt}^2 * 2.4 * [1 + 4 - 2 * \sqrt{4 * 1} * \cos(3 * 2.4)] \approx 6.16a_{fmrt}^2$$

Or
$$min_dis \approx 2.48a_{fmrt} \quad (3.25)$$

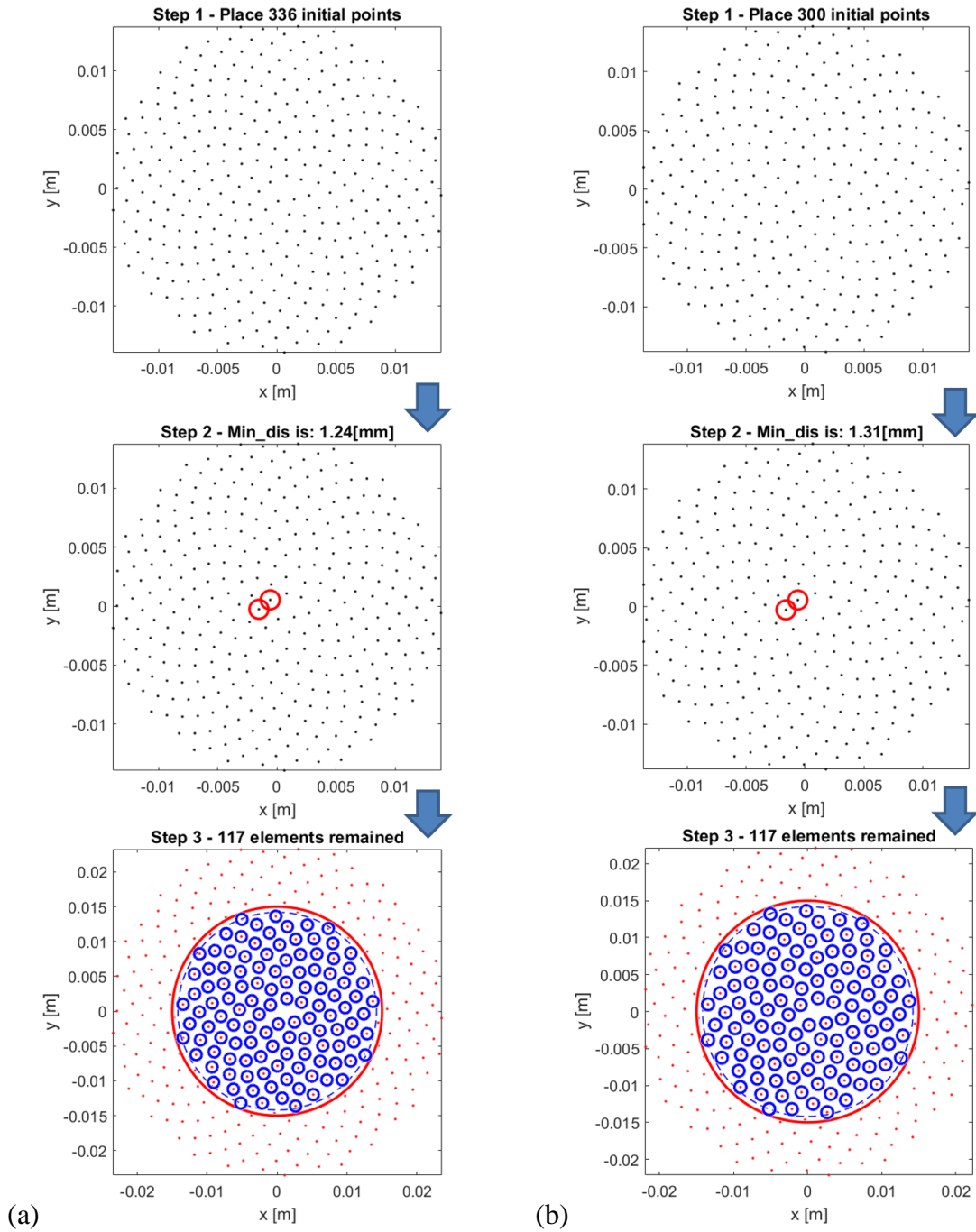


Figure 3.10 The process to generate a sunflower spiral array using (a). Method A and (b). Method B. The black dots represent the initial points. The red dots represent the new points after expanding the array which is formed by the initial points. The small red circles represent the pair of elements which gives min_dis . The small blue circles are the array elements. The dashed circle and the red circle are the reduced aperture size and the original aperture size separately.

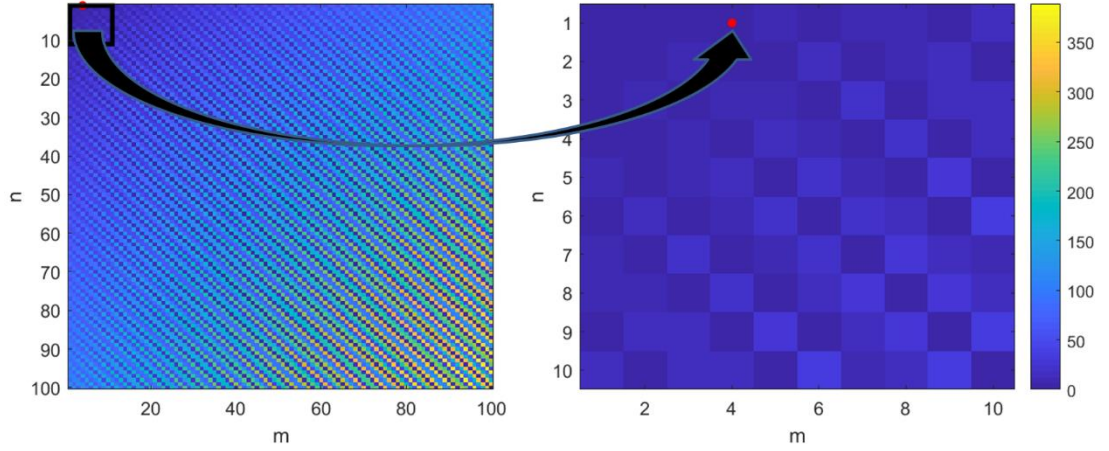


Figure 3.11 Change of d over n and m . The value of dis is represented by colour. The right figure is the zoomed in result of the area within the black rectangle in the left figure. Under condition $n < m$, dis reaches its minimum when $m = 4$ and $n = 1$. The minimum point is marked by the red point.

As shown in Figure 3.10, min_dis is 1.24 mm for Method A and 1.31 mm for Method B. Both of them are smaller than ele_pitch (2.1 mm). Thus, the 3rd step is expanding the whole array to make min_dis equal to ele_pitch . The scaling factor (sf) is:

$$sf = \frac{ele_pitch}{min_dis} = \frac{ele_pitch}{2.48a_fmrt} \quad (3.26)$$

The new points are represented by red dots in Figure 3.10. Only the red points within the aperture are selected to form the final array. This condition can be expressed as:

$$r_{last} * sf \leq R \quad (3.27)$$

This equation indicates that, for a sunflower spiral array with fixed ele_r and ele_g , there is an upper limit to the number of elements that can be placed within the aperture.

Combining Equations 3.22 and 3.26 gives:

$$r_{last} * sf = \sqrt{n_{last}\alpha} * \frac{ele_pitch}{2.48} \quad (3.28)$$

This can be combined with Equation 3.27, giving the upper limit of element number:

$$n_{max} = \left\lfloor \frac{2.48R^2}{\alpha * ele_pitch^2} \right\rfloor \quad (3.29)$$

This result indicates that the maximum number of elements that can be placed within the aperture area is independent on a_fmrt and n_{last} . In other words, as long as ele_r and ele_g stay unchanged, no matter which method ('Method A' or 'Method B') is used to generate the initial points, n_{max} is always the same. As shown in Figure 3.10, n_{max} is 117 for both Method A and Method B.

3.4. Optimisation Process

The optimisation process aims to find the array configuration which has an appropriate combination of *PSL* and *ISLR*. The parameters which are used to generate the array configurations are listed in Table 3.1. For each parameter, a set of alternative values are created. For comparison, the parameters common to all array configurations were set to have the same candidate values for all the array configurations. As indicated by Table 3.1, the generation of the log spiral array requires the largest number of parameters. The design of log spiral array utilised three rules introduced by [70]. The first one is that elements along the same arm are isolated by the same distance. The second one is that arrays with odd number of arms perform better in term of *PSL*. The last one is that introducing of an extra element in the centre of the array can help the orientation of the ultrasound beam while not influencing the array performance significantly.

The parameter ele_r , which is the array element radius, needs to be modified by all these three array configurations. For a 1-3 composite transducer, there should be at least 9 (3x3) elements under each electrode [114]. However, PZT fibres used in this project can only reach 75% of the properties for bulk PZT materials [35]. Thus, with 50% volume fraction and 250 μ m diameter PZT fibres, the minimum element-radius is set to be 0.7 mm. Moreover, ele_r will have effect on the element performance in terms of lateral resolution and maximum steering angle. As mentioned in Section 2.4.2, larger ele_r can achieve better lateral resolution at deeper distance into the loading material. Meanwhile, increase in ele_r will lead to decrease in the maximum steering angle. The parameter ele_g is the minimum gap between two elements. But for different array configurations, the definition of ele_g is slightly different. For random array and sunflower spiral array, ele_g is the minimum distance between two elements within the same array. For log spiral array, ele_g is the gap between two adjacent elements along the same arm. As the transducer is planned to be manufactured as a CECAT, to avoid fibres from neighbouring elements to cross to each other, the lower limit of ele_g is set to 0.2 mm for random array and sunflower array, and 0.4 mm for log spiral array. These numbers were determined based on a CECAT manufacturing trial. The minimum distance between elements in the log spiral array is affected by several variables. Thus, the minimum ele_g for the log spiral is set larger to try to avoid fibres crossing. ele_r and ele_g affect the maximum number of elements that can be placed within the fixed aperture. Also, large ele_g will influence the sensitivity of the transducer. Thus, ele_r

and ele_g cannot be set to be very large. The upper limits for ele_r and ele_g are chosen to be 1.5 mm and 1 mm for practical transducer fabrication reasons.

Table 3.1 Parameters and candidate values for each array configuration

PARAMETERS	INTERVAL	ARRAY TYPE
Element radius (ele_r)	0.7:0.05:1.5 [mm]	All three array configurations
Minimum gap between two elements within the array (ele_g)	0.2:0.05:1 [mm]	Random Array and Sunflower Spiral Array
	0.4:0.05:1 [mm]	Log Spiral Array
Number of elements within each log spiral arm (ele_per_arm)	3:1:10	Log Spiral Array
Number of log spiral arms (num_of_arm)	7:2:19	Log Spiral Array
Constant parameter b	1.2:0.1:1.5	Log Spiral Array

One thing to be noticed for the random array configuration is that the positions for elements cannot be guaranteed to be fixed for configurations which are generated by the same parameters, as the elements of a random array are randomly placed within the aperture. Figure 3.12 shows an example of this situation. 20 random array configurations are generated using the parameters of the representative configuration for random array. As shown in the Figure, there are fluctuations for both PSL and $ISLR$. To reduce the effect from this unstable performance, during the optimization process, 50 simulations have been produced for each set of input parameters.

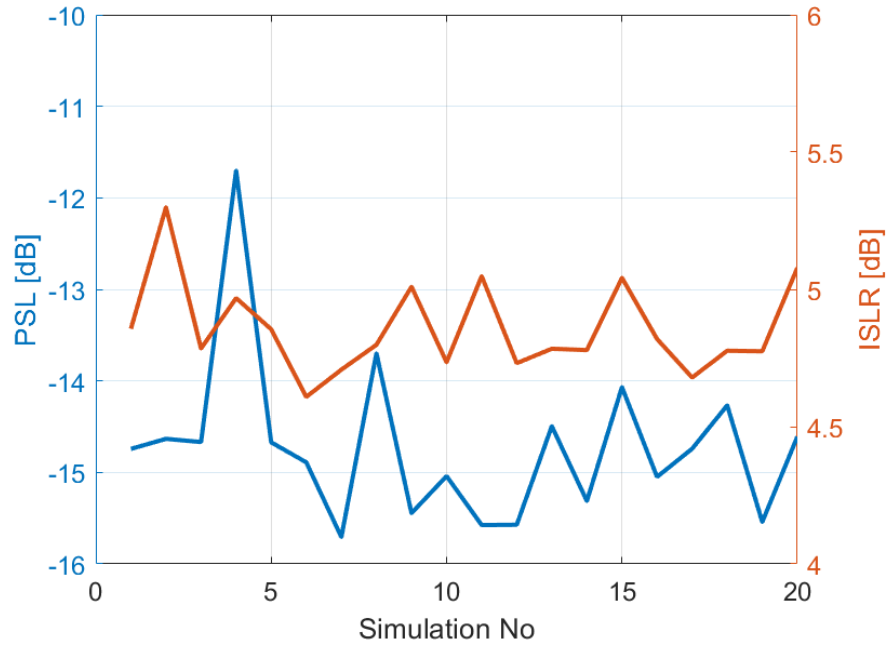


Figure 3.12 Change of performance for 20 random array configurations which are generated using the same parameters.

For the random array and the sunflower spiral array, the maximum number of elements varies with the settings of both ele_r and ele_g . Therefore, for these two configurations there is no requirement to introduce new parameters based on the number of elements. Simulations have been processed to find the relationship between element number and PSL , as well as $ISLR$. Figure 3.13 presents the performance of a random array configuration with respect to the number of elements. 50 samples have been simulated for each element number and the minimum values for PSL and $ISLR$ are presented in Figure 3.13. As shown in the Figure, both PSL and $ISLR$ tend to decrease with the increase in element numbers, although there is a local fluctuation between neighbouring

points. Thus, for the random array, the number of elements is set to equal to the upper limit as defined in Equation 3.3.

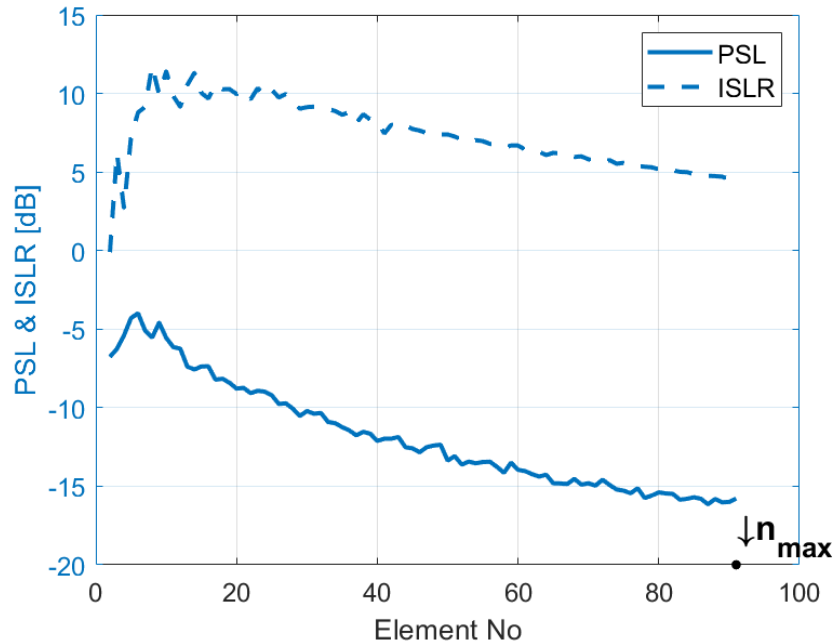


Figure 3.13 Performance of a random array configuration with respect to the number of elements within the array.

As mentioned in Section 3.3.3, there are two methods to form a sunflower array. Thus, influence of element number on the array’s performance needs to be explored for both methods. Figure 3.14 shows the *PSL*, *ISLR* and number of array elements results for a spiral array designed using Method A. As shown in the Figure, there is a critical point where increasing of a_{fmrt} will lead to the total number of elements becoming smaller than n_{max} . With an increase in parameter a_{fmrt} , the total number of elements decreases, while both *PSL* and *ISLR* increase. Thus, when using Method A, with the

fixed ele_r and ele_g , the configuration with n_{max} elements has the optimised performance.

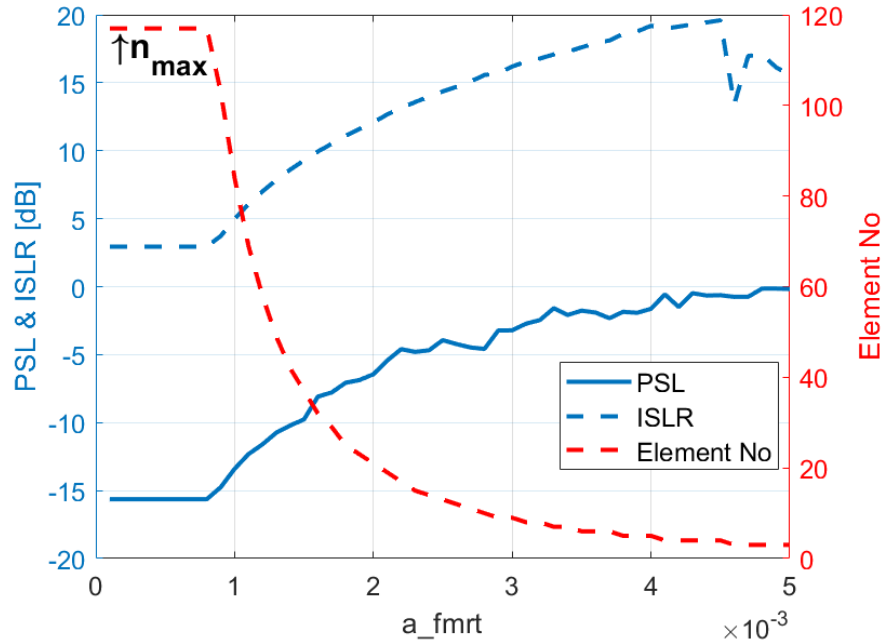


Figure 3.14 PSL and ISLR performance of sunflower array configuration with respect to number of elements within the array. The sunflower array is formed by setting 'a_fmrt' first (Method A).

Figure 3.15 illustrates the performance variation for the sunflower array configurations which are formed using Method B. A similar relationship between PSL , $ISLR$ and the number of elements is observed in both Figures 3.14 and 3.15, in which the increase in the number of array element produces a reduction in both PSL and $ISLR$. In other words, for sunflower arrays with the same ele_r and ele_g , no matter whether they are formed using Method A or Method B, the configuration with n_{max} elements has the best

performance. Thus, during the optimisation process, the number of elements within a sunflower array is set to equal n_{max} .

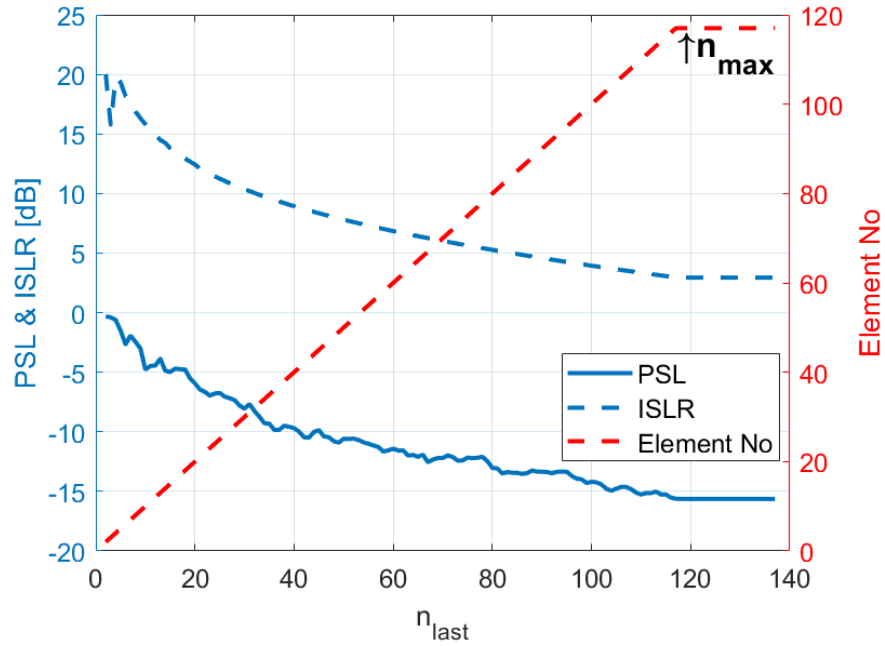


Figure 3.15 PSL and ISLR performance of sunflower array configuration with respect to number of elements within the array. The sunflower array is formed by setting ' n_{last} ' first (Method B).

In conclusion, for random array and sunflower array, the number of elements within an array is set to equal the upper limit of element number. Only ele_r and ele_g are variable in the optimisation process.

For the log spiral array, three other parameters, ele_per_arm , num_of_arm , and b , are required to form an array. ele_per_arm stands for the number of elements within an arm. The minimum number of ele_per_arm is set to 3 to form a curve. The number of arms (num_of_arm) is set based on a set of data which are acquired by simulating all

the possible combinations of parameter as listed in Table 3.2. The parameters listed in Table 3.2 are arbitrarily chosen. The resulted *PSL* and *ISLR* are displayed in Figure 3.16 with respect to *num_of_arm* . As shown in the Figure, configurations with *num_of_arm* between 7 and 19 produce a better combination of *PSL* and *ISLR* due to the larger number of arms in the device. The parameter *b* is set to vary between 1.2 and 1.5. This is selected manually to make sure overlapping between arms will not happen for any of the log array configurations. Recalling Equations 3.10, 3.15, and 3.16, the maximum number of elements within each log spiral arm ($n_{last_within_arm}$) can be expressed as:

$$n_{last_within_arm} \leq \left\lceil \frac{\left(R_{reduced} - \frac{ele_r}{\sin\left(\frac{\pi}{num_of_arm}\right)} - \frac{ele_g}{2} \right) \sqrt{1+b^2}}{pitch * b} + 1 \right\rceil \quad (3.30)$$

Equation 3.30 reaches its maximum value when *ele_r*, *ele_g*, *num_of_arm* reaches their lower limits and *b* reaches its upper limit. Thus, the maximum value for *ele_per_arm* is limited to 10.

Table 3.2 Parameters and candidate values used to determine interval of num_of_arm

PARAMETERS	INTERVAL
Element radius (ele_r)	0.3: 0.05:1.5 [mm]
Minimum gap between two elements within the array (ele_g)	0.4:0.05:1 [mm]
Number of elements within each log spiral arm (ele_per_arm)	1:1:20
Number of log spiral arms (num_of_arm)	1:2:19
Constant parameter b	1.2:0.1:1.5

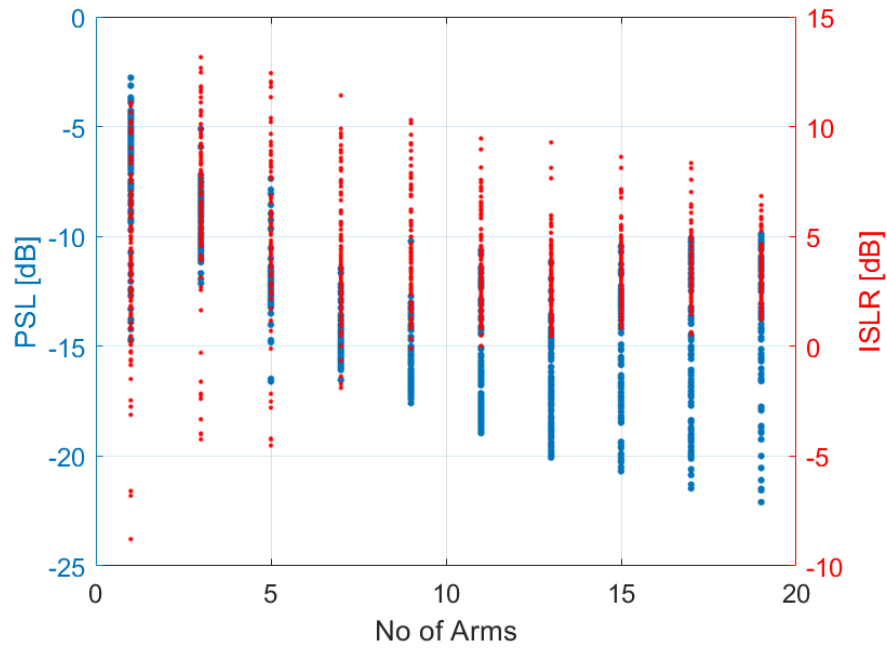


Figure 3.16 PSL and ISLR with change of the number of arms within a log spiral array. The blue dots stand for the PSL values, while the red dots stand for the ISLR values.

The optimisation process is divided into two steps:

1. Simulate all the possible combinations of parameters as listed in Table 3.1 and record the corresponding PSL and $ISLR$.

2. For each array configuration, record the lowest *PSL* and corresponding *ISLR*.

Based on these two values, set intervals for *PSL* and *ISLR* by rounding up and down to the nearest integers. Find the combinations whose *PSL* and *ISLR* are both inside the intervals. These combinations are selected as the candidates. Except for *PSL* and *ISLR*, other limits have also been considered to select the final design based on practical limitations, such as the manufacturing capability and the maximum number of channels in the phased array controller.

3.5. Optimisation Process – Phase I

3.5.1. Step 1 – Simulate All Three Configurations

The number of simulations produced for each array pattern is 14450 for the random array, 49504 for the log spiral array, and 289 for the sunflower array. Figures 3.17-3.19 show the performance for the three configurations in term of *PSL* values. The *x-axis* represents each configuration which are formed using a combination of the parameters listed in Table 3.1. For each kind of array, the configuration which gives the minimum *PSL* is marked by a red dot. The parameters which are used to form that configuration are listed in corresponding Figure's title. As illustrated in the Figures, the minimum *PSL* is -17.85 dB for the random array; -21.33 dB for the log spiral array; and -17.43 dB for the sunflower array. Thus, in terms of *PSL*, the log spiral array performs better than the other two array configurations.

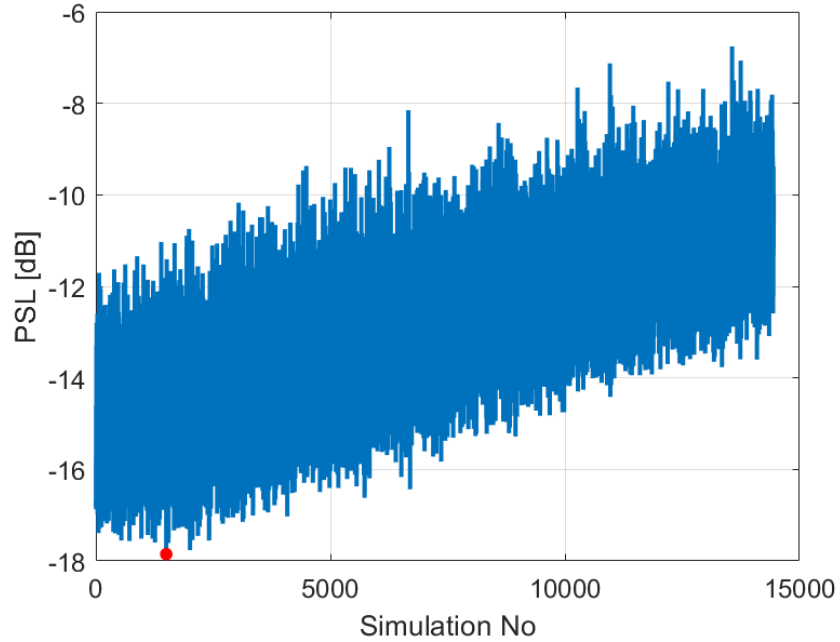


Figure 3.17 Optimisation results of the random array. The red dot represents the configuration that has the lowest PSL (-17.85 dB) with a corresponding ISLR of 2.92 dB. The configuration is formed using 0.9 mm ele_r , 0.25 mm ele_{gr} , and 94 ele_{num} .

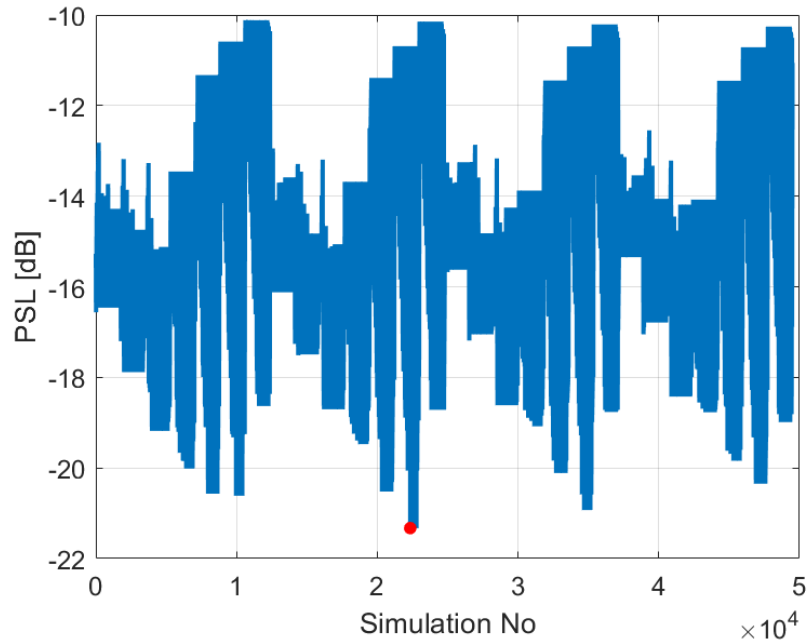


Figure 3.18 Optimisation results of the log spiral array. The red dot represents the configuration that has the lowest PSL (-21.33 dB) with a corresponding ISLR of 3.07 dB. The configuration is formed using 0.7 mm ele_r , 0.45 mm ele_{gr} , 8 ele_{per_arm} , 17 arms, and 1.3 b.

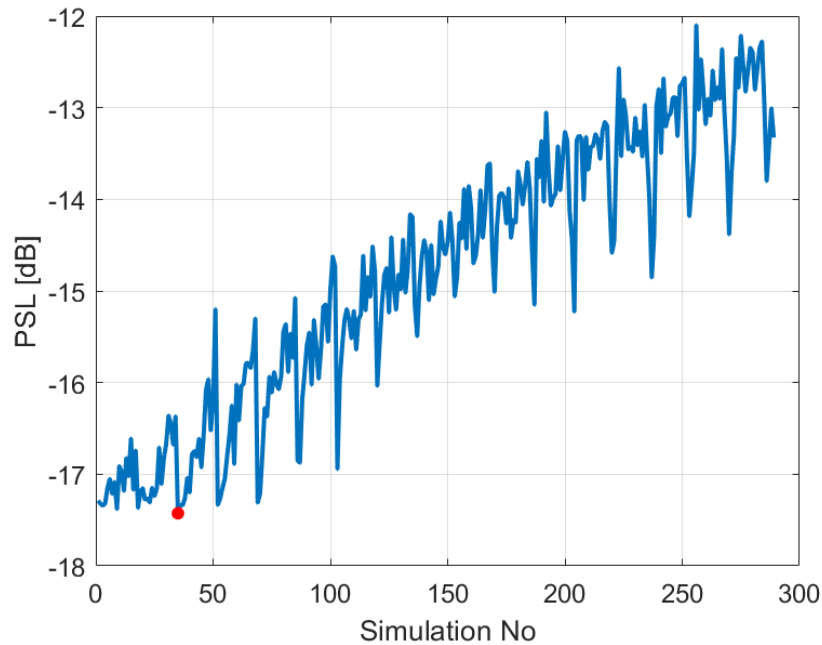


Figure 3.19. Optimisation results of the sunflower array. The red dot represents the configuration that has the lowest PSL (-17.43 dB) with a corresponding $ISLR$ of 1.8 dB. The configuration is formed using 0.7 mm ele_r , 0.3 mm ele_gr , and 181 ele_num .

However, further analysis indicates that the configuration with the lowest PSL has relatively higher $ISLR$ compared with other configurations with similar PSL . Figure 3.20 compares $ISLR$ values for simulated log spiral array configurations which has PSL lower than -19.5 dB. It can be observed that the $ISLR$ for the configuration with the lowest PSL is relatively higher compared to some of the other configurations which have similar PSL . So, for all the three configurations, further analysis has been taken to find the appropriate designs which have both low PSL and low $ISLR$. The acceptable intervals for PSL and $ISLR$ are set based on the selected minimum points in Figures 3.16-18. The upper limit for PSL 's interval is firstly set to equal the smallest integer which is larger than the minimum PSL . The lower limit for PSL is set to equal the largest integer which is smaller than the minimum PSL . The interval for $ISLR$ is decided

using the same approach. The lower limit for *ISLR* is set to 0 dB. The upper limit for *ISLR* is set to be the smallest integer which is larger than the *ISLR* of the minimum point. If no configuration can meet all these limits, then the upper limits of *PSL* will be increased by 1 dB. If there are configurations which meet the limit of *PSL*, but have much lower *ISLR* than the upper limit, then the upper limit of *ISLR* will be reduced by 1 dB. If two designs have similar *PSL* and *ISLR*, the one with higher possibility to be successfully manufactured will be chosen. The detailed selection processes for each array configuration are now described.

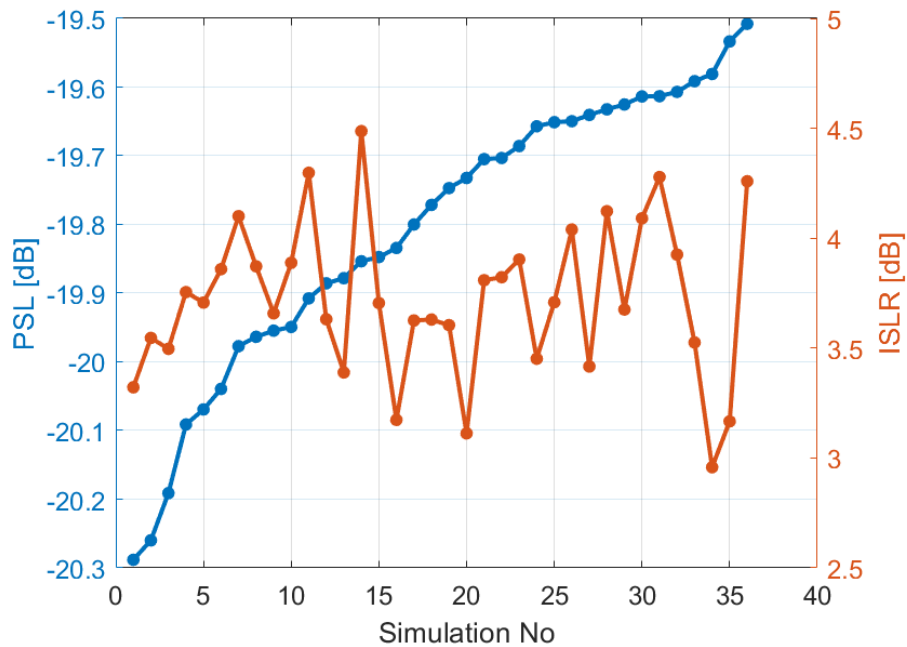


Figure 3.20 Comparison of *ISLR* for log spiral array configurations with *PSL* lower than -19.5 dB.

3.5.2. Step 2 – Analysis of Random Array Configuration

The chosen minimum *PSL* point for random array has -17.85 dB *PSL* and 2.92 dB *ISLR*. Based on this set of data, the interval is set to [-18 dB, -17 dB] for *PSL*, and [0 dB, 3 dB]

for *ISLR*, resulting in 68 and 803 simulations respectively. These results are presented in Figure 3.21. There are 30 configurations, represented by the black dots in Figure 3.21, which meet both conditions. However, some of these configurations have the same set of input parameters, i.e. *ele_r* and *ele_g*. In those situations, only the configuration which has the lowest PSL is kept. Eventually, 11 configurations are selected as the candidates. The parameters for these designs are listed in Table 3.3. The results indicate that the variation of PSL is in a wider range than that of the ISLR. Thus, PSL is selected as the primary criteria. Taking manufacturing difficulty into consideration, design #1 (highlighted row in Table 3.3) is selected as the representative configuration of a random array design.

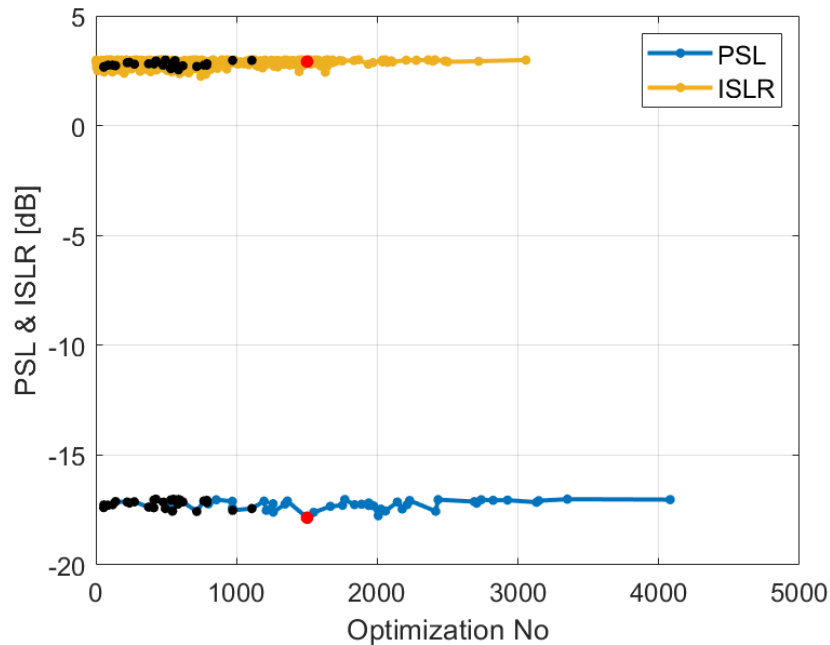


Figure 3.21 Random array configurations with PSL lower than -17 dB (blue line), or ISLR lower than 3 dB (yellow line) are shown in the plot. The black dots represent the configurations that meet both conditions. The red dots indicate the results of the minimum point as illustrated in Figure 3.16.

Table 3.3 Candidates for Random Array

	<i>PSL</i> [dB]	<i>ISLR</i> [dB]	Element		
			Radius <i>ele_r</i>	Gap <i>ele_g</i>	Number
1	-17.85	2.92	0.90	0.25	94
2	-17.57	2.69	0.80	0.20	124
3	-17.55	2.73	0.70	0.20	159
4	-17.51	2.97	0.80	0.25	117
5	-17.43	2.97	0.85	0.25	105
6	-17.40	2.83	0.85	0.20	110
7	-17.39	2.68	0.90	0.20	99
8	-17.27	2.66	0.95	0.20	89
9	-17.14	2.75	0.75	0.20	140
10	-17.06	2.82	1.00	0.20	80
11	-17.02	2.54	1.10	0.20	67

3.5.3. Step 2 – Analysis of Log Spiral Array

For the chosen minimum point in Figure 3.17, the *PSL* is -21.33 dB and the *ISLR* is 3.07 dB. Thus, the intervals for *PSL* and *ISLR* were initially set to be [-22 dB, -21 dB] and [0 dB, 4 dB], respectively. However, there is only one configuration that can meet both two conditions using these intervals and to get more candidates, the interval for *PSL* was extended to [-22 dB, -20 dB]. Again, the configurations which meet both conditions are represented by the black dots in Figure 3.22. As shown in the Figure, the interval for *ISLR* is not appropriate as there are many configurations which have similar *PSL* but much smaller *ISLR*. Thus, the interval for *ISLR* is reduced to [0 dB, 3 dB]. At this point,

there are 56 configurations which meet both two conditions. Although these configurations have different combination of parameters, some of them are the same in practice because of the fixed aperture size. This reduces the number of options to only 18 different designs. These configurations are selected as the candidates. The difference in *PSL* and *ISLR* between these configurations is very small, with a standard deviation of 0.21 for *PSL* and 0.18 for *ISLR*.

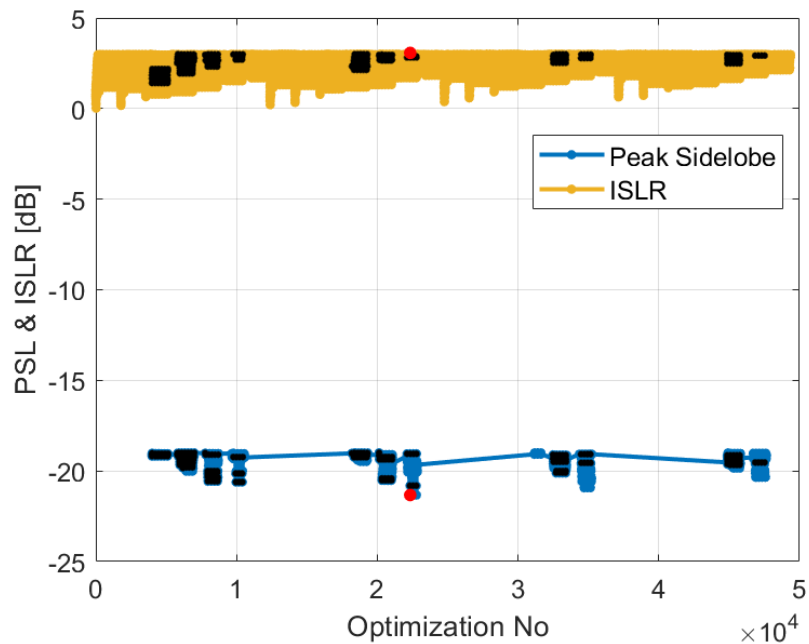


Figure 3.22 Log spiral array configurations with *PSL* lower than -20 dB (blue line), or *ISLR* lower than 4 dB (yellow line) are shown in the plot. The black dots represent the configurations that meet both conditions. The red dots indicate the results of the minimum point as illustrated in Figure 3.17.

Table 3.4 presents the key parameters of the final 18 alternative designs, including element radius, element gap, and the number of elements in each array. Importantly, the candidates are sorted based on their *PSL* values. Taking into consideration that larger

ele_r and ele_g can reduce manufacturing difficulties for CECAT, the #5 design listed in Table 3.4 (highlighted row) is chosen as the representative design of the log spiral array.

Table 3.4 Alternative Designs for Log Spiral Array

	PSL [dB]	$ISLR$ [dB]	Element			No. of Arms num_of_arm	b	Element No.
			Radius ele_r	Gap ele_g	Per Arm ele_per_arm			
1	-20.81	2.88	0.70	0.40	8	17	1.3	137
2	-20.61	2.89	0.70	0.45	8	17	1.2	137
3	-20.57	2.96	0.75	0.45	7	15	1.2	106
4	-20.53	2.99	0.70	0.45	7	15	1.2	106
5	-20.53	2.82	0.80	0.50	7	15	1.2	106
6	-20.52	2.66	0.80	0.40	7	15	1.3	106
7	-20.49	2.83	0.80	0.45	7	15	1.3	106
8	-20.47	2.98	0.70	0.40	7	15	1.3	106
9	-20.43	2.79	0.75	0.40	8	15	1.2	121
10	-20.41	2.95	0.75	0.40	7	15	1.3	106
11	-20.37	2.99	0.80	0.55	7	15	1.2	106
12	-20.35	2.65	0.80	0.45	7	15	1.2	106
13	-20.34	2.81	0.70	0.40	7	15	1.2	106
14	-20.21	2.80	0.75	0.40	7	15	1.2	106
15	-20.14	2.70	0.70	0.40	8	17	1.2	137
16	-20.11	2.32	0.85	0.40	7	15	1.2	106
17	-20.09	2.81	0.80	0.40	7	15	1.4	106
18	-20.00	2.48	0.80	0.40	7	15	1.2	106

3.5.4. Step 2 – Analysis of Sunflower Spiral Array

For sunflower spiral array, the *ISLR* for the chosen minimum *PSL* point is 1.8dB . Since the minimum *PSL* is -17.43 dB , the interval is set to $[-18\text{ dB}, -17\text{ dB}]$ for *PSL*, and $[0\text{ dB}, 2\text{ dB}]$ for *ISLR*. Figure 3.23 shows the results which meet both of these two conditions. The red dot represents the result for the minimum *PSL* point from the preliminary optimisation stage illustrated in Figure 3.19. Compared to other configurations which have similar *PSL*, the *ISLR* for the chosen minimum *PSL* point is relatively high. There are 30 configurations meet both of the conditions, but, as shown in Figure 3.23, there is more than one configuration which has *ISLR* lower than 1dB . Thus, only configurations with *ISLR* lower than 1 dB are selected as the alternative designs and the parameters for these 17 configurations are listed in Table 3.5. Again, the *PSL* and *ISLR* for the alternative designs are very similar, with standard deviations of 0.11 and 0.16 , for *PSL* and *ISLR* respectively. From Table 3.5, it can be observed that design #1 has the smallest *PSL* and the second smallest *ISLR* (highlighted row) and that one is selected as the representative design of sunflower spiral array.

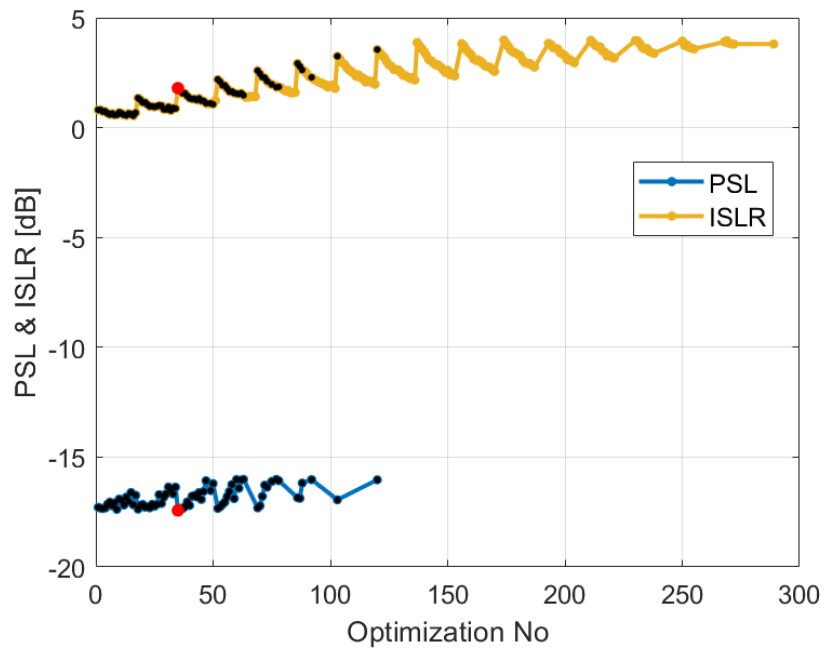


Figure 3.23 Sunflower spiral array configurations with PSL lower than -17 dB (blue line), or ISLR lower than 2 dB (yellow line) are shown in the plot. The black dots represent the configurations that meet both conditions. The red dots indicate the results of the minimum point as illustrated in Figure 3.18.

Table 3.5 Alternative Designs for Sunflower Spiral Array

	<i>PSL</i> [dB]	<i>ISLR</i> [dB]	Element		
			Radius <i>ele_r</i>	Gap <i>ele_g</i>	Number
1	-17.38	0.58	1.10	0.20	86
2	-17.34	0.73	0.80	0.20	159
3	-17.32	0.81	0.75	0.20	180
4	-17.32	0.74	0.85	0.20	142
5	-17.31	0.97	0.95	0.25	109
6	-17.29	0.81	0.70	0.20	204
7	-17.24	0.95	1.05	0.25	90
8	-17.21	0.64	1.00	0.20	103
9	-17.18	0.58	1.25	0.20	66
10	-17.17	0.54	1.45	0.20	49
11	-17.15	0.97	1.10	0.25	82
12	-17.15	0.97	1.00	0.25	99
13	-17.15	0.65	0.90	0.20	127
14	-17.11	0.99	1.20	0.25	69
15	-17.09	0.57	1.05	0.20	94
16	-17.05	0.60	0.95	0.20	114
17	-17.02	0.64	1.35	0.20	56

3.5.5. Summary of Optimisation Process – Phase I

Table 3.6 lists the key parameters for the final chosen representative configurations of each array, with their configurations and directivity functions illustrated in Figure 6.24.

The log spiral array configuration has the lowest *PSL*. The *PSL* values for the sunflower spiral array configuration and the random array configuration are similar to each other.

In terms of *ISLR*, the sunflower spiral array performs the best, while the other two configurations have similar performance. In other words, compared to the other two array configurations, the random array configuration does not have any advantages in terms of *PSL* and *ISLR* values. Thus, the random array is not taken forward as a possible sparse array option for manufacture.

As listed in Table 3.6, compared to the sunflower array configuration, the log spiral array configuration has a 3.15 dB lower *PSL* and a 2.24 dB higher *ISLR*. As mentioned in Section 3.2, the *PSL* has higher priority than the *ISLR*. Thus, the log spiral array configuration is considered to have advantage over the sunflower array pattern. Taking the number of elements into consideration, the log spiral array configuration has more advantages over the sunflower spiral array configuration. The chosen log spiral array has 106 elements, while the chosen sunflower spiral array has only 86 elements. The larger number of elements gives log spiral array more flexibility and controllability, which eventually increases transducer's imaging capability. Furthermore, since the elements in the log spiral array are placed more regularly than in the sunflower array, it is easier to make a CECAT with log spiral layout. Thus, the log spiral array configuration was chosen as the optimal design and proposed for manufacture.

Table 3.6 Key parameters for selected configurations.

Array Type	<i>PSL</i> [dB]	<i>ISLR</i> [dB]	Element No.
Log Spiral Array	-20.53	2.82	106
Sunflower Spiral Array	-17.38	0.58	86
Random Array	-17.85	2.92	94

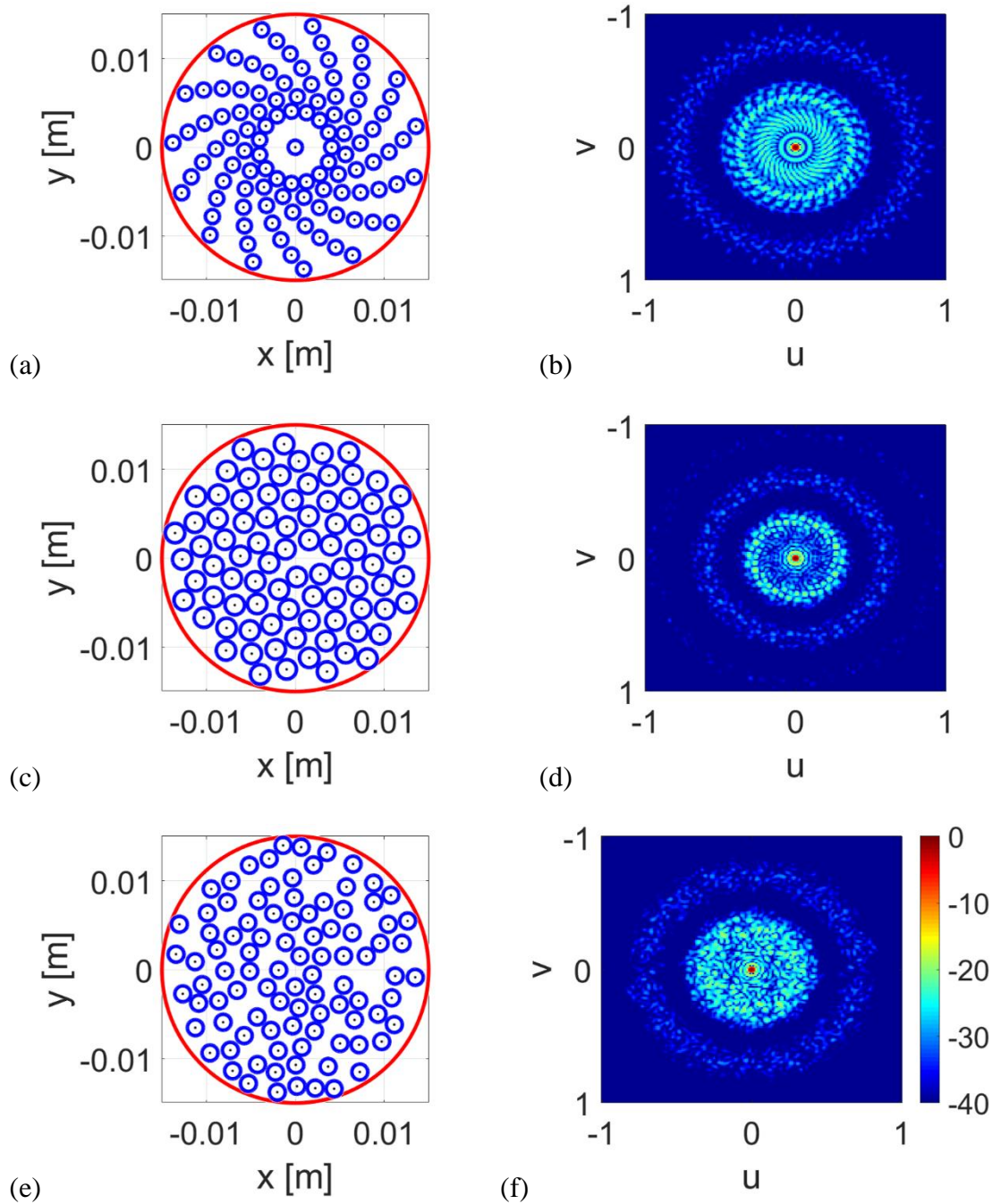


Figure 3.24 (a) The log spiral array, (c) the sunflower spiral array, and (e) the random array configurations designed from optimisation process (a) Phase I and (b, d, f) the corresponding directivity functions. The blue circles represent the array elements. The red circle represents the array aperture. The black dots are the centres of the array elements.

3.6. Optimisation Process – Phase II

The design selected by the initial optimisation design process, log spiral configuration identified as design #5 in Table 3.4, was sent to be manufactured as a CECAT transducer. However, the fabrication process, detailed in Section 4.2.1, failed as the fibres from different array elements were not sufficiently spaced apart and the fibres entangled through the thickness of the CECAT moulded block. This occurred among the first elements of each arm, which resemble a circle of elements. To solve this issue, the gap between these elements has been increased from $ele_g * \sin(\pi/\theta)$ to $ele_g/2$. The same optimisation process, as mentioned in Section 3.4 has been repeated for log spiral array with increased a , while all other parameters remain the same as the first optimisation process. Figure 3.24 shows the optimisation results of the new log spiral array in terms of PSL values. The minimum PSL is slightly increased to -20.29 dB. Based on this result, the interval for PSL is set to [-21 dB, -20 dB]. As the $ISLR$ for the minimum point is 3.32dB, the interval for $ISLR$ is set to [0 dB, 4 dB] first. There are 6 configurations who meet these two conditions as listed in Table 3.7. The $ISLR$ values for all these configurations are higher than 3 dB. If the representative configuration of the log spiral array is selected from these 6 configurations, then the new log spiral array has no advantage compared to the selected best random and sunflower arrays in terms of $ISLR$. Thus, instead of selecting from these 6 configurations, new intervals for PSL and $ISLR$ are introduced to find configurations with PSL s smaller than the other two arrays, although $ISLR$ values will be similar.

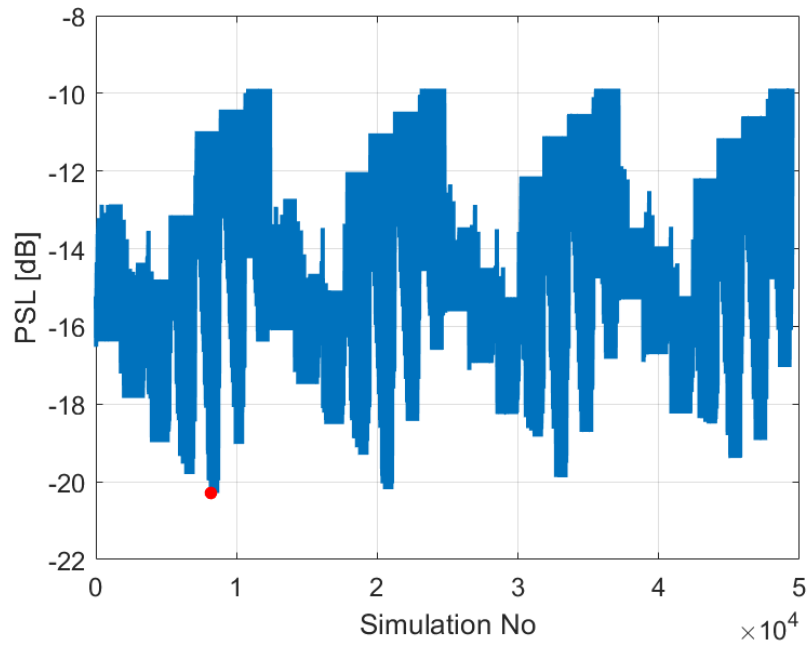


Figure 3.25 Optimisation results for log spiral array with increased parameter, a. The red dot represents the configuration that has the lowest PSL (-20.29 dB) with a corresponding ISLR of 3.32 dB. The configuration is formed using 0.7 mm ele_r , 0.4 mm ele_g , 8 ele_per_arm , 15 arms, and 1.2 b .

Table 3.7 Alternative Designs for Log Spiral Array - Second Analysis

	PSL [dB]	ISLR [dB]	Element			No of Arms num_of_arm	b	Element No
			Radius ele_r	Gap ele_g	Per Arm ele_per_arm			
1	-20.29	3.32	0.70	0.40	8	15	1.2	121
2	-20.26	3.55	0.70	0.45	8	15	1.2	121
3	-20.19	3.50	0.70	0.40	8	15	1.3	121
4	-20.09	3.75	0.70	0.50	8	15	1.2	121
5	-20.07	3.71	0.70	0.45	8	15	1.3	121
6	-20.04	3.86	0.75	0.55	7	15	1.3	106

The new intervals are [-20 dB, -21 dB] for PSL and [0 dB, 3 dB] for ISLR. The configurations who meet both of these two conditions are represented by the black dots

in Figure 3.25. There are 15 configurations in total, with Table 3.8 listing the parameters for these configurations. The average *PSL* is -19.27 dB which is still lower than that of the other two array configurations. The average *ISLR* is 2.7 dB which is similar to the previous alternative designs for the log spiral array and the random array. Thus, the log spiral array is still the preferred array configuration. The #4 design in Table 3.8 (highlighted row) has been selected as appropriate for manufacture, since it has relatively bigger inter-element gap which can help increase the possibility of successful manufacturing rate. Also, the 4th design has lower *PSL* and *ISLR* values compared to the other two configurations (the 13th and 14th designs) which has similar *ele_g*. Figure 3.27 illustrates the layout and the directivity function for the 4th design.

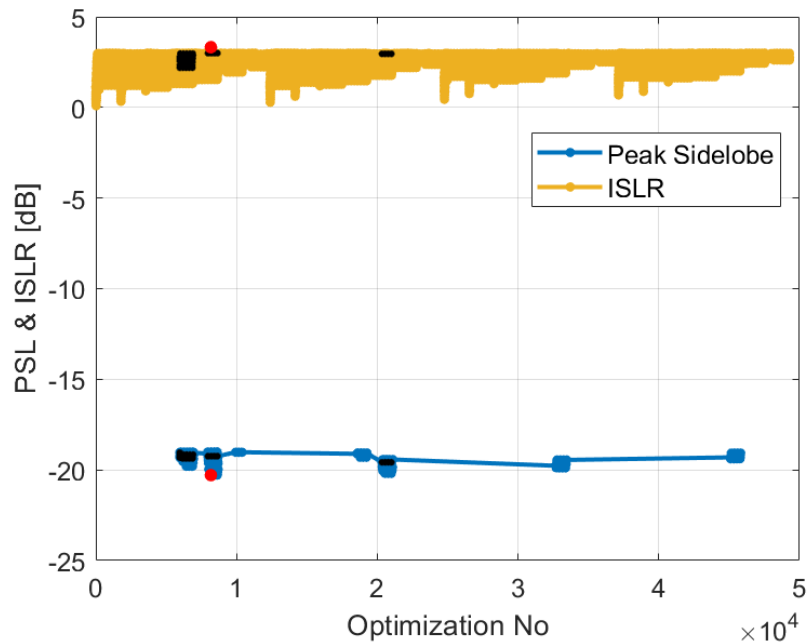


Figure 3.26 Log spiral array configurations with *PSL* lower than -19dB (blue line), or *ISLR* lower than 3dB (yellow line) are shown in the plot. The black dots represent the configurations that meet both conditions. The red dots indicate the results of the minimum point as illustrated in Figure 3.22.

Table 3.8 Alternative Designs for Log Spiral Array - Second Analysis with Reduced PSL interval

	PSL [dB]	ISLR [dB]	Element			No of Arms <i>num_of_arm</i>	<i>b</i>	Element No
			Radius <i>ele_r</i>	Gap <i>ele_g</i>	Per Arm <i>ele_per_arm</i>			
1	-19.58	2.96	0.80	0.40	7	15	1.3	106
2	-19.37	2.90	0.85	0.40	7	13	1.2	92
3	-19.33	2.52	0.95	0.45	6	13	1.2	79
4	-19.33	2.71	0.95	0.50	6	13	1.2	79
5	-19.32	2.19	1.00	0.40	6	13	1.2	79
6	-19.30	2.56	0.75	0.40	6	13	1.2	79
7	-19.30	2.69	0.85	0.40	6	13	1.2	79
8	-19.29	2.61	0.90	0.40	6	13	1.2	79
9	-19.27	2.67	0.80	0.40	6	13	1.2	79
10	-19.24	2.99	0.80	0.45	7	15	1.2	106
11	-19.21	2.80	0.90	0.45	6	13	1.2	79
12	-19.17	2.34	0.95	0.40	6	13	1.2	79
13	-19.17	2.97	0.90	0.50	6	13	1.2	79
14	-19.16	2.89	0.95	0.55	6	13	1.2	79
15	-19.05	2.79	0.70	0.40	6	13	1.2	79

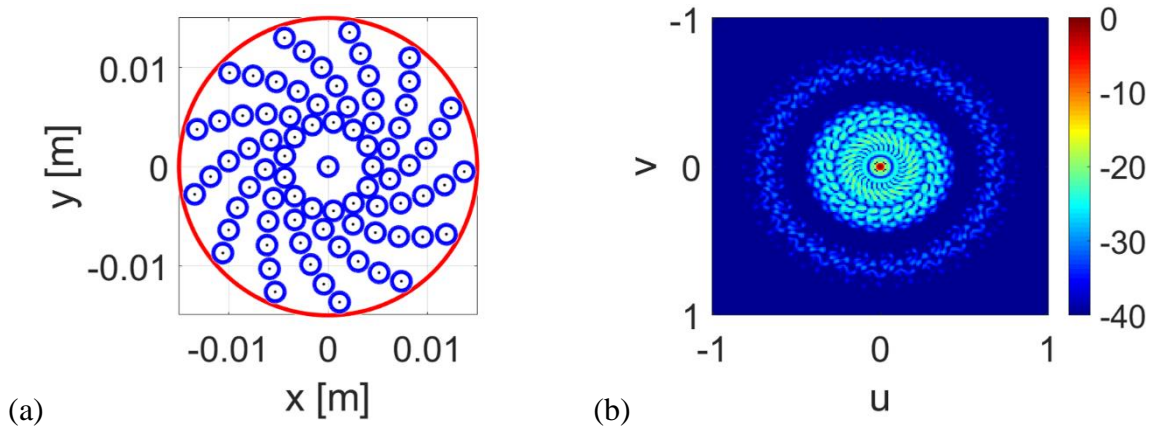


Figure 3.27 (a) The log spiral array configuration designed from optimisation process Phase II and (b) the corresponding directivity function. The blue circles represent the array elements. The red circle represents the array aperture. The black dots are the centres of the array elements.

3.7. Summary

During the design process, three array configurations have been simulated to find an appropriate 2D sparse array configuration for operation through the temporal window in the skull. Two array properties *PSL* and *ISLR* are used to estimate the performance of each array configuration. For each array configuration, a representative design which has both low *PSL* and low *ISLR* has been selected. The results indicate that the log spiral performs better in terms of *PSL* compared with the other two configurations, while the sunflower spiral array performs the best overall in terms of *ISLR*. Considering these two design criteria has led to one of the log spiral array configurations, which has 106 elements, being selected as the optimal design. However, this configuration could not be manufactured directly as a CECAT, using the fabrication approach described in Section 2.3.2, which resulted in a second simulation phase through which another log spiral design with 79 elements was selected for manufacture as a CECAT. The two array

patterns, illustrated in Figure 3.24(a) and Figure 3.27(a), are used to fabricate prototype transducers in Chapter 4.

A pair of prototype transducers with the 79-element log spiral array pattern have been manufactured, one using a fibre CECAT active layer configuration while the other incorporates a conventional 1-3 composite active layer. Both array devices will have the same electrode pattern but will have different piezoelectric microstructures. In addition to these two 79 elements log spiral array transducers, a third prototype transducer with the overall optimum 106-element log spiral array design has been produced. However, this is only produced using a standard 1-3 composite active layer and is included to provide a comparison between the manufactured CECAT array from the second design phase and the original optimal array configuration from the Phase I design process. It is considered that these three transducers will enable comparison between:

1. The fabrication processes in terms of acoustic performance of the log spiral array design.
2. Acoustic performance between the optimal and practical log spiral designs.

Table 3.9 is provided to detail the differences between the three array transducer configurations to be fabricated and provide a clear nomenclature for each device for the remainder of the Thesis.

Table 3.9 Array Configuration Details for Devices to be Manufactured

<i>Device Name</i>	<i>CECAT_79</i>	<i>C13_79</i>	<i>C13_106</i>
<i>Microstructure</i>	<i>CECAT</i>	<i>1-3 composite</i>	<i>1-3 composite</i>
<i>Array element size</i>	<i>0.95 mm</i>	<i>0.95 mm</i>	<i>0.8 mm</i>
<i>Inter-array elements gap</i>	<i>0.5 mm</i>	<i>0.5 mm</i>	<i>0.5 mm</i>
<i>Number of elements per arm</i>	<i>6</i>	<i>6</i>	<i>7</i>
<i>Number of arms</i>	<i>13</i>	<i>13</i>	<i>15</i>
<i>Total number of elements</i>	<i>79</i>	<i>79</i>	<i>106</i>

Chapter 4

Transducer Manufacturing and Characterisation

4.1. Introduction

This Chapter describes the manufacturing process for the prototype transducers that have been discussed in Section 3.7 and analyses their characterisation results. The manufacturing process of each prototype transducer consists of 5 steps:

1. Fabricate the active layer.
2. Applying electrical connection to achieve individual control of all array elements.
3. Packaging the active layer and electrical interconnection inside a housing.
4. Applying an appropriate matching layer.
5. Ensuring exit for external electrical cabling is water-proof.

Three transducer parameters, the electrical resonance frequency (f_e), the mechanical resonance frequency (f_m), and the coupling coefficient (k_t) are used to evaluate the piezoelectric performance of the active layers and the individual array elements. These transducer parameters were described in Section 2.3.1(b). Details of each step in the

fabrication process are explained in the remainder of this Chapter and Figure 4.1 will be referenced throughout the Chapter to illustrate each stage of the manufacturing process.

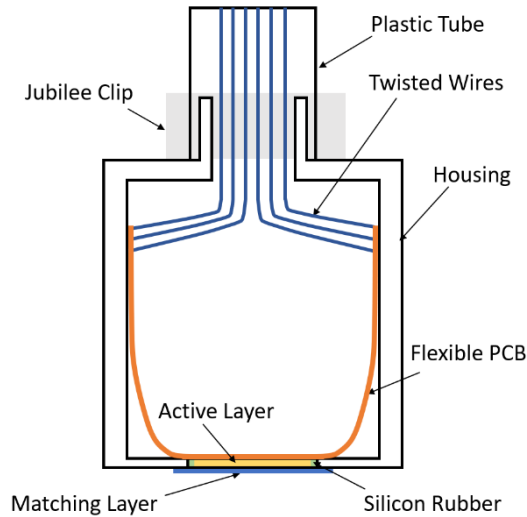


Figure 4.1 Illustration of the prototype transducers' structure.

4.2. Manufacturing Prototype Transducers

This Section will describe the manufacturing stages for the three prototype transducers, CECAT_79, C13_79, and C13_106, as detailed in Table 3.9. The basic CECAT and 1-3 composite microstructures were introduced in Section 2.3, with this Chapter building on these concepts.

4.2.1. Piezoelectric Active Layer

a. Fibre CECAT Piezocomposite – 79 Array Elements

The manufacturing process of the fibre CECAT active layer includes five steps:

1. Making a mechanical jig to hold the piezoceramic fibres in desired CECAT array positions.
2. Encapsulating the jig with a passive polymer phase and curing.
3. Slicing the bulk piezocomposite into the desired thickness.
4. Poling the piezocomposite slice to achieve the piezoelectric effect in the CECAT.
5. Applying metallic electrodes onto the CECAT array pattern.

Figure 4.2 illustrates the jig used in manufacturing the CECAT_79 active material. The jig consists of three plates. The top two plates are used to group PZT fibre bundles to form the desired array pattern. The distance between those two plates is set to 25 mm to ensure there is sufficient bulk piezocomposite for machining into individual active layers. The selected 79-element log spiral array pattern has been drilled into those two plates. The bottom plate is used to support the bottom ends of the PZT fibres during the curing process. Those three plates are placed in parallel with each other to avoid twisting the individual PZT fibres.

The volume fraction of each individual active array element was calculated to be 50%, which ensures good piezoelectric performance and manufacturability of the device [10]. 250 μ m PZT5A fibres (Smart Material Corp., Sarasota, FL) have been selected as the piezoelectric material. Therefore, each individual array element, which has a 0.95 mm radius, contains 28 individual fibres. Figure 4.3 shows views of the fibre CECAT assembly after inserting all the PZT fibres and prior to the polymer encapsulation process.

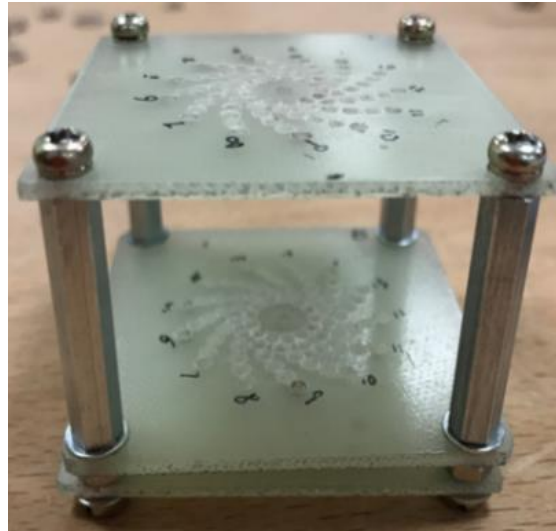


Figure 4.2 The jig which was used in manufacturing the CECAT active layer.

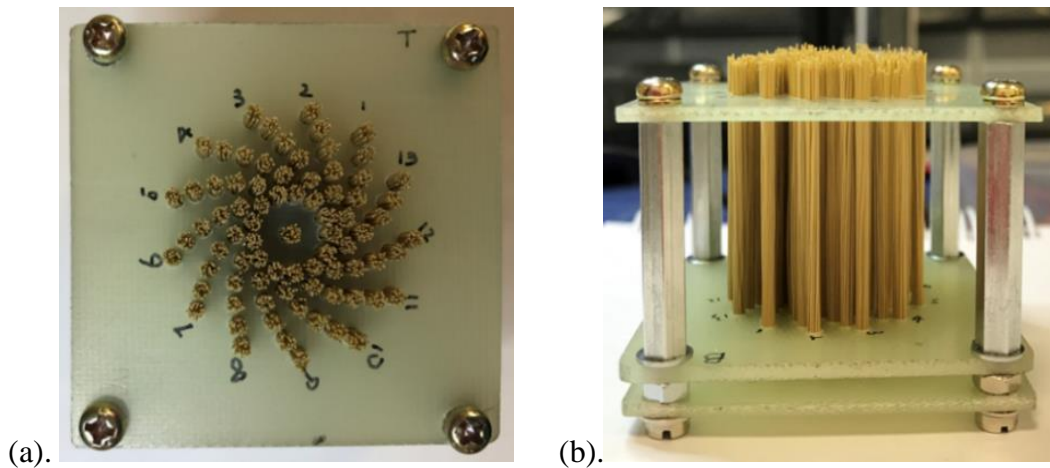


Figure 4.3 (a) Top view and (b) side view of the fibre CECAT assembly after inserting PZT fibres.

The jig containing the PZT5A fibres is then encapsulated with CIBA-GEIGY CY221-HY956 epoxy (medium set epoxy) to form the fibre CECAT piezocomposite [10]. This polymer phase was selected from the CUE materials database as it provided a compromise between low longitudinal attenuation and high shear attenuation (detailed

properties are included in Appendix A), whilst, importantly, being suitable for machining [115]. As shown in Figure 4.4(a), the fibre CECAT assembly was placed on a metal block and enclosed inside a rectangular aluminium mould into which medium set epoxy was poured. The metal block is used to help to conduct heat during the curing process away from the CECAT block, as the epoxy temperature will firstly increase, then decrease, before returning to the surrounding environmental temperature. These changes of internal temperature can cause damage to the manufactured part and may lead to cracks, as shown in the test sample presented in Figure 4.5. Hence, the curing process has been divided into four steps to avoid that issue. The two-part epoxy is first combined and degassed in a vacuum chamber, before being introduced into the mould, as shown in Figure 4.4(a). Next, the mixture was transferred into a freezer which was set to -25°C . After 24 hours, the mixture was removed from the freezer and left to cure at room temperature for 48 hours. Finally, the mixture was kept in an oven at 48°C for 24 hours. Figure 4.4(b) shows the fibre CECAT piezocomposite block after being taken out from the mould after this four-stage curing process. Importantly, no cracks have formed inside the composite block and Figure 4.4(b) presents a photograph of a side view of the block, after removal of some of the excess polymer encapsulation material.

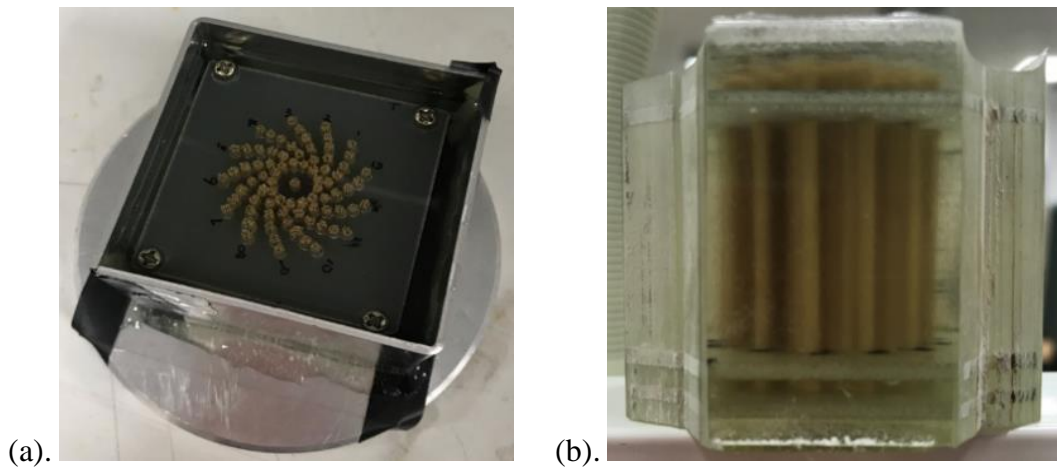


Figure 4.4 (a) The fibre CECAT assembly inside the rectangular mould. (b) The fully cured fibre CECAT piezocomposite block after removal from the mould.

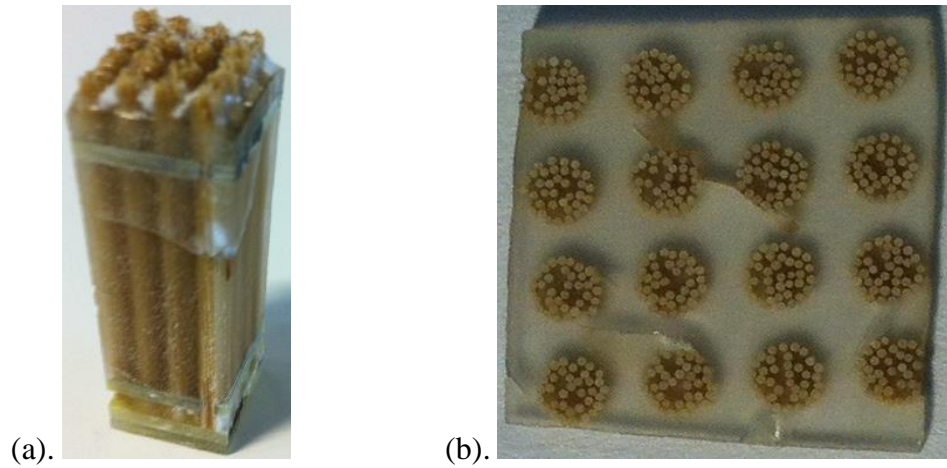


Figure 4.5 (a) A test sample of a fibre CECAT piezocomposite block which was improperly cured. (b) A piece of fibre CECAT piezocomposite sliced from the block shown in (a).

The intended operational frequency of the array transducer is ~ 2 MHz. To inform the next stage in the fabrication process – slicing of the CECAT piezocomposite block into individual CECAT layers – a finite element analysis (FEA) simulation has been conducted to determine the CECAT layer thickness. Figure 4.6 shows the FEA model

(PZFlex, OnScale Inc, Cupertino, CA) which has been used to predict the electrical impedance response for the array elements in the fibre CECAT active layer. Unlike the conventional 1-3 composite, which has a periodic microstructure and can be represented by a unit cell, as mentioned in Section 2.3.1(a), the fibre CECAT composite contains randomly placed piezoelectric fibres within each element area. Moreover, for the 79-element array pattern, the epoxy structure between array elements is not fixed due to the sparse array configuration. Thus, the entire CECAT_79 active layer has been modelled to increase the representativeness of the model. Within each element area, the method used to generate the random array pattern (as mentioned in Section 3.3.1) has been utilised to produce a random fibre layout. Figure 4.7 shows an example of the predicted electrical impedance results for the central array element and it can be identified that f_e is 1948 kHz, and f_m is 2491 kHz, when the thickness of the active layer is 0.75 mm. This results in a predicted k_t of 0.66, which indicates that the fibre CECAT active layer should have good energy conversion capability [19].

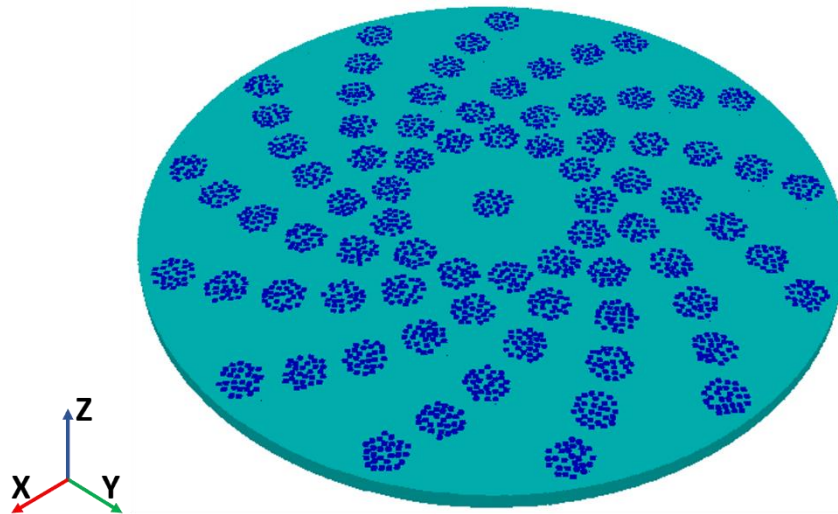


Figure 4.6 The PZFlex model used to simulate the electrical impedance response for the centre element in the CECAT_79 active layer. Blue represents the PZT fibre, while cyan represents the medium set epoxy.

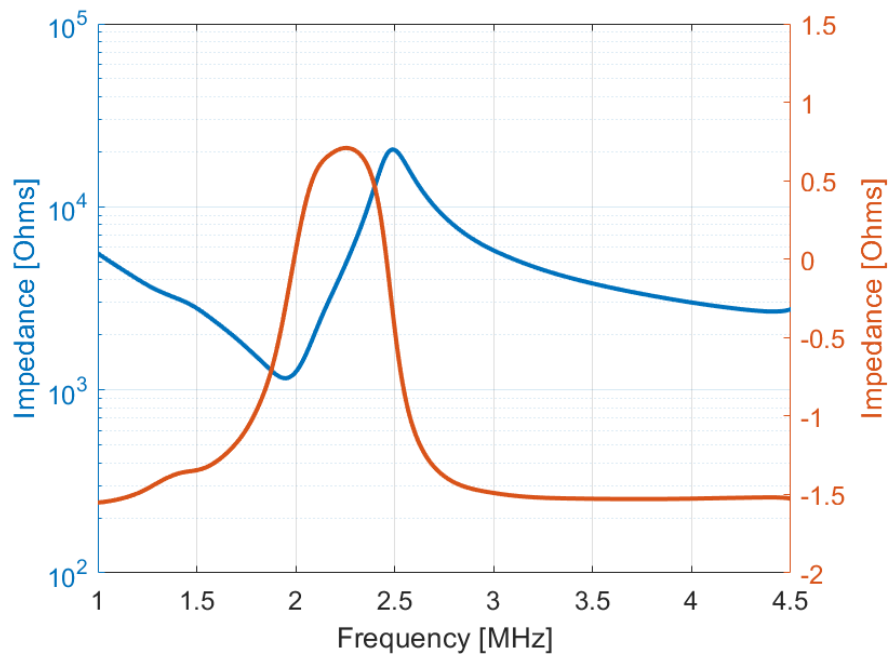


Figure 4.7 The simulated impedance response for the centre element in the CECAT_79 active layer. f_e is 1948 kHz, while f_m is 2491 kHz.

Consequently, a slice was removed from the fibre CECAT piezocomposite block and then lapped to 0.75 mm thickness to achieve the desired 2 MHz operating frequency, as shown in Figure 4.8(a). Before applying the log spiral electrode pattern, the fibre CECAT active layer was fully electroded using silver paint (AGG302, Agar Scientific Ltd, UK) and poled. The fibre CECAT active layer was polarized at 1.5kV for 15 minutes, at room temperature, in accordance with the PZT fibre manufacturer's guidelines [35]. For safety reasons, the ramp up/down time for the voltage should be at least 1 minute. Figure 4.9 shows the setup of the polarization process. The fibre CECAT active layer is fixed under a jig which is attached to the power supply. A multimeter is used to monitor the change of applied voltage. The poled active layer, with a uniform electrode applied to both the top and bottom faces, was then sent to measure its impedance response. The f_e for the entire active layer is 1986 kHz, and the measured f_m is 2460 kHz. The k_t of the whole CECAT active layer is 0.63. These experimental results indicate that the CECAT active layer could work properly as designed.

In the final preparation step for the CECAT active layer, electrodes have been added to the poled CECAT composite slice using metallic evaporation through a mask. Silver (Ag) is used as the material for electrodes (~500nm), with a thin layer (~20nm) of chrome (Cr) evaporated first to improve adhesion to the active material. The final CECAT_79 active layer with electrodes applied is shown in Figure 4.8(b). The impedance response of the centre element in the CECAT_79 active layer is as shown in Figure 4.10, alongside with the simulated results (shown earlier in Figure 4.7). The f_e for the centre element in the CECAT_79 active layer is 2035 kHz, and the measured f_m is 2538 kHz. The k_t of the

centre element in the CECAT active layer is 0.64. These experimentally measured transducer parameters correlate well with the FEA predicted values generated using PZFlex. As can be noticed from Figure 4.10, there exists some mis-match between the simulated and measured impedance response. This is mainly related to the difference between the simulated and measured impedance response. This is mainly related to the difference between the FEA model and the manufactured active layer in terms of the element microstructure, as the PZT fibres within each element was randomly placed.

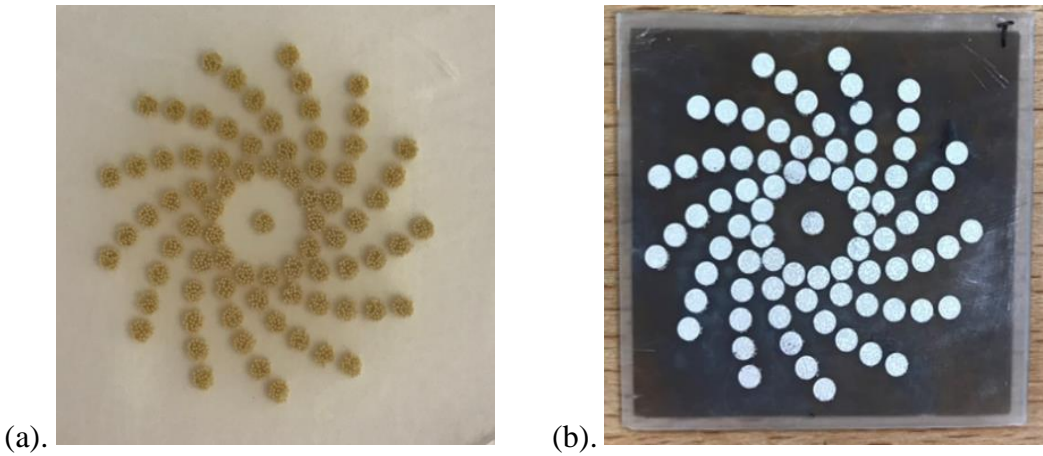


Figure 4.8 The fibre CECAT active layer with the 79-element log spiral array pattern (a) before and (b) after applying electrodes.

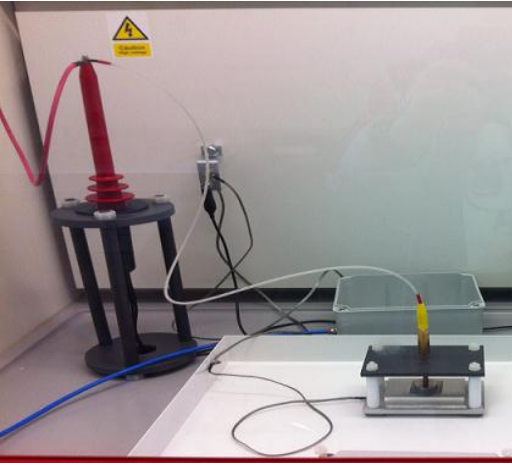


Figure 4.9 Poling process setup for the fibre CECAT active layer. The active layer is fixed under the circular plate of a jig. The poling voltage is 1.5kV.

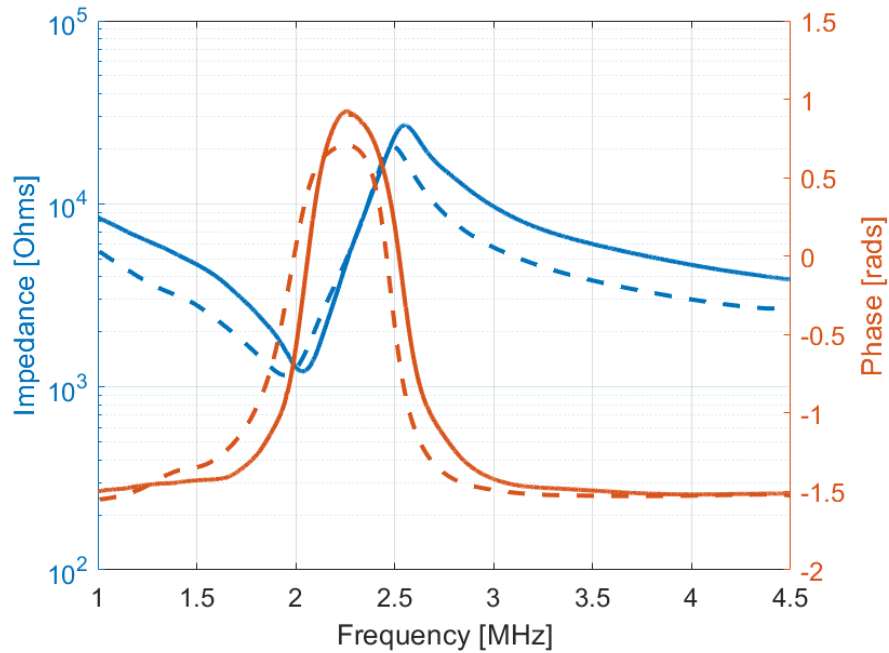


Figure 4.10 The electrical impedance response for the centre element in the CECAT_79 active layer. The solid lines represent the experimental results (blue for impedance and orange for phase), while the dashed line represents the simulated results. The measured f_e is 2035 kHz and the measured f_m is 2538 kHz.

b. Conventional 1-3 Connectivity Piezocomposite – 79 Array Elements (C13_79)

A second 79-element log spiral array was fabricated by deposition of the desired electrode pattern onto a diced 1-3 piezocomposite configuration. To keep the consistency between the two array devices, the following design parameters were kept constant.

1. PZT5A ceramic and medium set epoxy were used as the active and passive materials.
2. The volume fraction is set at 50%.

3. The layer thickness is set to 0.75 mm.

Again, FEA has been used to establish the fabrication parameters for a ~ 2 MHz operating frequency and the set transducer parameters above. Figure 4.11 illustrates the 4 x 4 pillar section modelled in PZFlex, with the model determining the ceramic pillar width is set to 0.22 mm and the kerf width is set to 0.09 mm. Recalling the radius of array element in the 79-element log spiral array pattern, which is 0.95 mm, each array element in the C13 configuration will consist of around 29 pillars. The predicted electrical impedance response is shown in Figure 4.12, in which f_e is 1928 kHz and f_m is 2438 kHz giving a predicted k_t of 0.65.

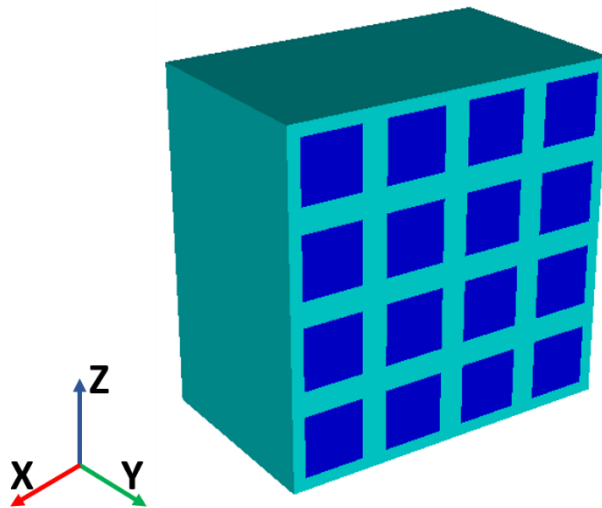


Figure 4.11 The PZFlex model used to simulate the impedance response for the C13 piezocomposite active layer. Blue represents the PZT5A pillar, while cyan represents the medium set epoxy.

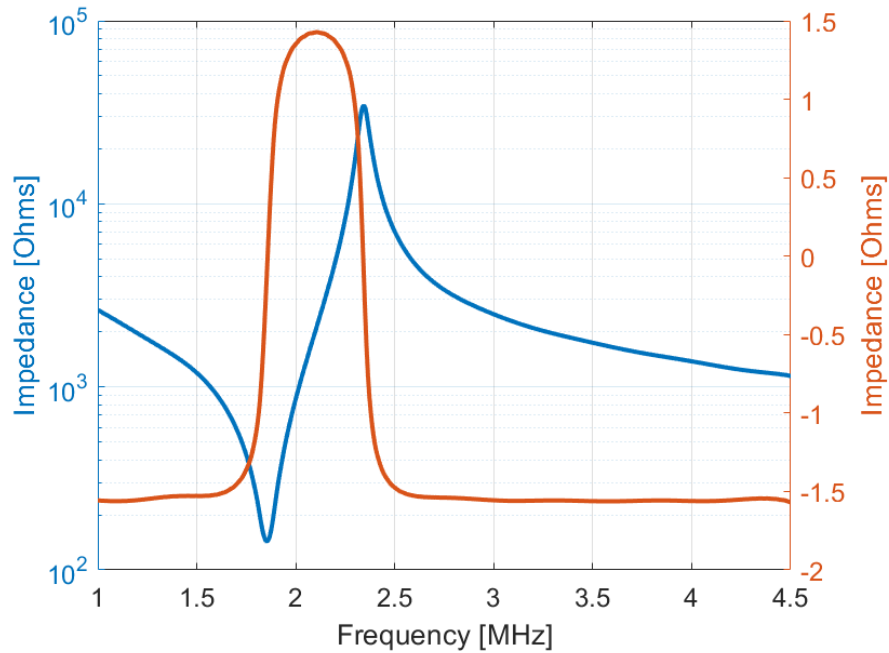


Figure 4.12 The simulated impedance response for the C13 composite active layer. f_e is 1928 kHz, while f_m is 2438 kHz.

The manufacturing process for a 1-3 piezocomposite active layer is well documented [33] and includes the following key four steps:

1. Dicing the bulk ceramic plate/disk into a matrix of square pillars.
2. Encapsulating the diced ceramic block with a passive polymer phase and curing.
3. Lapping the piezocomposite block to the desired thickness.
4. Applying metallic electrodes to form the desired array pattern.

A bulk PZT5A ceramic disk was firstly diced into pillars with 0.31 mm pitch and 0.09 mm kerf. Next, the device was placed into a plasticine mould and filled with medium set epoxy, as shown in Figure 4.13. Since the amount of epoxy used in C13 piezocomposite manufacturing is much less when compared to that of fibre CECAT piezocomposite, the

temperature rise during the curing process is not significant and no modification to the curing process was required. Hence, the encapsulated composite block was left to cure at room temperature for 48 hours.

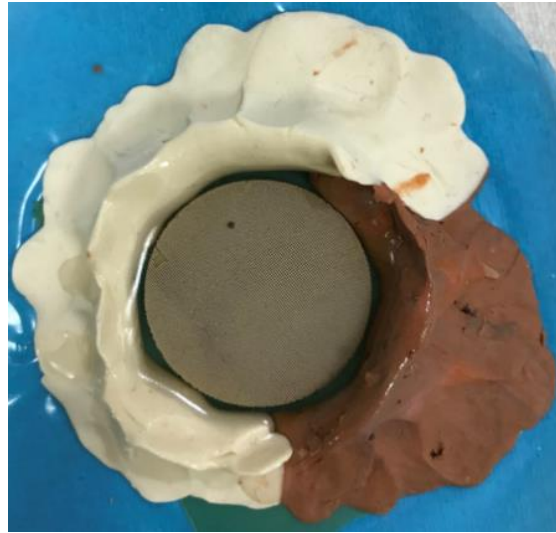


Figure 4.13 Diced ceramic inside the mould and filled with medium set epoxy.

After curing, the device was removed from the mould and excess epoxy and ceramic machined off. Initially, effort was made to machine the composite to 0.75 mm, to match the CECAT active layer. However, the composite fractured at the end of the lapping process. Thus, a compromise was made between the manufacturing capability and the designed thickness, and a second 1-3 piezocomposite fabricated using the same dicing specification. The final thickness of the composite was 0.78 mm, to minimise the risk of device fracture, and the pre- and post- electroding images for the epoxy filly composite are shown in Figure 4.14. It can be seen from these images that some of the pillars are missing from a specific section. Those missing pillars were broken because of the

vibration of the dicing saw, coupled with a likely manufacturing flaw within the bulk PZT5A ceramic material itself. However, since the gap is relatively small compared to the whole composite, most of it was avoided by careful positioning of the sparse array pattern, as shown in Figure 4.14(b). The PZFlex model has been modified to re-simulate the electrical impedance response of the 1-3 piezocomposite at the increased thickness. The result is shown in Figure 4.15, in which f_e is 1854 kHz and f_m is 2344 kHz giving a predicted k_t of 0.65. Comparison between Figure 4.15 and Figure 4.10 shows that the Q-factor, which can be calculated as the ratio between the central frequency and the half conductance bandwidth, is higher for the C13_79 (15.3) actively than that of the CECAT_79 active layer (10.8). This indicates that the CECAT_79 active layer can achieve a broader bandwidth, which will be proved by Pulse-echo test results shown later in Section 4.3.3.

The 1-3 composite active layer does not need to be poled since the manufacturer has poled the bulk ceramic used, and the dicing process does not significantly degrade the material poling. The measured impedance response of the whole active layer is shown in Figure 4.15, alongside the re-simulated 1-3 piezocomposite but at the increased thickness of 0.78mm. The measured f_e is 1877 kHz, and the measured f_m is 2308 kHz. Both are in good agreement with the re-simulated results. k_t for the whole C13 piezocomposite active layer is 0.62. The C13 piezocomposite active layer was then electroded with the sparse array pattern, using the same method as manufacturing the fibre CECAT active layer. The final C13 piezocomposite active layer with electrodes applied is shown in Figure 4.14(b). It is clear from this image that two of the array

elements contain less piezoceramic pillars as they overlap the section of the piezocomposite with missing pillars.

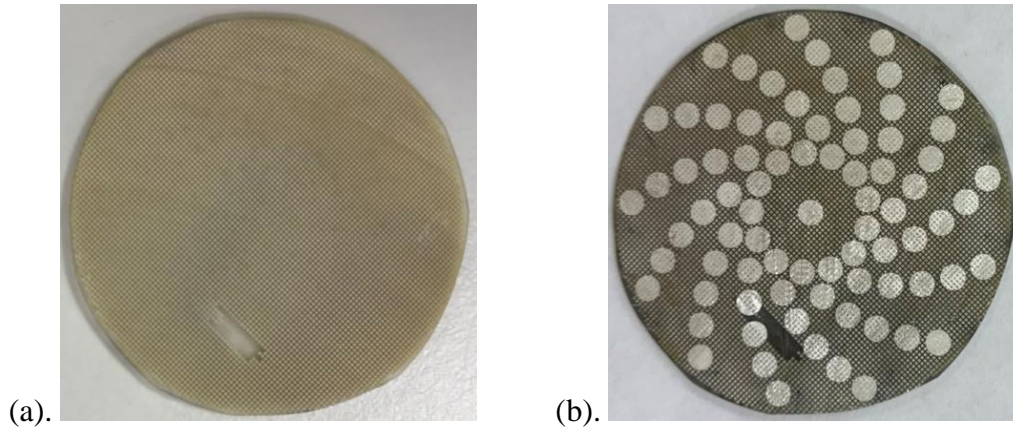


Figure 4.14 The C13_79 active layer (a) before applying electrodes and (b) after applying electrodes.

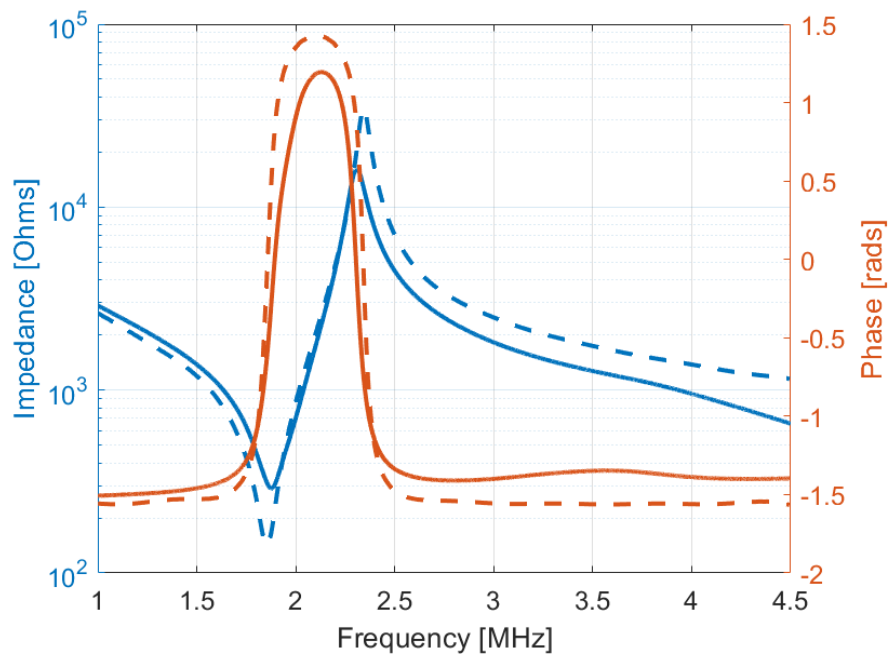


Figure 4.15 The impedance response of the C13_79 active layer. The solid lines represent the experimental results (blue for impedance and orange for phase), while the dashed line represents the re-simulated results at thickness of 0.78 mm. The measured f_e is 1877 kHz and the measured f_m is 2308 kHz. The simulated f_e is 1854 kHz and the simulated f_m is 2344 kHz.

c. Conventional 1-3 Connectivity Piezocomposite – 106 Array Elements (C13_106)

The same C13 piezocomposite configuration as for the C13_79 active layer has been used to fabricate a third active layer with the overall optimum array pattern (106 elements). With 0.31 mm piezoceramic pillar pitch and 0.8 mm array element radius, each array element will consist of roughly 22 pillars. Figure 4.16 shows the C13 piezocomposite layer before and after applying the electrodes. There are some black traces on the surface of the active layer which are delamination between the PZT and the epoxy filled by the lapping powder. Scanning of the active layer using the Laser Doppler Vibrometer (LDV) showed that it was still working under thickness-mode. The scanning has been processed for all 3 manufactured devices and are presented in Section 4.3.2.

The measured impedance response of the whole active layer is shown in Figure 4.17. The measured f_e is 1841 kHz, and the measured f_m is 2280 kHz. k_t for the entire C13 composite active layer is 0.63. The measured Q-factor for the C13_106 active layer is 23.1, which is higher than that of the C13_79 active layer, indicating a narrower bandwidth and results shown later in Section 4.3.3 have proven this.

Again, the C13 composite active layer was electroded using the same method as manufacturing the other two active layers. The final C13_106 active layer with electrodes applied is shown in Figure 4.16(b).

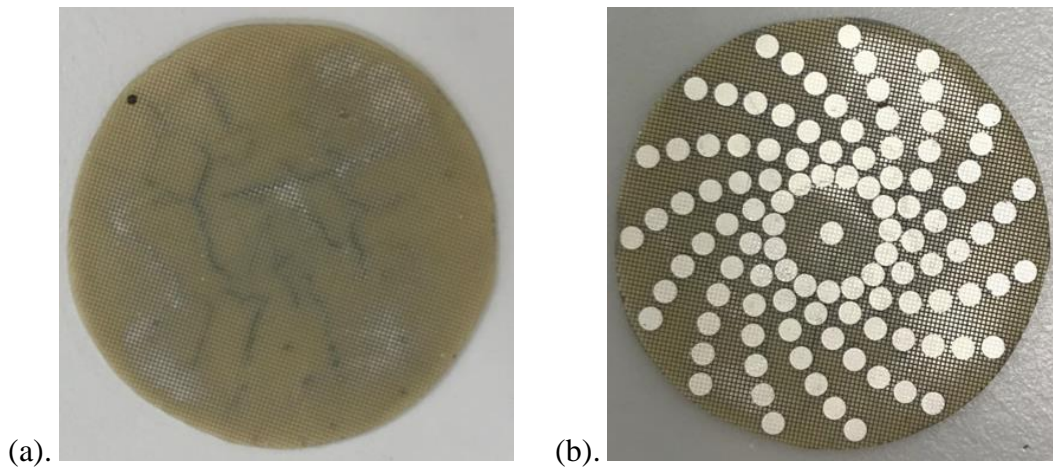


Figure 4.16 The C13_106 active layer (a) before applying electrodes and (b) after applying electrodes.

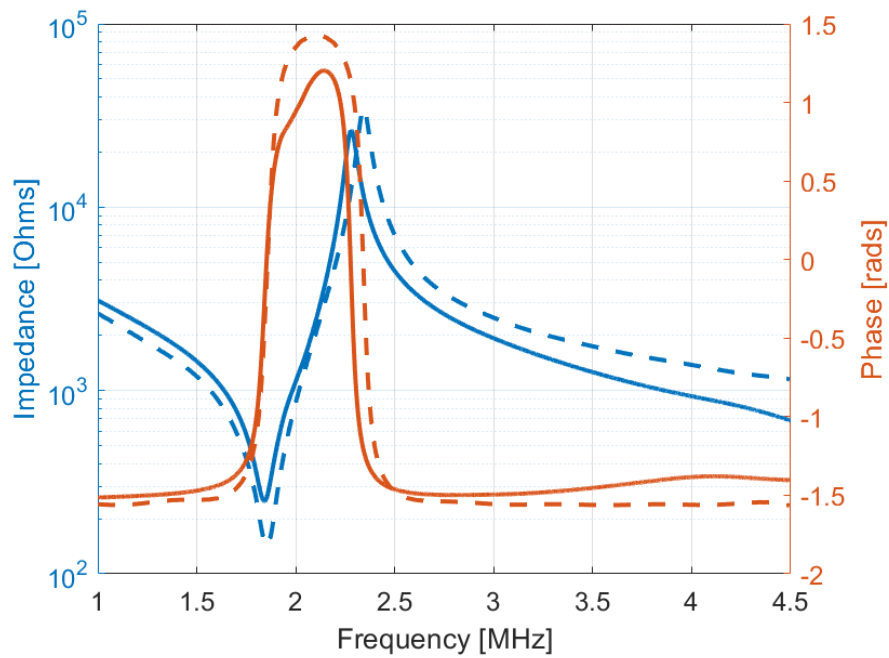


Figure 4.17 The impedance response of the C13_106 active layer. The solid lines represent the experimental results (blue for impedance and orange for phase), while the dashed line represents the re-simulated results at the increased thickness of 0.78 mm. The measured f_e is 1841 kHz and the measured f_m is 2280 kHz. The simulated f_e is 1854 kHz and the simulated f_m is 2344 kHz.

4.2.2. Electrical Connection

In this project, the electrical connection between the active layer and the external power source was achieved through two steps, first bonding the active layer to a flexible Printed Circuit Board (PCB), and then soldering twisted wires to specific areas on the PCB. Figure 4.18(a) shows an example of the flexible PCBs that have been used for in this project. Each piece of the flexible PCB consists two main parts, one is the copper pads pattern and copper tracks, the other is the general ground pad.

The circular copper pads pattern in the centre of the flexible PCB, as shown in Figure 4.18(b), replicates the selected log spiral array patterns. Each array element is connected to a single copper pad so that individual control of each array element is available. The active layer was firstly placed on a piece of plastic block, which was positioned on a mechanical clamp, as shown in Figure 4.19, with the positive side facing up. A small amount of anisotropic conductive epoxy (Creative Materials Inc., USA), which is only conductive in the thickness direction when its thickness is thinner than 0.127 mm [116], was painted over the whole surface of the positive side of the active layer. Then, the flexible PCB, with 0.1 mm thickness and 18 μm copper tracks, is placed on the active layer and a regular section of bulk metal used to ensure even distribution of pressure across the active area of the array material. Pressure was applied using a screw pushing down on the metal plate and was adjusted to make sure the flexible PCB was securely attached to the active layer. The whole system was then placed in the oven at 29°C for 24 hours to cure the conductive epoxy [116]. Since rear surface of the active layer has

been attached to the flexible PCB and the conductive epoxy, no extra backing material has been added, aiming to avoid further reduction in transducer sensitivity.

The ground side of the active layer is connected to the general ground pad of the PCB through 8 short wires as shown in Figure 4.18(c). One end of the wire is firstly bonded to the side edge of the active layer using super glue. The electrical connection between the ground side of the active layer and the wires is achieved using silver paint. Then, a 5-minute two-part epoxy (Araldite Rapid, Huntsman Advanced Materials, Switzerland) is applied to secure bonding between the wires and the active layer. The other end of the wires is soldered to the general ground pad of the PCB.

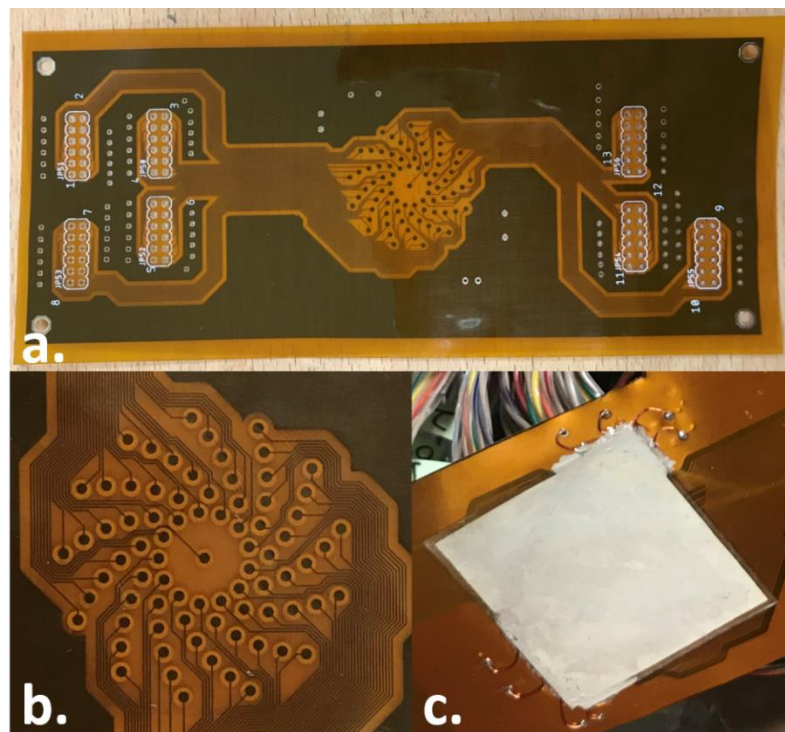


Figure 4.18 (a) The flexible PCB used to achieve electrical connection for CECAT_79 device. (b) Comparison of the circle pads pattern in flexible PCB and the array elements in the CECAT_79 active layer. (c) Illustration of how the ground side of the CECAT_79 active layer is connected to the PCB.

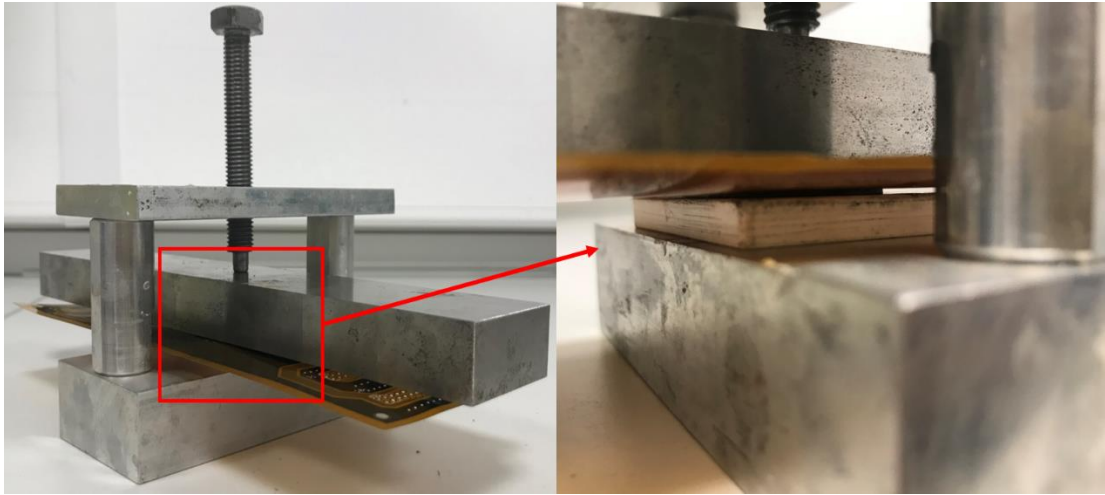


Figure 4.19 Illustration of the setup used to bond the active layer to the flexible PCB.

Twisted-pair wires are used to reduce noise between alternate signal channels within the array as they can provide electrical shielding. As shown in Figure 4.20(a), one wire is soldered to a via which is connected to a circle copper pad through a copper track on the flexible PCB, and the other is soldered to the ground pad of the PCB. The other end of the twisted wires is soldered to an external connector housing which will be able to connect to the phased array controller available in CUE through an adaptor, as shown in Figure 4.20(b) and Figure 4.20(c). The solder joints are covered using 5-minute epoxy to avoid short circuit with the inner wall of the housing.



Figure 4.20 (a) Illustration of how the twisted-pair wires are connected to the PCB. (b) Illustration of the adaptor and the phased array controller. (c) Illustration of how the twisted-pair wires are connected to the adaptor through external connector housings.

4.2.3. Housing

The active layer, the flexible PCB, and the twisted wires connected to the PCB, are packaged inside a metallic housing as shown in Figure 4.21. A rubber O-ring is placed inside the groove in the top surface of the body, as shown in Figure 4.21(c) to provide a waterproof seal. The ground side of the active layer is pushed through a square aperture at the front of the housing, which is slightly larger than the active layer, and the combined active layer and housing are placed on a flat plastic disk to ensure alignment of the components. The gap between the active layer and the edges of the square aperture is firstly filled with 5-minute epoxy to hold the array in place and then filled with silicone rubber to provide a waterproof seal. An electrical connection is made between the housing and the exposed ground side of the active layer using silver paint.

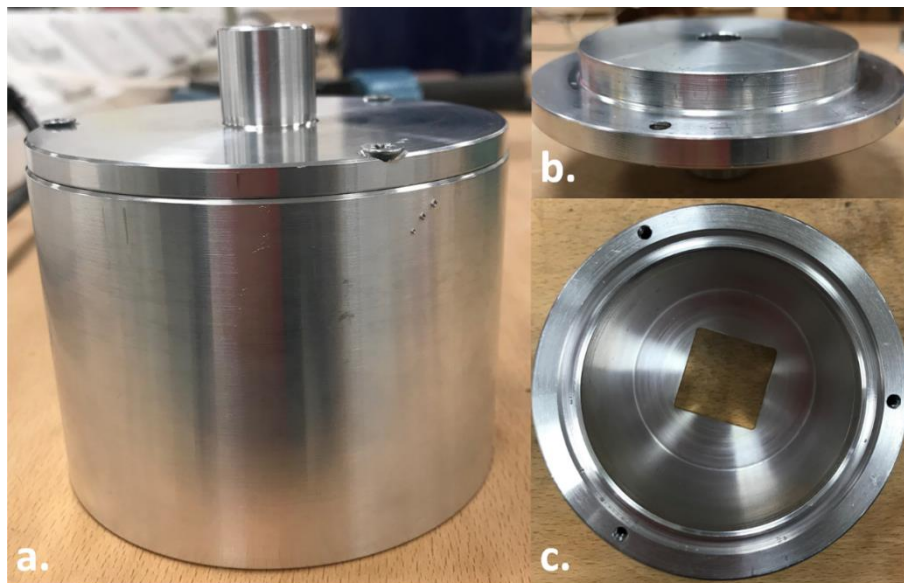


Figure 4.21 (a) The housing which is used to package the active layer and the flexible PCB. (b) The lid of the housing. (c) The body of the housing.

4.2.4. Matching Layer

The matching layer for the prototype transducer was designed to be a quarter wavelength matching layer, which aims to achieve broader bandwidth, as discussed in Section 2.4.1. Taking the desired acoustic impedance of the quarter wavelength matching layer, from Equation 2.15, and the materials available materials in CUE manufacturing lab into consideration [115] the matching layer is chosen to be a mixture of 4% tungsten and CIBA-GEIGY CY1301- HY1300 epoxy (hard set epoxy). The acoustic impedance of the matching layer is about 3.6MRayl. The measured speed of sound in the matching layer material from the database is 2188 m/s, which gives the thickness of the matching layer to be 273 μ m.

The transmitting voltage response (TVR) has been used to evaluate and compare the performance of the active layer before and after applying the matching layer. TVR can be expressed as:

$$TVR = P_{ac}/V_{in} \quad (4.1)$$

where P_{ac} is the acoustic pressure produced by the transducer and measured at 1m away and V_{in} is the input voltage [117].

Figure 4.22 shows the simulated TVR results, using a 3D FEA model for an element of the CECAT active layer with water load, with and without the matching layer. The results show that the bandwidth of the CECAT element increased from 26.0% to 51.1% with a 3.2 dB sacrifice of the maximum intensity. The reduction in intensity is associated with the change in electrical impedance, i.e. the impedance at f_e . Figure 4.23

shows the simulated impedance response for the CECAT active layer before and after applying the matching layer. As shown in the Figure, after applying the matching layer, the magnitude of the electrical impedance increases. With the same driving voltage, such an increase in the electrical impedance will cause a reduction in transducer vibration velocity, which will affect the transducer sensitivity.

The matching material was very flowable after mixing because the quantity of tungsten is low. Thus, to make the mixture more stable, it was left to slightly cure at room temperature for 2 hours before applying to the active layer. A bespoke jig was used to control the thickness of the matching layer which comprised a blade integrated into a horizontal bench, as shown in Figure 4.24, which ensured a regulated layer thickness was applied to the transducer front face. Effort has been made to keep the top surface of the active layer and the housing, as shown in Figure 4.24, at the same level so that the thickness of the matching layer could be uniformed across the whole active layer. However, due to manufacturing limits, the corners of the active layer were slightly lower than the centre. Thus, the final thickness of the matching layer varied across the active layer. The thickness of the active is thinner in the centre and becomes thicker at the corners. However, as the active layer has been sealed inside the housing, the real thickness of the matching layer has not been measured. Results shown later in Section 4.3 indicate that the variation in the matching layer thickness could have affected the uniformity of the array elements in the prototype transducers. Figure 4.25 shows the completed front faces of the CECAT_79, C13_79, and C13_106. Although the shape of the matching layers is not the exact same due to the manual manufacturing process, it

has been ensured that all the array elements have been covered by the matching layer. The interface between the edges of the matching layer and the housing is finally covered with silicone rubber for a waterproof seal.

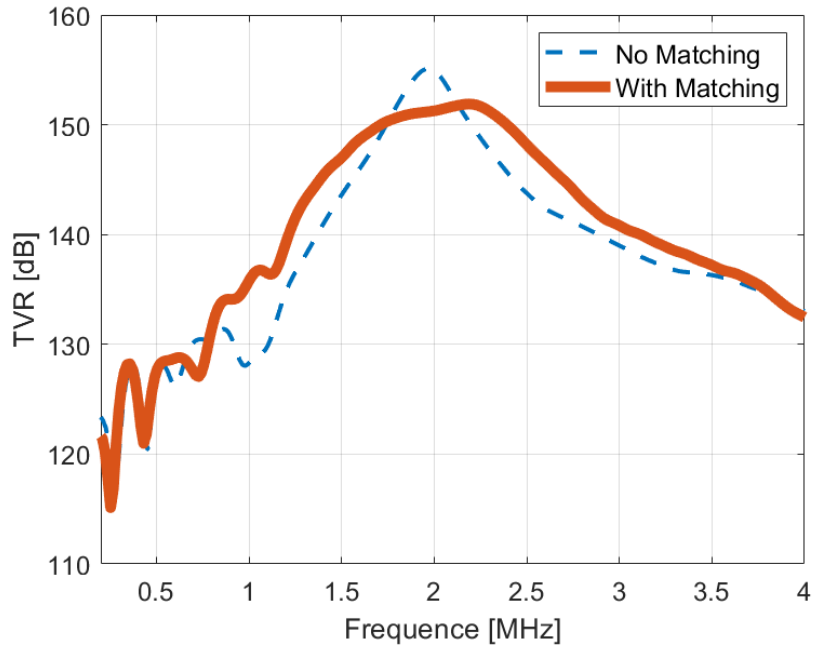


Figure 4.22 Simulated TVR results for an element of the CECAT active layer with (the solid line) and without (the dashed line) matching layer.

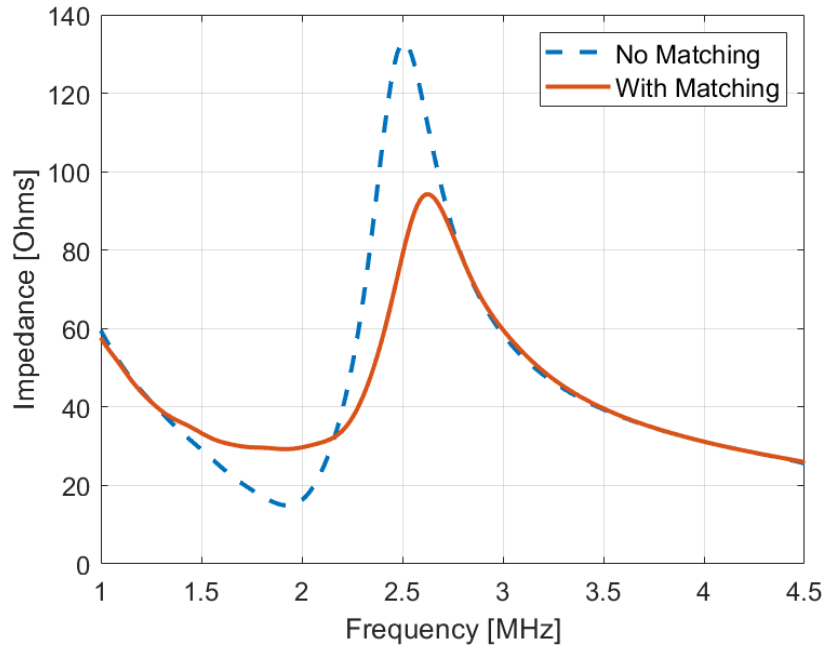


Figure 4.23 Simulated impedance response results for an element of the CECAT active layer with (the solid line) and without (the dashed line) matching layer.

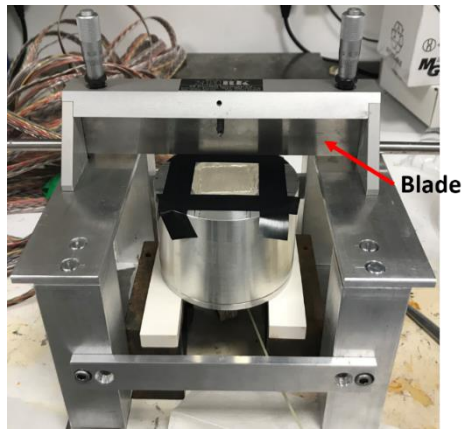


Figure 4.24 Illustration of the setup used to apply the matching layer.

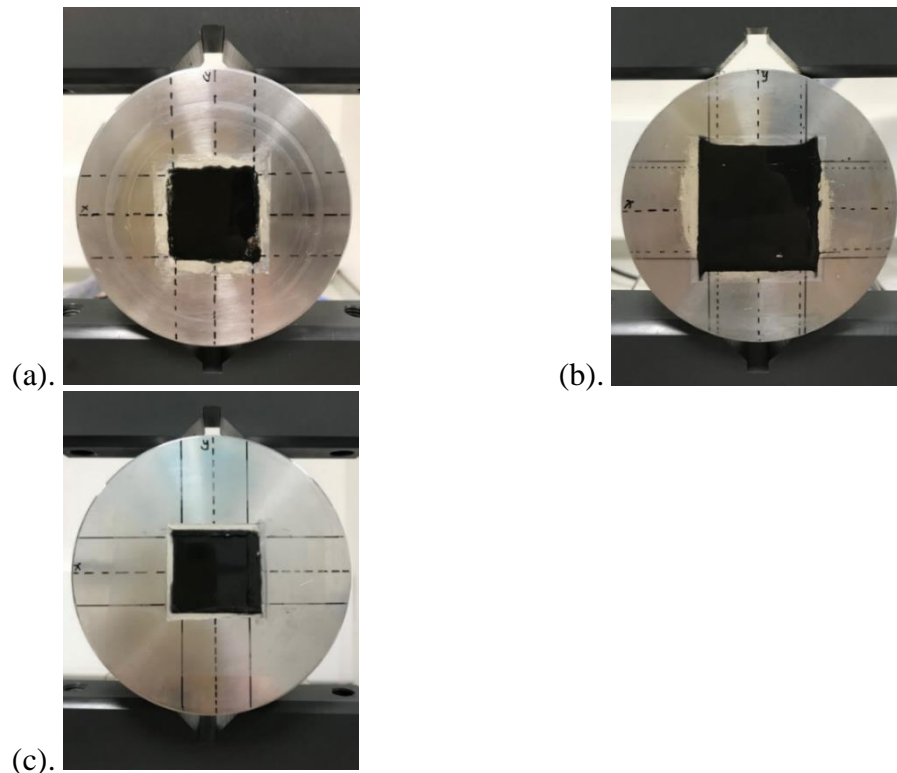


Figure 4.25 Front surface of (a) the C13_79, (b) the CECAT_79 and (c) the C13_106 after applying the matching layer.

4.2.5. Final Device Packaging

The length of twisted wires, used for external connection, is packaged inside a piece of plastic tubing. The interface between the end of the tube and the surface of the housing's lid is bonded using 5-min epoxy and covered using silicon rubber sealant. The tube is fixed to the lid using a jubilee clip. For waterproofing purposes, the gap between the lid of the housing and the body of the housing is covered using an additional layer of silicon rubber. Figure 4.26 shows an example of the final appearance of the prototype transducer.

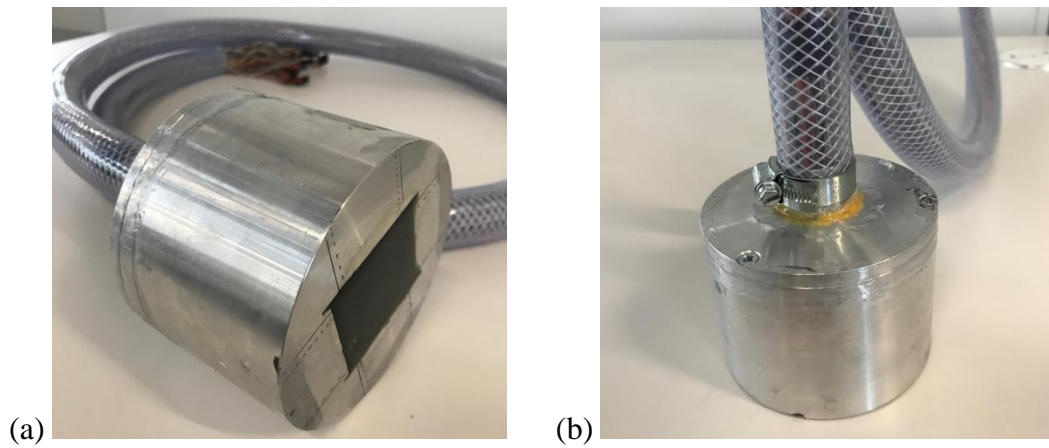


Figure 4.26 Appearance of the fibre CECAT prototype transducer from different angles.

4.3. Prototype Transducers Characterisation

4.3.1. Electrical Impedance Response

The electrical impedance response of all array elements has been measured before bonding to the flexible PCB. The active layers were air loaded when doing the measurement to minimise damping to the array elements. The results are shown in Figure 4.27. As shown in the Figure, for each active layer, the response lines vary within a limited range. Another thing to be noticed is that, the CECAT_79 has the highest electrical impedance while the C13_79 has the minimum one, which indicates that the C13_79 would perform the best in terms of the sensitivity. This prediction has been proved by the pulse-echo tests, which will be discussed later in Section 4.3.3.

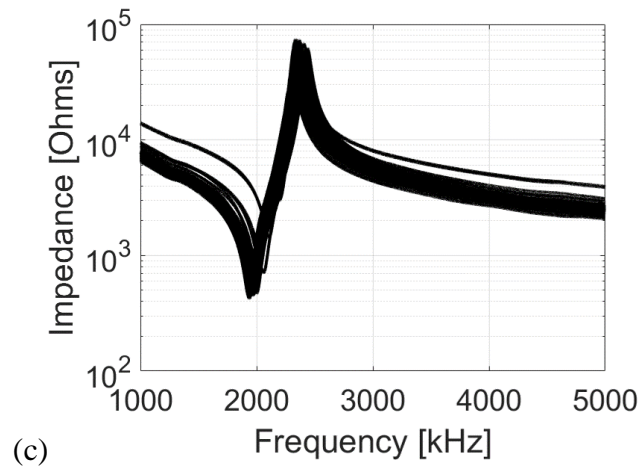
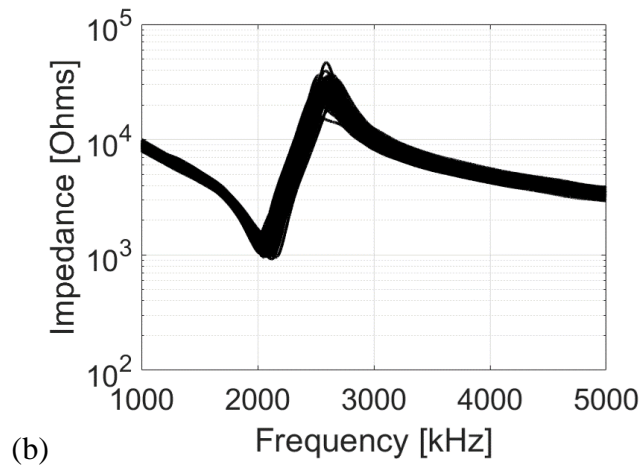
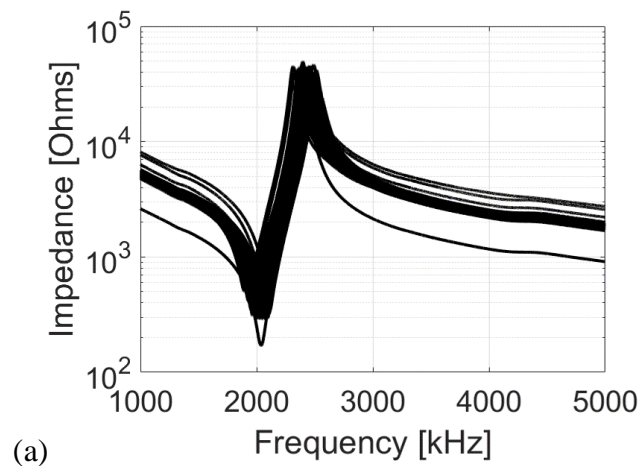


Figure 4.27 Impedance response of all array elements for (a) the C13_79 active layer, (b) the CECAT_79 active layer and (c) the C13_106 active layer.

Three parameters are measured and recorded based on the impedance response results: f_e , f_m , and k_t . These parameters have been used to evaluate the uniformity for each active layer. The averaged experimental values for each parameter are listed in Table 4.1. As shown in the table, the CECAT_79 and the C13_79 have similar f_e , while the CECAT_79 has higher f_m than the C13_79. This situation is associated with the better performance of the CECAT_79 in terms of the averaged experimental k_t of all the elements (0.64 to 0.59). Compared to the C13_79, although the C13_106 has lower values in both f_e and f_m , the performance of these two active layers, which have the same 1-3 composite microstructure, in terms of k_t , are the same.

For each parameter, a tolerance interval, as listed in Table 4.1, is created taking $\pm 5\%$ of the mean value to evaluate the uniformity of the array elements. This tolerance level has been selected based on the results shown in Figure 4.29, Figure 4.30, and Figure 4.31, which utilise the element numbering system shown in Figure 4.28 and illustrate the recorded parameters for each individual array element in the CECAT_79, the C13_79, and the C13_106, separately. Table 4.2 lists the number of array elements, in each active layer, falls outside the tolerance interval for each parameter. The results show that more than 95% of the array elements in all three active layers are performing within the tolerance interval.

The standard deviation results shown in Table 4.1 indicate that the C13_106 has the best uniformity in terms of f_e and f_m , while the C13_79 performs the best in k_t . The results also show that the CECAT_79 has better uniformity in terms of f_e and f_m , while the array elements in the C13_79 perform better in k_t .

Table 4.1 Analysed parameters for all three active layers

Parameters		CECAT_79	C13_79	C13_106
f_e [kHz]	<i>Ave</i>	2061	2030	1959
	<i>Std</i>	33.6	39.4	26.3
	Tolerance Interval	[1958, 2164]	[1929, 2132]	[1861, 2058]
f_m [kHz]	<i>Ave</i>	2587	2440	2352
	<i>Std</i>	43.5	44.5	21.5
	Tolerance Interval	[2458, 2716]	[2318, 2562]	[2234, 2470]
k_t	<i>Ave</i>	0.64	0.59	0.59
	<i>Std</i>	0.014	0.007	0.014
	Tolerance Interval	[0.61, 0.67]	[0.56, 0.62]	[0.56, 0.62]

Table 4.2 Number of array elements outside of the tolerance intervals for all three active layers

Device	f_e	f_m	k_t
CECAT_79	0	1	3
C13_79	1	2	0
C13_106	3	0	4

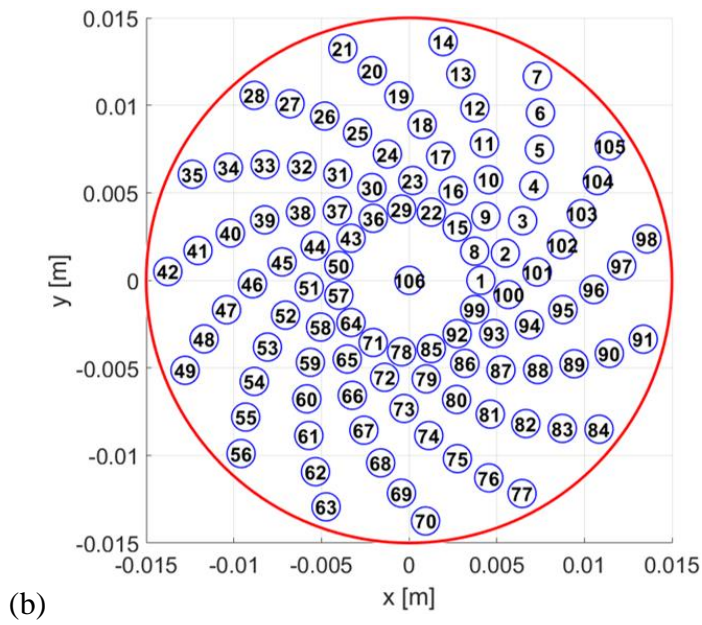
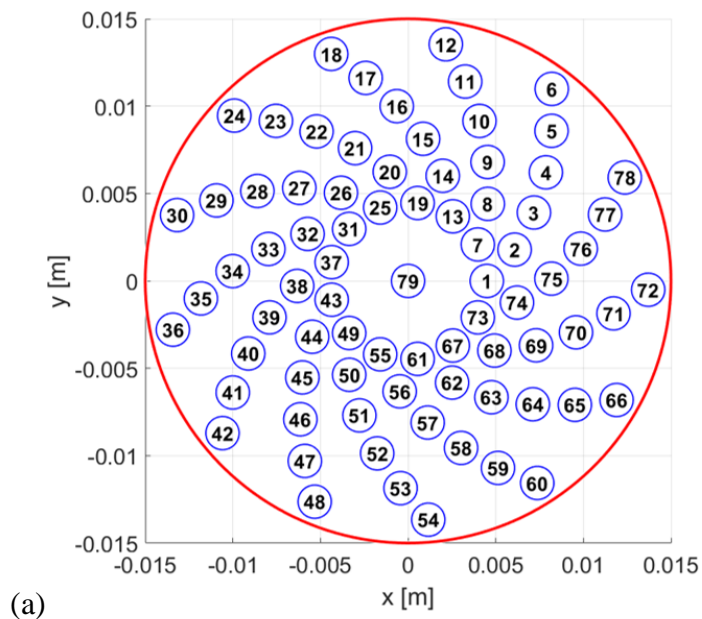
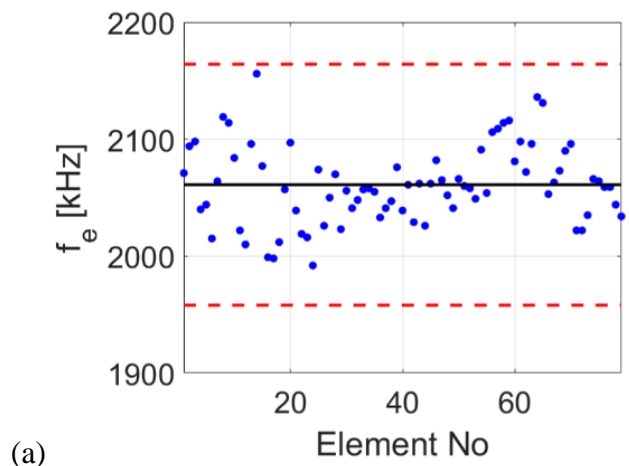
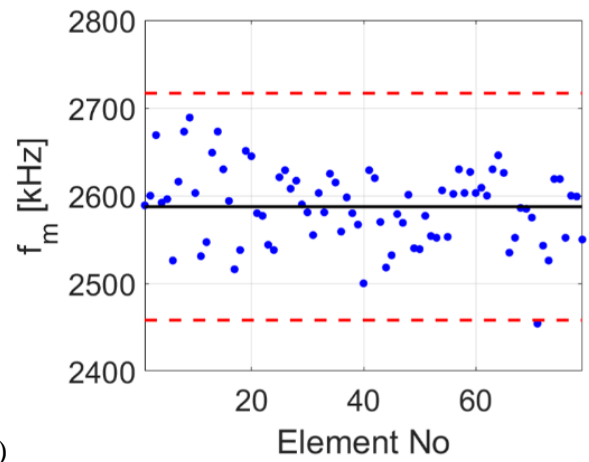


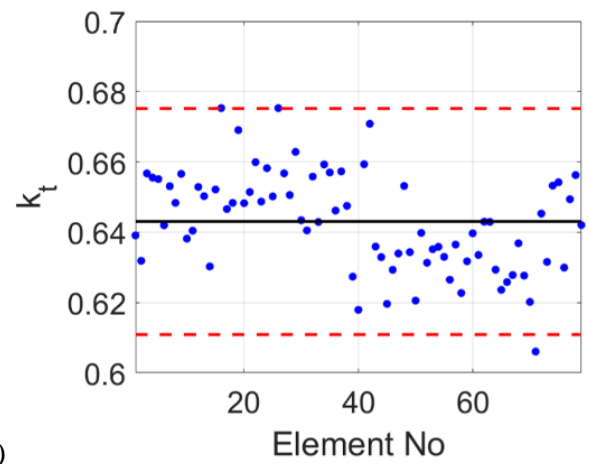
Figure 4.28 Illustration of the element numbering scheme for (a) the 79-element array configuration and (b) the 106-element array configuration.



(a)

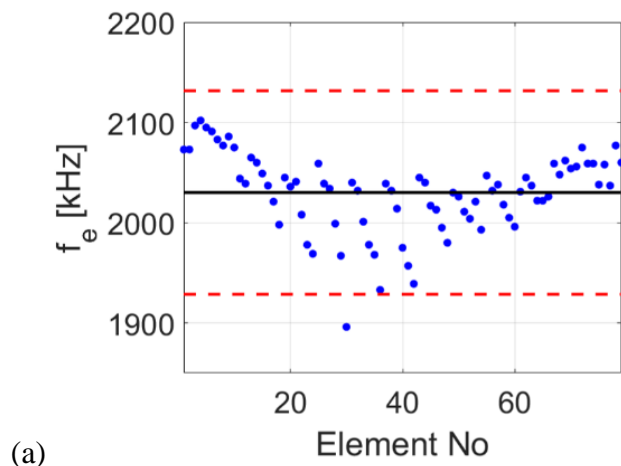


(b)

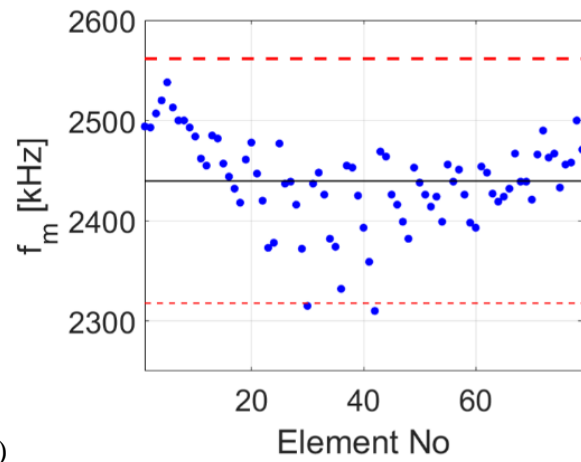


(c)

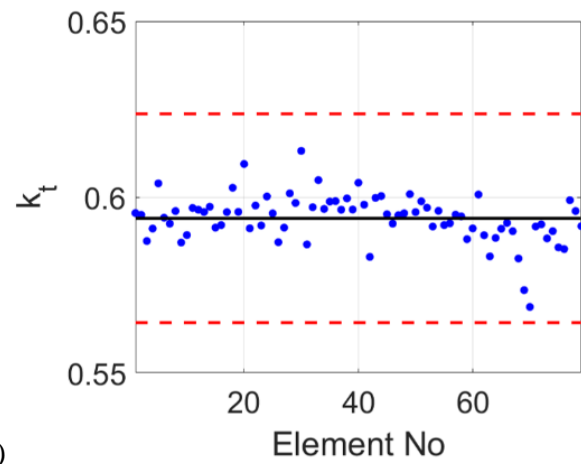
Figure 4.29 (a) f_e , (b) f_m and (c) k_t of all 79 array elements for the CECAT_79 active layer. The black solid lines represent the mean values, while the red dash lines represent the $\pm 5\%$ bars.



(a)

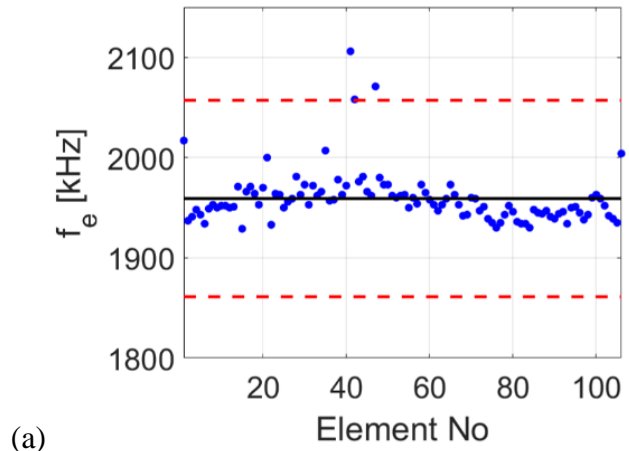


(b)

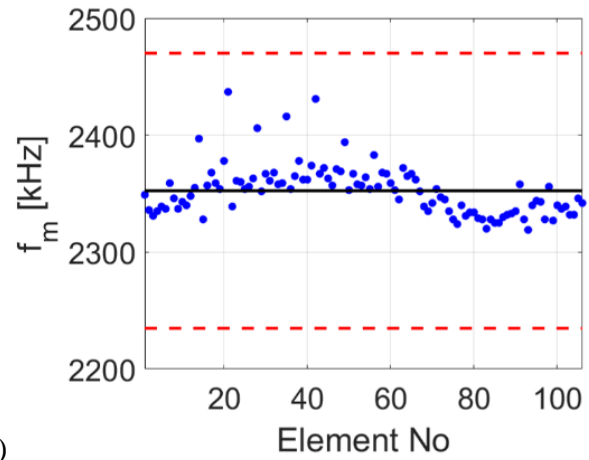


(c)

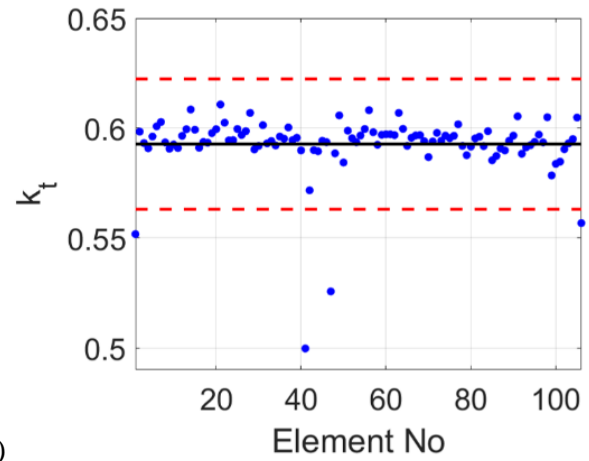
Figure 4.30 (a) f_e , (b) f_m and (c) k_t of all 79 array elements for the C13_79 active layer. The black solid lines represent the mean values, while the red dash lines represent the $\pm 5\%$ bars.



(a)



(b)



(c)

Figure 4.31 (a) f_e , (b) f_m and (c) k_t of all 106 array elements for the C13_106 active layer. The black solid lines represent the mean values, while the red dash lines represent the $\pm 5\%$ bars.

4.3.2. Mechanical Cross-Talk Between Neighbouring Array Elements

The cross-talk between neighbouring array elements has been measured using a 3D Laser Doppler Vibrometer (LDV) (Polytec Inc, Waldbronn, Germany). The measurement has been conducted with the active layer, the PCB, the twisted wires packaged in the housing and the matching layer attached. The experimental setup is shown in Figure 4.32. The transducer was placed on a platform with the front face of the transducer (i.e. the ground side of the active layer) in parallel to the laser source. The laser source was set to focus on the matching layer. Reflected laser signal was captured and analysed by the LDV.

An internal source of the LDV was used to drive the array element. For each scan, only one array element was fired. The electrical energy would be converted into mechanical energy, which would cause vibration of the active layer. Thus, the laser energy reflected from the transducer under test would contain information about the vibrational characteristic of the active layer. The reflected signal would be analysed to get the displacement of the active layer. This information can then be used to evaluate the cross-talk between the fired array element and its neighbouring array elements.

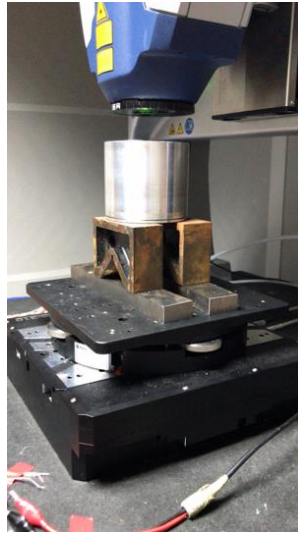


Figure 4.32 Illustration of the experimental set up for cross-talk measurement.

Recalling the 79-element array pattern illustrated in Figure 3.27(a); there are 13 arms with six elements in each arm, plus an element in the centre. Thus, there are seven types of element neighbouring situations in which mechanical cross-coupling should be investigated. Similarly, for the 106-element array pattern illustrated in Figure 3.24(a), there are 7 elements within each arm and 1 element in the centre, which means there are eight types of element neighbouring situations to be investigated. Since the array definition side of the active layer is packaged inside the housing, it was challenging to accurately identify the actual location of each array element with respect to the laser source on the matching layer surface. Here, the mask, which has been used to apply electrodes, was used to determine the approximate locations of the array elements. Aiming to minimise the scanning time, as opposed to scanning the entire active layer, only regions covering the fired element and its neighbouring elements, an example is shown in Figure 4.33, was scanned. The scanning point which has the maximum

displacement is assumed to be the centre of the corresponding fired array element. The cross-talk contours shown in this work indicate the degree of mechanical cross-talk into areas in which adjacent elements are located. As shown in Figure 4.33, for each array pattern, array element in an arm (arm 3 for the 79-element array pattern; arm 1 for the 106-element array pattern) plus the centre element have been scanned.

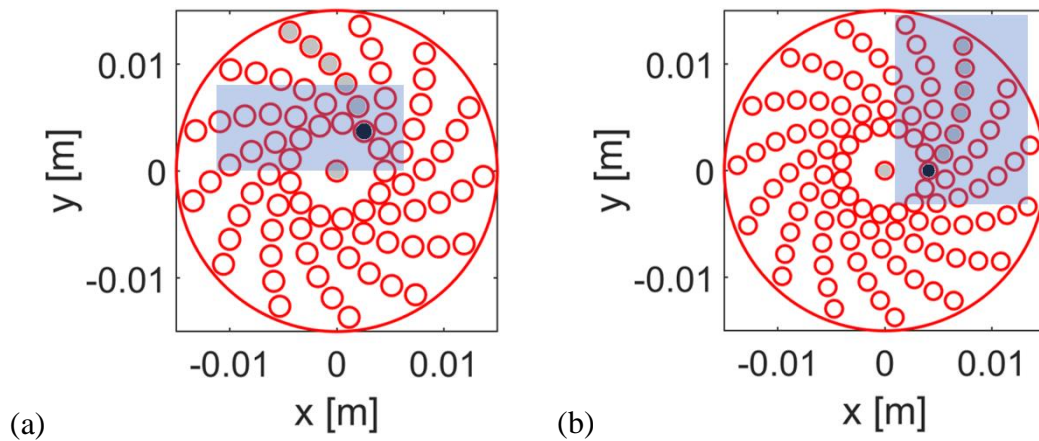


Figure 4.33 Illustration of how the LDV scanning has been processed for (a) the 79-element array pattern and (b) the 106-element array pattern. The black circle represents the fired array element, and the blue block represents the area that has been scanned. The grey circles represent the array elements which will be fired individually later.

Figure 4.34 and Figure 4.35 show the mechanical cross-talk contours in dB with a step size of 10 dB for the CECAT_79 and C13_79 respectively, when firing the central element and the elements in arm 3 individually. The mechanical cross-talk contours for the C13_106 are shown in Figure 4.36. The maximum cross-talk levels in the neighbouring elements for each transducer when firing different array elements are listed in Table 4.3. The results indicate that the CECAT_79 has a -10 dB lower maximum

cross-talk level than the C13_79, which indicates that the C13_79 might have more distorted directivity pattern. However, for both transducers, in all the element adjacent situations, the area with the maximum cross-talk corresponds to a small footprint. The mechanical cross-contours also indicate that the C13_79 has a smaller active aperture compared to the CECAT_79. This indicates that the C13_79 could achieve a better lateral resolution at a deeper distance inside the loading material. Moreover, the increase in active aperture will cause reduce in maximum steering angle, which will lead to higher noise in TFM images. The directivity pattern distortion and the better lateral resolution have been proved by results shown later in Section 6.2.

For the C13_106, the maximum cross-talk in the neighbouring elements is -10 dB, which is the same as the C13_79. However, taking -20 dB as the threshold, it can be clearly observed from Figure 4.35 and Figure 4.36 that there are more neighbouring elements effected by the fired element in the C13_106 than that of the C13_79. This is because the 106-element array pattern is more compact compared to the 79-element design.

Table 4.3 Maximum cross-talk level (dB) for all three prototype transducers

Fired Element		Prototype Transducer		
The n^{th} element in the arm (from centre to the sides)	n	CECAT_79	C13_79	C13_106
	1	-20	-10	-10
	2	-20	-10	-10
	3	-20	-10	-10
	4	-20	-10	-10
	5	-20	-10	-10
	6	-30	-20	-20
	7	NA	NA	-30
Centre element		-40	-40	-30

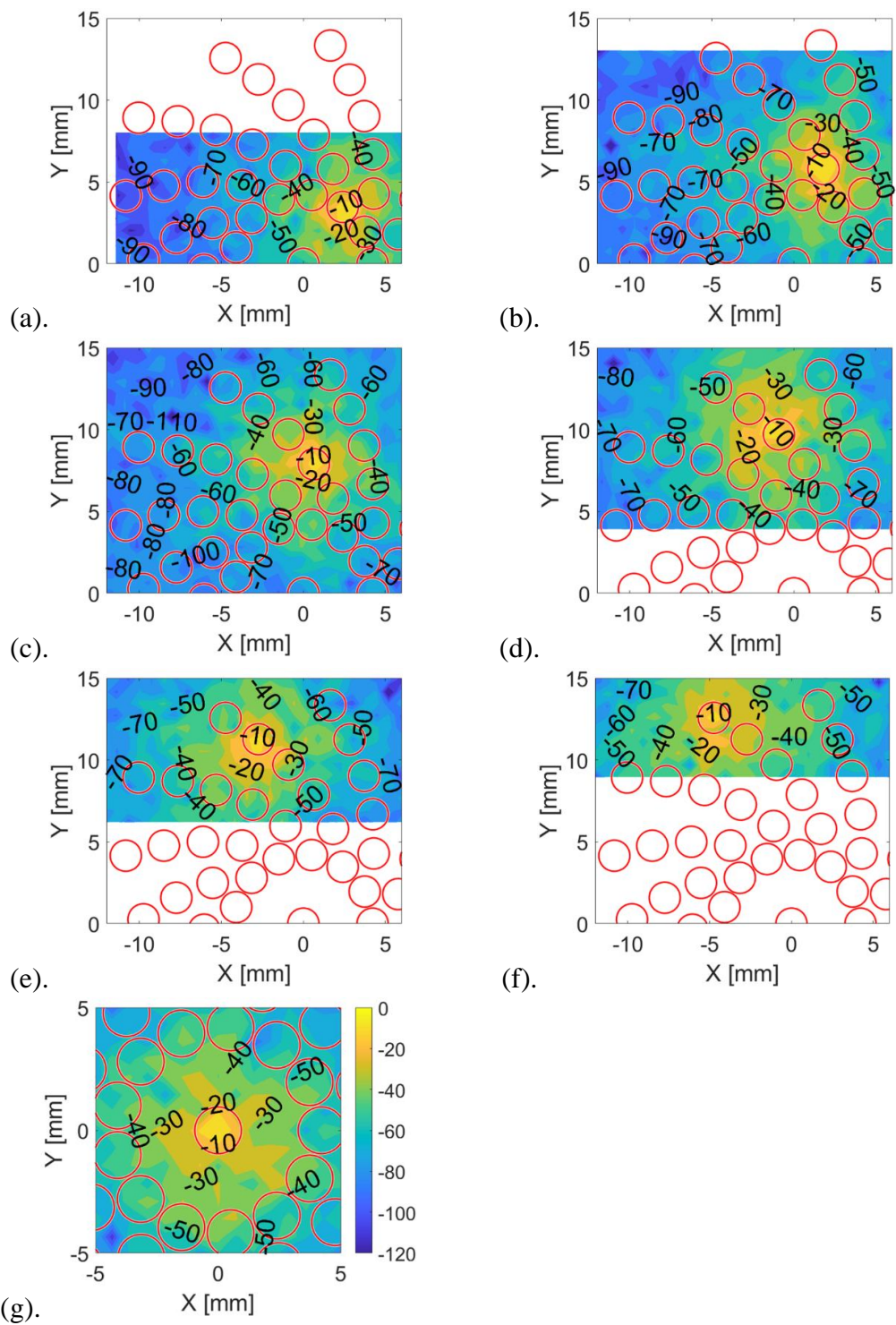


Figure 4.34 Mechanical cross-talk contours for the CECAT_79 when firing the central element and the elements in the 3rd arm individually. (a) is the first element in the arm through to (f) being the outer most element in the arm, with (g) presenting the centre element result. The red circles represent the theoretical position of the neighbouring elements.

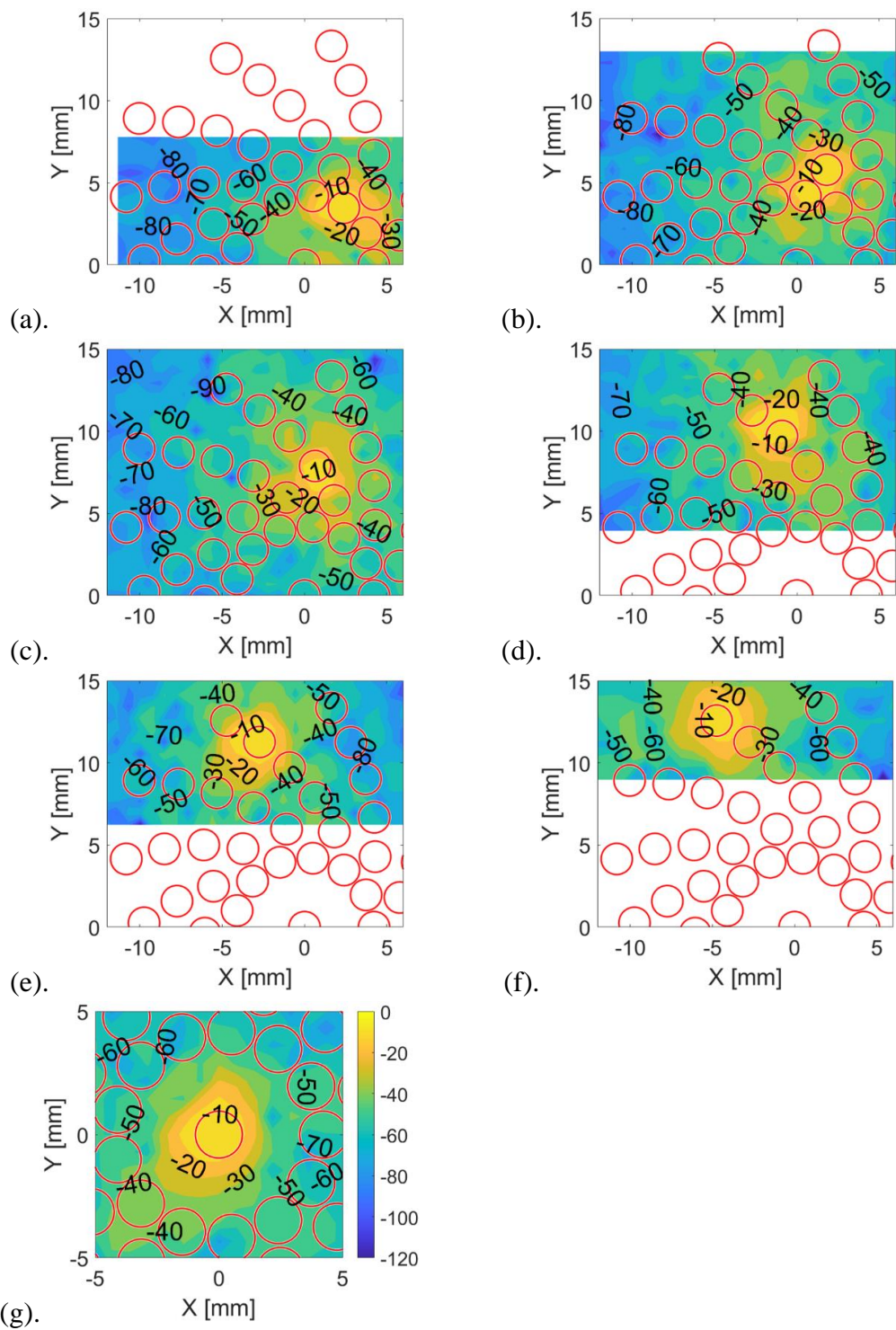


Figure 4.35 Mechanical cross-talk contours for the C13_79 when firing the central element and the elements in the 3rd arm individually. (a) is the first element in the arm through to (f) being the outer most element in the arm, with (g) presenting the centre element result. The red circles represent the theoretical position of the neighbouring elements.

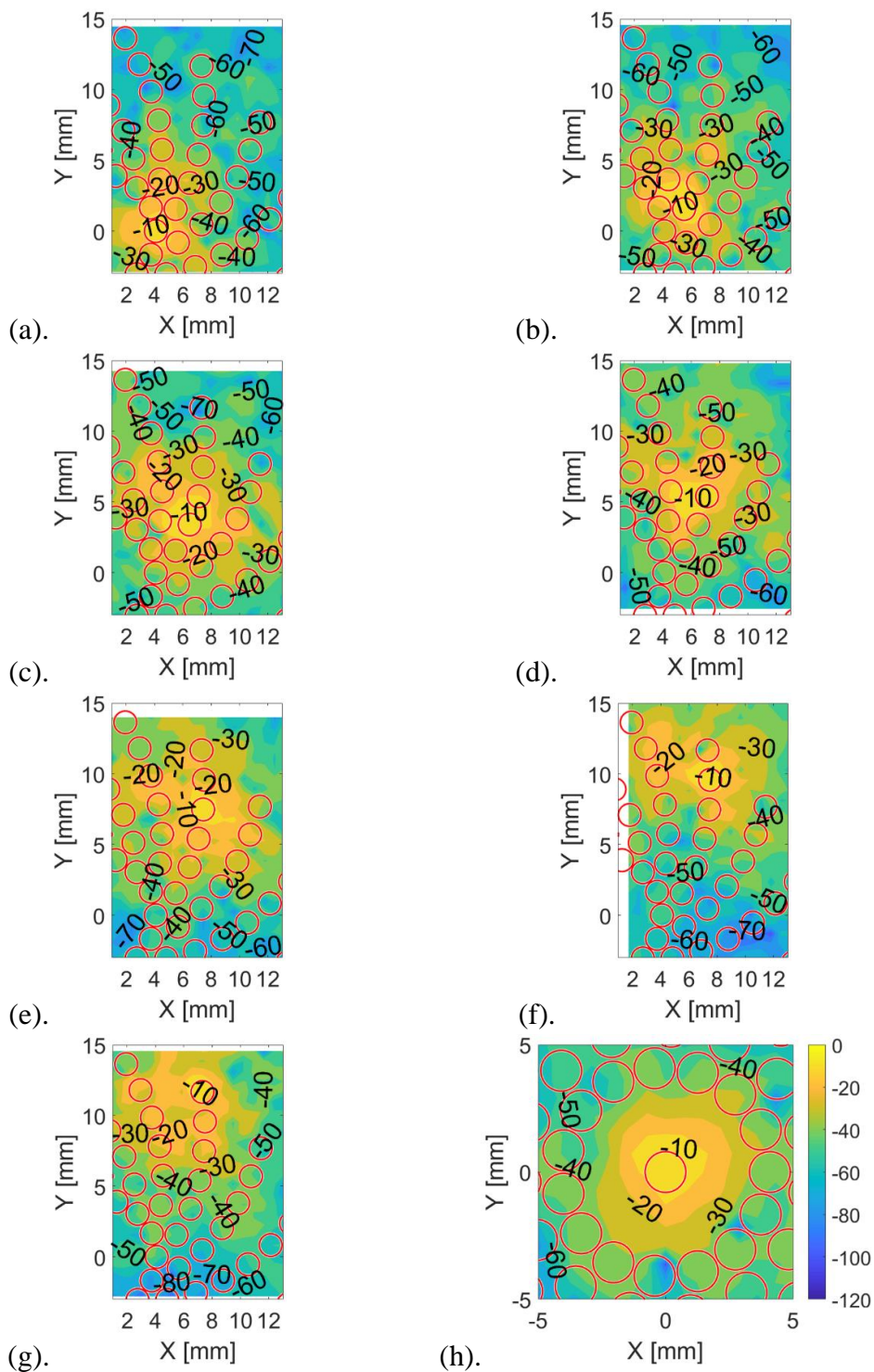


Figure 4.36 Mechanical cross-talk contours for the C13_106 when firing the central element and the elements in the 1st arm individually. (a) is the first element in the arm through to (g) being the outer most element in the arm, with (h) presenting the centre element result. The red circles represent the theoretical position of the neighbouring elements.

4.3.3. Pulse-Echo Test

Figure 4.37 illustrates the setup for the pulse-echo test, which will provide characterisation of the transducer sensitivity, bandwidth and pulse-length. A glass block was placed at the bottom of a tank, working as a reflector. The transducer was attached to a mechanical holder, which was supported on the top edges of the water tank such that the front surface of the transducer was parallel with the glass block. As the transducer was manually placed into the holder, the distance between the front surface of the transducer and the top surface of the glass block was not consistent between all experiments, but was nominally around 105 mm. The effect on receiving signals' intensity caused by the variation of the distance between the transducer front surface and the glass block is negligible since the attenuation of sound in water is 0.0087 dB/cm [118]. The transducer is connected to a phased array controller, FIToolbox (Diagnostic Sonar Ltd, UK), through an in-house adaptor, as shown in Figure 4.20, to achieve individual control of each array element. A 2 MHz half-cycle sine wave with 80V amplitude is generated from the FIToolbox to drive each array element. The first received echo is recorded and analysed to evaluate the performance metrics for each transducer.

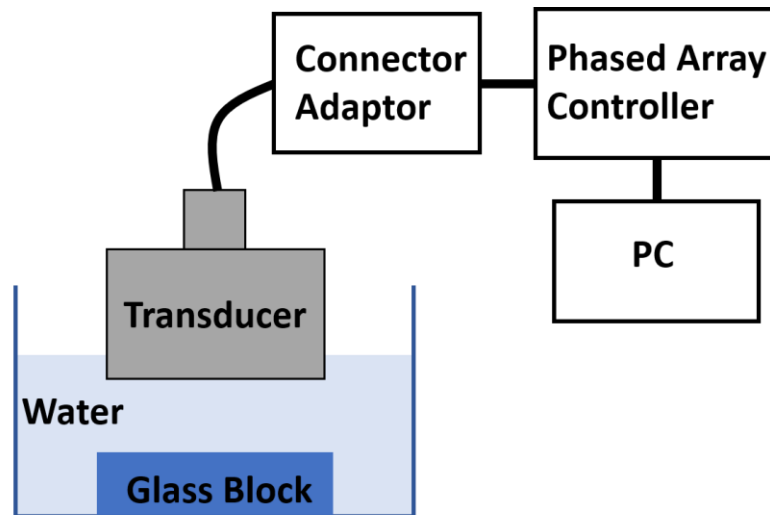


Figure 4.37 Pulse echo test setup.

Pulse-echo responses were successfully acquired from all the 79 array elements from the C13_79, with three array elements from the CECAT_79 failing to record a satisfactory response. Figure 4.38 and Figure 4.39 present the pulse-echo response and corresponding spectrum of the centre element from the CECAT_79 and the C13_79 separately. As shown in the figures, the element with fibre CECAT structure has shorter -20 dB pulse length and broader bandwidth, which indicates better resolution, while the C13 element performs better concerning sensitivity, i.e. the peak-to-peak amplitude (V_{pp}).

Receiving signals for all the 106 array elements from the C13_106 have been successfully captured and Figure 4.40 presents the pulse-echo response and spectral characteristics of the centre element from this device. As illustrated in this Figure, there are two resonance modes, one around 1.5 MHz, the other around 2 MHz. The former occurs after applying the matching layer. The latter is the resonance frequency when the

active layer is working under thickness mode. This situation is believed to be related to the manufacturing error of the matching layer. As the material used for the matching layer was flowable and required a curing process, which would contain shrinkage, the final thickness of the matching layer could not be accurately controlled. Thus, the variety in the thickness would have caused the extra resonance in the C13_106.

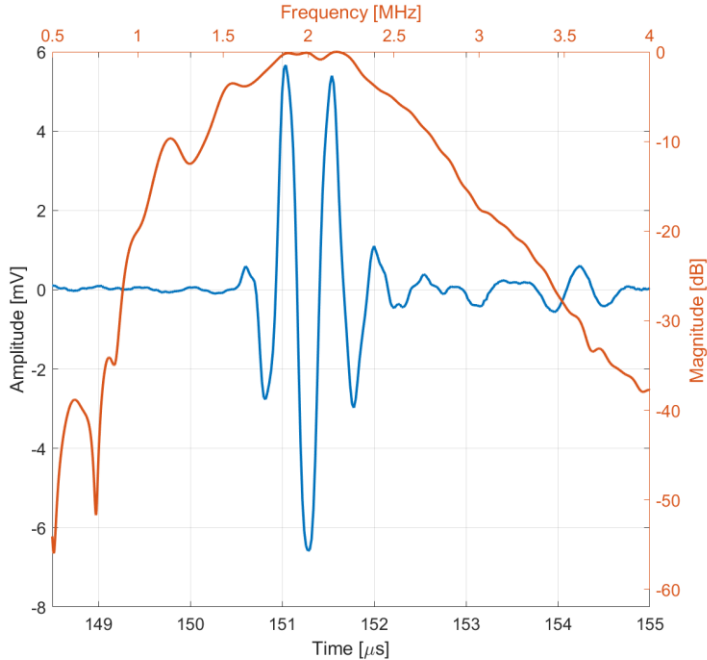


Figure 4.38 Pulse echo response of the centre element for the CECAT_79.

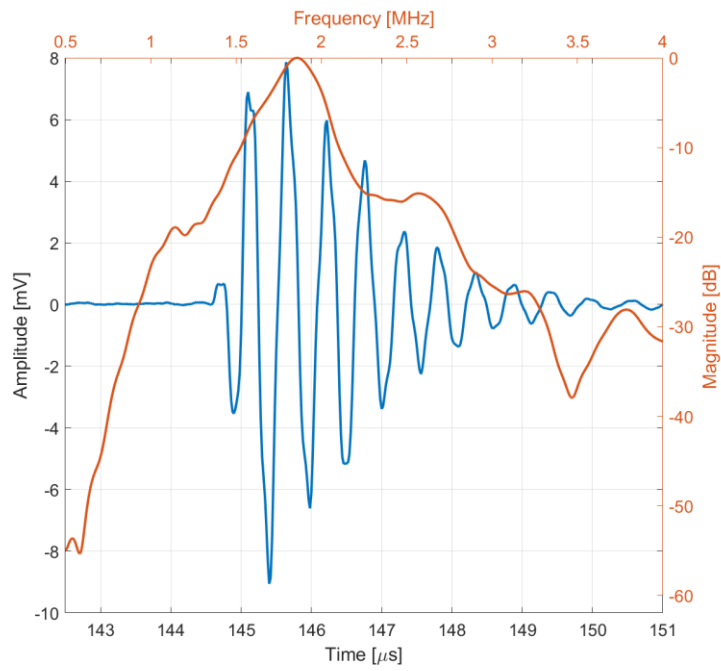


Figure 4.39 Pulse echo response of the centre element for the C13_79.

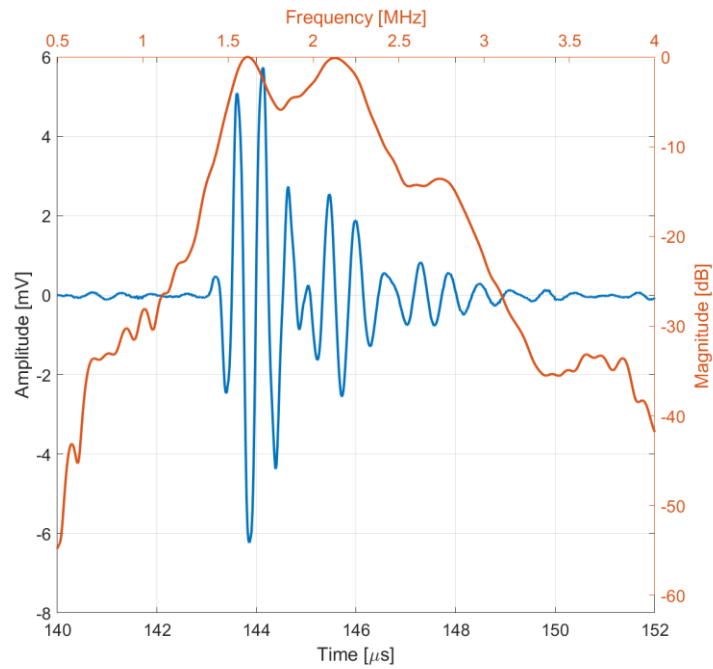


Figure 4.40 Pulse echo response of the centre element for the C13_106.

Table 4.4 lists the average values and the standard deviations of central frequency, -20 dB pulse length, bandwidth, and V_{pp} for all the working array elements in each transducer. The standard deviations indicate that the CECAT_79 has better utility than the C13_79 in terms of pulse length and V_{pp} , while the C13_79 performs better in centre frequency and bandwidth. The centre frequency is 1.95 MHz for the CECAT_79 and 1.86 MHz for the C13_79. Both are slightly lower than 2 MHz desired working frequency. The relationship between these two transducers in terms of the averaged pulse length and averaged bandwidth are the same as indicated in Figure 4.39 and Figure 4.40. The averaged V_{pp} is 11.17mV for the CECAT_79, which is lower than the 16.67mV for the C13_79. The results indicate that the CECAT_79 has better spatial resolution, while the C13_79 performs better in terms of sensitivity.

The standard deviations for the C13_79 are better in terms of centre frequency and pulse length when compared to that of the C13_106, while become slightly higher in bandwidth and V_{pp} . The averaged central frequency for the C13_106 is 2.01 MHz which is the closest as the desired working frequency. The averaged V_{pp} for the C13_106 is slightly lower than that of the C13_79 (14.89mV to 16.67mV). This is caused by the reduced element size of the 106-element array pattern. The averaged bandwidth is 23.3%, which is narrower than that of the other two transducers. This is caused by the extra mode happens near the thickness mode. Except for reducing the bandwidth, this extra mode will also affect the imaging performance of the C13_106 in terms of axial resolution, as it will lead to a second reflection. This will be discussed in more detail in Chapter 6.

Figure 4.41 show the pulse-echo response spectra for all the array elements in each prototype transducer. As indicated in the figures, for all three transducers, most of the pulse-echo spectra are varying within a limited range, with a few spectrums behave differently. The results further prove that the prototype transducers have achieved appropriate uniformity. Moreover, the differences in performance between the CECAT_79 and the C13_79 can be related to the difference of micro-structure.

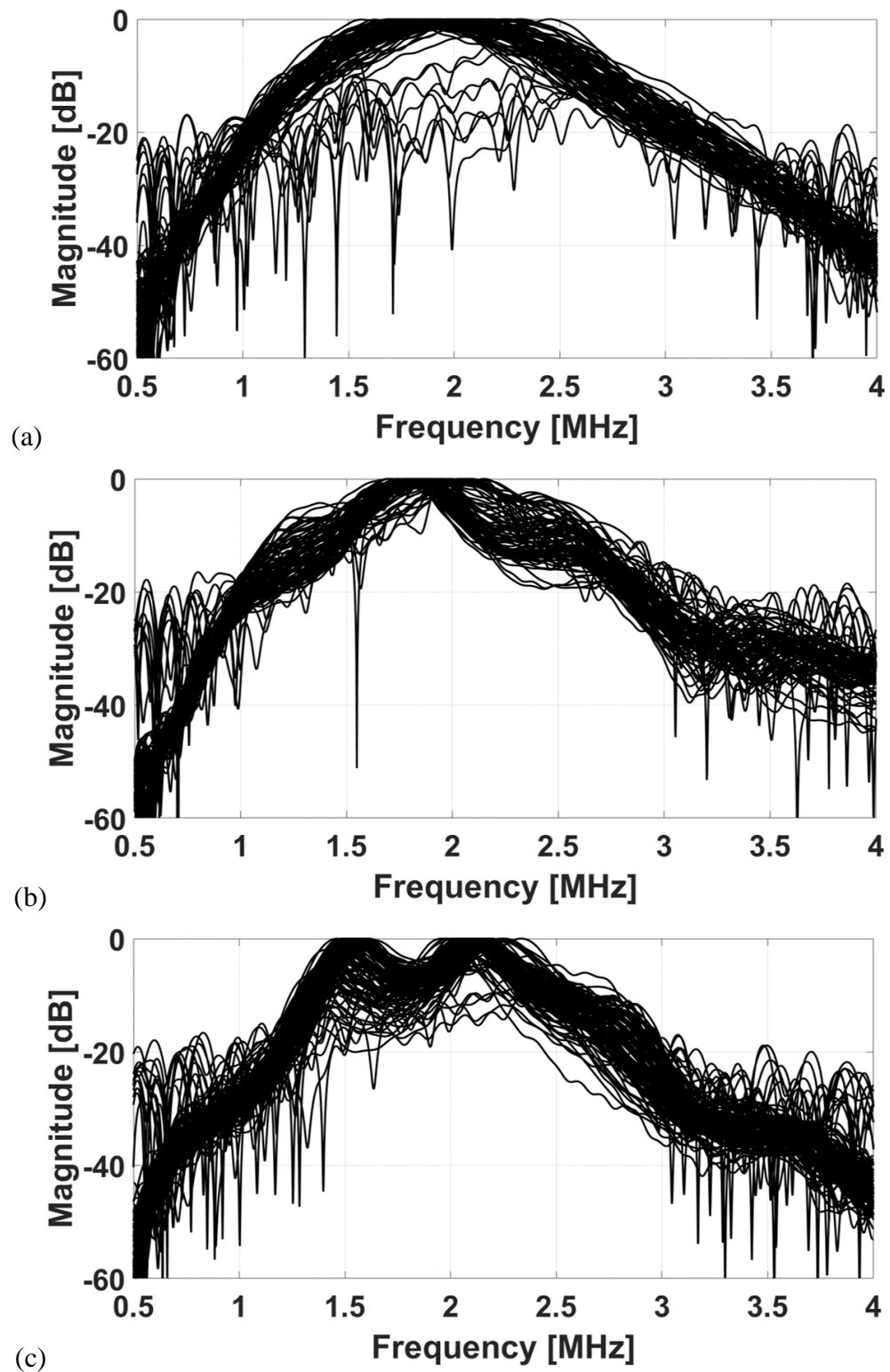


Figure 4.41 Pulse-echo response spectrum for all elements in (a) the CECAT_79, (b) the C13_79, and (c) the C13_106.

Table 4.4 Pulse-echo response for all three prototype transducers

		Centre Frequency [MHz]	Pulse Length [μs]	Bandwidth [%]	V_{pp} [mV]
CECAT_79	<i>Ave</i>	1.95	1.72	47.44	11.17
	<i>Std</i>	0.20	0.40	15.63	4.32
C13_79	<i>Ave</i>	1.86	2.67	30.95	16.67
	<i>Std</i>	0.10	0.62	10.27	6.65
C13_106	<i>Ave</i>	2.01	2.31	23.30	14.89
	<i>Std</i>	0.26	1.16	9.80	6.23

4.4. Summary

Three prototype transducers, one with fibre CECAT structure and the other two with the 1-3 piezocomposite structure, have been manufactured using the sparse array patterns designed in Chapter 3. The overall manufacturing processes for these three transducers are similar, with the main difference being the manufacturing method for the active layers. The current manufacturing process of the fibre CECAT active layer requires manually inserting the PZT fibres, which is time-consuming. However, for the fibre CECAT active layer, one manufacturing process can provide multiple pieces of active layers, while for the piezocomposite active layer, typically, only one piece of the active layer can be achieved from one manufacturing process. Incorporating a flexible PCB and conductive epoxy has made it easier to create an electrical connection between the array elements and external cables/adaptors. Overall, the manufacturing process for these 2D array configurations has produced completed devices with large housing dimensions, but this is not particularly an issue in this proof of concept stage in the development cycle.

The prototype transducers have been characterised using three experimental tests: electrical impedance response test; mechanical cross-talk test; and pulse-echo characterisation. Results from the impedance response tests show that the utility of array elements is in a good level for all three active layers, while the averaged k_t for the fibre CECAT active layer is slightly higher than that of the C13 piezocomposite active layers. Results from the LDV scanning show that the cross-talk level between neighbouring array elements is lower overall for the fibre CECAT structure, with the higher array element density associated with the 106-element array producing the poorest mechanical cross-talk result. Pulse-echo tests show that the CECAT_79 performs best in terms of pulse length and bandwidth, while both piezocomposite transducers demonstrate a higher sensitivity. For the C13_106 pulse echo test, an extra mode is observed close to the main thickness mode, as a result of the application of the matching layer.

Chapter 5

Development of Image Processing Algorithms

5.1. Introduction

As mentioned in Chapter 1, this project was initially motivated to reduce the operator dependency of current transcranial ultrasound techniques. In addition to the 2D sparse array transducer to provide more flexibility for transcranial imaging, an image processing algorithm that could automatically detect anomalies in the blood vessel is also of interest. As this project is at the proof of concept stage, instead of using complex biomedical phantoms to simulate the anomalies, the anomaly has been simply defined as solid particles that appear in the vessels. Two image processing algorithms have been developed based on data collected from imaging a simple tube-tank phantom; one is to measure the size of the tube, the other is to detect the particles and estimate their size. This Chapter explains the development process of these algorithms in detail and presents the preliminary results of their application.

5.2. Data Acquisition

A laboratory experimental setup, called the tube-tank phantom, has been made to represent a simple model of a blood vessel. Figure 5.1 illustrates this setup for imaging the tube-tank phantom. A plastic tube with a 3.5 mm inner diameter is positioned within a plastic tank that has been filled with water, with the tube located parallel to the transducer front face by feeding the tube through two aligned holes in a plastic frame. One end of the tube is placed underwater within a separate water tank, while the other end is connected to a syringe that is used to create a water flow through the tube. A 2.25 MHz, which is close to the desired 2 MHz working frequency in this project, 1D linear array transducer with 128 elements (Vermon, Tours, France) is used to image the tube-tank phantom. This transducer was used to provide array imaging capability to feed into the image processing development stage of the work, while the sparse 2D arrays discussed in Chapters 3 and 4 were being developed. The transducer is placed above the tube and in parallel with the bottom surface of the tank. The FIToolbox is used to control the transducer to collect data using the Full Matrix Capture (FMC) method under a sampling frequency of 50 MHz. The FMC data is then processed using the Total Focusing Method (TFM) to generate the image of the detected area. Taking the sound velocity in water (1480 m/s [119]) and the sampling frequency into consideration, the resolution of the TFM image should be no smaller than 0.015 mm, which is the minimum distance that the sound wave could travel within a single sampling period.

The experiment started by imaging the tube with only water inside. Then, ball bearings with diameters of 1 mm, 1.5 mm, and 2 mm are placed at various positions inside the

tube corresponding to the imaging area covered by the transducer aperture. The concept here is to consider scenarios with and without artefacts within a blood vessel.

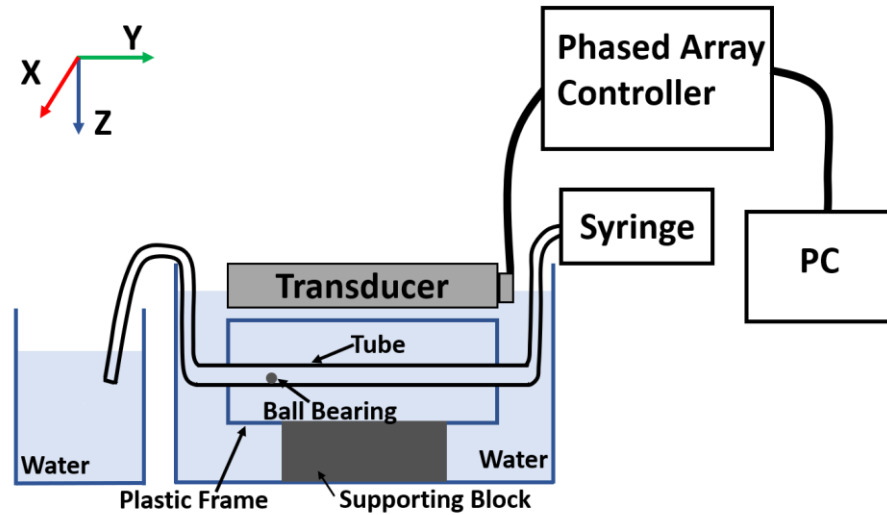


Figure 5.1 Illustration of the experimental setup for imaging the tank-tube phantom using the 2.25 MHz 1D linear Array transducer.

5.3. Development Process of the Tube Size Estimation

Algorithm

Figure 5.2 shows an example TFM image of the tube with no particles from the 1D Linear Array Transducer. The TFM image is displayed in decibels within range -30 dB to 0 dB. The imaging area is 10 mm in height (z -axis) and 100 mm (y -axis) in width so that the image could cover the full tube and match the transducer aperture size. The image resolution is 0.05 mm in z -axis and 0.1 mm in y -axis, which is a compromise between the image quality and the data processing time. Because increasing image resolution will cause an increase in the pixel numbers, which will eventually lead to long

data processing time. This gives the size of the image in pixels as 201x1001, i.e., 201201 pixels in total.

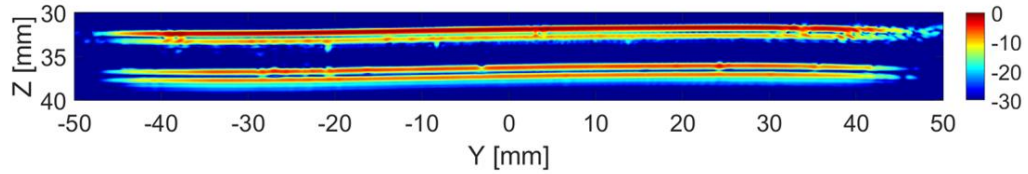


Figure 5.2 TFM image of the tube with no particles from the 1D linear array transducer.

During the image processing, all the TFM images are converted into greyscale images with pixel intensity varying between 0 and 1 (with 256 levels) so that image processing algorithms could be applied to analyse objects contained in the images. The conversion can be expressed as:

$$I_{Gray} = \left\lfloor \frac{I_{TFM} - I_{TFM_min}}{(I_{TFM_max} - I_{TFM_min})/255} \right\rfloor / 255 \quad (5.1)$$

where I_{Gray} and I_{TFM} are the pixel intensity in the greyscale image and the TFM image, separately. I_{TFM_max} is the maximum pixel intensity in the TFM image, while I_{TFM_min} is the minimum one.

In the greyscale image, pixels with an intensity equal to 1 are shown as white in the image, while pixels with an intensity equal to 0 are shown as black. The higher the intensity, the brighter the pixel will be. Here, the greyscale image shown in Figure 5.3(a) will be used, which has been converted from the original TFM image shown in Figure 5.2, as an example to explain the imaging algorithm that has been developed to detect the tube and to estimate its diameter. This image will be referred to as the Original

Frame (*OrgF*) for the rest of this section. Overall, the algorithm consists of three main steps:

1. Determine a threshold to apply on the greyscale image so that the background noise in the *OrgF* can be reduced.
2. Equally split the entire image into several blocks, so that the piece of the tube within each block can be treated as a straight line.
3. Within each block, detect the top and bottom inner walls and estimate the inner diameter of the tube.

As shown in Figure 5.3(b) – a zoomed-in area of the *OrgF*, there are four bright lines in the *OrgF*, which, from top to bottom, represent 1) the top outer wall, 2) the top inner wall, 3) the bottom inner wall and 4) the bottom outer wall of the tube. In addition to these bright lines, there are some pixels within the area between the top inner wall and the bottom inner wall which are representative of the mid-range of the greyscale, with these pixels considered to be noise and likely to have an effect on the detection of the tube (the four bright lines). One way to reduce the effect from these pixels is to set a threshold that could separate the noise from the bright lines. This would make the tube walls become clearer in the image so that they can be more easily detected later using the Hough transform. The thresholding can be expressed as:

$$I_T = \begin{cases} 0, & \text{if } I_{Org} < \textit{Threshold} \\ I_{Org}, & \text{Otherwise} \end{cases} \quad (5.2)$$

where I_{Org} and I_T is the pixel intensity before and after applying the threshold, separately. Thus, the first step of the tube size estimation algorithm is to find a threshold

that can accurately extract the four lines of interest while simultaneously eliminating the noise.

The pixels in the *OrgF* are separated into three groups based on their intensities. The first group contains pixels that have 0 intensity are considered to have no effect on the detection of the bright lines. The second group is for pixels that have intensity larger than -5 dB compared to the maximum pixel intensity (i.e., 1). These pixels are considered to be carrying significant information of the objects in the image, which, in this situation, are the four bright lines. The rest of the pixels are classified as the third group. Some of the pixels in the third group may also carry information of interest, while some others should be treated as noise. Thus, pixels in the third group should be picked selectively. The thresholding is achieved by sorting the pixels in group three in ascending order based on their intensity and reducing the intensity of the first 40% of pixels to 0. The parameters, including the -5 dB and 40%, have been empirically selected. Results that are going to be shown in this Chapter, as well as in Chapter 6, will demonstrate the appropriateness of the parameters selected. However, in other situations, such as when images have high background noise, these two parameters might need to be modified to achieve appropriate performance. The image after thresholding is defined as the Thresholded Frame (*TF*). Figure 5.3(c) and Figure 5.3(d) shows the *TF* and a zoomed-in area of the *TF*, respectively. There are small, but discernible differences when comparing Figure 5.3(b) and Figure 5.3(d), which demonstrate the effect of the thresholding algorithms. The *TF* image has less noise in the area between the tube inner walls, and the wall reflections are sharper, especially for the shadow around the bottom

outer wall. Although, the noise suppression is not very obvious in this example, this is because the commercial transducer used in this process is a dense array with relatively high imaging performance. Thus, the background noise level is not very high in the *OrgF*. However, it was expected that for the prototype array transducers developed in this work, they may have more noisy images due to the sparse array patterns and manufacturing limitations. Hence, it was expected that this thresholding process would be applicable in this work.

As shown in Figure 5.3, the tube curved through the imaging area, which means it cannot be represented by straight lines, and it could be complex to measure the inner diameter of the tube by directly analysing the whole imaging area. Thus, to simplify the analysis process, the Thresholded Frame image is equally divided into ten blocks, each with 10 mm length, as shown in Figure 5.4(a). Figure 5.4(b) shows an example of one of these blocks. Within each block, the tube is assumed to be straight and could be represented by four straight lines. As the tube is placed in *y-axis* (row direction) in the image, for each column in the image block, there should be four points (as shown in Figure 5.4(b)), which represent the positions of the four tube walls. As shown in Figure 5.4(c), the four pixels are located by finding the peak pixels of each column. Then, those four pixels are set to 1, while all the other pixels within that column are set to 0. The same approach has been applied to all columns within the block so that each layer of the tube wall will be represented by a one-pixel wide line.

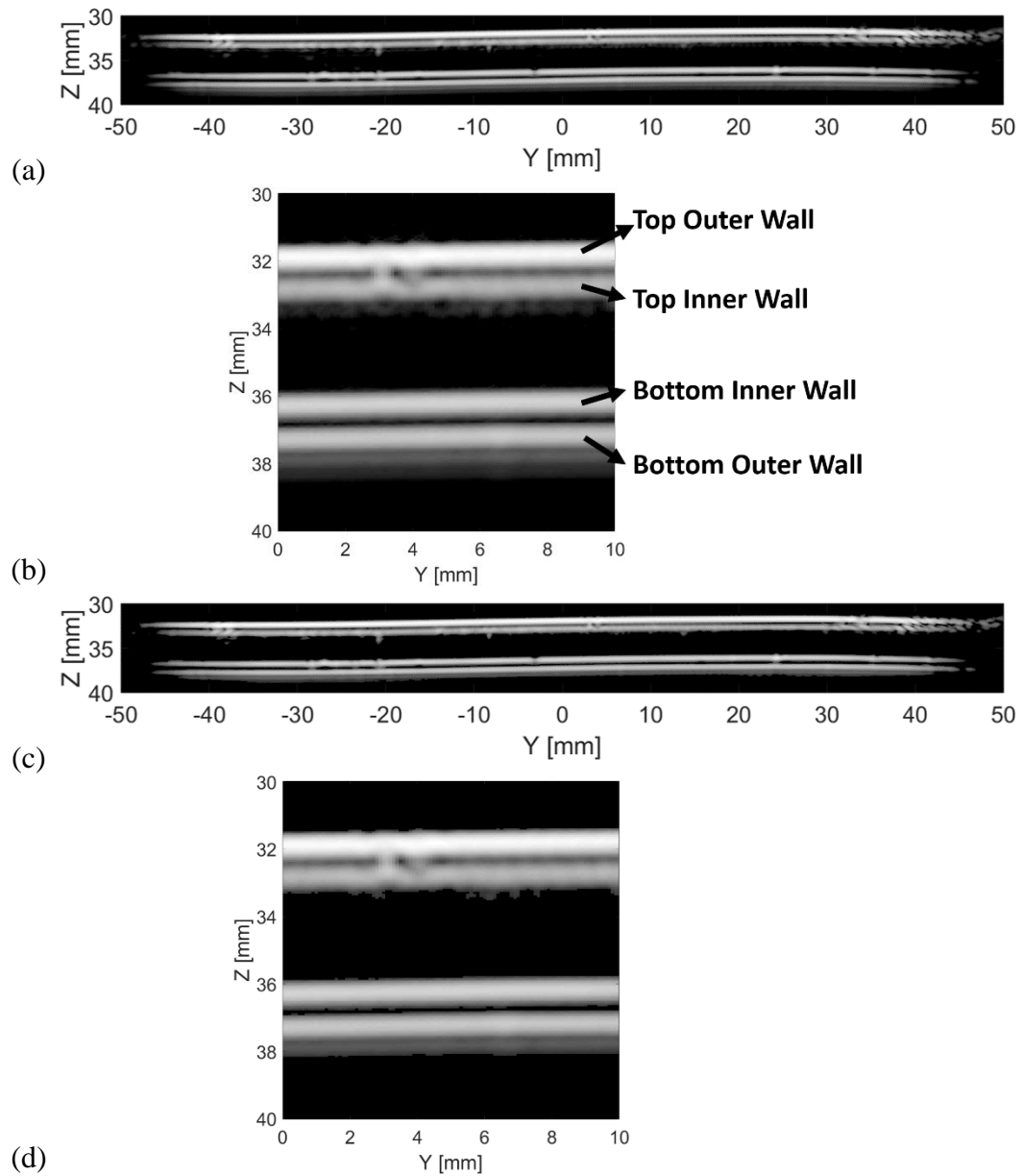


Figure 5.3 (a) The Original Frame (*OrgF*). (b) A zoomed-in area extracted from (a). (c) The Thresholded Frame (*TF*). (d) A zoomed-in area extracted from (c).

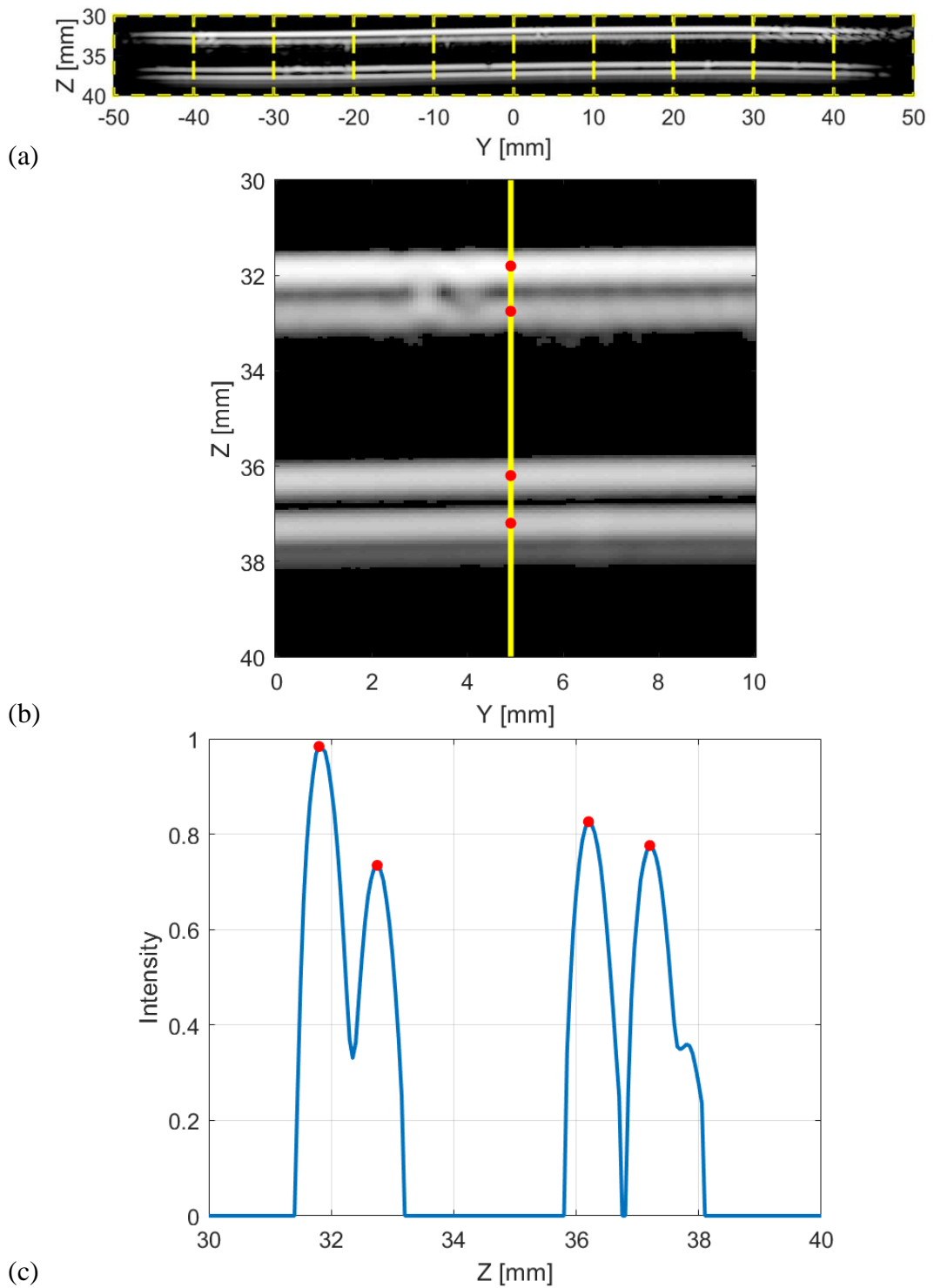


Figure 5.4 (a) Illustration of how the TF has been divided into blocks. The yellow dashed lines represent the block edges. (b) A block picked from the TF. (c) The intensity for the pixels marked using the yellow line, as shown in (b). The red dots are the pixels that have been selected to represent the tube wall.

The peak pixel locating process has been applied column by column across the width of a block and the result is shown in Figure 5.5, where, each part of the tube wall is represented by a white line. This peak locating process has simplified the tube wall structures in the image, which makes it easier for the Hough Transform to detect the tube walls. The Hough Transform has been used to detect the straight lines (l), which are represented by the green lines in Figure 5.5. From top to bottom, the lines are labelled from 1 to 4. Each line is defined by its two endpoints, $pleft$, and $pright$. The inner walls of the tube can be extracted by measuring and comparing the distance between the $pleft$ along the z -axis (dis_pleft):

$$dis_pleft(i) = pleft_z(i + 1) - pleft_z(i), i = 1,2,3 \quad (5.3)$$

where i represents the line number and $pleft_z$ represents the z coordinate of the $pleft$. For the tube used in this project, its wall thickness (1 mm) is smaller than its inner diameter (3.5 mm). Thus, the pair of $pleft$ that gives the maximum dis_left should be the left endpoints of the lines that represent the inner walls, i.e., the $l(2)$ and the $l(3)$. The distance from the middle point of $l(2)$ to $l(3)$ is used to estimate the inner diameter of the tube.

The same processing steps have been applied to all the blocks. Figure 5.6 and Figure 5.7 illustrate the collated results from each block. As shown in the figure, all the results vary closely around the actual inner diameter (3.5 mm). The averaged value of result from all the blocks is 3.47 mm, which is used as the estimated tube size.

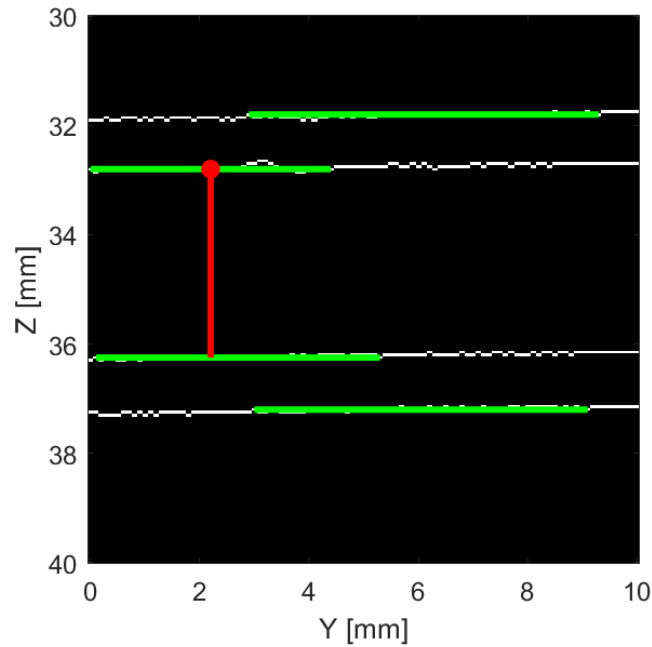


Figure 5.5 The block from Figure 5.4(a) with only the four peak pixels of each column (the white pixels) remaining. The solid green lines represent the tube walls. The solid red line illustrates the distance from the middle point of the detected top inner wall (the red dot) to the bottom inner wall. The estimated inner diameter for the piece of the tube within this block is 3.45 mm.

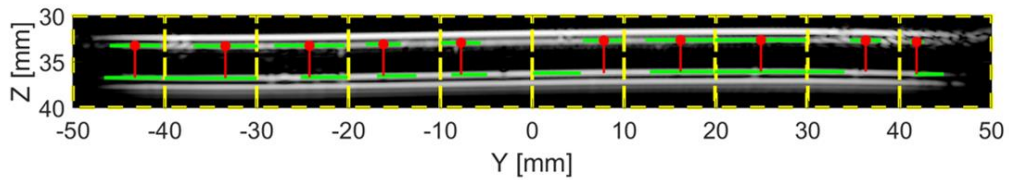


Figure 5.6 The results after applying the tube size estimation algorithm across the entire Original Frame. The yellow dashed lines illustrate the edges of the blocks. The solid green lines are the detected inner walls. The red dots represent the middle point of the corresponding top inner wall, while the solid red lines illustrate the inner diameter estimated for each block.

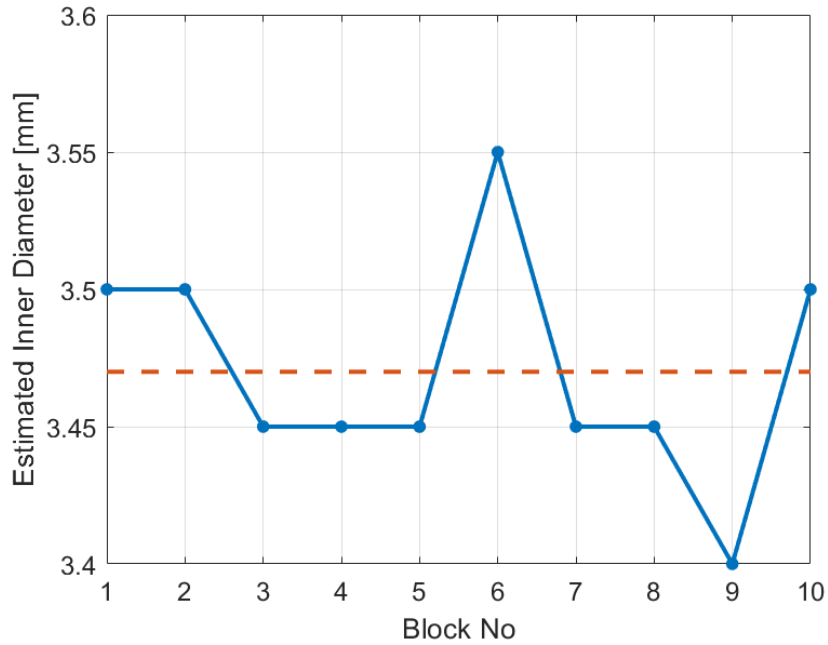


Figure 5.7 The blue line represents the estimated inner diameter for each block. The dashed red line represents the averaged inner diameter of the results, which is 3.47 mm.

5.4. Development Process of the Particle Detection

Algorithm

To simulate the concept of particles travelling through the imaging area, a series of TFM images starting with no particle and then with particles at different positions within the tube have been captured and processed. Again, during the analysis process, all the TFM images have been converted into greyscale images (frames). Figure 5.8 shows a block diagram of the particle detecting algorithm. There are two main objectives of this algorithm, first is to locate the particle(s), and second is to estimate the size of the particle(s) relative to the tube dimensions. Both pieces of information are important

because, in the real stroke diagnosis scenario, the ability to locate and estimate the size of the clot(s) in the blood vessel could help the operator to make a fast and accurate diagnosis. The whole processing approach can be divided into five steps:

1. Creating the Background Frame (*BF*).
2. Generating the Difference Frame (*DF*) based on the Current Frame (*CF*) and the Background Frame (*BF*).
3. Thresholding the Difference Frame (*DF*).
4. Applying Morphological Opening on the Thresholded Difference Frame (*TDF*),
5. Finding the region(s) which contain(s) the particle(s).
6. Within each region, estimating the position of the particle and the distance from the particle to the top and the bottom inner walls of the tube.

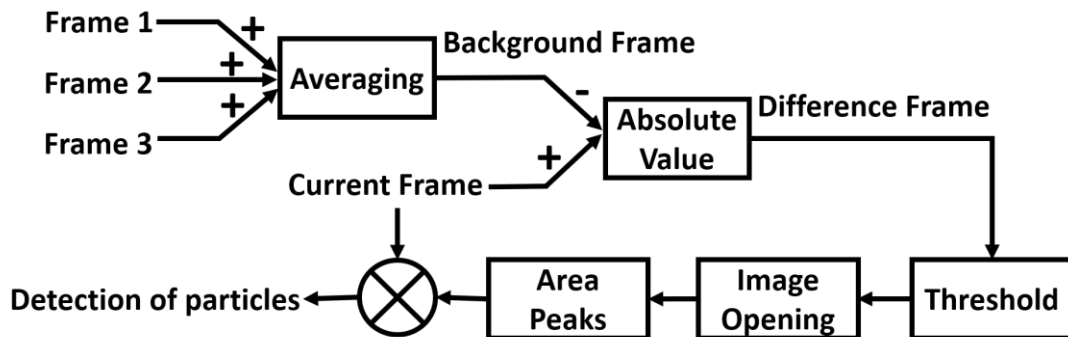


Figure 5.8 Block diagram to illustrate the particle detecting algorithm.

This Section explains in detail the proposed particle detecting algorithm using the TFM image, as shown in Figure 5.9(a), which contains three ball bearings of different sizes: 1 mm, 1.5 mm, and 2 mm. The greyscale image shown in Figure 5.9(b), which has been

converted from Figure 5.9(a), is defined as the Current Frame denoted, CF . As shown in the Figures, the particles appear as bright spots in the TFM images.

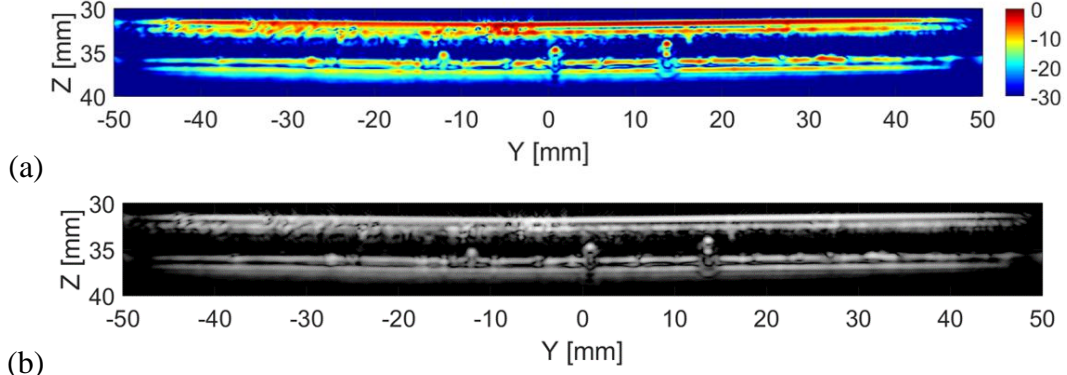


Figure 5.9 (a) TFM image of the tube-tank phantom with three ball bearings (the bright spots between the tube walls) inside the tube from the 1D linear array transducer. (b) Greyscale image (Current Frame), which has been converted from (a).

The algorithm starts by detecting the appearance of the particles using the Difference Imaging method [96]. The first step is to define a Background Frame (BF), which could represent the motionless objects in the image, which in this case, is the tube. In this algorithm, the Background Frame (BF) is generated from the first three frames of the image series using:

$$BF = \sum_{i=1}^N F(i) / N \quad (5.4)$$

where $F(i)$ is the i^{th} frame and N denotes the number of frames used in the calculation, i.e., $N = 3$. Here, only three frames have been used because the relative position between the transducer and the tube has been kept the same during the imaging process, which means there will not be significant changes in the tube walls in adjacent frames.

Thus, three frames would be a reasonable number considering both the accuracy of the resulted BF and the data processing time. In practice, especially for medical imaging systems that have more powerful data processing capability, more frames can be used to ensure the appropriate quality of the BF. Figure 5.10(a), (b), and (c) show the three frames that have been used to create the Background Frame (d). As shown in the Figures, although the particle has appeared in the second frame (Figure 5.10(b), near the 50 mm end in *y-axis*), the averaging process has successfully reduced its effect and resulted in the Background Frame being similar to the first frame (Figure 5.10(a)) which has been captured without particles. In practice, when the situation inside the vessel is unknown, this approach can provide a representable frame (Background Frame) of the vessel in its typical situation.

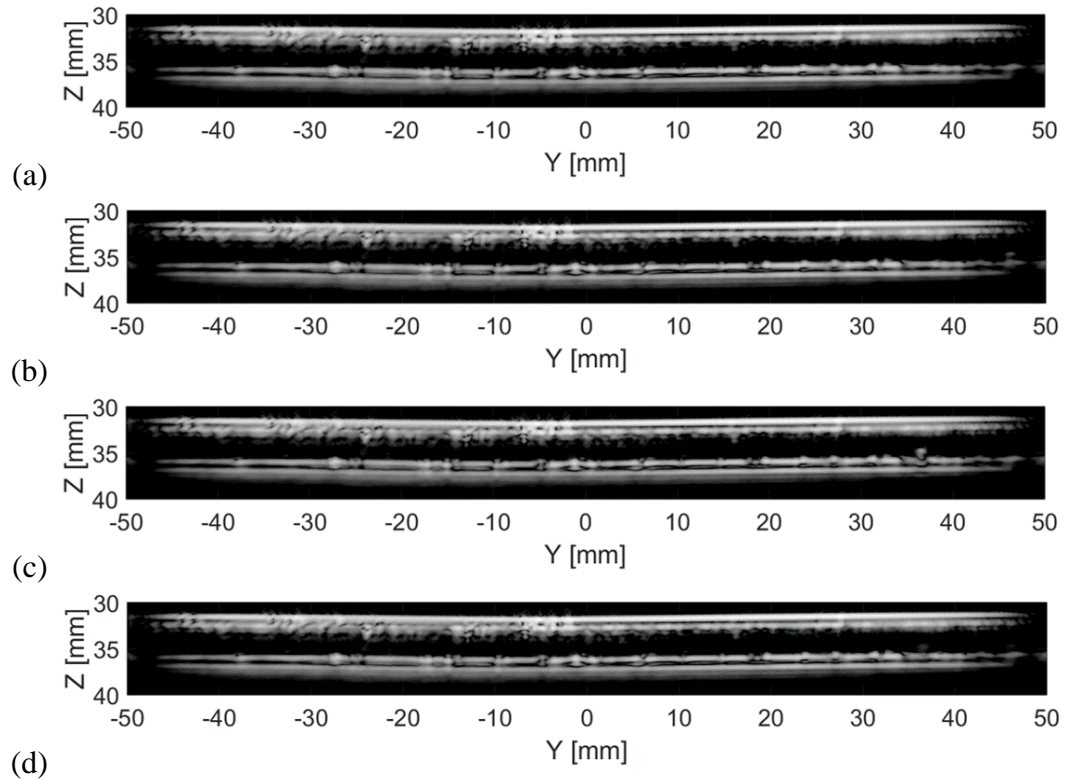


Figure 5.10 (a), (b), and (c) are the first three frames from the image series, which have been used to create (d) the Background Frame.

The second step is to generate the Difference Frame (DF) using:

$$DF = |CF - BF| \quad (5.5)$$

The idea is that for the same area in the image, the pixels' intensity should remain the same unless a new object appears in that area. Figure 5.11 shows the DF , which has been created from Figure 5.9(b) and Figure 5.10(d). As shown in the Figure, the four bright lines, which represent the tube wall in previous figures, have disappeared because they are motionless and, as a result, are contained in BF . The bright spots which indicate the presence of particles in CF , remain in DF . However, in addition to markers for the

particles, there is also some noise in the DF image, which should not be included in any subsequent analysis or measurement.

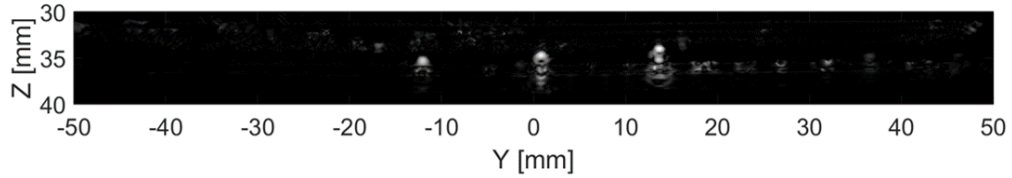


Figure 5.11 The Difference Frame (DF) generated using the example Current Frame (CF) and the Background Frame (BF).

Noise suppression has been achieved by thresholding DF and post-processing the result. The resultant image, as shown in Figure 5.12, is called the Thresholded Difference Frame, TDF . This thresholding process has been achieved using:

$$I_{TDF} = \begin{cases} 0, & \text{if } I_{DF} < \text{Threshold} \\ 1, & \text{Otherwise} \end{cases} \quad (5.6)$$

where I_{DF} and I_{TDF} is the pixel intensity in DF and TDF , separately. The threshold is set to be -5 dB of the maximum intensity in DF .

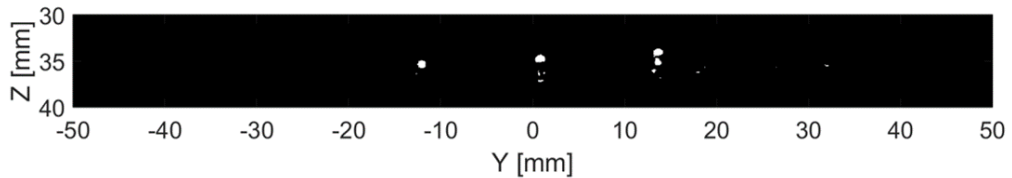


Figure 5.12 The Thresholded Difference Frame (TDF).

After thresholding, most of the noise in the DF has been eliminated, as shown in Figure 5.12. However, some noise still remains in the TDF . These noisy pixels cannot be

eliminated by increasing the threshold because their intensities are very close to the maximum intensity in the DF . Another step is therefore needed to avoid any undesired effects arising from these noisy pixels. As shown in Figure 5.12, the bright spots which represent the particles are much larger compared to the bright dots, which consist of the noisy pixels. Thus, in this algorithm, Morphological Opening [100] is applied to the TDF to remove these noisy pixels. A 5x5 disk Structuring Element (SE), as shown in Figure 5.13, has been applied to the TDF , and the resulting image, called the Opened Frame ($OpnF$), is shown in Figure 5.14. As shown in this Figure, only the bright spots that represent the particles are retained in the image. One thing to be noticed is that there does exist a risk that this algorithm becomes overfitted to the specific image which is used here. However, results from the prototype transducers, which will be introduced in Chapter 6, proved that this algorithm could achieve appropriate accuracy when being used for images generated from different transducers. Moreover, even if it is overfitted to the specific image, the parameters used in this algorithm can always be modified to suit different imaging situations, such as when the reflector has different shapes or when the reflector has different pixel intensities.

The next step is to locate the regions that contain the particles. Each region is marked by a bounding box denoted, $RG(i)$, and delimited by four points, $w_start(i)$, $w_end(i)$, $h_start(i)$, and $h_end(i)$. The first two parameters represent the starting column and the ending column of the i^{th} particle counting from the left side of the image, while the last two parameters represent the starting and ending rows. As shown in Figure 5.14, pixels representing the same particle are within columns which are continuously

connected and contained within a single bounding box. Thus, the locating step starts from finding the first column, from left to right, that contains a pixel that is not 0. That column is recorded as $w_start(1)$. The algorithm then proceeds, column by column, judging if there is pixel within each column which has an intensity equal to 1. The first column which meets these two conditions, 1) contains pixel with 1 intensity and 2) its following column consists of pixels all equal to 0, is recorded as $w_end(1)$. Within the region delimited from $w_start(1)$ to $w_end(1)$, the first row that contains none 0 pixels is recorded as $h_start(1)$, while the last row that has none 0 pixels is recorded as $h_end(1)$. Subsequently, starting from the first column at the right hand of $w_end(1)$, the algorithm finds the next column that contains no 0 pixels, and records this as $w_start(2)$ and then repeating the previous steps until it reaches the last column of the *OpnF*.

However, the *RG* delimited by those four parameters, which is represented by the blue lines in Figure 5.14, only containing the particle. To estimate the size and distance from each particle to the tube wall, a larger block (*BLK*), which contains both the particle and the tube walls, should be created. The size of the *BLK* is set to have rows equal to that of the *OpnF* and columns equal to 100, which is represented by the dashed yellow lines in Figure 5.14, which has been created for each *RG*. The columns for *RG* are in the middle of each *BLK*.

0	0	1	0	0
0	1	1	1	0
1	1	1	1	1
0	1	1	1	0
0	0	1	0	0

Figure 5.13 The 5x5 disk mask that has been used in the Morphological Opening step of the particle detection algorithm.

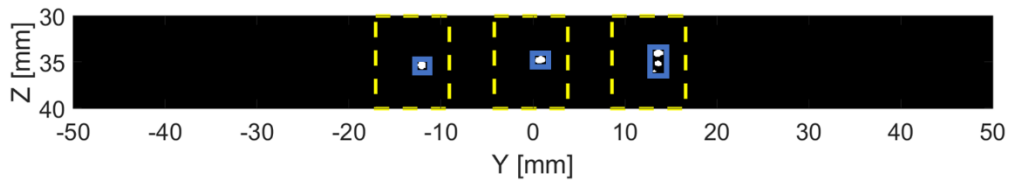


Figure 5.14 The Opened Frame (OpnF). The blue lines represent the RG, within which a particle has been detected. The dashed yellow lines indicate regions in which a particle has been detected.

The second stage of this algorithm is to locate the position of each particle and to estimate the distance from each particle to the top and bottom inner walls of the tube. In this work, as the particles are located in the bottom inside wall of the tube, the distance from the particle to the bottom inner wall can be used to estimate the size of the particle, and the sum of the distances to both inner walls can provide information about the tube size. For other applications, where the particle may be in contact with the top inner wall or suspend between the inner walls, the way to estimate particle size needs to be modified. But the way used to estimate the inner diameter is still valid. Figure 5.15 shows an example of locating the position of the 2 mm particle. The $RG(3)$ (Figure

5.15(b)), which has been detected from the *OpnF* (the third *RG* – the blue rectangle – counting from the left as shown in Figure 5.14(a)), is used as a mask and multiplied to a region (Figure 5.15(a)), which has been extracted from the *CF* and delimited by the same parameters as for *RG(3)*. The resulted region is shown in Figure 5.15(c). This process will ensure only the pixels in Figure 5.15(a), which have an intensity equal to 1 in Figure 5.15(b), will be kept, while the remaining pixels will be set to 0 (i.e., black). The coordinates of the pixel in Figure 5.15(c), which has the maximum intensity has been recorded as the position of the 2 mm particle.

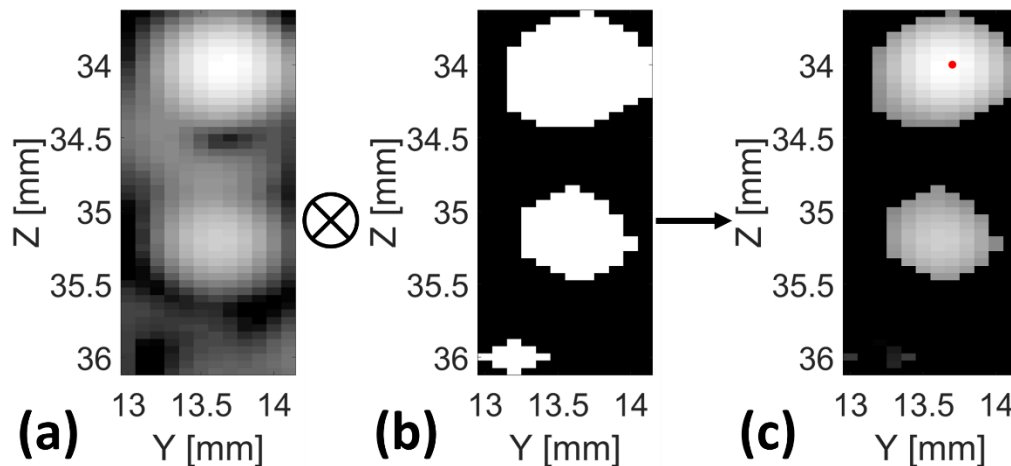


Figure 5.15 The *RG* in (a) the *Current Frame* and (b) the *Opened Frame* where contains the 2 mm particle. (c) The result after multiplying (a) and (b). The red dot represents the estimated position of the 2 mm particle.

To estimate the size of the particle, the inner walls of the tube within each *BLK* need to be detected first. However, as shown previously in Figure 5.9, the appearance of the particles has caused parts of the bottom inner wall to disappear from the image. Thus, instead of the *CF*, the *BF*, which contains continuous tube walls, has been used to detect

the inner walls. Figure 5.16 shows an example of the $BLK(3)$, which has been extracted from the BF . The inner walls within that block have been detected by applying the tube size estimation algorithm, as described in Section 5.3. The distance from the estimated position of the 2 mm particle to the top inner wall and the bottom inner wall is 1.45 mm and 2.05 mm, respectively. The latter is also the estimated size of the particle. The inner diameter of the piece of the tube within $BLK(3)$ is $1.45 \text{ mm} + 2.05 \text{ mm} = 3.5 \text{ mm}$.

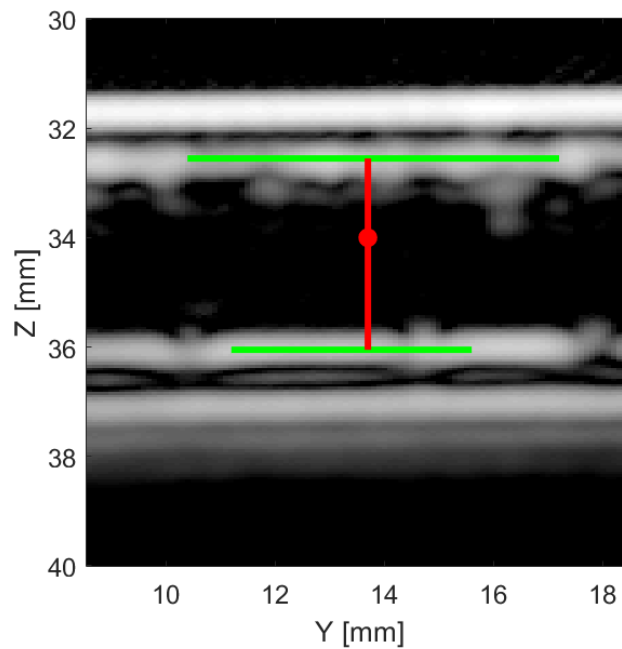


Figure 5.16 The $BLK(3)$ which has been extracted from the Background Frame. The green lines indicate the detected inner walls of the tube. The red lines represent the distance from the detected position of the 2 mm particle (red dot) to the inner walls of the tube.

The inner walls and the position of the particle are then marked in the CF , as illustrated in the example presented in Figure 5.17. All three particles have been successfully

detected and located. The results are listed in Table 5.1. As shown in the Table, all the particles inside the phantom, as well as the tube, have been successfully dimensioned to ± 0.1 mm precision.

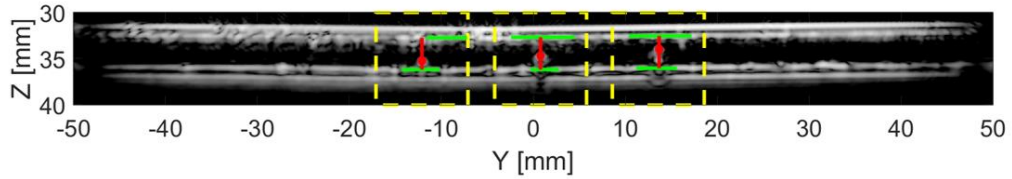


Figure 5.17 The Current Frame with the particles detected. The dashed yellow lines indicate the regions in which a particle has been detected. The solid red lines represent the distance from the particles (red dots) to the top and bottom inner walls of the tube (solid green lines).

Table 5.1 The estimated results for the example Current Frame.

Real Particle Size [mm]	Estimated Particle Size [mm]	Estimated Inner Diameter [mm] (Real Inner Diameter is 3.5 mm)
1	0.95	3.5
1.5	1.5	3.45
2	2.05	3.5

To test the accuracy of the particle detection algorithm, more data has been collected by imaging the tube-tank phantom using the 1D Linear Array Transducer. For each experiment, the transducer is fixed above the tube, while a single particle is placed at different positions inside the tube and imaged by the transducer. For each particle, 14 measurements have been processed, and the results are shown in Figure 5.18. The average estimated size is 2.02 mm for the 2 mm particle, 1.53 mm for the 1.5 mm

particle, and 0.99 mm for the 1 mm particle, while the estimated tube inner diameters are 3.46 mm, 3.47 mm, and 3.45 mm, respectively.

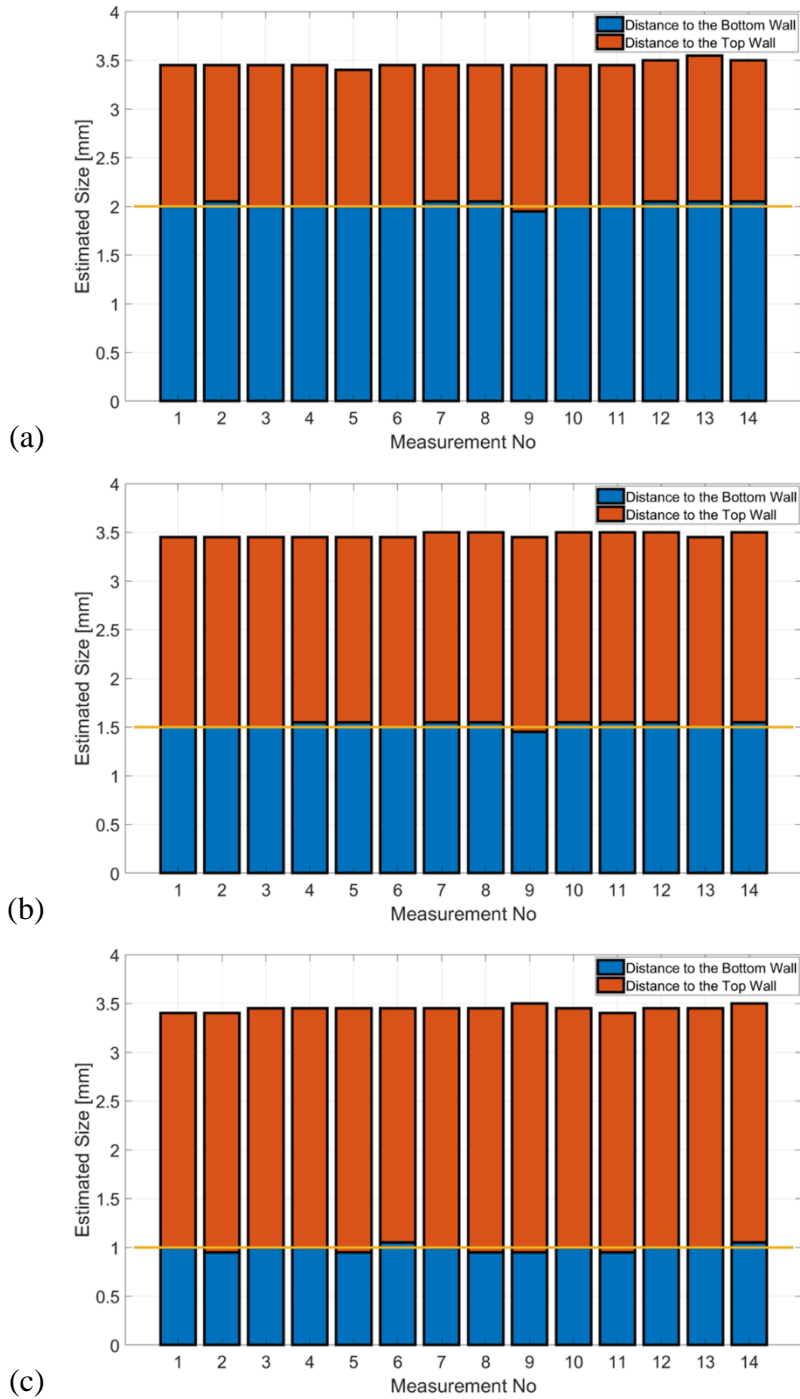


Figure 5.18 Results for (a) the 2 mm particle, (b) the 1.5 mm particle, and (c) the 1 mm particle. The yellow lines represent the real size of the particles. The averaged estimated particle size is 2.02 mm for the 2 mm particle, 1.53 mm for the 1.5 mm particle, and 0.99 mm for the 1 mm particle., while the averaged tube inner diameter is 3.46 mm, 3.47 mm, and 3.45 mm, separately.

5.5. Summary

Two image analysing algorithms have been developed based on data collected from imaging a tank-tube phantom with multi-size ball bearings using a commercial 1D Linear Array Transducer. The first algorithm is designed to measure the inner diameter of the tube, and the second one is designed to detect the particles inside the tube. Image processing methodologies such as the Hough Transform, the Difference Imaging, and the Morphological Opening have been successfully used in these algorithms. Both algorithms have achieved appropriate accuracy when estimating the size of the particles and the tube using images getting from the commercial transducer. These two imaging algorithms have been shown to be able to automatically detect and size the particles and tube walls, and hence, have the potential to reduce the operator dependence of current transcranial ultrasound imaging. However, it is recognised that these two algorithms have been developed and tested using a high quality commercial array transducer and will now be further evaluated using two experimental phantom scenarios and the designed and fabricated sparse array transducers, from Chapters 3 and 4. Details of these experimental results will be described in Chapter 6.

One more thing to notice is that the images used in developing the image analysing algorithms are captured with the reflectors staying stable in the phantom. In the situation of imaging moving target of lower echo strength, the reflected signal from the target will be lower and spread, which may increase the difficulty of detecting the target from the image. However, by modifying the parameters used in the algorithms, it is still possible to detect and size the moving target with appropriate precision.

Chapter 6

System Integration and Evaluation

6.1. Introduction

This Chapter presents five sets of experiments which were designed to test the imaging capability of the developed prototype transducers and associated feature detection and sizing results.

- The first set of experiments was designed to test and compare the sizing capability and imaging resolution between the fibre CECAT transducer (the CECAT_79) and the conventional 1-3 piezocomposite transducers (the C13_79 and the C13_106), and to check if the CECAT_79 is capable of imaging reflectors within a specific range. Since the prototype transducers are 2D arrays, small diameter reflectors have been used to ensure the reflecting situation is the same in both *x-axis* and *y-axis*.
- The second set of experiments is to further compare the imaging performance of the prototype transducers when imaging multiple reflectors are present. A wire phantom has been designed and imaged using all three prototype transducers.

- The third set of experiments is to use the fibre CECAT transducer to image a tank-tube phantom, which is the same as used in Chapter 5, to test if the CECAT_79 can produce a TFM image of the tube of sufficient quality to be analysed using the algorithms developed in Chapter 5.
- The last two experiments are designed to test whether the CECAT_79 has the potential to be used in real scenarios, i.e. provide high-quality images of the human tissues. These will use bespoke, small, laboratory scale medical phantoms.

Before introducing the details and results of the experiments, there are a few points that need to be clarified. Firstly, all the coordinates mentioned in this Chapter are built based on the coordinate system which has been used to describe the sparse array patterns in Chapter 3 (Figure 3.26). Secondly, to make it easier to evaluate and compare the imaging performance of different prototype transducers, only 2D images of the object under test have been processed. Thirdly, the resolutions for the TFM images shown in this Chapter have been determined by taking both image quality and image processing time into consideration. Fourthly, for comparison purposes, all the TFM images are shown in the *Y-Z plane*. Moreover, unless stated, the *Y-Z plane* TFM image shown in this Chapter is the one which has the lowest background noise (i.e. the highest image quality) along the *x-axis*.

6.2. Imaging Small Diameter Reflectors

6.2.1. Imaging Small Diameter Reflectors with Different Size

Figure 6.1 illustrates the experimental setup for imaging a single small diameter reflector. The transducer is placed in parallel with the bottom of the water tank. It's connected to the FIToolbox (Diagnostic Sonar Ltd, UK) through a connector adaptor and utilised to collect data using the FMC method. Brass rods (Albion Alloys, Bournemouth, Dorset) with diameters varying from 0.4 mm to 2 mm are immersed in water, working as small diameter reflectors. The acoustic impedance mismatch between brass and water ensures there will be a strong reflection of the ultrasound wave at the interface between these two materials. Since the ultrasound wavelength in the water at 2 MHz is 0.74 mm, the diameter range of the brass rods covers a range from $\sim 0.5\lambda$ to $\sim 2.7\lambda$. For each imaging process, one brass rod is placed with one end directly facing to the front surface of the transducer and the other end fixed to a holder, which is placed on the bottom of the water tank. The distance between the front surface of the transducer and the upper end of the brass rod has been controlled to be within the same range (55 mm to 65 mm) for all the prototype transducers. The distance range has been selected as it is within the positional range of the blood vessels from the temporal window [104] [120] - [124]. An effort has been made to place the brass rod right under the central point of the transducer's array pattern.

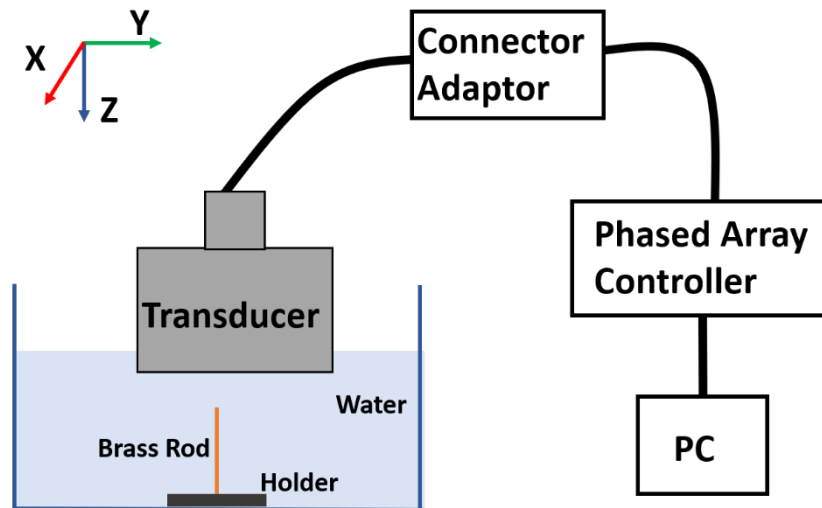


Figure 6.1 Illustration of the experimental setup for imaging a single small diameter reflector (brass rod).

Since the ultrasound wavelength in the water at 2 MHz is 0.74 mm, the experiment started from imaging the 2 mm brass rod, which is larger than 2λ , to ensure all the prototype transducers can detect the reflector. The resulting TFM images are shown in Figure 6.2. The bright spot in each image represents the reflector detected by corresponding transducer. Since the brass rods were manually placed, the real positions of the brass rods have slightly deviated from the central point of the array pattern. For comparison purpose, all the images have been normalized into a 6 mm by 6 mm square with the 0 dB (maximum amplitude) pixel centred at the original point. The spatial resolution for the TFM image is 0.015 mm by 0.015 mm (401 pixels by 401 pixels).

As shown in Figure 6.2, the CECAT_79 performs better than both of the C13 piezocomposite transducers in terms of the axial resolution, as it can achieve a single, well-defined and narrow indication of a reflector along the z -axis. The C13_106 device

has produced a similar axial performance for the main reflected component to the CECAT_79, however, multiple reflections also are evident in Figure 6.2(c). These phenomena are associated with the C13_106 pulse-echo response results as discussed in Section 4.3.3. Importantly, the shorter pulse-length of the CECAT_79 compared to the C13_79, also discussed in Section 4.3.3, has produced a better imaging axial resolution.

Other brass rods with a diameter of 1.5 mm, 1 mm, 0.8 mm, 0.5 mm, and 0.4 mm have been successively imaged using the same experimental setup. Corresponding TFM images for the larger four reflectors are included in Appendix B as they present very similar imaging performance results, however, the results will be included in a quantifiable feature size study later this Section. The TFM images for the smallest reflector (0.4 mm) are shown in Figure 6.3, and it is apparent that for this smallest reflector size, the background noise in the TFM images from all three transducers has been significantly increased. This is expected as the reflector size reduces below the wavelength of the ultrasonic signal. Moreover, the 0.4 mm reflector (0.5λ), can be treated as a point reflector and used to investigate the point spread function (PSF), which reflects the lateral resolution performance, for each prototype transducer.

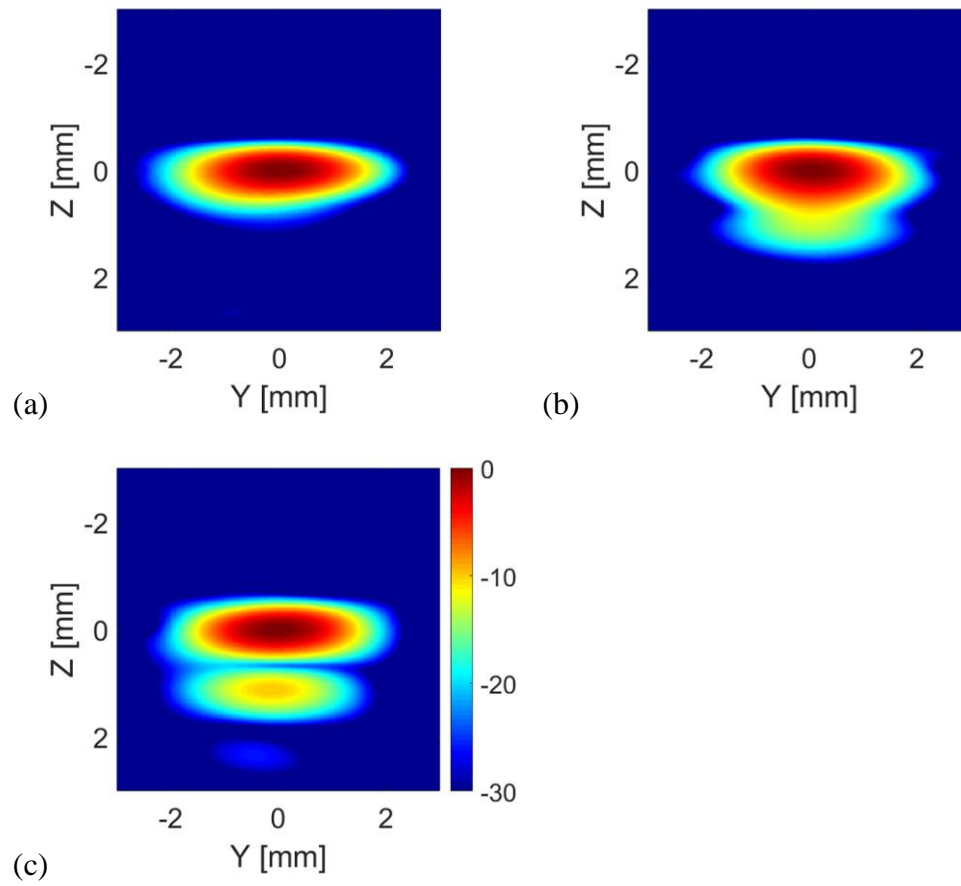


Figure 6.2 TFM images for imaging the 2 mm small diameter reflector using (a) the CECAT_79, (b) the C13_79, and (c) the C13_106. Colour scale is in dB.

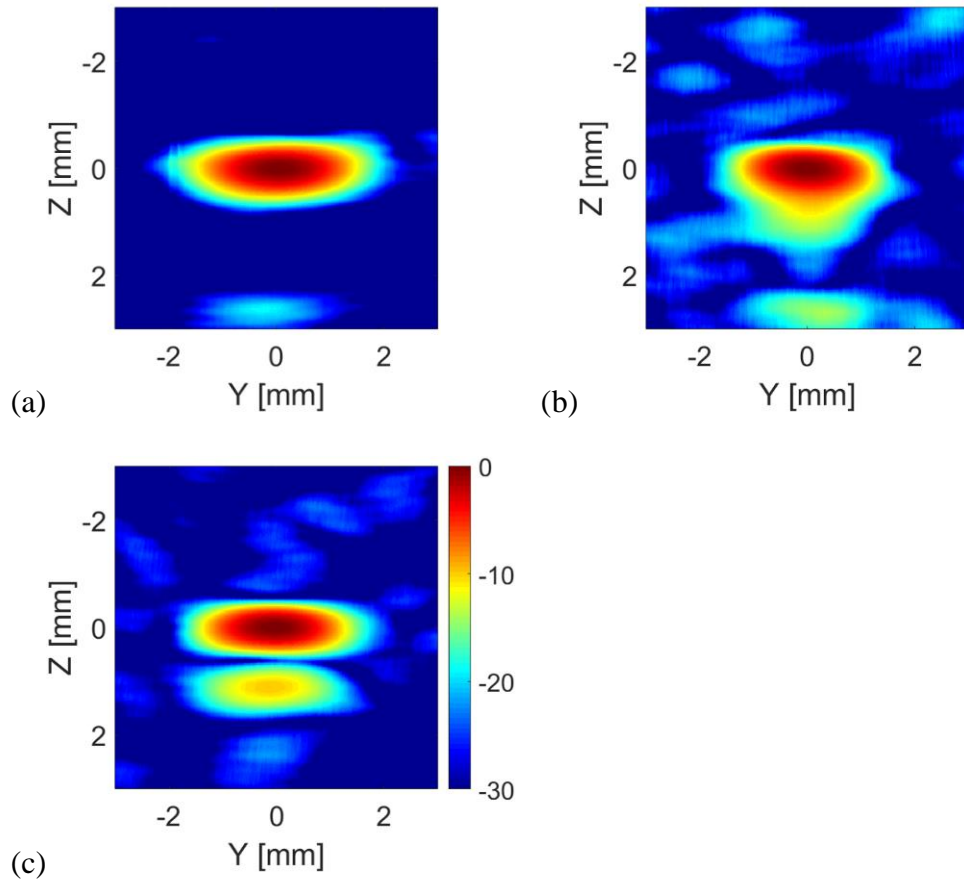


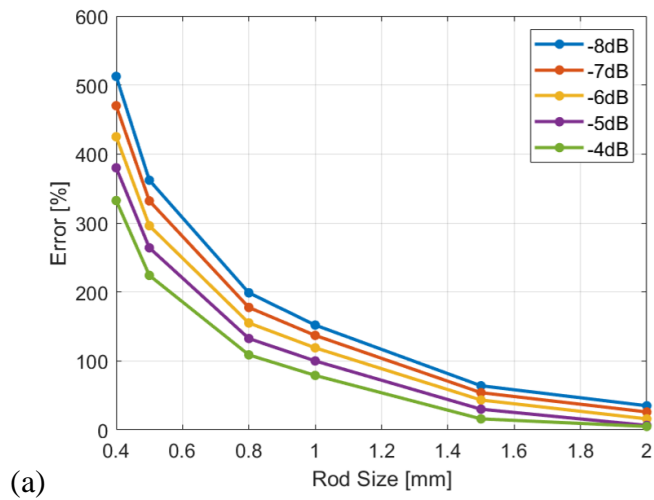
Figure 6.3 TFM images for imaging the 0.4 mm small diameter reflector using (a) the CECAT_79 (b) the C13_79, and (c) the C13_106. Colour scale is in dB.

The TFM images of the single reflector can be used to estimate the size of the reflector by measuring the length of the line, which is parallel to the y -axis, through the 0 dB point (i.e. the centre of the reflector), and contains pixels with intensity higher than a specific threshold. To compare the sizing capability of the transducers, a fixed threshold is needed, which will be applied on TFM images from all the prototype transducers. Measurements have been processed with different thresholds (-8 dB to -4 dB) for all three transducers, and the results are shown in Figure 6.4. The measurement error ($error_m$) has been calculated by:

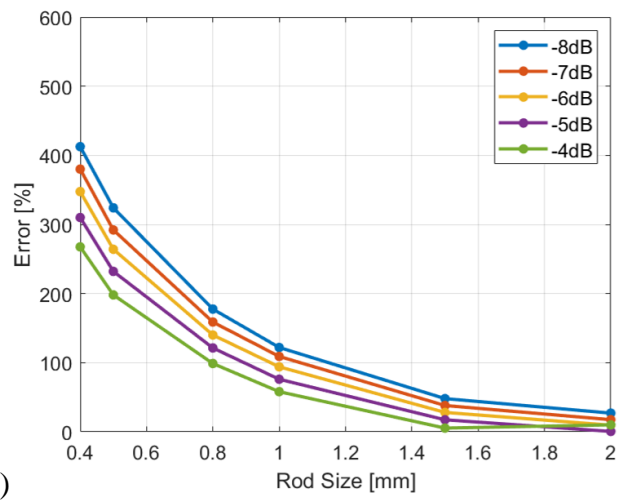
$$error_m = |size_m - size_r|/size_r \quad (6.1)$$

where $size_m$ and $size_r$ represent the measured size from the TFM image and the real size of the reflector (brass rod), separately. As illustrated in Figure 6.4, for all three transducers, the $error_m$ for the same reflector is inversely proportional to the threshold. However, this relationship breaks down for the -4 dB threshold results for the 2 mm diameter bar, where the estimation error increases in relative terms. Thus, in this project, the threshold that is used by the prototype transducers for reflector size measurement is set to -5 dB.

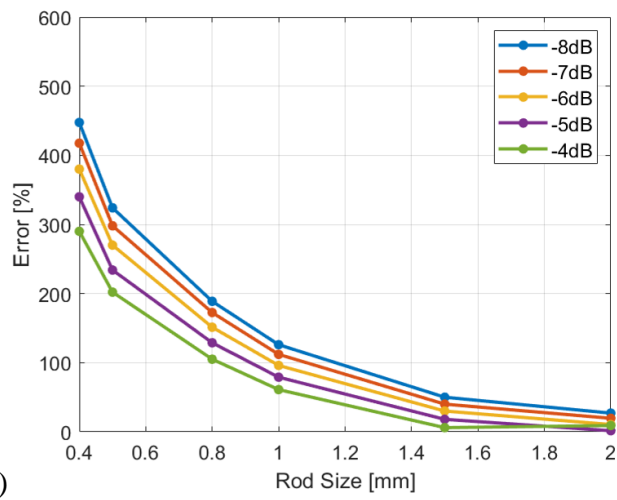
Table 6.1 listed the absolute predicted reflector size from each prototype transducer. The results clearly indicate that the lateral resolution for the CECAT_79 is around 2 mm, which is larger than that of the C13 devices (around 1.7 mm). This is related to the increased active aperture for the C13 devices, as mentioned in Section 4.3.2.



(a)



(b)



(c)

Figure 6.4 Rod size measurement errors with different thresholds for (a) the CECAT_79, (b) the C13_79, and (c) the C13_106.

Table 6.1 Rod size measurement results for all three prototype transducers using -5 dB threshold.

$size_r$ [mm]	$size_m$ [mm] ($error_m$)		
	CECAT_79	C13_79	C13_106
2	2.15 (6.5%)	2.04 (0.5%)	2.03 (1.5%)
1.5	2.03 (30.0%)	1.82 (17.3%)	1.77 (18.0%)
1	2.09 (100.0%)	1.82 (76.0%)	1.79 (79.0%)
0.8	1.95 (132.5%)	1.83 (121.3%)	1.83 (128.8%)
0.5	1.92 (264.0%)	1.71 (232.0%)	1.67 (234.0%)
0.4	2.00 (380.0%)	1.69 (310.0%)	1.76 (340.0%)

From Table 6.1, it can be observed that the $error_m$ from the C13 transducers are close to each other, while the CECAT_79 performs poorly in comparison. This situation may be caused by the incomplete array pattern of the CECAT_79, as mentioned in Section 4.3.3, where there are three array elements in the CECAT_79 which are not working properly. To consider this difference in lateral resolution performance, the beam profiles for the two 79-element devices have been evaluated. This is a simulation-based approach using Huygens' principle, which treats each array element as a point source, with the only difference between the two simulations is that the CECAT device has three non-functioning elements. Figure 6.5 shows the simulated unfocused beam profile for the CECAT_79 and the C13_79 devices, which shows a strong axial beam and high sidelobe levels in each simulation. The reason that the sidelobe levels are large is because the simulation is using continuous wave (CW) as the driven signal. As mentioned in Section 2.5.1, the sidelobe level should be reduced with a pulsed driving signal. Figure 6.5(c) and Figure 6.5(d) illustrate the range 55 mm to 65 mm along the z -

axis, which corresponds to where the bar reflectors were positioned in the preceding tests. These results illustrate that these missing elements have introduced a skew in the main axial beam response for the CECAT_79 device and it is considered that this has contributed to the degradation in lateral resolution capability for this device.

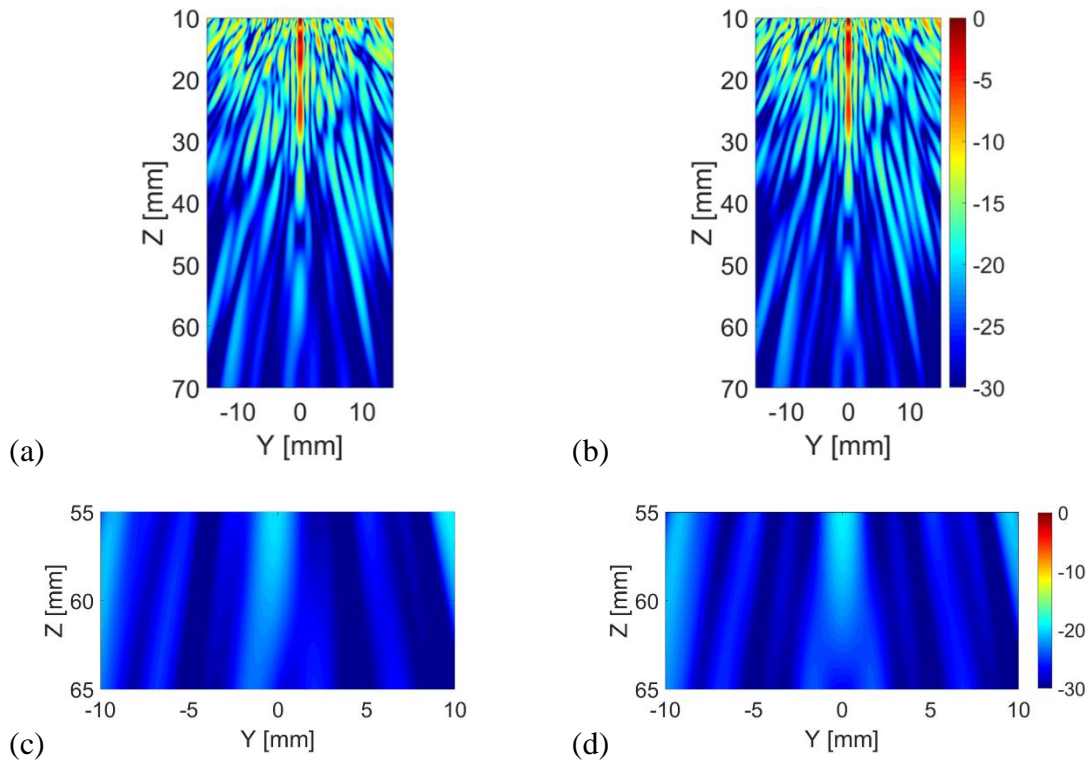


Figure 6.5 Simulated beam profile in Y-Z plane for (a) the CECAT_79 and (b) the C13_79. (c) and (d) are zoomed in images which have been extracted from (a) and (b), respectively.

The -5 dB threshold has also been used to measure the axial resolution of the three transducers from the TFM results presented in Figure 6.2, 6.3 and Appendix B, as shown in Figure 6.6. The C13_106 has the best axial resolution, but the CECAT_79 has outperformed the 1-3 piezocomposite with the same number of elements. Considering

the axial resolution is mainly limited by the transducer impulse response, the results shown here agree well with the pulse-echo response results, as mentioned in Section 4.3.3, which indicate that the C13_106 has the highest resonance frequency and C13_79 has the lowest one.

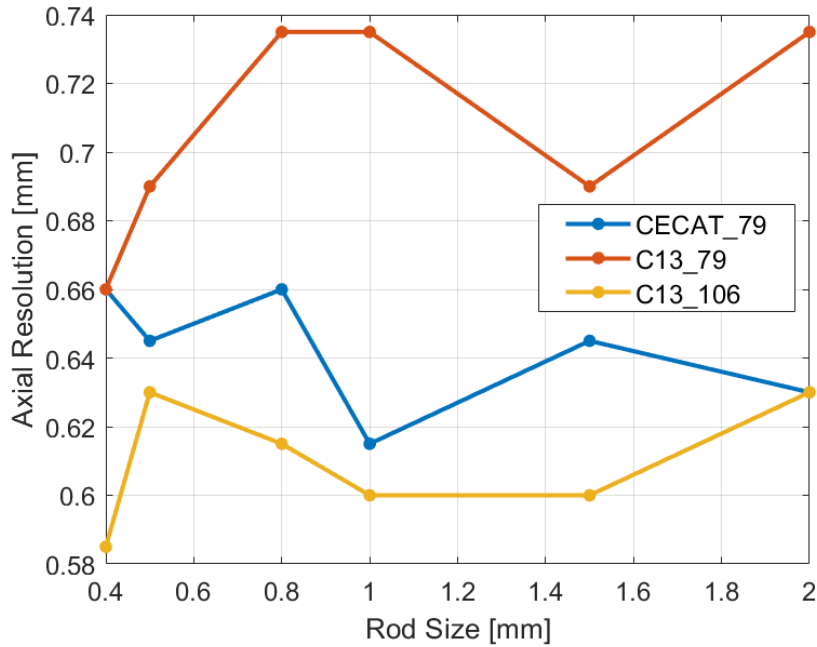


Figure 6.6 Axial resolution for all three transducers with -5 dB threshold.

6.2.2. Imaging Single Small Diameter Reflector at Different Distances

The CECAT_79, which combines a well-designed sparse array pattern and a conformal active layer structure, is the main achievement of this project. To test whether the CECAT_79 has the potential to be applied as a transcranial transducer, an experiment

has been designed to test if it can detect reflectors within the depth range where the blood vessels are located. According to [104] [120] - [124], there are several blood vessels located at a distance from 30 mm to 80 mm away from the temporal window. Thus, the test is processed by using the same experimental setup as illustrated in Figure 6.1, with the distance between the front surface of the CECAT_79 and the top end of the brass rod varying from 30 mm to 80 mm with a 5 mm step size. The 0.8 mm ($\sim 1\lambda$) rod has been used as the small diameter reflector during the test. Within each depth range, a TFM image has been processed with the 0 dB pixel normalized at the centre of the image. The size of the TFM images is 5 mm by 5 mm with a resolution of 0.015 mm by 0.015 mm, i.e. 331 pixels by 331 pixels. Figure 6.7 shows the TFM image of the 0.8 mm small diameter reflector within the depth range of 30 mm to 35 mm and 75 mm to 80 mm. As shown in the figure, the CECAT_79 has successfully detected the 1λ small diameter reflector in both situations. This proves that the CECAT_79 is capable of covering the desired 30 mm-to-80 mm imaging depth. The TFM images with the reflector placed between 35 mm to 75 mm are included in Appendix C.

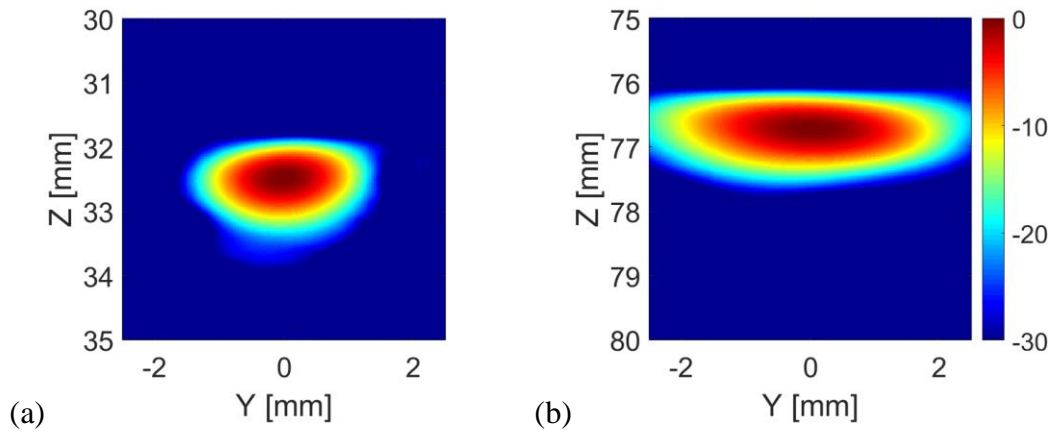


Figure 6.7 The TFM image of the 0.8 mm rod within the depth range of (a) 30 mm to 35 mm and (b) 75 mm to 80 mm.

Figure 6.8 shows the $error_m$ of the 0.8 mm reflector calculated using the TFM images which have been acquired at different distance range using the CECAT_79 transducer, while Table 6.2 lists the $size_m$ and the $error_m$ for each depth range. As shown in Figure 6.8 and Table 6.2, the $error_m$ tends to increase when the reflector is located further away from the front surface of the transducer. The sizing error is lower than 100% in the range 30-50 mm, but exceeds 200% at the furthest range of 70-80 mm. The relationship between the sizing error and the distance is associated to the beam divergence. Recalling the simulated beam profile of the CECAT_79 (shown in Figure 6.5(a)), the main lobe tends to diverge with increase of the distance, and the contrast between the main lobe and the side lobes is decreased. Moreover, the increase in the distance between the reflector and the transducer will also cause increase of attenuation, which will reduce energy contained in the reflected signal and lead to higher sizing error. This seems to be a potential problem for sizing the anomalies in the medical application. However, the results from imaging the medical phantoms will present that when more information is

available and image processing algorithms are applied, the sizing accuracy could be maintained at a high level and become independent of the distance.

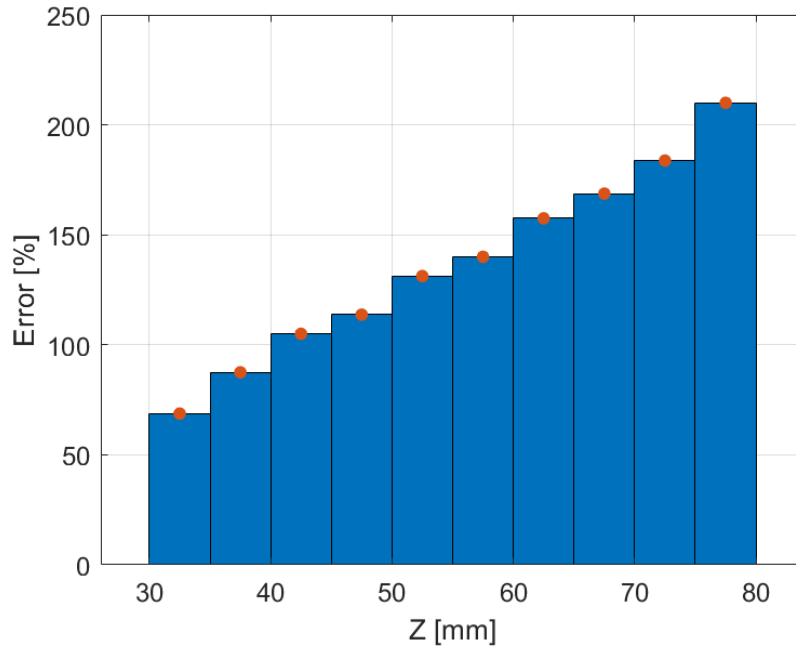


Figure 6.8 Measurement errors of the 0.8 mm rod imaged at a depth between 30 mm to 80 mm using the CECAT_79. The dots represent the values of the errors, while the bars represent the depth ranges.

Table 6.2 Size measurement results for the 0.8 mm rod imaging at different distances using the CECAT_79 transducer.

Range [mm]	$size_m$ [mm] ($error_m$)	Range [mm]	$size_m$ [mm] ($error_m$)
30 – 35	1.35 (68.8%)	55 – 60	1.92 (140.0%)
35 – 40	1.50 (87.5%)	60 – 65	2.06 (157.5%)
40 – 45	1.64 (105.0%)	65 – 70	2.15 (168.8%)
45 – 50	1.71 (113.8%)	70 – 75	2.27 (183.8%)
50 – 55	1.85 (131.3%)	75 – 80	2.48 (210.0%)

6.3. Imaging Multiple Reflectors

A wire phantom consisting of four brass rods with different diameters, held in a plastic frame, has been used to evaluate the performance of the transducers in imaging multiple reflectors. The brass rods are fixed into a parallel orientation with respect to the transducer front face, through a pair of drilled holes within opposing walls of the frame. The top of the frame is open to ensure a clear propagation path for the ultrasound. According to the results shown in Section 6.2.1, the smallest brass rods used in the wire phantom is determined to be the 0.5 mm one. The diameters of the other three brass rods are 0.8 mm ($\sim 1\lambda$), 1.5 mm ($\sim 2\lambda$), and 2 mm ($>2\lambda$). The rods are sorted in ascending order of size from right to left (in 10 mm increments) and the distance from the transducer also varies in 10 mm increments, with the largest rod located furthest from the transducer. This experimental setup is illustrated in Figure 6.9. The wire phantom is immersed in water with the transducer placed above it. Efforts have been made to ensure the rods are in parallel with the transducer front face. For comparison purposes, the wire phantom has been kept within the same imaging area for all three transducers. The FIToolbox has been used to collect the FMC data, which will be processed into TFM images.

Three measurements have been processed, two with the wire phantom placed, as shown in Figure 6.9, the other with the phantom reversed. The TFM images getting from the first measurement are shown in Figure 6.10, while the TFM images from the other two measurements are included in Appendix D. As shown in Figure 6.10, when imaging multiple reflectors, the C13_106 has the lowest background noise level, while the

CECAT_79 and the C13_79 have similar performance in terms of the background noise level.

The diameter (width in *y-axis*) of the rods in each TFM image has been measured using the -5 dB threshold method described in Section 6.2.1. For each rod, a 6 mm by 6 mm square is manually created with the maximum pixel of that rod placed in the centre. The resolution of the square is set to be 0.015 mm by 0.015 mm. The $size_m$ results for each rod are presented in Figure 6.11, and the averaged $size_m$ values are listed in Table 6.3. Overall, the C13_106 has more accurate $size_m$ compared to the two 79-element devices, although the CECAT_79 demonstrates a similar sizing performance. This is associated with the smaller element size in the C13_106, which provides larger steering angle so that more area of the imaging field can be covered to achieve better image quality. Moreover, the C13_79 has produced the poorest sizing performance. Hence, it is considered that the CECAT_79 has produced acceptable performance metrics with respect to this more realistic multi-reflector imaging scenario.

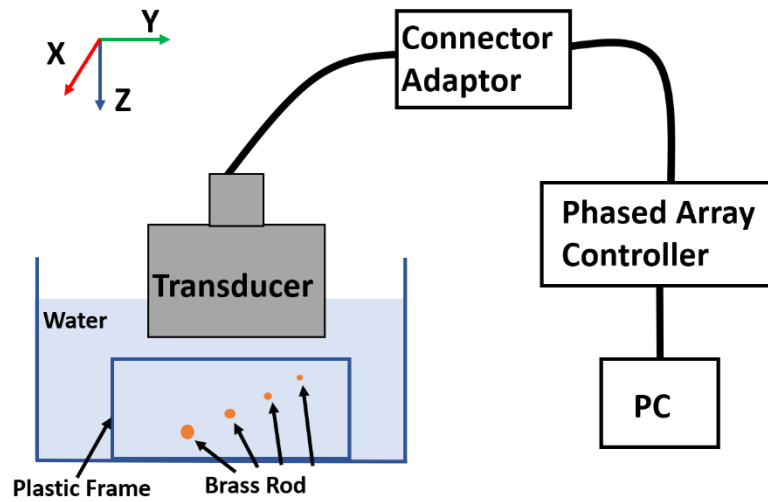


Figure 6.9 Illustration of the experimental setup for imaging the wire phantom (Brass rods and the plastic box).

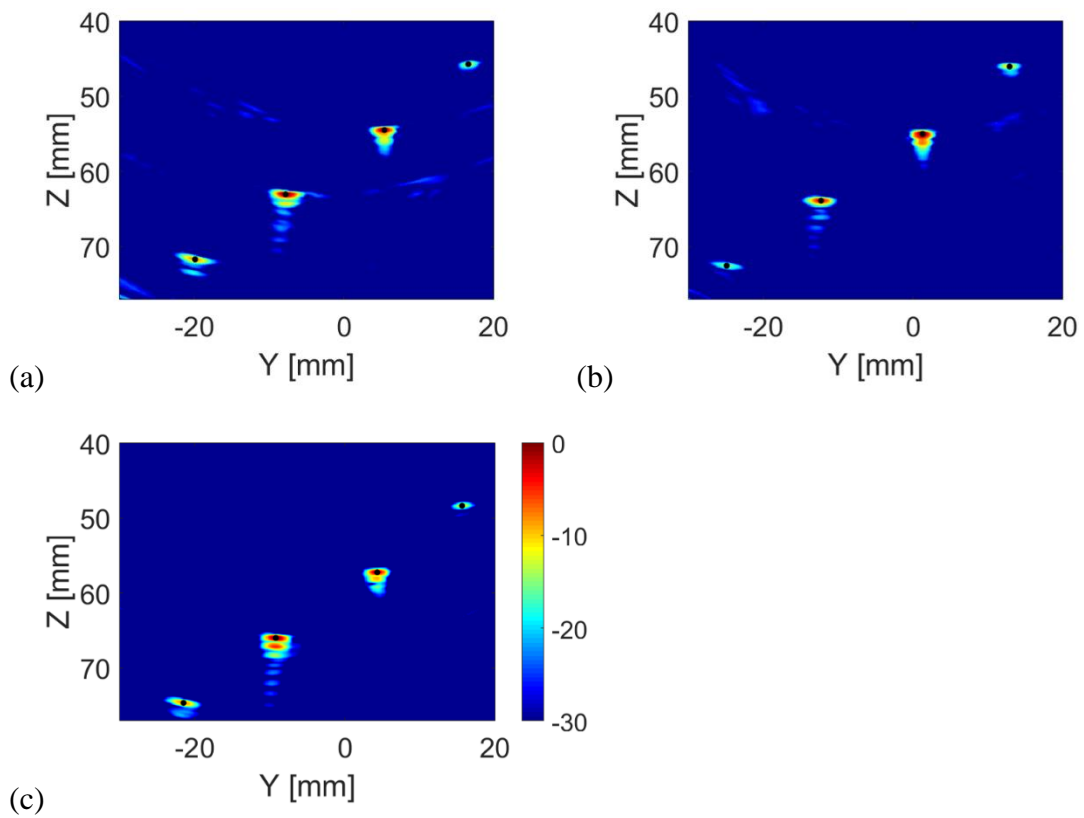


Figure 6.10 The TFM images of the wire phantom from (a) the CECAT_79, (b) the C13_79, and (c) the C13_106.

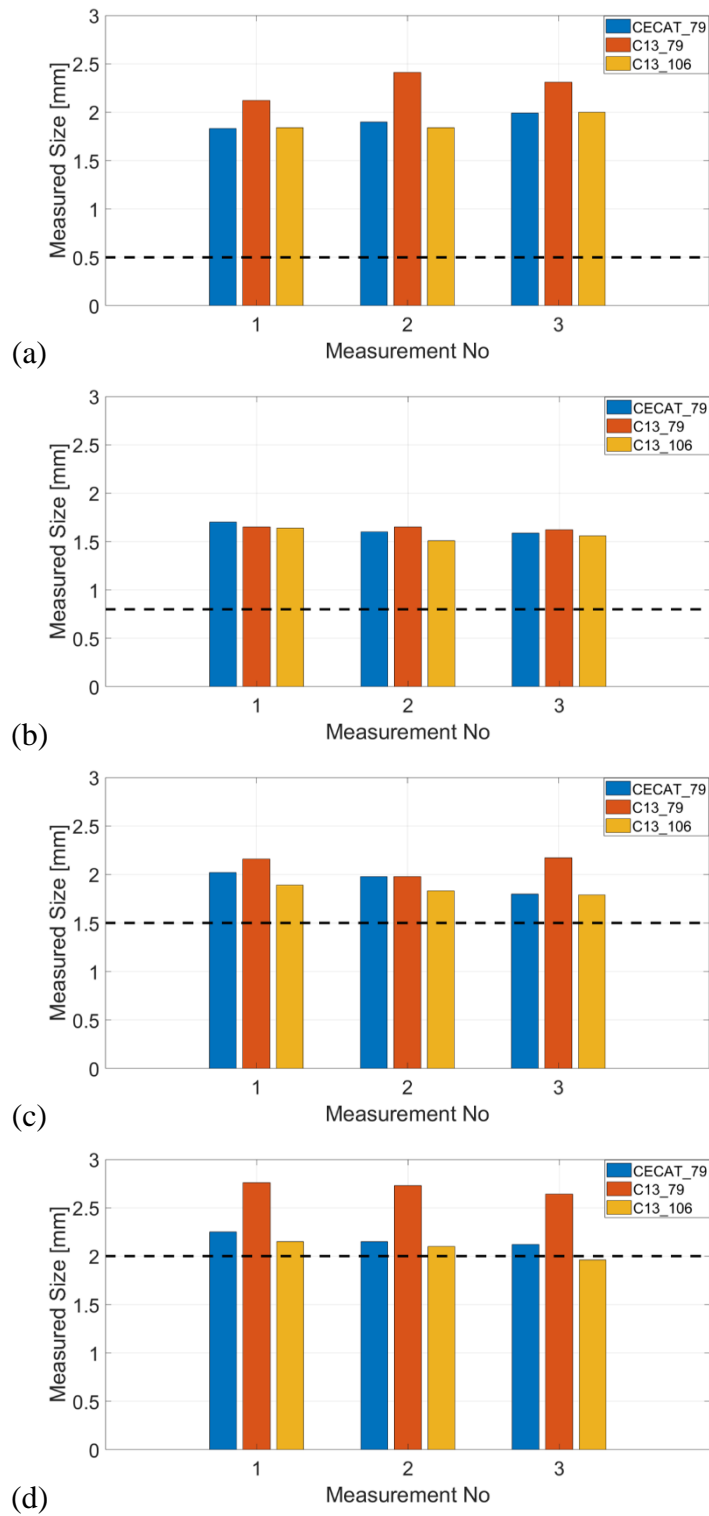


Figure 6.11 The size_m results of (a) the 0.5 mm rod, (b) the 0.8 mm rod, (c) the 1.5 mm rod, and (d) the 2 mm rod. The black dashed lines represent the real size of the rods.

Table 6.3 Size measurement results of the wire phantom

$size_r$ [mm]	Averaged $size_m$ [mm] ($error_m$)		
	CECAT_79	C13_79	C13_106
0.5	1.91 (282.0%)	2.28 (356.0%)	1.89 (278.0%)
0.8	1.63 (103.8%)	1.64 (105.0%)	1.57 (96.3%)
1.5	1.93 (28.7%)	2.10 (40.0%)	1.84 (22.7%)
2.0	2.17 (8.5%)	2.71 (35.5%)	2.07 (3.5%)

6.4. Imaging Tube-Tank Phantom

Results from Section 6.2 and Section 6.3 have demonstrated that, compared to the transducer that has the same array pattern but using the conventional 1-3 composite configuration (C13_79), the CECAT_79 has better imaging performance in terms of axial resolution and sizing capability when imaging multiple reflectors. Thus, the third experiment is to test if the CECAT_79 could be used to detect anomalies (particles) in the tube and to estimate the size of the tube. The experimental setup is shown in Figure 5.1. The CECAT_79 is used to image the same tank-tube phantom, which was introduced in Chapter 5. The tube is placed under the transducer within the 30 mm to 50 mm depth range, which is within the depth range of the potential application field (30 mm to 80 mm as mentioned in Section 6.2.2). The CECAT_79 is controlled by the phased array controller (the FIToolbox) to collect the FMC data, which will be used to process the TFM image of the imaging area. The same ball bearings, which have been discussed in Chapter 5, with diameters of 1 mm, 1.5 mm, and 2 mm are used to simulate the anomalies. The tube and anomaly sizing algorithms, introduced in Chapter 5, are

used to analyse the TFM images from the CECAT_79 only. The resolution of the TFM image is set to be 0.05 mm in both *y-axis* and *z-axis*.

The experiment started with imaging the tube with no particles inside. Figure 6.12 shows an example TFM image of the tube and the corresponding frame which has been extracted from it. The width of the image area is set to 30 mm (-15 mm to 15 mm), which is the aperture size of the CECAT_79. As shown in the Figure, the tube wall can be clearly identified within the area from -10 mm to 10 mm in the *y-axis*. That area is analysed using the tube size estimation algorithm, with the area equally divided into two blocks (each is 10 mm by 10 mm). The average value of the results from each block, which is 3.4 mm, is recorded as the estimated inner diameter of the tube. Given the real inner diameter of the tube used in the tube-tank phantom is 3.5 mm, the estimated inner diameter has an appropriate accuracy.

Next, the CECAT_79 is used to image the tube with a single particle (ball bearing) placed within the area that is within the field of view of the transducer aperture. For each particle, four FMC datasets have been collected with the particle placed at different positions within the tube and then processed into TFM images. This is to evaluate the accuracy of analysing TFM image generated from the CECAT_79 using the particle detection algorithm. Figure 6.13 presents some example TFM images of the tube with the 2 mm particle placed at different positions. The particle detection algorithm has been used to analyse the frames that have been converted from the TFM images. The results are shown in Figure 6.14 and represent the distance of the detected feature to the inner walls of the tube. Encouragingly, the position of the particle does not have a significant

effect on the particle size estimation result. The averaged estimated size is 1 mm for the 1 mm particle, 1.44 mm for the 1.5 mm particle, and 2.06 mm for the 2 mm particle. The size of the tube has also been estimated in this configuration, and the results are 3.4 mm for all three situations.

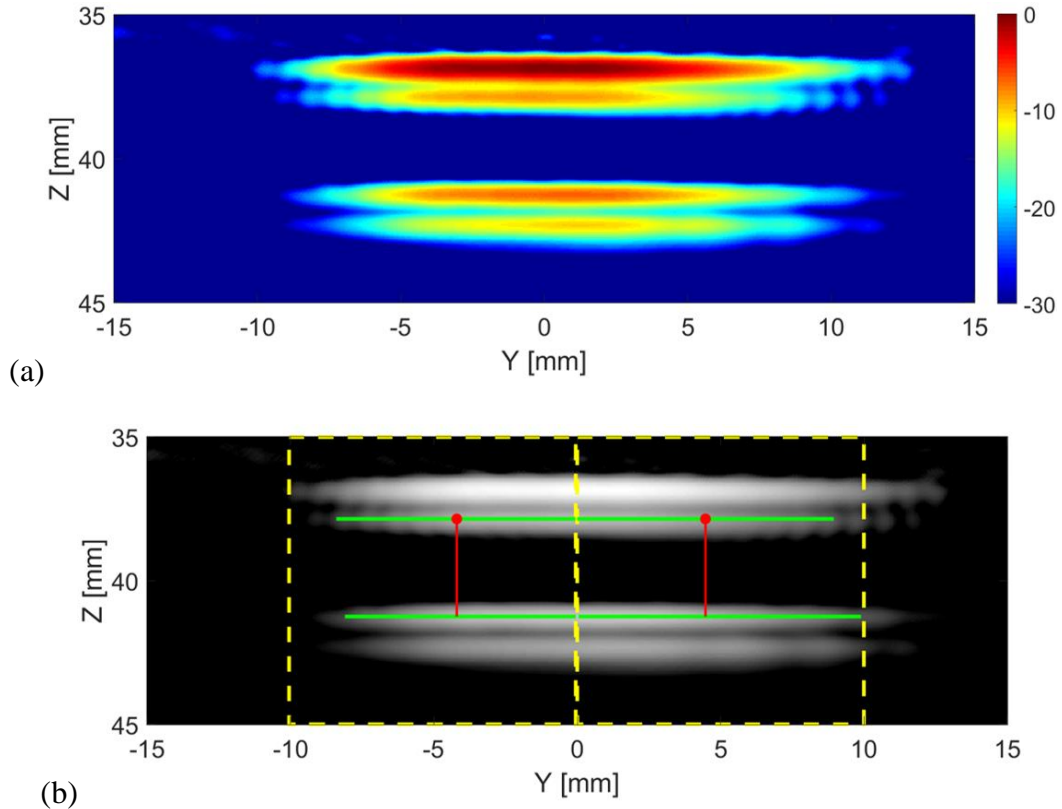


Figure 6.12 (a) An example TFM image of the tube with no particles inside from the CECAT and (b) the corresponding frame converted from (a). The yellow dashed lines illustrate the edges of the blocks that have been extracted from the frame. The solid green lines are the detected inner walls. Within each block, the red dot represents the middle point of the top inner wall, while the solid red lines illustrate the estimated inner diameter. The averaged estimated inner diameter of the tube computed from this frame is 3.4 mm.

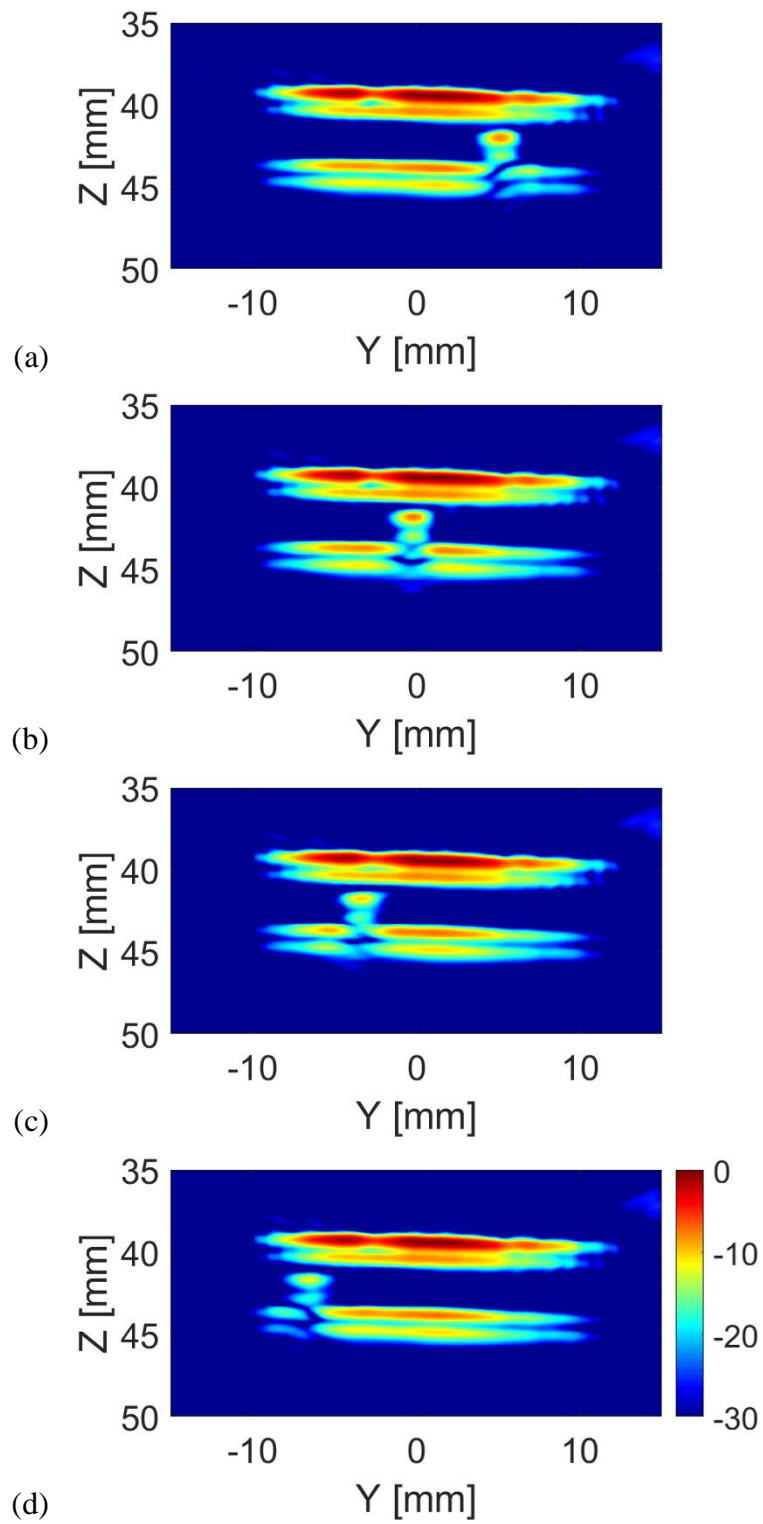


Figure 6.13 TFM images of the tube with the 2 mm particle at different positions from the CECAT_79.

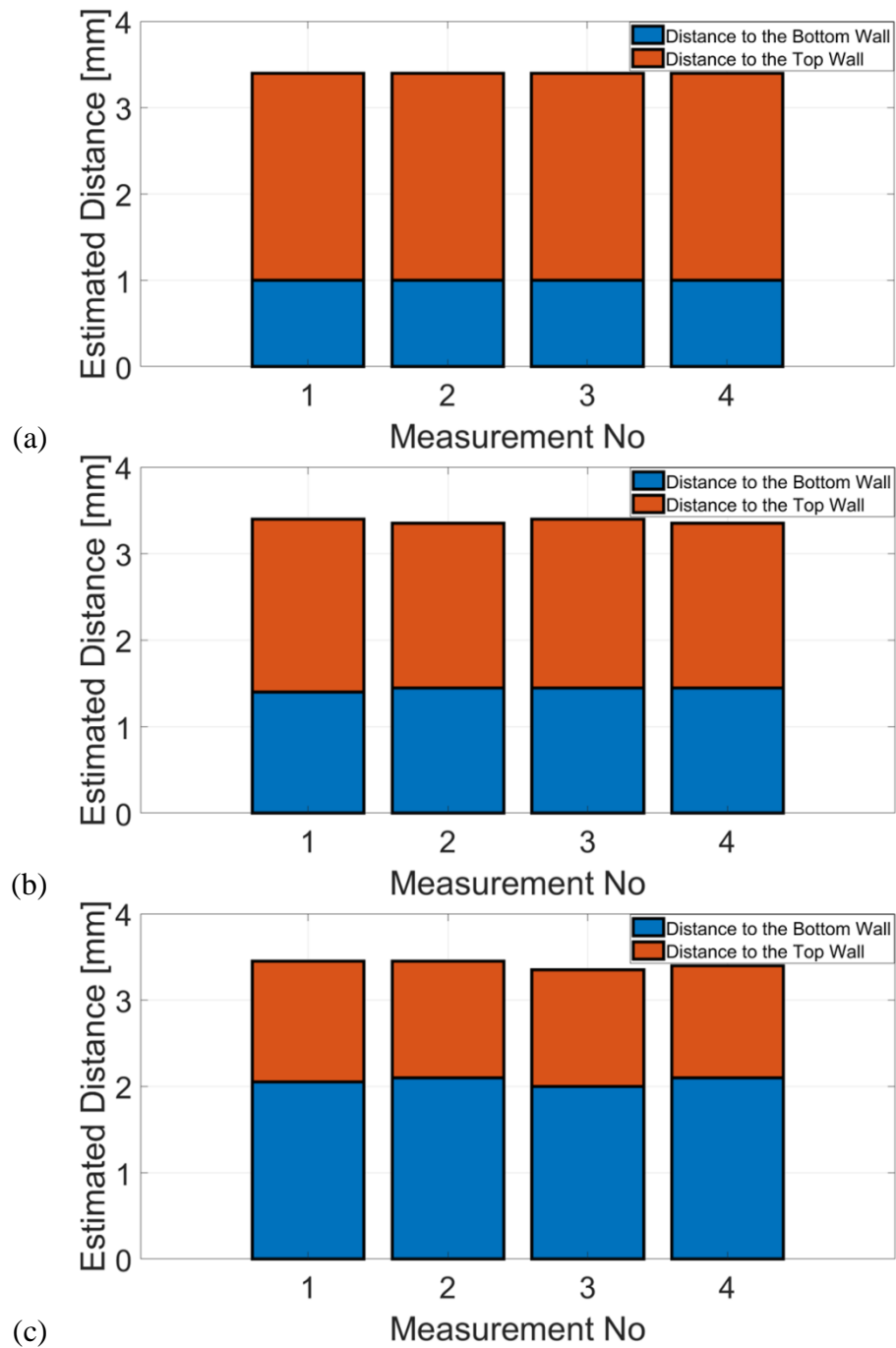


Figure 6.14 Results of (a) the 1 mm particle, (b) 1.5 mm particle, and (c) the 2 mm particle. The averaged estimated particle size is 1 mm for the 1 mm particle, 1.44 mm for the 1.5 mm particle, and 2.06 mm for the 2 mm particle. The estimated inner tube diameters are 3.4 mm for all three situations.

Then, three particles, one 1 mm, one 1.5 mm, and one 2 mm, are placed inside the tube and imaged using the CECAT_79 at the same time. This step is to further test the accuracy of applying the particle detection algorithm with TFM images generated from the CECAT_79. Figure 6.15(b) shows an example frame that has been converted from the corresponding TFM image, Figure 6.15(a). The particle detection algorithm has been used to analyse this frame. As shown in Figure 6.15(b), all three particles have been successfully detected from the frame. The estimated size is 1.05 mm for the 1 mm particle, 1.65 mm for the 1.5 mm particle, and 2.1 mm for the 2 mm particle. The averaged inner diameter of the tube which has been calculated from results of all three pieces of the tube within each *BLK* (defined in Section 5.4; represented by the rectangle with dashed yellow edges in Figure 6.15), is 3.4 mm.

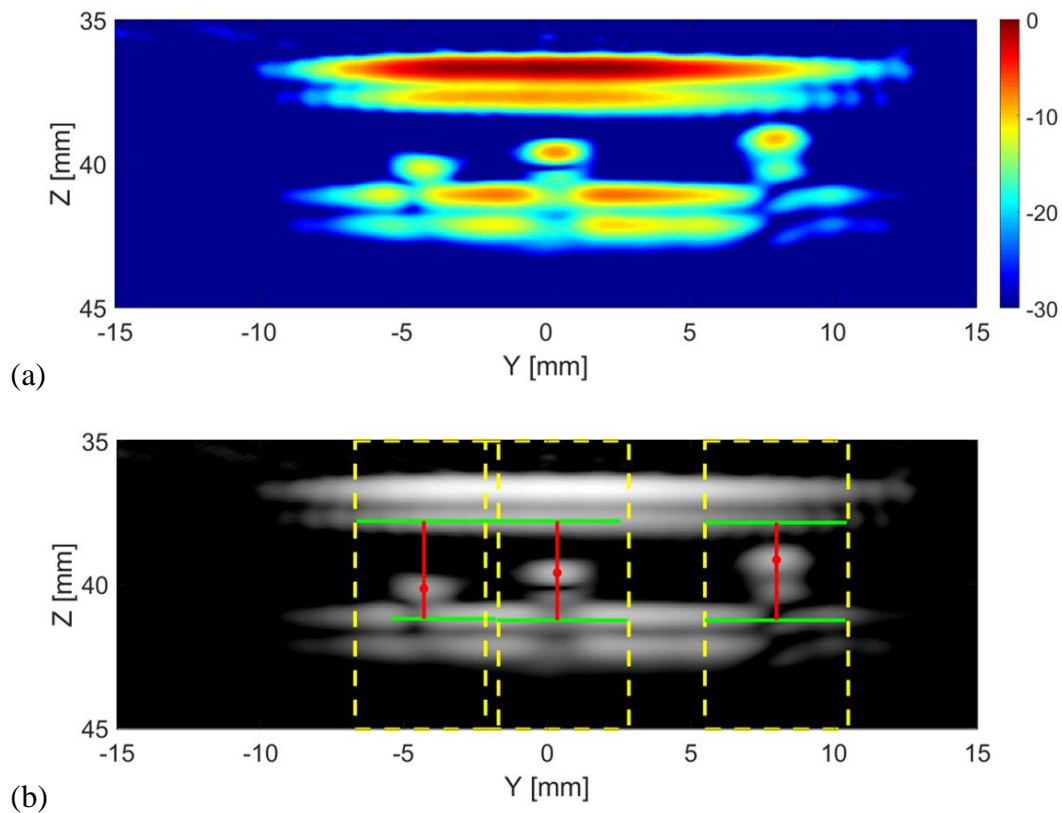


Figure 6.15 An example Current Frame from the CECAT_79 with the particles detected. The dashed yellow lines indicate the regions in which a particle has been detected. The solid red lines represent the distance from the particles (red dots) to the top and bottom inner walls of the tube (solid green lines). The estimated size is 1.1 mm for the 1 mm particle, 1.6 mm for the 1.5 mm particle, and 2.15 mm for the 2 mm particle. The averaged estimated inner diameter calculated from results of all three pieces of the tube within each BLK (the rectangle with dashed yellow edges) is 3.4 mm.

6.5. Imaging Medical Phantom

A medical phantom from the NHS Greater Glasgow & Clyde Medical Devices Unit (MDU) has been used to evaluate the imaging performance of the CECAT_79. The MDU phantom [125] was originally developed with a focus on the Tissue Mimicking Material (TMM) characteristics to ensure that appropriate scattering properties and

acoustic properties that meets the International Electrotechnical Commission (IEC) standards [126]. MDU suggested that this existing phantom might prove a useful vehicle for evaluation of the developed 2D sparse array technology. The configuration of the MDU phantom and the experimental setup are illustrated in Figure 6.16. The TMM is placed inside a perspex mould, surrounded by artificial grass (Express Grass, Sittingbourne, Kent) which is used to attenuate the sound reflected from the phantom walls [125]. The TMM and the artificial grass are immersed in water to prevent the TMM from cracking. A tube (Cole-Parmer UK, St Neots, Cambridgeshire) is placed inside the TMM to create a channel for the fluid, which in this project is sterile water (Baxter, Newbury, Berkshire). The CECAT_79 is attached to the top surface of the TMM and controlled by the FIToolbox to collect FMC data. An effort has been made to align the centre of the transducer to be directly above the tube.

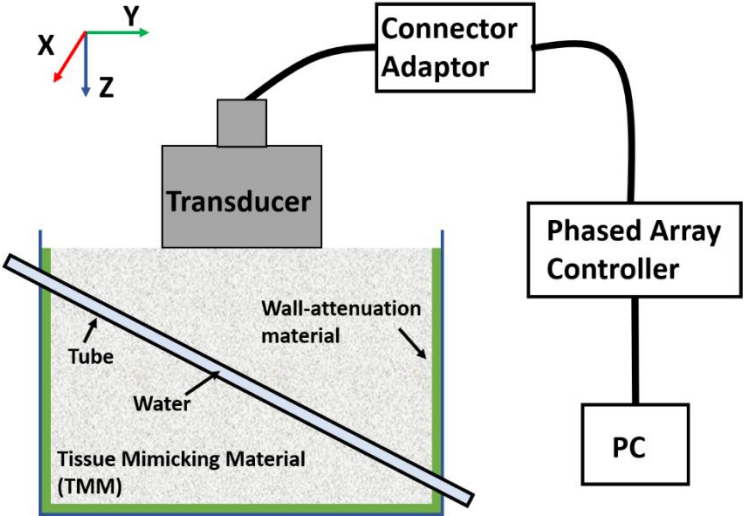


Figure 6.16 2D illustration of the experimental setup for imaging the MDU phantom using the CECAT_79.

Figure 6.17 shows an example TFM image of the MDU phantom from the CECAT_79. Although the tube walls can be separated from the background (i.e. the TMM), they have been highly blurred. Thus, the tube detection algorithm, as introduced in Chapter 5, cannot be used to detect the tube walls and to estimate the size of the tube. On consideration, this issue might be associated with the working status of the CECAT_79 and the structure of the MDU phantom. These two conjectures have been experimentally examined, and the details are described below.

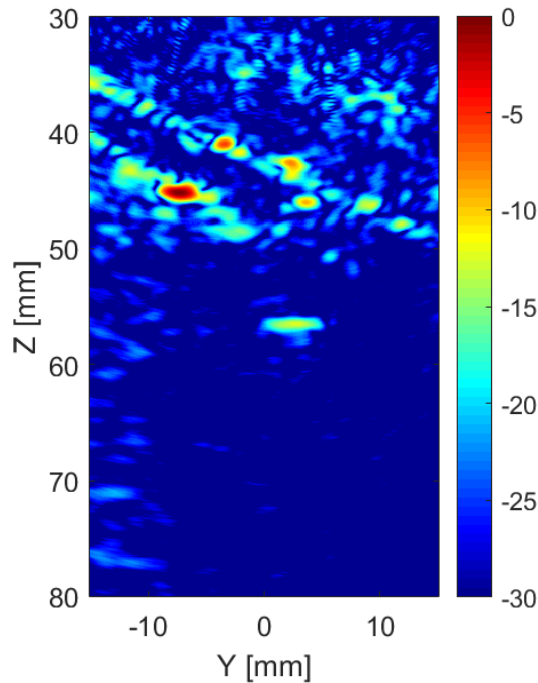


Figure 6.17 TFM image of the MDU phantom from the CECAT_79.

Since the tests on the MDU phantom were processed a few months later than those on the tube-tank phantom, the working status of the CECAT_79 may have changed in the

time that elapsed between experiments. Thus, the first thing was to test if the CECAT_79 was still working properly by using the CECAT_79 to image the tube-tank phantom with the same experimental setup, as illustrated previously in Figure 5.1. The resulted TFM image is shown in Figure 6.18, where the tube walls have been successfully imaged to demonstrate that the CECAT_79 is still working properly.

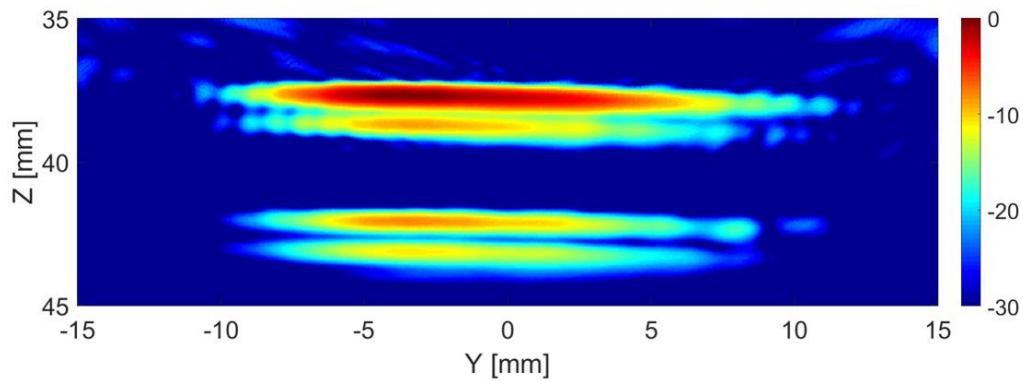


Figure 6.18 TFM image of the tube-tank phantom from the CECAT_79.

As the CECAT_79 has been shown not to be the cause of the blurring issue, the next step is to test how the structure of the MDU phantom affect the imaging results. Comparing the tube-tank phantom and the MDU phantom, the biggest difference between them in terms of structure is the tube position and orientation. For the tube-tank phantom, the tube is placed in parallel with the bottom surface of the tank, i.e. the tube is in parallel with the front surface of the transducer. However, the tube inside the MDU phantom is placed at an angle of 30° with the bottom surface of the tank. As illustrated in Figure 6.19, when the angle between the transducer and the angle increased, to produce TFM image, the beam pattern has to be broad enough to capture reflected

signals from the angled reflector. In other words, when the angle exceeds the maximum steering angle of the array, the TFM method will result in low quality images. Besides, as the aperture size decreased, a proportion of the reflected sound waves may not be captured by the transducer as they may be reflected outside of the transducer aperture. In summary, the angle between the tube and the transducer as well as the limited aperture size of the transducer may have caused the reduced image quality. Two groups of experiments have been designed to evaluate this.

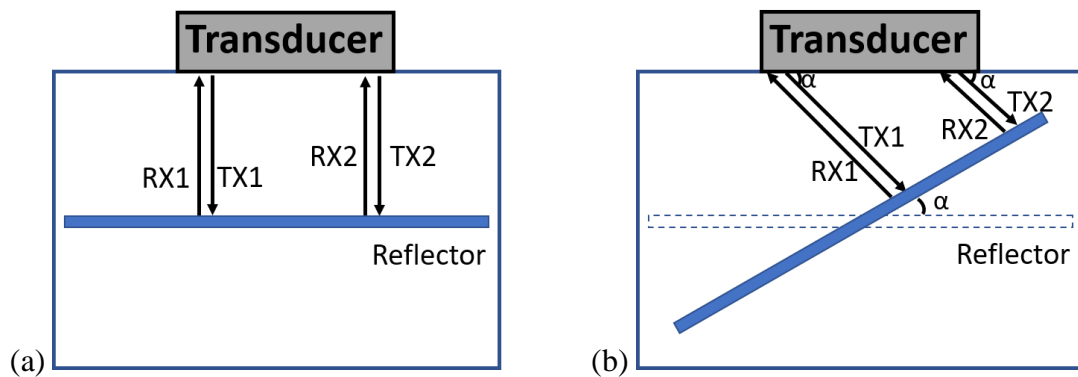


Figure 6.19 Illustration of how the reflected signals are affected by the angle between the tube and the transducer. The angle between the tube and the transducer is (a) 0° (in parallel) and (b) α . TX represents the transmitted sound waves, and RX represents the reflected sound waves.

Figure 6.20 shows the experimental setup, which aims to explore the relationship between the tube angle and the image quality. The tube-tank phantom was immersed in water with the CECAT_79 fixed above the tube. Supporting blocks with different heights were placed under the tube-tank phantom to create angles, which vary from 5° and 20° , between the tube and the front surface of the CECAT_79. The resulting TFM images acquired at each orientation are shown in Figure 6.21, from which it can be

observed that when the angle between the tube and the transducer increased, only the part of the tube, which is within the footprint of the transducer can be clearly imaged. Moreover, the size of the detectable part of the tube decreases as the angle increased. The detected tube walls start to become blurred when the angle reaches 15°, and the situation becomes worse when the angle is increased to 20°.

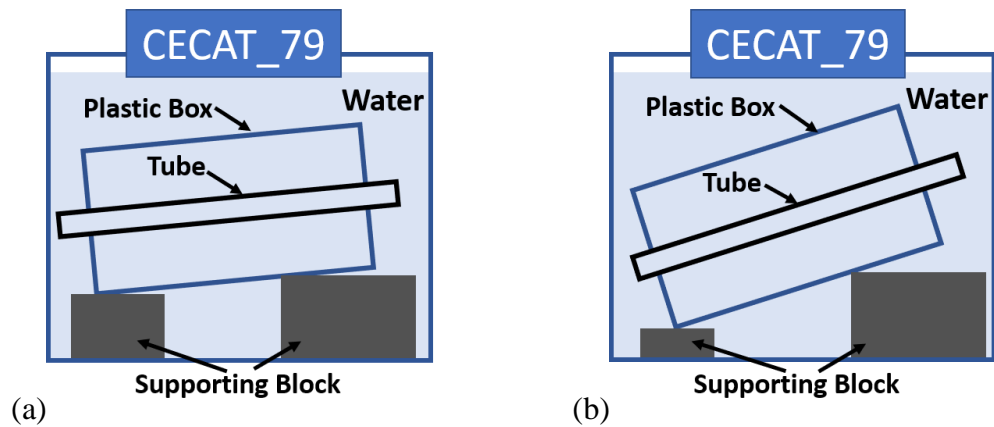


Figure 6.20 Illustration of creating different angles between the tube and the CECAT_79.

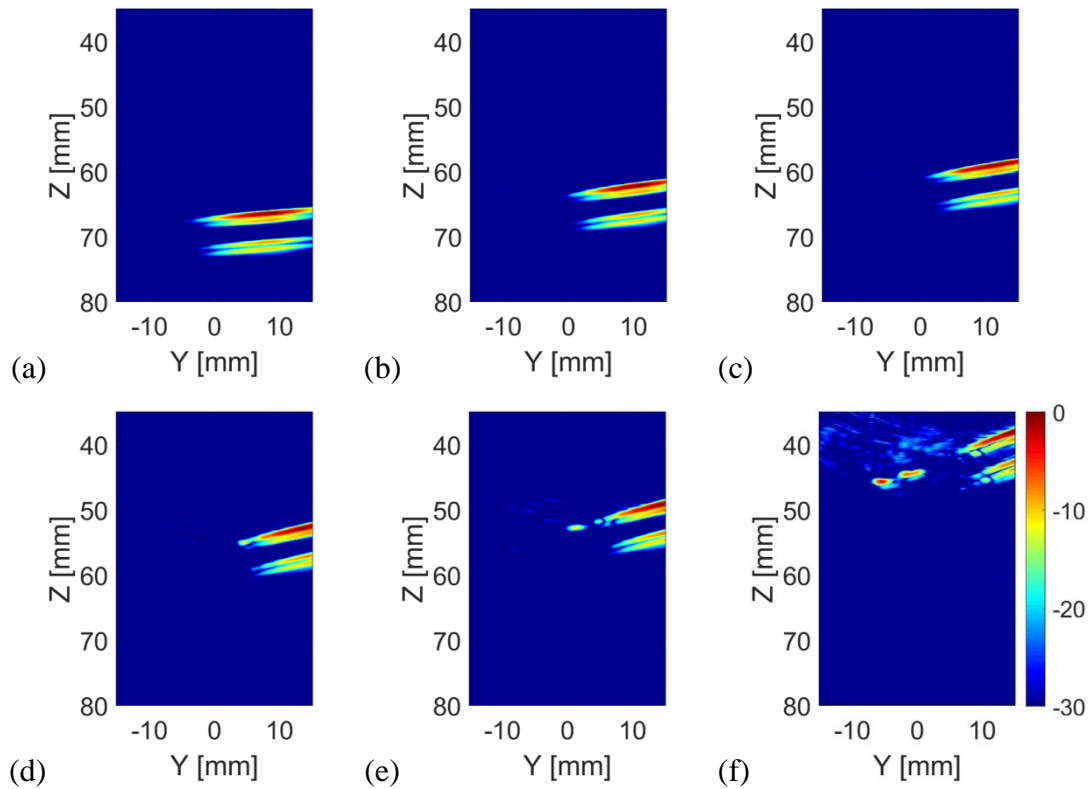


Figure 6.21 TFM images of the tank tube phantom with the tube placed at different angles. From (a) to (f), the angle between the tube and the transducer are 5° , 8° , 10° , 13° , 15° , and 20° , respectively.

The 1D Linear Array Transducer, previously used in Chapter 5, has been used to study the effect from the transducer aperture size on the blurring issue. This transducer consists of 128 array elements, in which the distance between two adjacent array elements is 0.75 mm resulting in an active array aperture of 96 mm. Thus, by controlling the number of elements utilised, it is possible to simulate transducers with different aperture sizes. For comparison purpose, two measurements have been processed, one using the total 128 array elements, while the other one using the first 40 array elements to match the 30 mm aperture of the CECAT_79. The resulting TFM images are shown in Figure 6.22. As shown in Figure 6.22(a), the tube inside the MDU phantom can be

successfully detected and clearly presented in the TFM image, when the full array aperture is utilised. However, when the aperture size is reduced to 30 mm, tube walls become highly unclear and hard to be identified from the background noise, as shown in Figure 6.22(b).

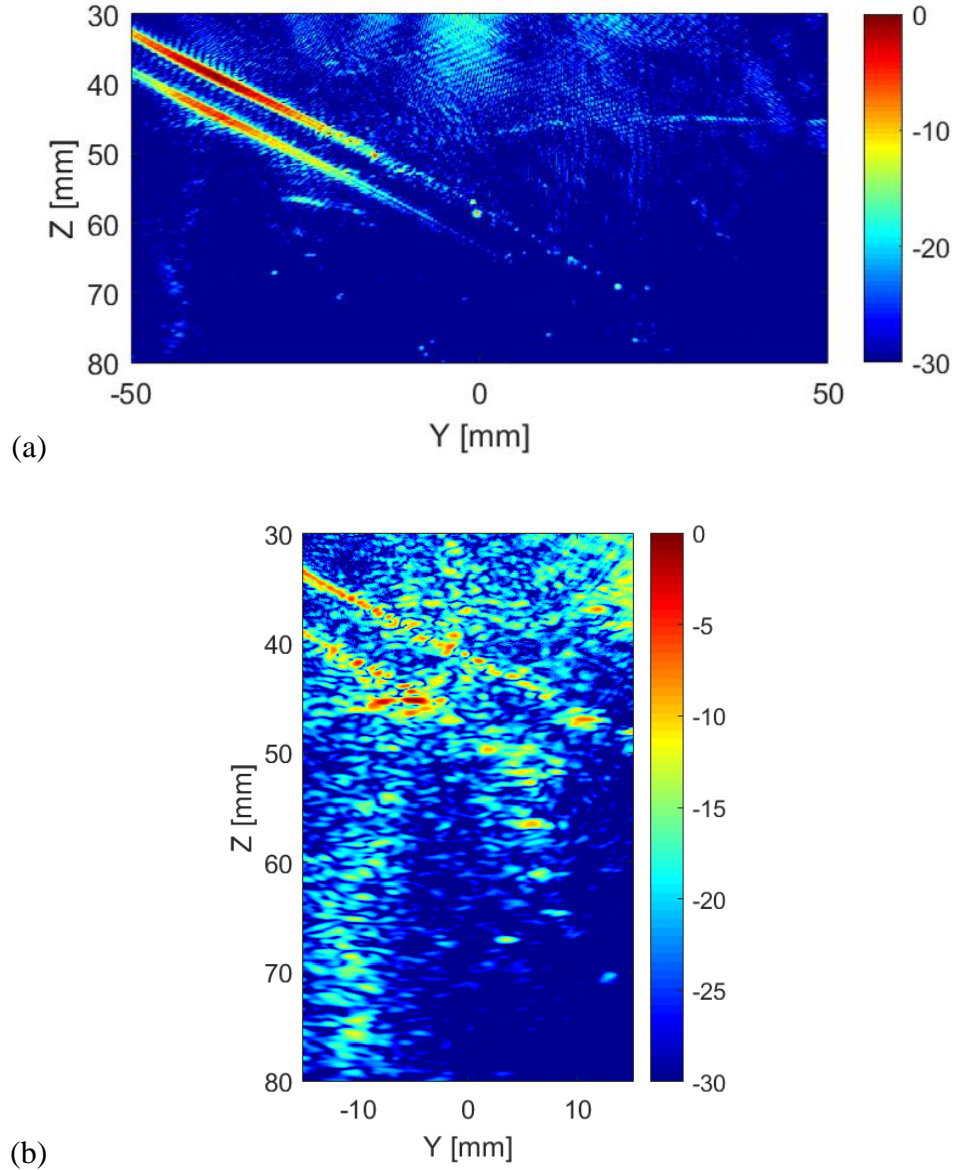


Figure 6.22 TFM images of the MDU phantom from the 1D Linear Array Transducer with (a) the full 128 array elements and (b) the first 40 array elements.

In summary, the increased angle between the tube and the transducer led to the reflected sound waves deviating from the transmitted sound waves. For a transducer with limited aperture size, there will not be enough received sound waves to process a TFM image with appropriate quality. This problem could be solved by either reducing the angle between the tube and the transducer or using a transducer with a larger aperture size.

6.6. Imaging Lab Phantoms

To test the potential of the CECAT_79 to be used in the biomedical field, it is necessary to test its performance imaging through a TMM experimental set-up. Since the MDU phantom has been shown not suitable to be imaged using the CECAT_79, phantoms consisting of the same materials as in the MDU phantom have been fabricated in CUE's laboratory. The same TMM recipe, the same fabrication process, and the same tube as that of the MDU phantom have been used. Figure 6.23 shows one of the lab phantoms that have been fabricated.



Figure 6.23 Example lab phantom.

Figure 6.24 illustrates the basic structures of these lab phantoms. For the first three lab phantoms, as shown in Figure 6.24(a) to Figure 6.24(c), the tubes were placed in parallel with the *y-axis* at depths of 55 mm, 65 mm, and 75 mm from the top surface of the TMM, respectively. These distances were picked to match typical distances from the targeted blood vessels to the temporal window [121] [123] [124], with the tube aligned in parallel to the transducer front face.

To broaden the scope of this experimental evaluation, two additional configurations, at a distance of 65 mm, have been fabricated with the tube located with a small angular orientation with respect to the configuration shown in Figure 6.24(b). For the phantom shown in Figure 6.24(d), the tube was firstly placed along the *y-axis* at 65 mm from the top surface of the TMM and then adjusted to have a 5° angle with respect to the *y-axis* in *Y-Z plane* (i.e. vertical to the front surface of the transducer). For the phantom shown in Figure 6.24(e), the tube was firstly placed along the *x-axis* at 65 mm from the top surface of the TMM, i.e. at right angles to the original configuration illustrated in Figure 6.24(b). Moreover, the tube was also adjusted to have a 5° angle with respect to the *x-axis* in the *X-Y plane* (i.e. horizontal to the front surface of the transducer). These phantoms will be referred to as the 55 mm phantom, the 65 mm phantom, the 75 mm phantom, the Angle V phantom, and the Angle H phantom, respectively.

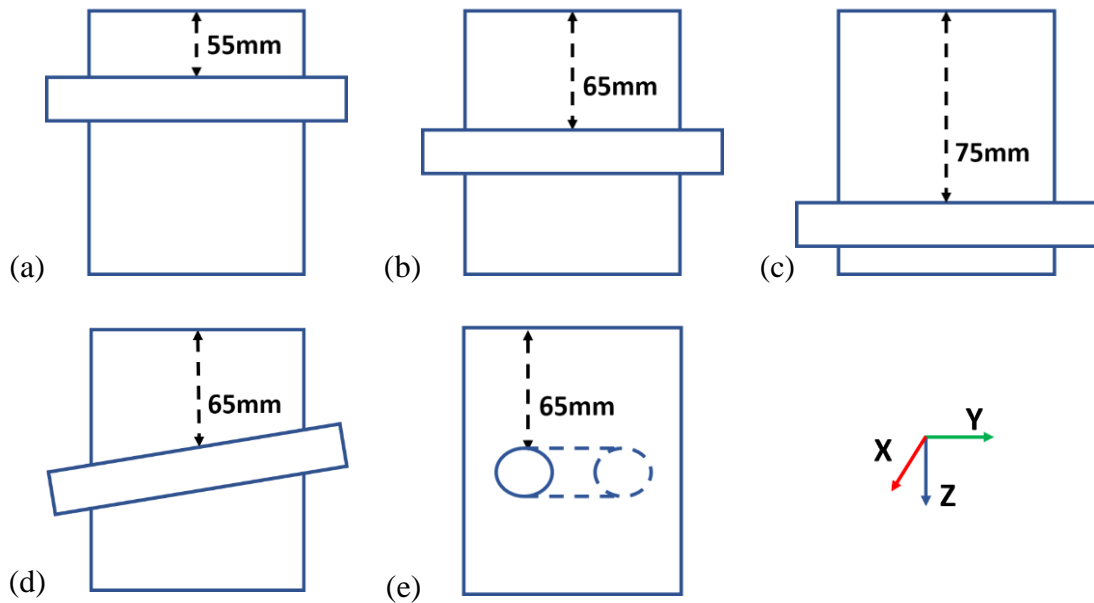


Figure 6.24 Illustrations of the basic structures of the lab phantoms. Name of the phantoms from (a) to (e) is the 55 mm phantom, the 65 mm phantom, the 75 mm phantom, the Angle V phantom, and the Angle H phantom, respectively.

Figure 6.25 illustrates the experimental setup for imaging the lab phantoms using the CECAT_79. The setup is very similar to that of the tank-tube phantom. A syringe is used to fill water from a separate water tank into the tubes. The FMC method has been used to collect data, while the TFM method has been used to process images of the lab phantoms. Since the lab phantoms can be divided into two groups depending on whether the tube is placed along the y -axis or not, the results for each group will be discussed in separate sections. The 55 mm phantom, the 65 mm phantom, the 75 mm phantom, and the Angle V phantom are within the same group, i.e. the tube is placed along the y -axis, and the results for them will be explained in Section 6.6.1. Section 6.6.2 will present results for the Angle H phantom.

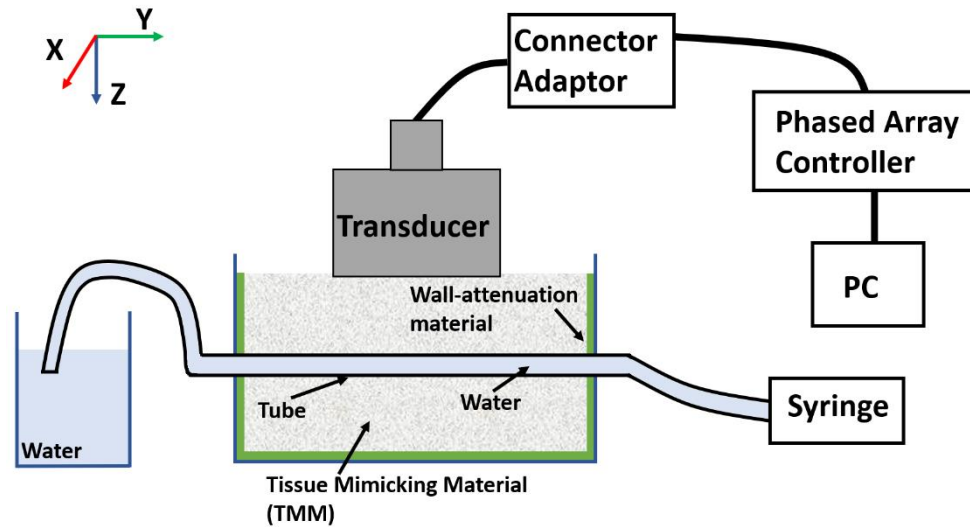


Figure 6.25 Illustration of the experimental setup for imaging the lab phantom using the CECAT_79.

6.6.1. Imaging Lab Phantoms with Tube Placed Along the *y-axis*

Figure 6.26 shows some example TFM images for the phantoms which have the tube placed along the *y-axis* and filled with water. As shown in Figure 6.26, the tube in the phantom has been successfully imaged and can be clearly identified from the image background in all situations. This demonstrates that the CECAT_79 has the potential to detect objects inside the TMM, which is designed for the transcranial ultrasound. The TFM images shown in Figure 6.26 have been converted into greyscale frames and analysed using the tube size estimation algorithm. The results are shown in Figure 6.27. For each image, a part of the frame along the *y-axis*, which contains the tube walls, has been equally divided into four blocks and analysed. The averaged value of the results from those four blocks is recorded as the estimated inner diameter of the tube. The

detailed settings and the estimated tube inner diameter for these lab phantoms are listed in Table 6.4. The estimated tube inner diameter is 3.2 mm for the 55 mm phantom and the 65 mm phantom, and 3.1 mm for the 75 mm phantom and the Angle V phantom. They are all very close to the real tube inner diameter, which is 3.175 mm (1/8 inch). For the Angle V phantom, the tube walls detected by the tube size estimation algorithm can also be used to estimate the angle between the tube and the transducer. This has been achieved by fitting a line to the detected inner walls and then calculate its slope. The estimated angle is 4.1° and is close to the designed 5° angle.

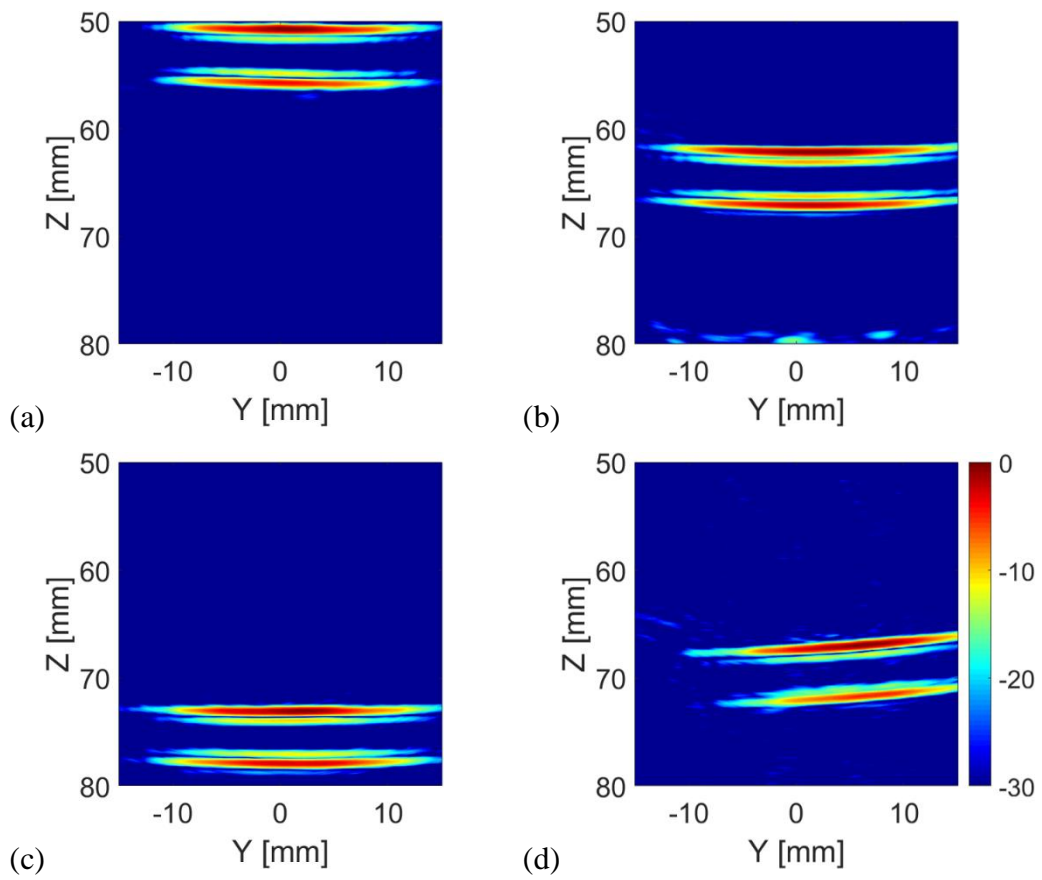


Figure 6.26 Example TFM images of (a) the 55 mm phantom, (b) the 65 mm phantom, (c) the 75 mm phantom, and (d) the Angle V phantom, with no particles from the CECAT_79.

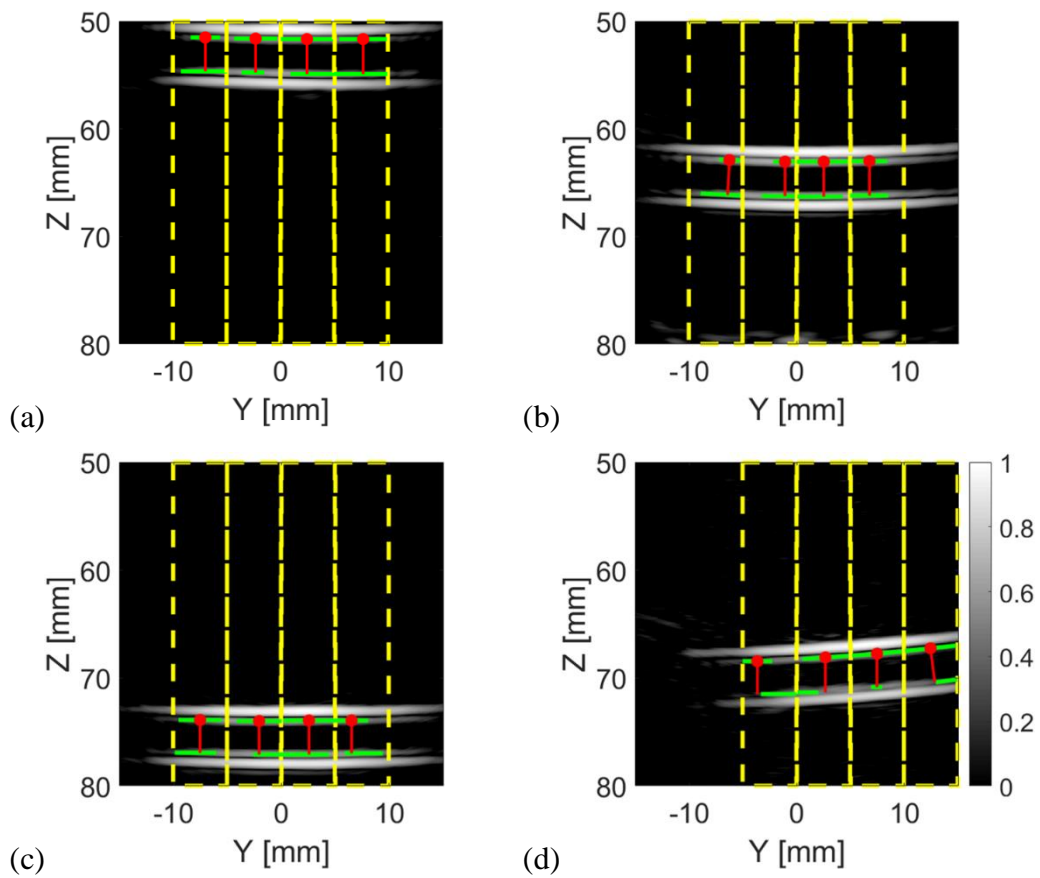


Figure 6.27 The results after applying the tube size estimation algorithm to the frames which have been converted from the example TFM images of (a) the 55 mm phantom, (b) the 65 mm phantom, (c) the 75 mm phantom, and (d) the Angle V phantom, with no particles from the CECAT_79. The yellow dashed lines illustrate the edges of the blocks. The solid green lines are the detected inner walls. The red dots represent the middle point of the corresponding top inner wall, while the solid red lines illustrate the inner diameter estimated for each block.

Table 6.4 Tube size estimation settings and results for the lab phantoms with the tube placed along the *y*-axis.

Phantom Name	<i>Y</i> -axis Settings		Estimated Inner Diameter [mm]
	Range	Block Size	
55 mm Phantom	-10 mm – 10 mm	5 mm	3.2
65 mm Phantom			3.2
75 mm Phantom			3.1
Angle V Phantom	-5 mm – 15 mm		3.1

These lab phantoms were then used to test if the CECAT_79 could detect particles inside the tube, which was surrounded by the TMM. A small piece of the TMM, as shown in Figure 6.28, was input into the tube. The TMM particle has an irregular shape as it was manually cut from a bulk of TMM and the property of the TMM makes it difficult to be machined into a regular small sphere. As shown in Figure 6.28, the edge length of the TMM particle varies between 1 mm and 2 mm. The TMM particle was firstly injected into the lab phantom using the syringe, as shown in Figure 6.25. Next, the CECAT_79 was moved along the *y*-axis until the TMM particle can be seen from the TFM image. The CECAT_79 was then fixed at that position and captured another three TFM images of the lab phantom with the TMM particle removed using the syringe. Those three TFM images were used to process the Background Frame (*BF*) for the particle detection algorithm, as explained in Section 5.4.



Figure 6.28 Illustration of the size and shape of the TMM particle. The 2 mm ball bearing is used as a reference.

Figure 6.29 shows the TFM images of the phantoms with the TMM particle inside the tube. As expected, the intensity of the bright spots in the TFM images which represent the TMM particle is much lower than that of the ball bearings (as shown in Figure 6.13 and Figure 6.15(a)). This is because the acoustic impedance of the TMM particle is much closer to water than the steel ball bearing, which means less sound energy will be reflected at the TMM-water interface than the steel-water interface. It can also be noticed that bright spots of the TMM particle have different intensities and shapes in different lab phantoms. This is mainly caused by the irregular shape of the TMM particle, because when different edges of the TMM particle face the transducer, the reflection/scattering of the incident sound wave will vary. These TFM images have been analysed using the particle detection algorithm and the results are shown in Figure 6.30. The estimated TMM particle size and the estimated inner diameter of the tube are listed in Table 6.5. The estimated particle sizes are all within the range of the TMM particle's edge length. Moreover, the estimated tube inner diameters are all very close to the real tube size.

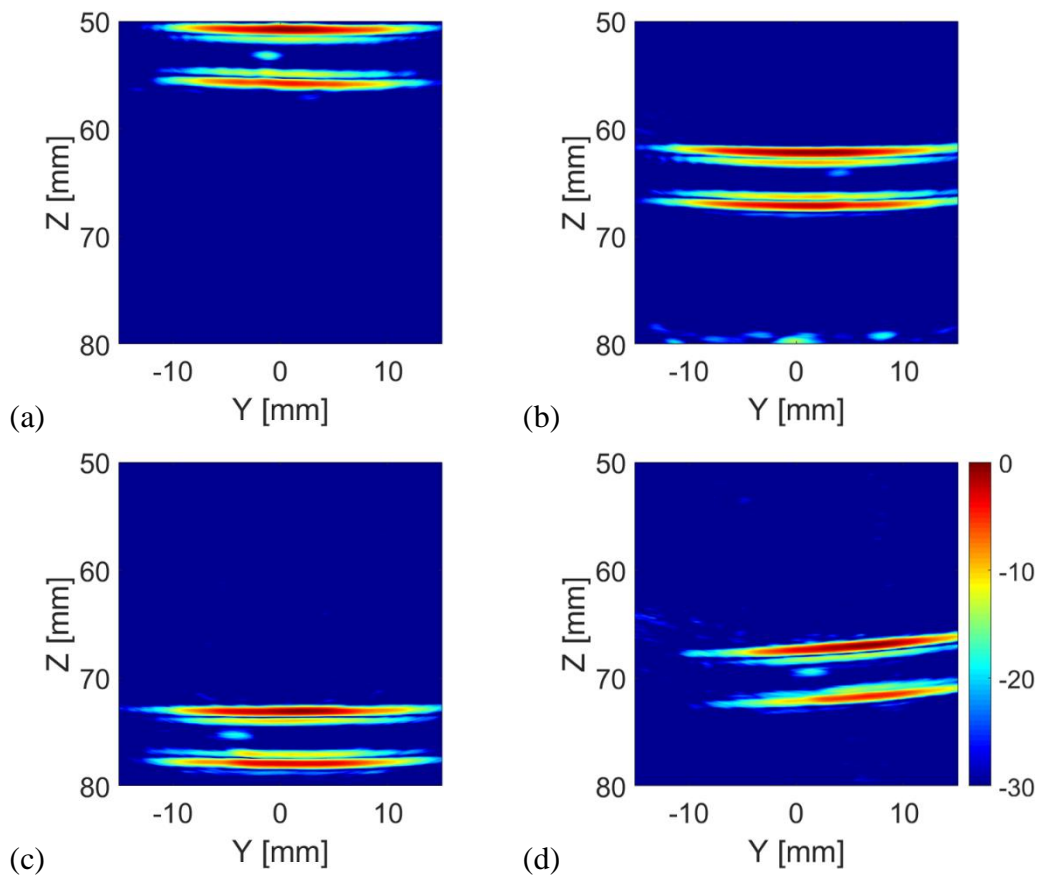


Figure 6.29 TFM image of (a) the 55 mm phantom, (b) the 65 mm phantom, (c) the 75 mm phantom, and (d) the Angle V phantom with the TMM particle placed inside the tube from the CECAT_79.

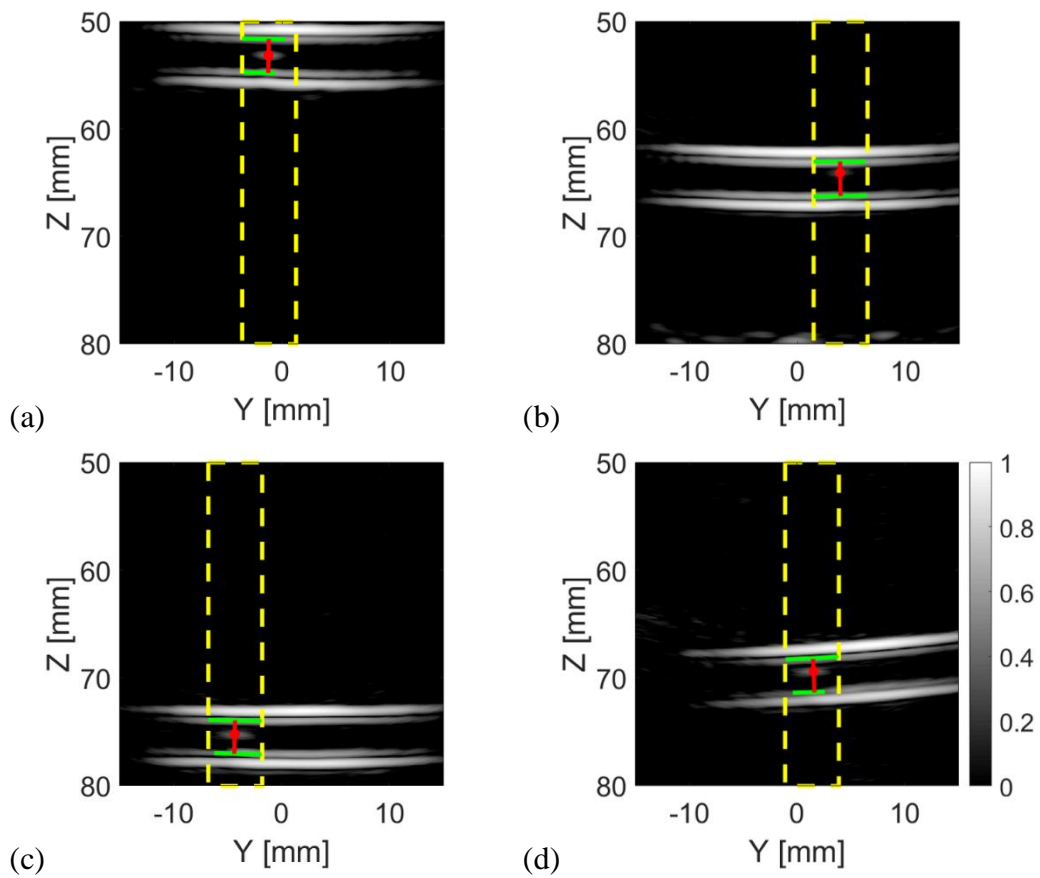


Figure 6.30 The results after applying the particle detection algorithm to the frames which have been converted from the example TFM images of (a) the 55 mm phantom, (b) the 65 mm phantom, (c) the 75 mm phantom, and (d) the Angle V phantom, with the TMM particle placed inside the tube from the CECAT_79. The dashed yellow lines indicate the regions in which a particle has been detected. The solid red lines represent the distance from the particles (red dots) to the top and bottom inner walls of the tube (solid green lines).

Table 6.5 Results for applying the particle size estimation algorithm on TFM images shown in Figure 6.30.

Phantom Name	Estimated Particle Size [mm]	Estimated Inner Diameter [mm]
55 mm Phantom	1.64	3.2
65 mm Phantom	2.15	3.2
75 mm Phantom	1.79	3.1
Angle V Phantom	1.93	3.2

6.6.2. Imaging the Angle H Phantom

For the Angle H phantom, the tube is located along the x -axis. Thus, the TFM image of the Angle H phantom in the Y - Z plane, as shown in Figure 6.31(a), can only show a slice of the tube. This TFM image can still be analysed using the tube size estimation algorithm, as shown in Figure 6.31(b), by zooming in to the area which contains the tube walls. The estimates of the inner diameter of the slice of the tube shown in Figure 6.31 is determined to be 3.2 mm using the proposed tube size estimation algorithm.

The Angle H phantom has also been imaged with the TMM particle placed inside the tube. The experimental process is the same as described in Section 6.6.1. Figure 6.32(a) shows an example TFM image of the Angle H phantom with the TMM particle inside the tube. This TFM image has been successfully analysed by the particle size estimation algorithm, as shown in Figure 6.32(b). The estimated size is 1.65 mm for the TMM particle and 3.2 mm for the tube.

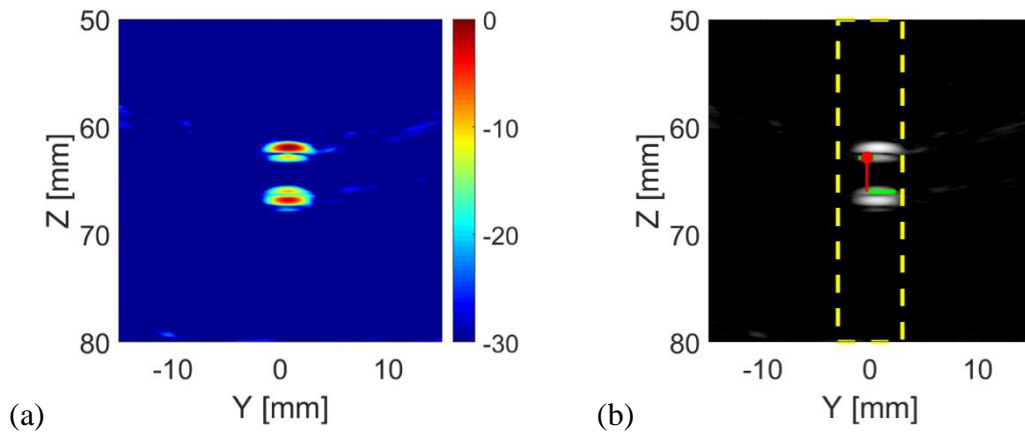


Figure 6.31 (a) An example TFM image of the Angle H phantom with no particles from the CECAT_79. (b) The frame converted from (a) which has been analysed using the tube size estimation algorithm. The yellow dashed lines illustrate the edges of the block that have been extracted from the frame. The solid green lines are the detected inner walls, while the red dot represents the middle point of the top inner wall. The solid red line illustrates the estimated inner diameter, which is 3.2 mm.

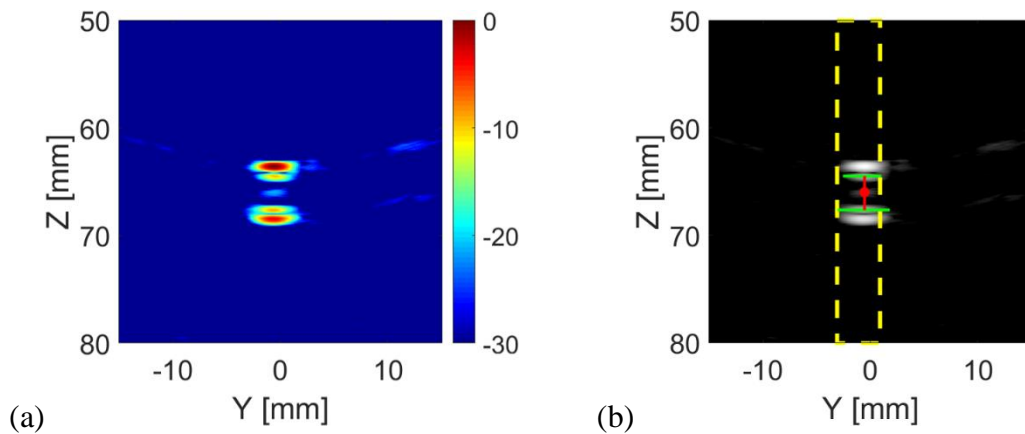


Figure 6.32 (a) An example TFM image of the Angle H phantom with the TMM particle from the CECAT_79. (b) The frame converted from (a) which has been analysed using the particle size estimation algorithm. The dashed yellow lines indicate the region in which the TMM particle has been detected. The solid red line represents the distance from the particle (red dot) to the top and bottom inner walls of the tube (solid green lines). The estimated size of the TMM particle is 1.65 mm, while the estimated tube inner diameter is 3.2 mm.

6.7. Summary

This Chapter has explored and compared the imaging performance of the three prototype transducers. The results from imaging the single small diameter reflector and the wire phantom have shown that the C13_106, which utilised the overall optimal design as discussed in Chapter 3, has the lowest background noise when imaging multiple reflectors and the best sizing accuracy. However, the multiple reflections caused by the second resonance mode makes the C13_106 not suitable to be selected for further imaging tests. For the transducers which have the same array pattern, the one using the CECAT configuration (CECAT_79) has better axial resolution than the one using the C13 configuration (C13_79), which is associated with the CECAT_79's shorter pulse length and wider bandwidth as presented in Chapter 4. In terms of the sizing capability, the C13_79 performs better than the CECAT_79 when sizing the single small diameter rod. Simulation results show that this is related to the three failure elements in the CECAT_79, as they caused a skew of the main lobe in the distance range where the single reflector has been placed in the experiments. However, results from imaging the wire phantom show that when there are multiple reflectors placed in a wider distance range, which is closer to the practical medical scenario, the CECAT_79 would achieve smaller sizing error than the C13_79. Thus, the CECAT_79 has been selected as the acceptable option and has been further analysed. Results from imaging the brass rods also indicate that the sizing result tends to become more accurate as of the size of the reflector increase.

The CECAT_79 has shown potential to be used in the transcranial ultrasound field as it can detect reflectors within the desired distance range of the transcranial ultrasound test. Results from imaging the tank-tube phantom show that the CECAT_79 is capable of estimating the tube size and of detecting the particles inside the tube. The results are very close to the that from the commercial 1D Linear Array Transducer, which proves that, compared to a dense array, the 2D sparse array designed in Chapter 3 could provide appropriate image quality while reducing the total number of elements. The sizing accuracy of the ball bearings is much better compared to that of the brass rods, which indicates that better size estimation can be achieved when more information is available in the image and appropriate imaging algorithms are applied.

Analysis of the results from imaging the MDU phantom using the CECAT_79 shows that there is an upper limit to the angle between the detectable tube and the transducer front face, which is associated with the maximum steering angle of the array. This indicates that as a potential transcranial application, the CECAT_79 may not be able to image blood vessels which have angles with the temporal window exceed the upper limit (15°). Lab phantoms made of the same TMM with the tubes placed at different depths and orientations have proved that the CECAT_79 can detect reflectors, which in this case is the tube, inside the TMM. The tube walls can be clearly identified from the TFM images. These TFM images are suitable to be analysed using the tube size estimation algorithm, and the results are very close to the real tube size. Results from imaging the lab phantoms have also shown that the CECAT_79 can detect the particle which has close acoustic impedance to the surrounding fluid and can estimate the size of the

particle by analysing corresponding TFM images. Moreover, results from imaging the Angle H phantom indicate that, the CECAT_79, as a 2D sparse array transducer, can provide more information of the object under test compared to the 1D Linea Array transducer. For the 1D Linear Array transducer, when the relative position between the transducer and the object under testing is fixed, only one TFM image can be processed. However, for the CECAT_79, multiple Y - Z plane TFM images can be processed along the x -axis, so that as long as the anomaly is within the transducer footprint, the transducer would be able to detect the anomaly.

In summary, the experimental results in this Chapter have confirmed that the CECAT_79, which utilises the fibre CECAT configuration and a well-designed sparse array pattern, has appropriate imaging performance and has the potential to perform well in the real scenario. There are two things to be noticed. First is that, although 2D arrays have been used in imaging the phantoms, only 2D, instead of 3D plots have been produced. The main reason for not producing 3D images is that, this Chapter aimed on exploring the potential of the prototype transducers to be used in transcranial applications, instead of improving the image quality. Moreover, 3D plots require longer processing time, which is not desired in medical applications. So, decision has been made to only produce 2D images. Secondly, although most of the TFM images shown in this Chapter have achieved relatively high image quality, it is not a commonly used imaging method in clinical environment. The idea for the TFM about focusing on all the pixels within the imaging area is not realistic in practice, as the finite size of array elements means they can not cover the whole imaging area. Besides, for the sparse array,

where grating lobes could be an issue, TFM could have resulted lower image quality. Thus, in circumstantial situations, such as when imaging the angled tube-tank phantom, other imaging method, like sector scan, should have utilised to improve image quality.

Chapter 7

Conclusion and Future Work

7.1. Conclusion

This Thesis is concerned with the design, fabrication and evaluation of a 2D sparse array ultrasonic transducer, whose design specification was developed for the potential to be applied for transcranial ultrasound imaging through the temporal window. The project started with designing an appropriate sparse array pattern, which could cover the temporal window and provide low side lobe levels. Prototype transducers were fabricated and characterised. Image processing algorithms to estimate the tube size and anomaly size in an ultrasound image were developed using a commercial linear array and the performance of the developed prototype 2D array transducers and sizing algorithms were experimentally evaluated on a variety of phantoms.

Three aperiodic 2D array configurations, the random array, the sunflower spiral array, and the log spiral array, have been studied by simulating their far-field directivity functions. The performance of each configuration has been evaluated by two criteria, Peak Side Lobe Level (*PSL*) and Integrated Side Lobe Ratio (*ISLR*), with the *PSL* given higher priority to ensure detection of weak reflectors within the main lobe path.

Simulation results demonstrate that a compromise between *PSL* and *ISLR* is required to select a suitable array pattern for fabrication and further evaluation. A log spiral array pattern with 106 elements was selected as the best compromise between optimal *PSL* and *ISLR* through an initial simulation phase, in which a total number of 64243 different aperiodic sparse array configurations were considered. However, due to in-house manufacturing limitations, a second simulation phase was required and resulted in a 79-element log spiral array pattern with a greater separation between array elements to enable fabrication using piezoceramic fibre technology.

Three prototype transducers have been fabricated based on those two array patterns, two with the 79-element configuration but different piezoelectric microstructure (the C13_79 and the CECAT_79), and one with the 106-element configuration (the C13_106). Except for the active layer, the manufacturing processes for the rest components within each transducer are identical. For the active layer, those two C13 transducers used the conventional ‘dice and fill’ fabrication method [33], while the CECAT device used the ‘place and fill’ method using piezoceramic fibres [10]. The ‘place and fill’ method is relatively time-consuming but can produce multiple samples of active layers through one manufacturing cycle. The use of flexible PCB and conductive epoxy is used to achieve an individual electrical connection to the array elements. The final size of the prototype transducers is too large for most applications, in particular for use in a medical scenario, but was not considered to be an issue at this proof of concept stage.

Characterisation results of the prototype transducers showed that all three prototype transducers were operational, although there was some performance variation across

array elements and unfortunately, some dead (null response) elements. All the array elements from C13_106 and C13_79 have successfully captured responses in the pulse-echo test, with three elements from the CECAT_79 failing to do so. Comparison between C13_79 and CECAT_79 demonstrates that the CECAT structure, which has aperiodic microstructure and only contains active piezoceramic material with the array element areas, can efficiently reduce the overall mechanical cross-talk level between neighbouring array elements (10 dB lower compared to the C13_79) and improve the operational bandwidth of the transducer (47.44% to 30.95%), although the sensitivity is slightly lower than for the C13 structure (11.17mV to 16.67mV). Compared to the C13_79; the C13_106 has a lower sensitivity and higher cross-talk level due to the smaller element size and higher elements density of the 106-element array pattern. An extra mode is generated near the fundamental thickness mode of the C13_106 after application of the matching layer. This extraneous mode resulted in a reduction of C13_106's bandwidth and introduced an additional artefact when imaging small diameter reflectors in the concluding experimental phase. These results indicate that the manufacturing tolerance, e.g. the thickness of the matching layer, could have great effect on the transducer performance and thus thickness variation should be minimised across the aperture.

In addition to transducer design, image processing algorithms were explored in this Thesis to detect objects in a tube and simulate anomaly detection in a blood vessel associated with transcranial ultrasound. Initially, a simple tank-tube phantom with ball bearings placed inside the tube was imaged using a commercial 1D linear array to

provide datasets for algorithm development. By combining Difference Imaging, the Hough transform, and Morphological Opening, two image processing algorithms were developed, one for tube size estimation and one for particle detection. These two algorithms can automatically detect the tube and the object inside it from a processed Total Focussing Method (TFM) image. Moreover, the algorithms will estimate the inner diameter of the tube and the size of the particle.

The first experimental tests considered imaging performance from small diameter reflectors and demonstrated that the C13_106 performs the best in terms of image background noise and has better axial resolution than the C13_79. This is associated with the higher resonance frequency of the CECAT_106 as demonstrated in results from the pulse-echo response. PSF for each prototype transducer can be achieved based on results from imaging the $\sim 0.5\lambda$ reflector. Results show that the C13 devices perform better in terms of the lateral resolution. This conclusion can also be derived from the LDV scanning as the C13 devices show increased active aperture size. The CECAT_79 failed to match the performance of the C13_79 when sizing the single small diameter reflector due to the three improperly-working elements. However, results from imaging the wire phantom show that the CECAT_79 could achieve better sizing performance when multiple reflectors exist in the imaging area, which is closer to the practical scenario. Overall, the CECAT_79 device demonstrated a good imaging performance when compared to the other two devices, and was then used exclusively in the remaining phantom experiments as this technology was key to the original medical device proposal through discussions with the NHS Greater Glasgow & Clyde Medical Devices Unit team.

Results from imaging the same single reflector at different depths demonstrated that the CECAT_79 can cover the desired depth range associated with transcranial ultrasound. The CECAT_79 has then been applied to image the tank-tube phantom with ball bearings placed inside the tube, which was used to develop the image processing algorithms. The results show that the CECAT_79 is capable of providing images which have comparable quality to those generated by the commercial linear array, importantly with a much smaller active footprint. Moreover, the images from the CECAT_79 can provide an accurate estimation of the tube size and the particle (the ball bearing) size, with overall 0.1 mm precision, when being analysed by the image processing algorithms. Finally, bespoke phantoms incorporating Tissue Mimicking Material (TMM) were fabricated, with tubes inserted at different depths and orientations to evaluate the imaging performance of the CECAT_79 device. A small piece of TMM was placed inside the tube to simulate the blockage of a blood vessel. Importantly, both the tube and the TMM particle are clearly detected in the processed TFM images and dimensions of the tube and the anomaly were accurately estimated (with 0.1 mm precision) by applying the developed image processing algorithms.

In summary, an ultrasonic array system has been designed, fabricated, characterised and evaluated for potential to be used in a transcranial ultrasound imaging application through the temporal window. The system comprises a 2D aperiodic ultrasonic array and signal/image processing algorithms. Laboratory tests on targeted TMM phantoms demonstrated the potential for this technology for this application, although further

modifications should be developed to improve the system performance. These are addressed in the next Section.

7.2. Future Work

7.2.1. Modification of the Manufacturing Process

Future work in manufacturing process consists of two aspects.

1. Simplify the manufacturing process for the fibre CECAT active layer.
2. Reduce the overall transducer housing dimensions.

The manufacturing method for the fibre CECAT active layer, as described in Chapter 4, requires manually placing the piezoelectric fibres into a jig, which consists of two parallel plates, each incorporating holes representing the desired array pattern, and separated by a distance of 25 mm. It is a time-consuming process to manually place the piezoceramic fibres into these holes, which becomes more challenging as the number of elements increases. Moreover, there is a manufacturing limitation with respect to array element density, size and spacing. The manufacturing process could be modified as follows:

1. Build a jig with the same structure as described in Chapter 4, but with only one hole which has the same size as the array element drilled on the plates.
2. Process through the ‘place and fill’ method and cut the desired number of slices, i.e. the number of elements in the array. The thickness of each slice should be thicker than the designed thickness of the active layer.

3. Build a base with the desired array pattern using 3D printing technique to hold the single element slices at desired positions.
4. Fill the base with the desired epoxy and cure.
5. Machine the composites into the desired dimension.

The final dimensions of the housed prototype transducer fabricated for this Thesis is large because the housing has to be big enough to package the twisted paired wires and the flexible PCB inside – note that this was necessary to align the project to other array development work in CUE. To reduce the overall transducer dimensions, finer scaled wires should be incorporated, with this technology readily available within commercial transducer organisations, and medical device research centres. More importantly, the layout of the flexible PCB should be modified to package it into a smaller space – this was not necessary for this work as the Thesis focussed on a proof-of-concept approach rather than engineering a finished product. Moreover, the overall transducer size would have to be reduced to enable it to be embedded into a mechanical head-frame, which could be attached to the patient without being held by an operator.

7.2.2. Modification of the Phantoms

During the experimental evaluation process, as described in Chapter 6, water has been used to fill up the tube inside the TMM phantom, but it was not possible to create flow conditions. To make the evaluation process more representative of the practical situation, blood mimicking material (BMM) should be used instead of water. Moreover, a pump should be used to control the fluid and/or the particle running through the tube at the velocities corresponding to typical blood flow conditions. In addition, phantoms with

more complex tube structure would be more representative of the main blood vessels observed through the temporal window.

7.2.3. Modification of the Ultrasonic Imaging Methods

Firstly, Doppler imaging should be evaluated as it can provide information associated with the direction and speed of the liquid flow. The Doppler image can be overlapped with an ultrasound image, such as a TFM image, to increase the amount of information contained in one image.

Secondly, aberration correction should be applied to improve image quality. In this project, the standard TFM method has been used to produce ultrasound images for relatively simple structures. However, in more complex situations, images created using the basic TFM method may contain aberrations due to the attenuation, multi-scattering, and variations in the sound propagation speed [127]. For the transcranial ultrasound, aberration correction can be achieved by using low-frequency transducers, or using MRI/CT images as references, or using two transducers at the opposite sides of the temporal windows [127]. The motion detection method can also be used to provide aberration correction for the blood flow images [128].

Thirdly, 3D images should be considered and produced using the 2D sparse arrays developed in this work, as they could provide information of the object under detecting in a more visual way.

References

- [1]. S. Hatano, "Experience from a multicentre stroke register: a preliminary report", *Bulletin of the World Health Organization*, vol. 54, pp. 541-553, 1976.
- [2]. E. Donkor, "Stroke in the 21st Century: A Snapshot of the Burden, Epidemiology, and Quality of Life", *Stroke Research and Treatment*, vol. 2018, pp. 1-10, 2018.
- [3]. T. Musuka, S. Wilton, M. Traboulsi and M. Hill, "Diagnosis and management of acute ischemic stroke: speed is critical", *Canadian Medical Association Journal*, vol. 187, no. 12, pp. 887-893, 2015.
- [4]. A. Amar, "Brain and Vascular Imaging of Acute Stroke", *World Neurosurgery*, vol. 76, no. 6, pp. S3-S8, 2011.
- [5]. J. Porres, J. Cerezuela, O. Luque and P. Marco, "Computed Tomography Scan and ICD Interaction", *Case Reports in Medicine*, vol. 2009, pp. 1-3, 2009.
- [6]. R. Aaslid, T. Markwalder and H. Nornes, "Noninvasive transcranial Doppler ultrasound recording of flow velocity in basal cerebral arteries", *Journal of Neurosurgery*, vol. 57, no. 6, pp. 769-774, 1982.
- [7]. M. E. Schafer, J. Alleman, A. Alexandrov and K. Barlinn, "Development of an operator independent ultrasound therapeutic device for stroke treatment," *2012 IEEE International Ultrasonics Symposium*, Dresden, 2012, pp. 1948-1951.
- [8]. G. Tsivgoulis and A. Alexandrov, "Ultrasound-enhanced thrombolysis in acute ischemic stroke: Potential, failures, and safety", *Neurotherapeutics*, vol. 4, no. 3, pp. 420-427, 2007.
- [9]. A. Demchuk, B. Menon and M. Goyal, "Comparing Vessel Imaging Noncontrast Computed Tomography/Computed Tomographic Angiography Should Be the New Minimum Standard in Acute Disabling Stroke", *Stroke*, vol. 47, no. 1, pp. 273-281, 2016.
- [10]. G. Harvey, A. Gachagan, J. Mackersie, T. Mccunnie and R. Banks, "Flexible ultrasonic transducers incorporating piezoelectric fibres", *IEEE Transactions on*

Ultrasonics, Ferroelectrics and Frequency Control, vol. 56, no. 9, pp. 1999-2009, 2009.

- [11]. K. Uchino, "Piezoelectric ceramics for transducers," in *Ultrasonic Transducers*, K. Nakamura, Ed. Cambridge, UK: Woodhead Publishing Limited, 2012, pp. 70–116.
- [12]. S. Moheimani and A. Fleming, *Piezoelectric transducers for vibration control and damping*. London: Springer, 2006.
- [13]. D. Ensminger and L. Bond, *Ultrasonics*, 3rd ed. Boca Raton, FL: Taylor & Francis, 2012.
- [14]. M. Lethiecq, F. Levassort, D. Certon and L. Tran-Huu-Hue, "Piezoelectric Transducer Design for Medical Diagnosis and NDE", in *Piezoelectric and Acoustic Materials for Transducer Applications*, 1st ed., A. Safari and E. Akdogan, Ed. New York: Springer US, 2008, pp. 191-215.
- [15]. J. F. Tressler, "Piezoelectric Transducer Design for Sonar Applications", in *Piezoelectric and Acoustic Materials for Transducer Applications*, 1st ed., A. Safari and E. Akdogan, Ed. New York: Springer US, 2008, pp. 191-215.
- [16]. H. Liu, J. Zhong, C. Lee, S. Lee and L. Lin, "A comprehensive review on piezoelectric energy harvesting technology: Materials, mechanisms, and applications", *Applied Physics Reviews*, vol. 5, no. 4, p. 041306, 2018.
- [17]. *IEEE standard on piezoelectricity*. 176-1987, ANSI/IEEE Standard, 1987.
- [18]. H. Jaffe and D. Berlincourt, "Piezoelectric transducer materials", *Proceedings of the IEEE*, vol. 53, no. 10, pp. 1372-1386, 1965. Available: 10.1109/proc.1965.4253.
- [19]. S. Cochran, "Piezoelectricity and basic configurations for piezoelectric ultrasonic transducers," in *Ultrasonic Transducers*, K. Nakamura, Ed. Cambridge, UK: Woodhead Publishing Limited, 2012, pp. 3–35.
- [20]. T. Stevenson et al., "Piezoelectric materials for high temperature transducers and actuators", *Journal of Materials Science: Materials in Electronics*, vol. 26, no. 12, pp. 9256-9267, 2015. Available: <https://doi.org/10.1007/s10854-015-3629-4>.

- [21]. H. Shekhani and K. Uchino, "Evaluation of the mechanical quality factor under high power conditions in piezoelectric ceramics from electrical power", *Journal of the European Ceramic Society*, vol. 35, no. 2, pp. 541-544, 2014. Available: <https://doi.org/10.1016/j.jeurceramsoc.2014.08.038>. [Accessed 15 October 2019].
- [22]. R. Newnham, D. Skinner and L. Cross, "Connectivity and piezoelectric-pyroelectric composites", *Materials Research Bulletin*, vol. 13, no. 5, pp. 525-536, 1978. Available: 10.1016/0025-5408(78)90161-7.
- [23]. W. Smith and B. Auld, "Modeling 1-3 composite piezoelectrics: thickness mode oscillations", *IEEE Transactions on Ultrasonics, Ferroelectrics and Frequency Control*, vol. 38, no. 1, pp. 40-47, 1991. Available: 10.1109/58.67833.
- [24]. J. Hossack and G. Hayward, "Finite-element analysis of 1-3 composite transducers", *IEEE Transactions on Ultrasonics, Ferroelectrics and Frequency Control*, vol. 38, no. 6, pp. 618-629, 1991. Available: 10.1109/58.108860.
- [25]. G. Hayward, J. Bennett and R. Hamilton, "A theoretical study on the influence of some constituent material properties on the behavior of 1-3 connectivity composite transducers", *The Journal of the Acoustical Society of America*, vol. 98, no. 4, pp. 2187-2196, 1995. Available: 10.1121/1.413333.
- [26]. J. T. Bennett, "Development of a Finite Element Modelling System for Piezocomposite Transducer," PhD Thesis, University of Strathclyde, 1995.
- [27]. G. Hayward and J. Bennett, "Assessing the influence of pillar aspect ratio on the behavior of 1-3 connectivity composite transducers", *IEEE Transactions on Ultrasonics, Ferroelectrics and Frequency Control*, vol. 43, no. 1, pp. 98-108, 1996. Available: 10.1109/58.484469.
- [28]. R. Banks, R. O'Leary and G. Hayward, "Enhancing the bandwidth of piezoelectric composite transducers for air-coupled non-destructive evaluation", *Ultrasonics*, vol. 75, pp. 132-144, 2017. Available: 10.1016/j.ultras.2016.10.007.
- [29]. T. Gururaja, W. Schulze, L. Cross, R. Newnham, B. Auld and Y. Wang, "Piezoelectric Composite Materials for Ultrasonic Transducer Applications. Part I: Resonant Modes of Vibration of PZT Rod-Polymer Composites", *IEEE*

Transactions on Sonics and Ultrasonics, vol. 32, no. 4, pp. 481-498, 1985.
Available: 10.1109/t-su.1985.31623.

- [30]. W. A. Smith, A. Shaulov and B. A. Auld, "Tailoring the Properties of Composite Piezoelectric Materials for Medical Ultrasonic Transducers," *IEEE 1985 Ultrasonics Symposium*, San Francisco, CA, USA, 1985, pp. 642-647.
- [31]. C. Oakley, "Analysis and Development of Piezoelectric Composites for Medical Ultrasound Transducer Applications," PhD Thesis, The Pennsylvania State University, 1991.
- [32]. F. Craciun, L. Sorba, E. Molinari and M. Pappalardo, "A coupled-mode theory for periodic piezoelectric composites", *IEEE Transactions on Ultrasonics, Ferroelectrics and Frequency Control*, vol. 36, no. 1, pp. 50-56, 1989. Available: 10.1109/58.16968.
- [33]. H. P. Savakus, K. A. Klicker, and R. E. Newnham, "PZT-epoxy piezoelectric transducers: A simplified fabrication procedure," *Mater. Res. Bull.*, vol. 16, no. 6, pp. 677-680, Jun. 1981.
- [34]. G. Harvey, A. Gachagan, J. W. Mackersie and R. Banks, "P2O-2 Exploring the Advantages of a Random 1-3 Connectivity Piezocomposite Structure Incorporating Piezoelectric Fibres as the Active Element," *2006 IEEE Ultrasonics Symposium*, Vancouver, BC, 2006, pp. 1903-1906.
- [35]. "PZT Fibers", *Smart-material.com*, 2017. (Online). Available: <http://www.smart-material.com/PZTFiber-product-main.html>. [Accessed: 23-Jan-2017].
- [36]. R. Hamilton and G. Hayward, "The design of low volume fraction 1-3 connectivity composite transducers using finite element modelling techniques," *IEEE 1992 Ultrasonics Symposium Proceedings*, Tucson, AZ, USA, 1992, pp. 531-534.
- [37]. J. Brown, E. Cherin, Jianhua Yin and F. Foster, "Fabrication and performance of high-frequency composite transducers with triangular-pillar geometry", *IEEE Transactions on Ultrasonics, Ferroelectrics and Frequency Control*, vol. 56, no. 4, pp. 827-836, 2009.

- [38]. J. Yin, M. Lee, J. Brown, E. Cherin and F. Foster, "Effect of triangular pillar geometry on high- frequency piezocomposite transducers", *IEEE Transactions on Ultrasonics, Ferroelectrics and Frequency Control*, vol. 57, no. 4, pp. 957-968, 2010.
- [39]. J. A. Hossack, B. A. Auld and H. D. Batha, "Techniques for suppressing spurious resonant modes in 1:3 composite transducers," *IEEE 1991 Ultrasonics Symposium*, Orlando, FL, USA, 1991, pp. 651-655 vol.1.
- [40]. J. R. Yuan, P. Marsh, K. Liang and H. Kunkel, "The dynamic characteristics of composites with periodic and random structure," *1996 IEEE Ultrasonics Symposium. Proceedings*, San Antonio, TX, USA, 1996, pp. 949-954 vol.2.
- [41]. R. Rouffaud, F. Levassort, M. Pham Thi, C. Bantignies, M. Lethiecq and A. Hladky-Hennion, "Super-Cell Piezoelectric Composite With 1–3 Connectivity", *IEEE Transactions on Ultrasonics, Ferroelectrics, and Frequency Control*, vol. 63, no. 12, pp. 2215-2223, 2016.
- [42]. H. Yang, J. Cannata, J. Williams and K. Shung, "Crosstalk reduction for high-frequency linear-array ultrasound transducers using 1-3 piezocomposites with pseudo-random pillars", *IEEE Transactions on Ultrasonics, Ferroelectrics, and Frequency Control*, vol. 59, no. 10, pp. 2312-2321, 2012.
- [43]. H. Yang *et al.*, "Low cross-talk kerfless annular array ultrasound transducers using 1–3 piezocomposites with pseudo-random pillars," *2012 IEEE International Ultrasonics Symposium*, Dresden, 2012, pp. 1560-1563.
- [44]. H. Fang, Z. Qiu, A. Mulholland, R. O'Leary and A. Gachagan, "Broadband 1–3 Piezoelectric Composite Transducer Design Using Sierpinski Gasket Fractal Geometry", *IEEE Transactions on Ultrasonics, Ferroelectrics, and Frequency Control*, vol. 65, no. 12, pp. 2429-2439, 2018.
- [45]. S. Huang *et al.*, "Preparation and performance of 1–3 multi-element piezoelectric composites", *Ceramics International*, vol. 41, no. 5, pp. 6759-6763, 2015.

- [46]. C. He, Y. Wang, Y. Lu, Y. Liu and B. Wu, "Design and Fabrication of Air-Based 1-3 Piezoelectric Composite Transducer for Air-Coupled Ultrasonic Applications", *Journal of Sensors*, vol. 2016, pp. 1-11, 2016.
- [47]. L. Qin, L. Wang, D. Long, C. Zhong, B. Zhang and J. Liu, "The study of 1-1-3 piezoelectric composite based on relaxor ferroelectric single crystal," *2014 Joint IEEE International Symposium on the Applications of Ferroelectric, International Workshop on Acoustic Transduction Materials and Devices & Workshop on Piezoresponse Force Microscopy*, State College, PA, 2014, pp. 1-4.
- [48]. X. Mi, L. Qin, Q. Liao and L. Wang, "Electromechanical coupling coefficient and acoustic impedance of 1-1-3 piezoelectric composites", *Ceramics International*, vol. 43, no. 9, pp. 7374-7377, 2017.
- [49]. C. Zhong, L. Wang, L. Qin and Y. Zhang, "Characterisation of an improved 1-3 piezoelectric composite by simulation and experiment", *Journal of Applied Biomaterials & Functional Materials*, vol. 15, no. 1, pp. 0-0, 2017.
- [50]. Y. Zhang, L. Wang and L. Qin, "Equivalent parameter model of 1-3 piezocomposite with a sandwich polymer", *Results in Physics*, vol. 9, pp. 1256-1261, 2018.
- [51]. A. Abrar, D. Zhang, B. Su, T. Button, K. Kirk and S. Cochran, "1–3 connectivity piezoelectric ceramic–polymer composite transducers made with viscous polymer processing for high frequency ultrasound", *Ultrasonics*, vol. 42, no. 1-9, pp. 479-484, 2004.
- [52]. C. E. M. Démore, S. Cochran, L. Garcia-Gancedo, F. Dauchy, T. W. Button and J. C. Bamber, "1–3 piezocomposite design optimised for high frequency kerfless transducer arrays," *2009 IEEE International Ultrasonics Symposium*, Rome, 2009, pp. 1-4.
- [53]. S. Gebhardt, P. Günther, H. Neubert and S. Fröhlich, "Towards fabrication of high frequency ultrasonic transducers using soft mold process," *2016 IEEE International Ultrasonics Symposium (IUS)*, Tours, 2016, pp. 1-4.
- [54]. P. Gunther, P. Neumeister, H. Neubert and S. Gebhardt, "Development of 40-MHz Ultrasonic Transducers via Soft Mold Process", *IEEE Transactions on*

Ultrasonics, Ferroelectrics, and Frequency Control, vol. 66, no. 9, pp. 1497-1503, 2019.

- [55]. Z. Chen et al., "3D printing of piezoelectric element for energy focusing and ultrasonic sensing", *Nano Energy*, vol. 27, pp. 78-86, 2016. Available: 10.1016/j.nanoen.2016.06.048.
- [56]. Z. Chen et al., "Three-Dimensional Printed Piezoelectric Array for Improving Acoustic Field and Spatial Resolution in Medical Ultrasonic Imaging", *Micromachines*, vol. 10, no. 3, p. 170, 2019. Available: 10.3390/mi10030170.
- [57]. S. Rienstra and A. Hirschberg, *An Introduction to Acoustics*. 2019, pp. 66-68.
- [58]. G. Kossoff, "The Effects of Backing and Matching on the Performance of Piezoelectric Ceramic Transducers", *IEEE Transactions on Sonics and Ultrasonics*, vol. 13, no. 1, pp. 20-30, 1966.
- [59]. T. Gomez Alvarez-Arenas, "Acoustic Impedance Matching of Piezoelectric Transducers to the Air", *IEEE Transactions on Ultrasonics, Ferroelectrics and Frequency Control*, vol. 51, no. 5, pp. 624-633, 2004.
- [60]. C. S. Desilets, J. D. Fraser and G. S. Kino, "The design of efficient broad-band piezoelectric transducers," in *IEEE Transactions on Sonics and Ultrasonics*, vol. 25, no. 3, pp. 115-125, May 1978.
- [61]. N. Tole, *BASIC PHYSICS OF ULTRASONOGRAPHIC IMAGING*. Malta: Interprint Limited, 2005.
- [62]. K. K. Shung and M. Zippuro, "Ultrasonic transducers and arrays," in *IEEE Engineering in Medicine and Biology Magazine*, vol. 15, no. 6, pp. 20-30, Nov.-Dec. 1996.
- [63]. B. Drinkwater and P. Wilcox, "Ultrasonic arrays for non-destructive evaluation: A review", *NDT & E International*, vol. 39, no. 7, pp. 525-541, 2006. Available: 10.1016/j.ndteint.2006.03.006.
- [64]. D. G. Wildes, R. Y. Chiao, C. M. W. Daft, K. W. Rigby, L. S. Smith and K. E. Thomenius, "Elevation performance of 1.25D and 1.5D transducer arrays," in

- IEEE Transactions on Ultrasonics, Ferroelectrics, and Frequency Control, vol. 44, no. 5, pp. 1027-1037, Sept. 1997.
- [65]. B. Steinberg, *Principles of Aperture and Array Systems Design*. New York: Wiley, 1976, p. 54.
- [66]. P. Wilcox and J. Zhang, "Quantification of the Effect of Array Element Pitch on Imaging Performance", *IEEE Transactions on Ultrasonics, Ferroelectrics, and Frequency Control*, vol. 65, no. 4, pp. 600-616, 2018.
- [67]. O. Martínez-Graullera, C. Martín, G. Godoy and L. Ullate, "2D array design based on Fermat spiral for ultrasound imaging", *Ultrasonics*, vol. 50, no. 2, pp. 280-289, 2010.
- [68]. S. Smith, H. Pavy and O. von Ramm, "High-speed ultrasound volumetric imaging system. I. Transducer design and beam steering", *IEEE Transactions on Ultrasonics, Ferroelectrics and Frequency Control*, vol. 38, no. 2, pp. 100-108, 1991.
- [69]. J. Dziewierz, "2D ultrasonic phased arrays for quantitative characterisation of complex defects", PhD, University Strathclyde, 2015.
- [70]. A. Tweedie, "Spiral 2D Array Designs for Volumetric Imaging", PhD, University of Strathclyde, 2011.
- [71]. J. W. Choe, Ö Oralkan and P. T. Khuri-Yakub, "Design optimisation for a 2-D sparse transducer array for 3-D ultrasound imaging," *2010 IEEE International Ultrasonics Symposium*, San Diego, CA, 2010, pp. 1928-1931.
- [72]. P. Yang, B. Chen and K. Shi, "A novel method to design sparse linear arrays for ultrasonic phased array", *Ultrasonics*, vol. 44, pp. e717-e721, 2006.
- [73]. A. Moffet, "Minimum-redundancy linear arrays," in *IEEE Transactions on Antennas and Propagation*, vol. 16, no. 2, pp. 172-175, Mar 1968.
- [74]. A. Ramalli, E. Boni, A. S. Savoia and P. Tortoli, "Density-tapered spiral arrays for ultrasound 3-D imaging," in *IEEE Transactions on Ultrasonics, Ferroelectrics, and Frequency Control*, vol. 62, no. 8, pp. 1580-1588, August 2015.

- [75]. B. Diarra, M. Robini, P. Tortoli, C. Cachard and H. Liebgott, "Design of Optimal 2-D Nongrid Sparse Arrays for Medical Ultrasound," in *IEEE Transactions on Biomedical Engineering*, vol. 60, no. 11, pp. 3093-3102, Nov. 2013.
- [76]. M. Viganó, G. Toso, G. Caille, C. Mangenot and I. Lager, "Sunflower Array Antenna with Adjustable Density Taper", *International Journal of Antennas and Propagation*, vol. 2009, pp. 1-10, 2009.
- [77]. Shiwei Zhou, G. L. Wojcik and J. A. Hossack, "An approach for reducing adjacent element crosstalk in ultrasound arrays," in *IEEE Transactions on Ultrasonics, Ferroelectrics, and Frequency Control*, vol. 50, no. 12, pp. 1752-1761, Dec. 2003, doi: 10.1109/TUFFC.2003.1256316.
- [78]. G. Hayward and J. Hyslop, "Determination of lamb wave dispersion data in lossy anisotropic plates using time domain finite element analysis. Part I: theory and experimental verification," in *IEEE Transactions on Ultrasonics, Ferroelectrics, and Frequency Control*, vol. 53, no. 2, pp. 443-448, Feb. 2006, doi: 10.1109/TUFFC.2006.1593383.
- [79]. G. Hayward and J. Hyslop, "Determination of lamb wave dispersion data in lossy anisotropic plates using time domain finite element analysis. Part II: application to 2-2 and 1-3 piezoelectric composite transducer arrays," in *IEEE Transactions on Ultrasonics, Ferroelectrics, and Frequency Control*, vol. 53, no. 2, pp. 449-455, Feb. 2006, doi: 10.1109/TUFFC.2006.1593384.
- [80]. N. Lamberti, P. Gori, G. Caliano, A. Iula, R. Carotenuto and M. Pappalardo, "Radiation pattern distortion caused by the interelement coupling in linear array transducers," *1999 IEEE Ultrasonics Symposium. Proceedings. International Symposium (Cat. No.99CH37027)*, Caesars Tahoe, NV, 1999, pp. 1071-1075 vol.2, doi: 10.1109/ULTSYM.1999.849185.
- [81]. E. Franco, M. Andrade, J. Adamowski and F. Buiocchi, "Acoustic beam modeling of ultrasonic transducers and arrays using the impulse response and the discrete representation methods", *Journal of the Brazilian Society of Mechanical Sciences and Engineering*, vol. 33, no. 4, pp. 408-416, 2011.

- [82]. J. W. Wind, Y H. Wijnant and A. de Boer, "Fast evaluation of the Rayleigh integral and applications to inverse acoustics," International Congress on Sound and Vibration, 2006.
- [83]. S. Kirkup, "Fortran codes for computing the acoustic field surrounding a vibrating plate by the Rayleigh integral method", in *WSEAS international conference on Mathematical methods, computational techniques and intelligent systems*, 2008, pp. 364-369.
- [84]. S. Warshaw, "Time-domain acoustic pressure fields from axisymmetric impulse sources by Rayleigh's Integral", *The Journal of the Acoustical Society of America*, vol. 123, no. 5, pp. 3844-3844, 2008.
- [85]. J. Jensen, "Ultrasound Imaging and Its Modeling", in *Imaging of Complex Media with Acoustic and Seismic Waves*, M. Fink, W. Kuperman, J. Montagner and A. Tourin, Ed. Springer Verlag, 2000, pp. 135-166.
- [86]. J. Goodman, *Introduction to Fourier optics*. New York: McGraw-Hill, 1968.
- [87]. Y. Du, H. Jensen and J. A. Jensen, "Angular spectrum simulation of pulsed ultrasound fields," *2009 IEEE International Ultrasonics Symposium*, Rome, 2009, pp. 2379-2382.
- [88]. N. Ilyina, J. Hermans, K. Van Den Abeele and J. D'hooge, "Extension of the angular spectrum method to model the pressure field of a cylindrically curved array transducer", *The Journal of the Acoustical Society of America*, vol. 141, no. 3, pp. EL262-EL266, 2017.
- [89]. L. Ziomek, *Fundamentals of acoustic field theory and space-time signal processing*. Boca Raton: CRC Press, 1995, p. 416.
- [90]. B. Steinberg, "The peak sidelobe of the phased array having randomly located elements," in *IEEE Transactions on Antennas and Propagation*, vol. 20, no. 2, pp. 129-136, Mar 1972.
- [91]. "OnScale Cloud Engineering Platform | Multiphysics Simulation Software", *OnScale*, 2020. [Online]. Available: <https://onscale.com/>. [Accessed: 30- Mar- 2020].

- [92]. C. Holmes, B. Drinkwater and P. Wilcox, "Post-processing of the full matrix of ultrasonic transmit–receive array data for non-destructive evaluation", *NDT & E International*, vol. 38, no. 8, pp. 701-711, 2005.
- [93]. N. Dube, A. Lamarre and F. Mainguy, "Dynamic Focusing of Phased Arrays for Nondestructive Testing: Characterisation and Application", in *NDE in Relation to Structural Integrity for Nuclear and Pressurised Components*, Amsterdam, 1998, pp. 690-697.
- [94]. J. Hwang, "Principles of Ultrasound", in *Endosonography*, 4th ed., R. Hawes, P. Fockens and S. Varadarajulu, Ed. Elsevier, 2019, pp. 2-14.
- [95]. W. McDicken and T. Anderson, "The Difference Between Colour Doppler Velocity Imaging and Power Doppler Imaging", *European Heart Journal - Cardiovascular Imaging*, vol. 3, no. 3, pp. 240-244, 2002.
- [96]. L. Huckvale, "DIFFERENCE IMAGING ANALYSIS FOR VISTA VARIABLES IN THE V'IA LACTEA", PhD, University of Manchester, 2015.
- [97]. C. Alard and R. Lupton, "A Method for Optimal Image Subtraction", *The Astrophysical Journal*, vol. 503, no. 1, pp. 325-331, 1998.
- [98]. R. M. Haralick, S. R. Sternberg and X. Zhuang, "Image Analysis Using Mathematical Morphology," in *IEEE Transactions on Pattern Analysis and Machine Intelligence*, vol. PAMI-9, no. 4, pp. 532-550, July 1987.
- [99]. R. Gonzalez and R. Woods, *Digital image processing*, 2nd ed. Prentice Hall, 2002, pp. 519-532.
- [100]. R. Srisha and A. Khan, "Morphological Operations for Image Processing : Understanding and its Applications", in *National Conference on VLSI, Signal processing & Communications*, 2013.
- [101]. P. Hough, "Method and means for recognizing complex patterns", 3069654, 1962.
- [102]. R. Duda and P. Hart, "Use of the Hough transformation to detect lines and curves in pictures", *Communications of the ACM*, vol. 15, no. 1, pp. 11-15, 1972.

- [103]. B. Sit and M. Quraishi, "A Review Paper on Hough Transform and it's Applications in Image Processing", *International Journal of Innovative Research in Science, Engineering and Technology*, vol. 5, no. 13, pp. 206-213, 2016.
- [104]. S. Sarkar, S. Ghosh, S. Ghosh and A. Collier, "Role of transcranial Doppler ultrasonography in stroke", *Postgraduate Medical Journal*, vol. 83, no. 985, pp. 683-689, 2007.
- [105]. G. Tsivgoulis and A. Alexandrov, "Ultrasound-enhanced thrombolysis in acute ischemic stroke: Potential, failures, and safety", *Neurotherapeutics*, vol. 4, no. 3, pp. 420-427, 2007.
- [106]. "Ultrasonography Test (Transcranial Doppler) Test Details | Cleveland Clinic", *Cleveland Clinic*, 2020. [Online]. Available: <https://my.clevelandclinic.org/health/diagnostics/4998-ultrasonography-test-transcranial-doppler/test-details>. [Accessed: 20- Jan- 2016].
- [107]. *UPMC | Life Changing Medicine*, 2020. [Online]. Available: <https://www.upmc.com/health-library/article?hwid=hw4477#hw4492>. [Accessed: 04- Jan- 2020].
- [108]. N. Ivancevich, J. Dahl, G. Trahey and S. Smith, "Phase-aberration correction with a 3-D ultrasound scanner: feasibility study", *IEEE Transactions on Ultrasonics, Ferroelectrics and Frequency Control*, vol. 53, no. 8, pp. 1432-1439, 2006.
- [109]. N. M. Ivancevich *et al.*, "7A-5 Real-Time 3D Contrast-Enhanced Transcranial Ultrasound," *2007 IEEE Ultrasonics Symposium Proceedings*, New York, NY, 2007, pp. 550-553.
- [110]. B. Lindsey, E. Light, H. Nicoletto, E. Bennett, D. Laskowitz and S. Smith, "The ultrasound brain helmet: new transducers and volume registration for in vivo simultaneous multi-transducer 3-D transcranial imaging", *IEEE Transactions on Ultrasonics, Ferroelectrics and Frequency Control*, vol. 58, no. 6, pp. 1189-1202, 2011.
- [111]. M. Feldman, S. Katyal and M. Blackwood, "US Artifacts", *RadioGraphics*, vol. 29, no. 4, pp. 1179-1189, 2009.

- [112]. L. Lic. Mirko Panozzo Zéner, "SAR Image Quality Assesment", Master Degree, Universidad Nacional de Córdoba, 2012
- [113]. B. B. Baker and E. T. Copson, *The Mathematical Theory of Huygens' Principle*. American Mathematical Soc., 2003. 28
- [114]. J. Dziewierz, S. N. Ramadas, A. Gachagan, R. L. O'Leary and G. Hayward, "A 2D Ultrasonic array design incorporating hexagonal-shaped elements and triangular-cut piezocomposite substructure for NDE applications," *2009 IEEE International Ultrasonics Symposium*, Rome, 2009, pp. 422-425.
- [115]. R. L. O 'Leary, G. Hayward, G. Smillie, and A. C. S. Parr, "CUE Materials Database," Version 1., 2005.
- [116]. "Anisotropic Adhesives", *Creativematerials.com*, 2019. [Online]. Available: https://server.creativematerials.com/datasheets/DS_124_19.pdf. [Accessed: 08-Jan- 2019].
- [117]. L. Bjørnø, "Sonar Systems", in *Applied Underwater Acoustics*, T. Neighbors and D. Bradley, Ed. United States: Elsevier Science Publishing Co Inc, 2017.
- [118]. Mordfin, L. (2002). *Handbook of reference data for nondestructive testing*. West Conshohocken, Pa: ASTM International.
- [119]. "Material Sound Velocities | Olympus IMS", *Olympus-ims.com*, 2019. [Online]. Available: <https://www.olympus-ims.com/en/ndt-tutorials/thickness-gage/appendices-velocities/>. [Accessed: 02- May- 2019].
- [120]. L. Orloff, *Head and neck ultrasonography*, 2nd ed. San Diego: Pulral Publishing, Inc., p. 436.
- [121]. P. Blanco and A. Abdo-Cuza, "Transcranial Doppler ultrasound in neurocritical care", *Journal of Ultrasound*, vol. 21, no. 1, pp. 1-16, 2018. Available: 10.1007/s40477-018-0282-9.
- [122]. A. Atchabahian and R. Gupta, *The anesthesia guide*. New York: McGraw-Hill Medical, 2013.
- [123]. J. Kirsch, M. Mathur, M. Johnson, G. Gowthaman and L. Scutt, "Advances in Transcranial Doppler US: Imaging Ahead", *RadioGraphics*, vol. 33, no. 1, pp. E1-E14, 2013. Available: 10.1148/rg.331125071.

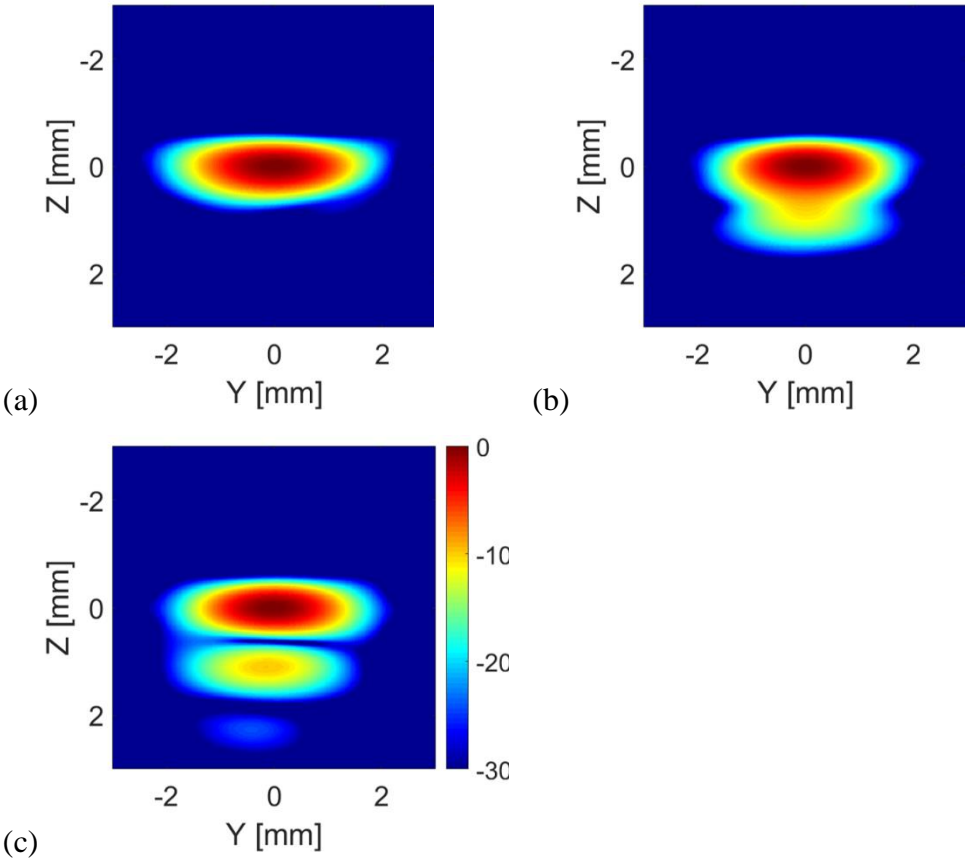
- [124]. M. Kassab et al., "Transcranial Doppler: An Introduction for Primary Care Physicians", *The Journal of the American Board of Family Medicine*, vol. 20, no. 1, pp. 65-71, 2007. Available: 10.3122/jabfm.2007.01.060128.
- [125]. A. J. Weir, R. Sayer, C. Wang and S. Parks, "A wall-less poly(vinyl alcohol) cryogel flow phantom with accurate scattering properties for transcranial Doppler ultrasound propagation channels analysis," *2015 37th Annual International Conference of the IEEE Engineering in Medicine and Biology Society (EMBC)*, Milan, 2015, pp. 2709-2712.
- [126]. *Ultrasonics - Flow measurement systems - Flow test object*. Geneva: International Electrotechnical Commission (IEC), 2001.
- [127]. K. Haworth, "MEDICAL ULTRASOUND ABERRATION CORRECTION VIA ACOUSTIC DROPLET VAPORIZATION AND TIME-REVERSAL ACOUSTICS", PhD, The University of Michigan, 2009.
- [128]. L. Bohs and G. Trahey, "A novel method for angle independent ultrasonic imaging of blood flow and tissue motion", *IEEE Transactions on Biomedical Engineering*, vol. 38, no. 3, pp. 280-286, 1991.

Appendices

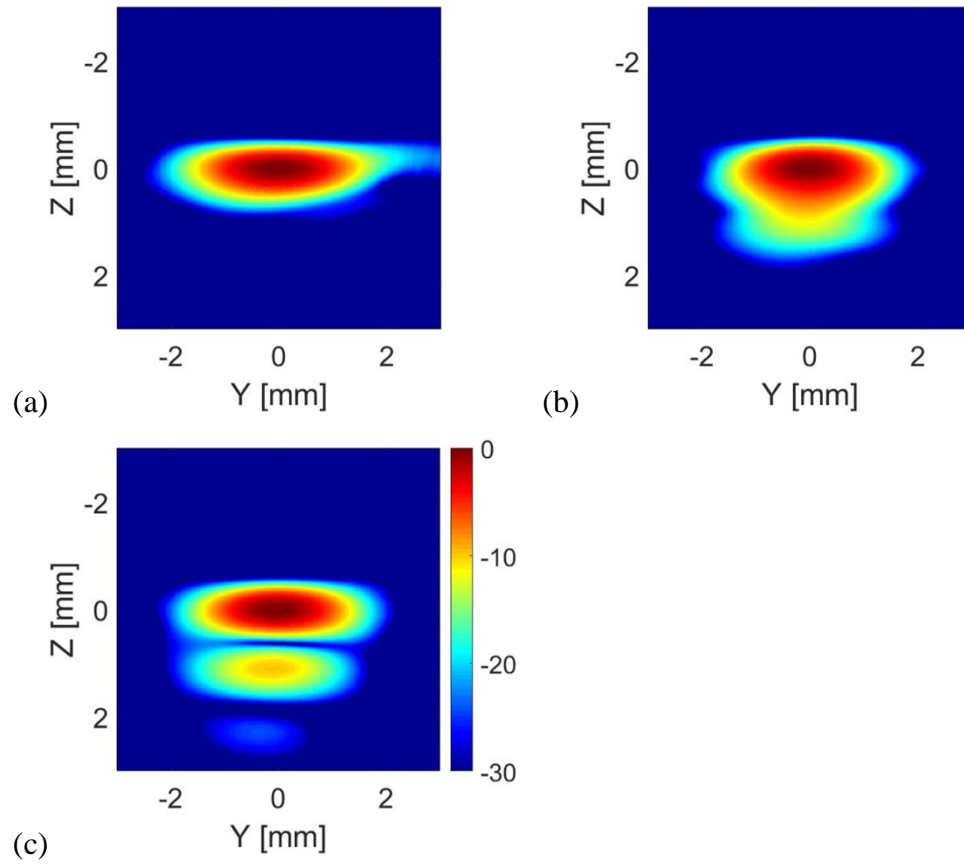
Appendix A: Properties for Materials Selected from CUE Database

	CIBA-GEIGY CY221-HY956 epoxy (medium set epoxy)		4% tungsten and CIBA- GEIGY CY1301- HY1300 epoxy (hard set epoxy)	
	1 MHz	2.25 MHz	1 MHz	2.25 MHz
Longitudinal Velocity [m/s]	2452	2441	2143	2188
Shear Velocity [m/s]	1110	1085	1027	1034
Density [kg/m^3]	1134		1677	
Impedance [$MRayl$]	2.8	2.8	3.6	3.6
Longitudinal Attenuation [dB/m]	895	1711	525	977
Shear Attenuation [dB/m]	4108	8147	979	2111

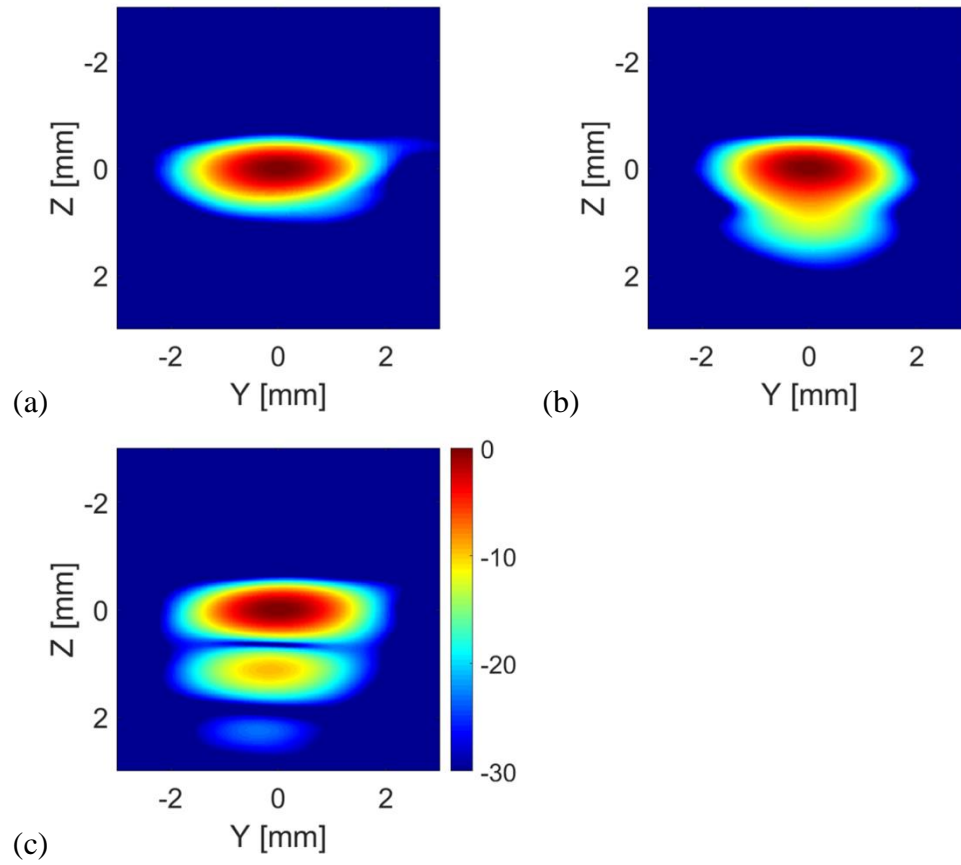
Appendix B: TFM Images of Single Small Diameter Reflectors with Different Size from the Three Prototype Transducers



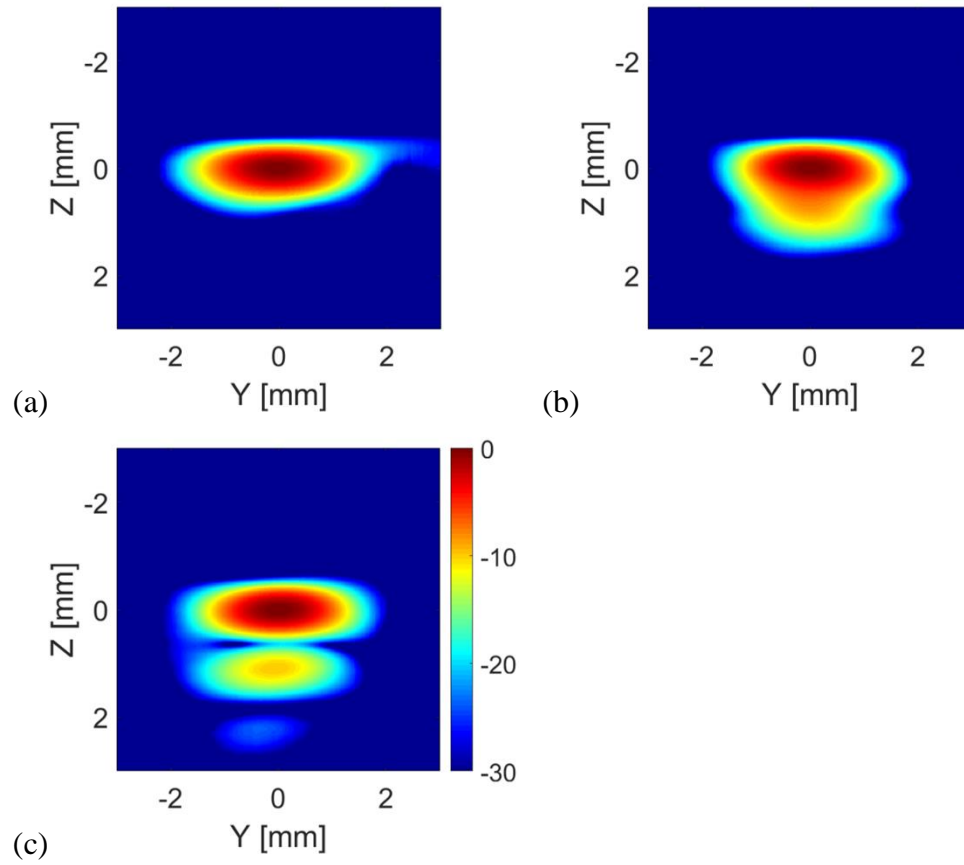
Appendix B.1 TFM images for imaging the 1.5 mm small diameter reflector using (a) the CECAT_79, (B) the C13_79, and (c) the C13_106



Appendix B.2 TFM images for imaging the 1 mm small diameter reflector using (a) the CECAT_79, (B) the C13_79, and (c) the C13_106

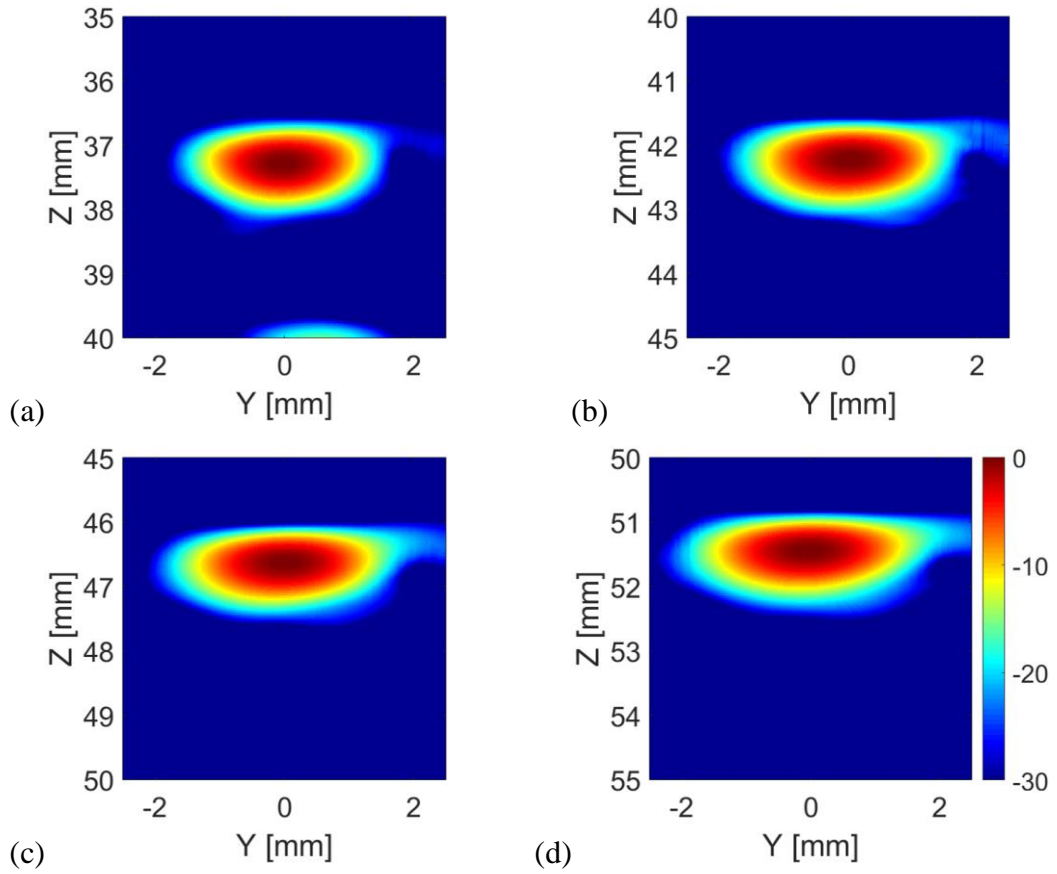


Appendix B.3 TFM images for imaging the 0.8 mm small diameter reflector using (a) the CECAT_79, (B) the C13_79, and (c) the C13_106

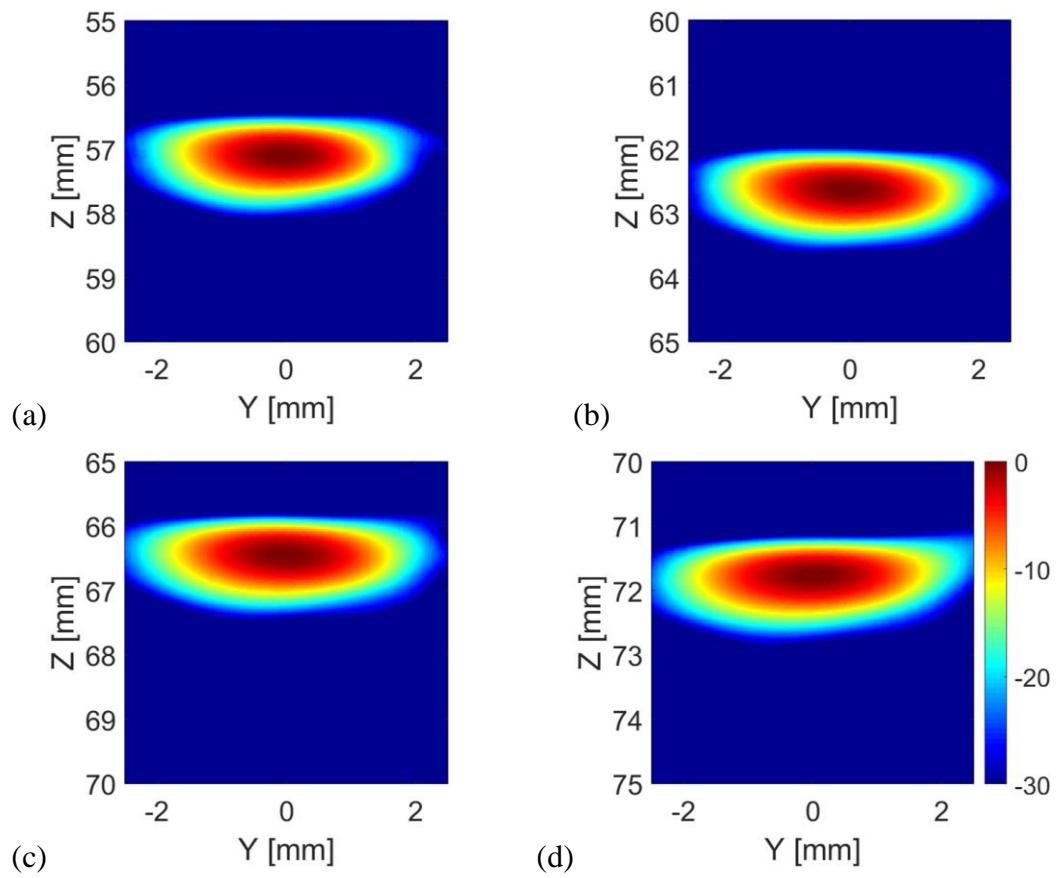


Appendix B.4 TFM images for imaging the 0.5 mm small diameter reflector using (a) the CECAT_79, (B) the C13_79, and (c) the C13_106

Appendix C: TFM Images of 0.8 mm Small Diameter Reflector within Different Depth Range from CECAT_79



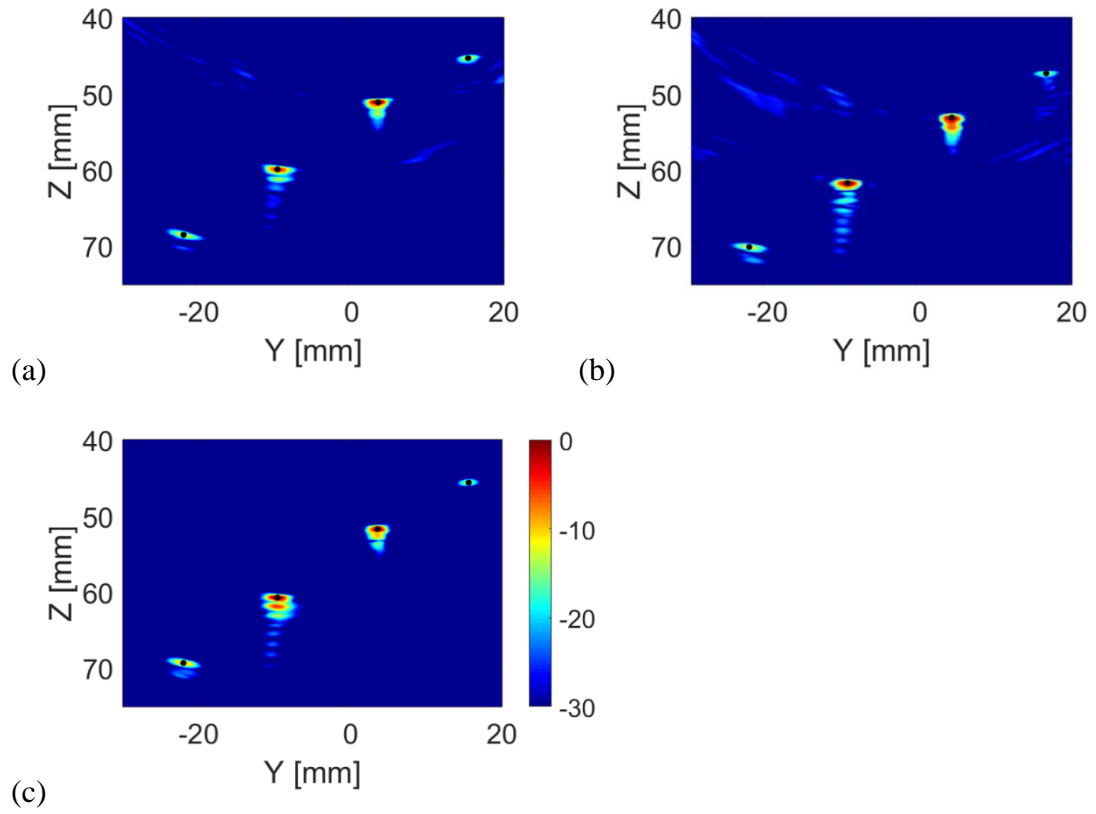
Appendix C.1 The TFM image of the 0.8 mm rod within the depth range of (a) 35 mm to 40 mm, (b) 40 mm to 45 mm, (c) 45 mm to 50 mm, and (d) 50 mm to 55 mm.



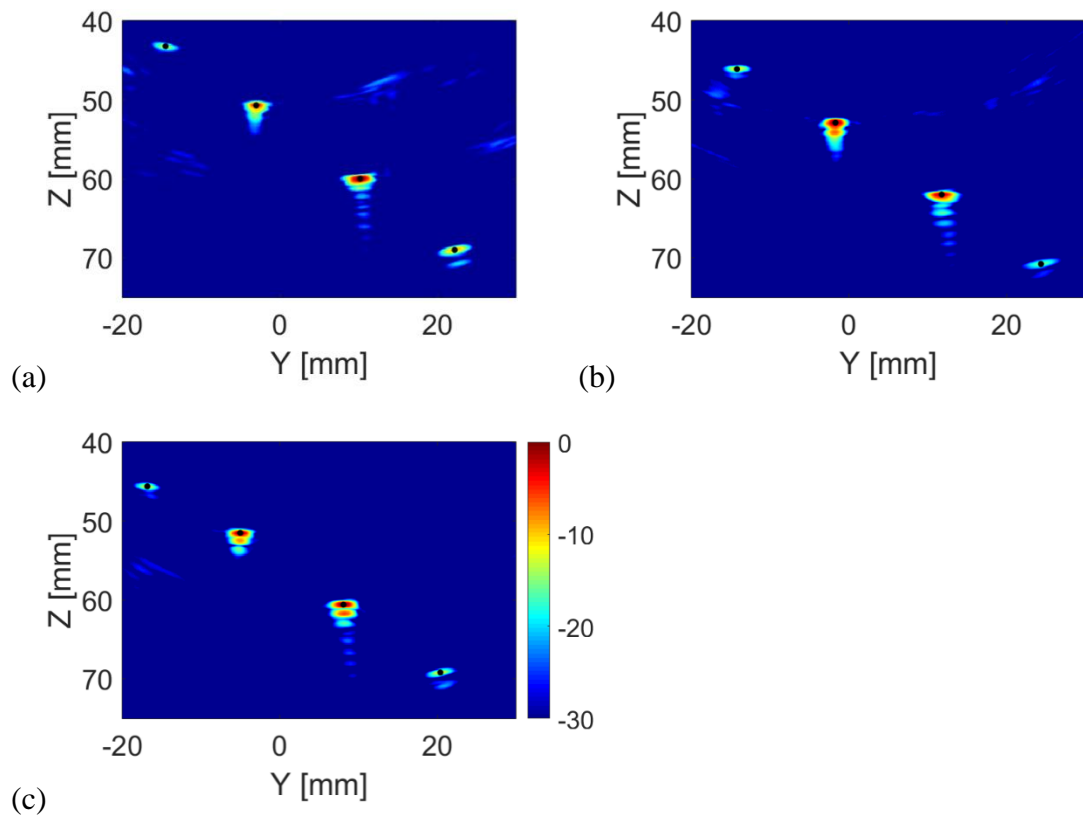
Appendix C.2 The TFM image of the 0.8 mm rod within the depth range of (a) 55 mm to 60 mm, (b) 60 mm to 65 mm, (c) 65 mm to 70 mm, and (d) 70 mm to 75 mm.

Appendix D: TFM Images of the Wire Phantom

from the Three Prototype Transducers



Appendix D. 1 The second group of the TFM images of the wire phantom from (a) the CECAT_79, (b) the C13_79, and (c) the C13_106.



Appendix D. 2 The third group of the TFM images of the wire phantom from (a) the CECAT_79, (b) the C13_79, and (c) the C13_106.